

## Formation of metallic-like nanodomains and vacancy defects in photochromic rare-earth oxyhydride films

Wu, Z.

### DOI

[10.4233/uuid:f9c335ad-3969-46a7-8531-249c9893c84e](https://doi.org/10.4233/uuid:f9c335ad-3969-46a7-8531-249c9893c84e)

### Publication date

2024

### Document Version

Final published version

### Citation (APA)

Wu, Z. (2024). *Formation of metallic-like nanodomains and vacancy defects in photochromic rare-earth oxyhydride films*. [Dissertation (TU Delft), Delft University of Technology].  
<https://doi.org/10.4233/uuid:f9c335ad-3969-46a7-8531-249c9893c84e>

### Important note

To cite this publication, please use the final published version (if applicable).  
Please check the document version above.

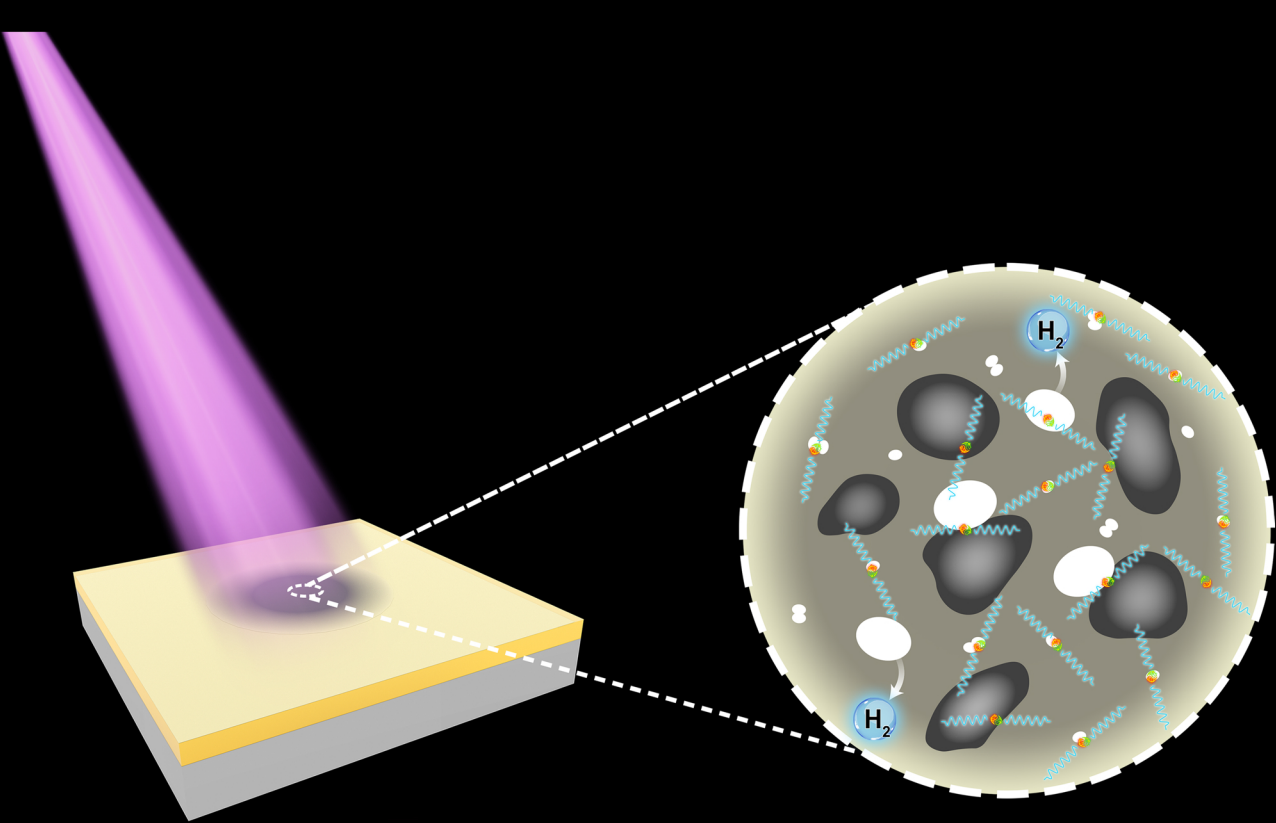
### Copyright

Other than for strictly personal use, it is not permitted to download, forward or distribute the text or part of it, without the consent of the author(s) and/or copyright holder(s), unless the work is under an open content license such as Creative Commons.

### Takedown policy

Please contact us and provide details if you believe this document breaches copyrights.  
We will remove access to the work immediately and investigate your claim.

# Formation of metallic-like nanodomains and vacancy defects in photochromic rare-earth oxyhydride films



Ziying Wu



# **Formation of metallic-like nanodomains and vacancy defects in photochromic rare- earth oxyhydride films**

Ziying WU



# **Formation of metallic-like nanodomains and vacancy defects in photochromic rare- earth oxyhydride films**

Dissertation

for the purpose of obtaining the degree of doctor  
at Delft University of Technology  
by the authority of the Rector Magnificus prof. dr. ir. T.H.J.J. van der Hagen  
chair of the Board for Doctorates  
to be defended publicly on  
Thursday 12 December 2024 at 15:00 h

by

**Ziying WU**

Master of Science in Medicinal Biology  
South China University of Technology, China  
Born in Dongguan, China

This dissertation has been approved by the promotor.

Composition of the doctoral committee:

Rector Magnificus,	chairperson
Prof. dr. E. H. Brück	Delft University of Technology , promotor
Dr. S. W.H. Eijt	Delft University of Technology, promotor

Independent members:

Dr. A. Baldi	Vrije Universiteit Amsterdam
Prof. dr. mgr. J. Čížek	Charles University Prague, Czech Republic
Prof. dr. P. Dorenbos	Delft University of Technology
Prof. dr. ir. O. Isabella	Delft University of Technology
Dr. E. van der Kolk	Delft University of Technology (reserve member)

Other members:

Em. prof. dr. B. Dam	Delft University of Technology
----------------------	--------------------------------



The research presented in this thesis was carried out at the Fundamental Aspects of Materials and Energy (FAME) group of the Department of Radiation Science and Technology, Faculty of Applied Sciences, Delft University of Technology, the Netherlands, in close collaboration with Prof. dr. B. Dam, Materials for Energy Conversion and Storage (MECS) group, Department of Chemical Engineering. This research is financially supported by the Oversea Study Program of Guangzhou Elite Project and the Materials for Sustainability (Mat4Sus) research programme (project number 680.M4SF.034) financed by the Dutch Research Council (NWO).

ISBN: 978-94-6384-686-8

Copyright © 2024 by Ziyang Wu

Printed by Proefschrift specialist

An electronic version of this dissertation is available at: <http://respository.tudelft.nl/>.

*Dedicated to my family*



# Contents

<b>1. Introduction .....</b>	<b>1</b>
1.1 Inorganic photochromic materials and potential applications .....	2
1.2 Rare-earth oxyhydride thin films .....	4
1.3 Positron annihilation spectroscopy and spectroscopic ellipsometry .....	6
1.4 Thesis outline .....	11
References.....	13
 <b>2. Formation of vacancies and metallic-like domains in photochromic rare-earth oxyhydride thin films studied by in-situ illumination positron annihilation spectroscopy .....</b>	 <b>19</b>
Abstract.....	20
2.1 Introduction.....	21
2.2 Experiment.....	22
2.3 Results and discussion .....	24
2.3.1 Open-volume defects in Y-based thin films examined by PALS.....	24
2.3.2 Evolution of the electronic structure of Y-based and Gd-based thin films observed by DB-PAS .....	30
2.3.3 In-situ illumination positron Doppler study of the nanostructural evolution of photochromic $\text{YH}_x\text{O}_y$ and $\text{GdH}_x\text{O}_y$ films during photo-darkening and bleaching.....	31
2.4 Conclusions.....	44
References.....	45
Supplementary information for Chapter 2 .....	51
 <b>3. The memory effect in photochromic rare-earth oxyhydride thin films studied by in-situ positron annihilation spectroscopy upon photodarkening-bleaching cycling.....</b>	 <b>59</b>
Abstract.....	60
3.1 Introduction.....	61
3.2 Experimental .....	62
3.3 Results.....	65
3.3.1 Photochromic responses upon cycling .....	65
3.3.2 Microstructural changes investigated by in-situ illumination positron annihilation.....	67
3.3.3 Correlation between photochromic responses and microstructural changes .....	70
3.3.4 Nature of the vacancy-related defects induced by cycling investigated by PALS .....	71

3.4 Discussion .....	75
3.5 Conclusions.....	78
References.....	79
Supplementary information for Chapter 3 .....	83
References.....	89
<b>4. Time dependent evolution of vacancies and metallic domains and their correlation with the photochromic effect in yttrium oxyhydride films revealed by in-situ illumination positron annihilation lifetime spectroscopy.....</b>	<b>91</b>
Abstract .....	92
4.1 Introduction.....	93
4.2 Experimental .....	94
4.3 Results and discussion .....	96
4.3.1 Photochromic properties .....	96
4.3.2 In-situ illumination positron lifetime experiments .....	97
4.3.3 Second PALS experiment .....	111
4.4 Conclusions.....	113
References.....	115
Supplementary information for Chapter 4 .....	121
<b>5. The formation of metallic domains by Anderson-Mott insulator-to-metal transition in photochromic yttrium oxyhydride films studied by in-situ spectroscopic ellipsometry .....</b>	<b>127</b>
Abstract.....	128
5.1 Introduction.....	129
5.2 Experimental .....	130
5.3 Results and discussion .....	132
5.3.1 The crystal structure and optical constants of as-prepared semiconducting $\text{YH}_x\text{O}_y$ and metallic Y, $\text{YH}_x$ , $\text{YH}_{-2}$ thin films .....	132
5.3.2 The photochromic effect .....	135
5.3.3 Spectroscopic ellipsometry study during photodarkening.....	136
5.4 Conclusions.....	144
References.....	145
Supplementary information for Chapter 5 .....	149
References.....	155
<b>6. General conclusions and future outlook.....</b>	<b>157</b>



<b>Summary .....</b>	<b>159</b>
<b>Samenvatting.....</b>	<b>163</b>
<b>Acknowledgements .....</b>	<b>167</b>
<b>Curriculum Vitae.....</b>	<b>169</b>
<b>List of publications .....</b>	<b>171</b>



# 1. Introduction

## 1.1 Inorganic photochromic materials and potential applications

Photochromism is defined as a light-induced reversible transformation of a substance between two forms that have two different optical absorption spectra. The photochromic phenomenon was first reported in 1867 by J. Fritzsche, who observed the bleaching of orange tetracene solutions in sunlight and the recovery of the orange color in the dark [1]. In 1951, Yehuda Hirshberg created the term "photochromism" to describe a reversible and repeatable color change upon light exposure [2]. In addition to light, other stimuli such as electric fields, temperature, gases, chemical species, mechanical forces can also trigger a color change in certain materials. These phenomena are termed photochromic, electrochromic, thermochromic, gasochromic, chemochromic, and mechanochromic, respectively.

The photochromic phenomenon can occur in both inorganic and organic systems. Inorganic photochromic materials offer distinct advantages over organic ones, such as high thermal stability and excellent chemical resistance [3]. A broad spectrum of inorganic photochromic materials exists, including silver halide glasses [4], transition metal oxides ( $\text{WO}_3$ ,  $\text{MoO}_3$ ,  $\text{V}_2\text{O}_5$ ,  $\text{Nb}_2\text{O}_5$ , etc.) [5], rare-earth doped  $\text{CaF}_2$  [6], certain natural minerals (Hackmanite  $\text{Na}_8\text{Al}_6\text{Si}_6\text{O}_{24}\text{Cl}_2$  and Tugtupite  $\text{Na}_4\text{AlBeSi}_4\text{O}_{12}\text{Cl}$ ) [7], and so on. These materials exhibit various absorption characteristics and corresponding photochromic mechanisms.

Among the classic inorganic photochromic materials, silver halide glasses have attracted significant attention due to their photochromic effect since the 1960s [4]. These glasses are composed of a glass matrix, typically borosilicate or aluminoborosilicate, homogeneously embedded with copper-doped silver halides crystallites. In commercialized photochromic glasses, the concentration of Cu-doped AgCl crystallites, with an average diameter of  $\sim 10$  nm, is about 0.2-0.7 wt% (weight percent), and the distance between these crystallites is of the order of  $\sim 100$  nm [6,8]. Silver halide crystals are wide-bandgap semiconductors, with bandgaps ranging from  $\sim 3.2$  eV to 2.4 eV for AgCl to AgI, respectively [9]. When illuminated by photons with an energy above the bandgap of the silver halide, electron-hole pairs are generated. The photo-excited electrons are captured by interstitial  $\text{Ag}^+$  ions to form  $\text{Ag}^0$  ( $e^- + \text{Ag}^+ \rightleftharpoons \text{Ag}^0$ ), which is mobile and can form clusters, while the holes are captured by  $\text{Cu}^+$  dopants to form  $\text{Cu}^{2+}$ , preventing the formation of  $\text{Cl}_2$  [10]. Ag clusters with sizes above about 1 nm absorb light, with an absorption peak with its maximum positioned in the wavelength range between 400 and 800 nm [11]. Note that the size of the metallic-like Ag clusters formed under illumination dominates the color of the glasses. For example, the color varies from yellow to purple as the size of Ag clusters increases from 8 to 30 nm [12]. Additionally, it was demonstrated that the shape of Ag nanoparticles significantly influences the absorption properties and color both in water solutions and when embedded in a  $\text{TiO}_2$  matrix [13,14]. The photochromism in Cu-doped AgCl can be described by a reduction-oxidation reaction ( $\text{Cu}^+ + \text{Ag}^+ \rightleftharpoons \text{Ag}^0 + \text{Cu}^{2+}$ ) and the reverse bleaching process occurs when the light source is removed [10].

Another well-known example of an inorganic photochromic material is tungsten oxide ( $\text{WO}_3$ ), which can repeatedly switch from transparent to blue upon light exposure.  $\text{WO}_3$  compounds are n-type semiconductors with an indirect bandgap ranging from 2.6 to 3.4 eV [15,16]. Initially, the formation of F-like color centers and a double-charge-injection model were proposed to explain the photochromism of  $\text{WO}_3$  [17]. In the double-charge-injection model [18], hydrogen tungsten bronze  $\text{H}_x\text{WO}_3$  is formed due to the injection of electrons and protons from the external environment upon above bandgap excitation. However, the expected increase in H content of the films was not experimentally observed [19]. Later, an advanced model involving absorbed  $\text{H}_2\text{O}$  was proposed [20]. This model was supported by findings in ref. [21], which linked the amount of absorbed  $\text{H}_2\text{O}$  at the surface to the photo-induced optical density of the films. When  $\text{WO}_3$  is illuminated by light with a photon energy above its bandgap, electron-hole pairs are generated. Subsequently, the holes react with the absorbed water molecules and generate protons and oxygen ( $4h^+ + 2\text{H}_2\text{O} \rightarrow 4\text{H}^+ + \text{O}_2(g) \uparrow$ ), while the photo-excited electrons reduce W ions and create  $\text{W}^{5+}$  cations ( $\text{WO}_3 + x\text{H}^+ + xe^- \rightarrow \text{H}_x\text{W}_{1-x}^{6+}\text{W}_x^{5+}\text{O}_3$ ), leading to a color change from transparent to blue. Bleaching of the film occurs when oxygen is absorbed by the film and the chemical reactions described above are reversed.

The reversible optical coloring and bleaching characteristics and the accompanying physical and chemical properties of inorganic photochromic materials render them promising for applications in sunglasses [8], smart windows [22], optical information storage [2], photocatalysis [23], wearable fabric [24]. Fig. 1.1 shows that research publications and citations on "inorganic photochromic materials" have steadily increased over the past decades.

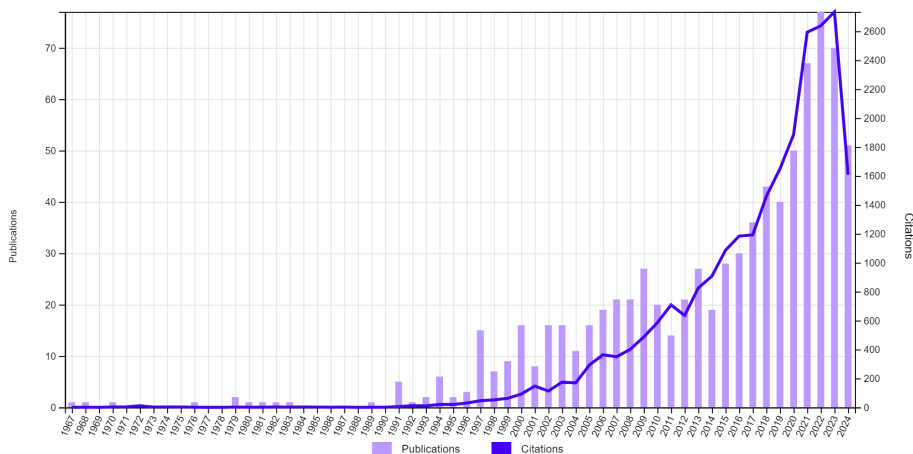


**Figure 1.1** Research publications and citations for different years for inorganic photochromic materials, using “inorganic photochromic” as the search word (Web of Science, July 20<sup>th</sup>, 2024).

## 1.2 Rare-earth oxyhydride thin films

Rare-earth oxyhydride ( $\text{REH}_x\text{O}_y$ ) thin films are an emerging class of inorganic photochromic materials. Polycrystalline yttrium oxyhydride thin films were first identified to exhibit photochromic properties under ambient conditions in 2011 [25].  $\text{REH}_x\text{O}_y$  are transparent semiconductors with a bandgap typically above  $\sim 2$  eV, depending on the cation and deposition pressure [26-30]. Upon optical excitation above the bandgap, these films exhibit a color-neutral photochromic effect in which they absorb light across a broad wavelength range (visible and near-IR up to  $\sim 2500$  nm), unlike most inorganic photochromic materials which have specific absorption peaks. When the light is switched off, the transparency of  $\text{REH}_x\text{O}_y$  films is recovered. So far, rare-earth (RE) oxyhydride thin films with the RE cation including Y, Gd, Sc, Nd, Dy, Er, and Sm have been discovered to exhibit the color-neutral photochromic effect [26-31].

The preparation of such photochromic  $\text{REH}_x\text{O}_y$  films involves a two-step process. First, rare-earth dihydride ( $\text{REH}_2$ ) films are deposited by reactive magnetron sputtering at room temperature on unheated fused-silica substrates above a critical pressure, necessary to ensure sufficient porosity for subsequent oxidation. The critical pressure is approximately 0.6 Pa for  $\text{NdH}_x\text{O}_y$ ,  $\text{SmH}_x\text{O}_y$ ,  $\text{GdH}_x\text{O}_y$ ,  $\text{DyH}_x\text{O}_y$ , and  $\text{ErH}_x\text{O}_y$ , and 0.3 Pa and 0.4 Pa for  $\text{ScH}_x\text{O}_y$  and  $\text{YH}_x\text{O}_y$  [26,29-32]. Second, upon exposure to air, these dihydride films oxidize and become transparent. This oxidation process is accompanied by a change in the valence state of RE from  $\text{RE}^{2+}$  to  $\text{RE}^{3+}$ . Assuming full oxidation of the RE cation to  $\text{RE}^{3+}$ , the minimum oxygen amount with  $x=0.5$  is obtained for semiconducting  $\text{REH}_{3-2x}\text{O}_x$  [27].

In  $\text{REH}_2$ , all hydrogen atoms are positioned at tetrahedral sites of the fcc lattice, while in  $\text{REH}_2\text{O}_{0.5}$ , each oxygen ion displaces one tetrahedral hydrogen ion to an octahedral site, resulting in half of the octahedral sites being occupied by hydrogen. This configuration is based on a face-centered cubic (fcc)-based model proposed by Cornelius et al. [27]. Subsequently, an EXAFS study confirmed that oxide anions preferentially occupy the tetrahedral sites, as this minimizes the electrostatic lattice energy [33]. The proposed occupancy of hydrogen and oxygen anions for  $\text{REH}_2$  and  $\text{REH}_x\text{O}_y$ , compared to that of  $\text{REH}_3$  and  $\text{RE}_2\text{O}_3$  is illustrated in Fig. 1.2 [27]. As the O:H ratio increases for  $\text{REH}_{3-2x}\text{O}_x$  when  $x$  increases from 0.5 to 1, the content of oxygen sitting at the tetrahedral sites increases, while the number of octahedral hydrogen decreases. When the O:H ratio reaches 1:1, there is no hydrogen occupying the octahedral sites, with tetrahedral sites equally occupied by oxygen and hydrogen.  $\text{REH}_x\text{O}_y$  films deposited at a higher pressure (exceeding the critical pressure) possess a higher O:H ratio due to the increased porosity and subsequently larger post-oxidation of the dihydride films, and exhibit a weaker photochromic effect [32,34]. In addition to the O:H ratio, other strategies such as cation variation [26,32], doping [35], and annealing [29] can significantly influence the photochromic properties. The tuneable color-neutral photochromic effect and additional light-induced properties, such as photo-

conductivity, make  $\text{REH}_x\text{O}_y$  films promising candidates for applications in smart windows [22,31], memory devices [36], and photo-catalysts [37].

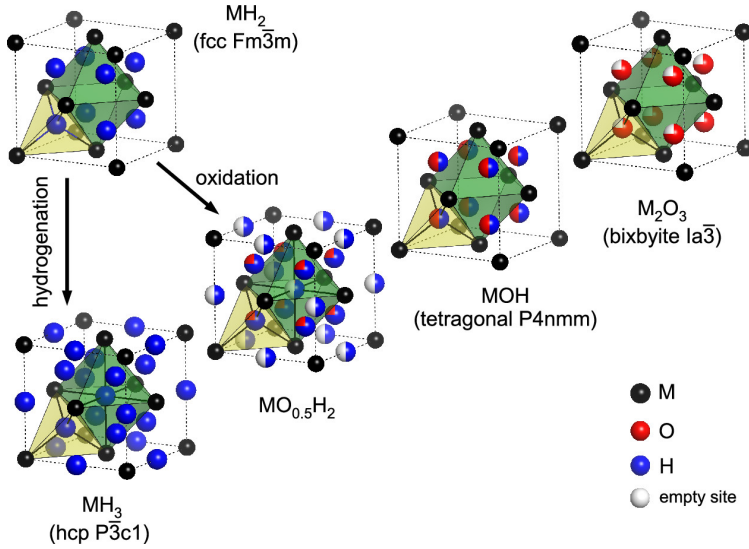


**Figure 1.2** Crystal structure and the lattice site occupancy of anions in  $\text{MH}_2$ ,  $\text{MH}_2\text{O}_{0.5}$ ,  $\text{MOH}$ ,  $\text{MH}_3$  and  $\text{M}_2\text{O}_3$  based on the fcc-fluorite ( $\text{Fm}\bar{3}\text{m}$ ) structure motif. Reprinted from [27].

However, at the time of starting this research, the mechanism underlying the photochromic effect and the memory effect (slower rate of bleaching upon cycling) [25] in  $\text{REH}_x\text{O}_y$  was not well understood, and studies on these mechanisms were limited.

In 2017, Montero et al. [38] proposed the formation of phase-segregated metallic domains to explain the photodarkening of  $\text{YH}_x\text{O}_y$  films, as the optical transmittance and ellipsometry data of  $\text{YH}_x\text{O}_y$  during illumination could be modelled well by the formation of metallic domains with a volume fraction up to 6%. Later, positron annihilation studies [39,40] showed that the S-parameter increases during UV illumination and remains after bleaching, suggesting the light-induced formation of open-volume defects and indirectly supporting (hydrogen) ion mobility during photodarkening. Significant findings and insights into the photochromism and mechanism in  $\text{REH}_x\text{O}_y$  films can be found in two recent review articles [31,41].

This thesis focuses on: i) investigating the nature of metallic domains and their evolution during photodarkening and bleaching to better understand the mechanism of the photochromism, and ii) examining the nature of open-volume defects before, during and after illumination, to elucidate their formation mechanism and their potential role in the slowing down of the bleaching kinetics in  $\text{REH}_x\text{O}_y$  films upon cycling (the so-called memory effect).

A deeper understanding of these aspects may enable optimizing the control and design of  $\text{REH}_x\text{O}_y$  films with desired photochromic properties for various future applications.

### 1.3 Positron annihilation spectroscopy and spectroscopic ellipsometry

1

In this section, the main features of the two most important techniques applied in this thesis to study properties of photochromic films are described, namely positron annihilation spectroscopy and spectroscopic ellipsometry.

#### 1.3.1 Positron annihilation spectroscopy

Positron annihilation spectroscopy (PAS) is a powerful non-destructive tool to characterize open-volume defects at the atomic scale in solids. The positron as the antiparticle of the electron was predicted by Paul Dirac in 1928 [42] and it was experimentally discovered by Carl Anderson in 1932 using a cloud chamber to observe cosmic rays [43]. Since the 1950s, the annihilation properties of positrons (e.g. annihilation rate and positron lifetime) with electrons have been widely studied in various types of materials. By the late 1960s, it became evident that positrons could be trapped by lattice defects and cavities in materials and positrons could be used for studies of defects in materials, for instance, the color center in NaCl crystals [44]. In the 1980s, the development of variable energy slow positron beams [45] and the theory of positrons in semiconductors and defects [46] enabled the application of PAS to thin films, which sparked increased interest in PAS from the 1990s onward. The investigation of vacancy-type defects in semiconductors and metals by the use of PAS have been thoroughly reviewed in several excellent review articles [47-50].

When implanted into a solid, positrons encounter a very fast ( $< 10^{-15}$  s) energy loss process through inelastic collisions with core electrons. This is followed by a thermalization process, during which the positrons further loose energy to around a few tens of meV over a period of  $10^{-12}$  s (typically 1-3 ps for semiconductors and metals [51,52]) via excitation of plasmons, electron-hole pairs or phonons. After thermalization, the positron diffuses through the space between atoms in the lattice until it annihilates with an electron, emitting in most cases two gamma rays of  $\sim 511$  keV in approximately opposite directions, according to the conservation laws of energy and momentum. In an ideal, defect-free crystal lattice, thermalized positrons are in a free delocalized Bloch-like state. In the presence of open-volume defects, positrons can be easily trapped at these vacant sites in most cases, due to the reduced Coulomb repulsion from the ion cores, leading to a localized positron state. Some thermalized positrons may form positronium (Ps), a bound state of a positron and an electron, particularly in the presence of pores/voids in semiconductors or insulators. Ps can exist in two forms based on the spin states: para-positronium (p-Ps), which is in a singlet state ( $S=0$ ,  $m_s=0$ ), and ortho-positronium (o-Ps), which is a triplet state ( $S=1$ ,  $m_s=0, \pm 1$ ). They typically form in a ratio of approximately 1:3 (as in vacuum). p-Ps has a lifetime of  $\sim 125$  ps in vacuum,



and it decays into two gamma rays of  $\sim 511$  keV each in opposite directions, while o-Ps has a lifetime of  $\sim 142$  ns in vacuum and it decays via three-gamma annihilation. In solids, o-Ps can pick up an electron from the local surrounding with a spin opposite to that of the positron and decay into two gamma rays, such that the effective lifetime of o-Ps can be reduced to a few ns in voids [53]. This process is named pick-off annihilation.

In addition, positrons can also be trapped by nanoclusters in a semiconducting or metallic matrix, provided that the nanoclusters (with a different electronic structure) have a higher positron affinity than the matrix [54]. The trapping of positrons at precipitates was first observed in single crystals of the Al-Zn alloy using one dimensional angular correlation of annihilation radiation (1D-ACAR) by Sedov et al. in 1970 [55]. Later, the kinetics of formation of nanoprecipitates in age-hardening metal alloys was extensively studied employing PAS [56,57]. Additionally, PAS has been used to investigate Cu nanoparticles embedded in Fe, as well as Li, Au, Kr nanoclusters and  $\text{Li}_2\text{CO}_3$  precipitates embedded in MgO [54,58-62].

Thus, PAS may provide key insights into the nature and evolution of metallic domains and open-volume defects in photochromic  $\text{REH}_x\text{O}_y$  films.

The most common positron annihilation techniques used for studying open-volume defects and nanoclusters in semiconductors and metals are Doppler broadening positron annihilation spectroscopy (DB-PAS) and positron annihilation lifetime spectroscopy (PALS).

### DB-PAS

In the annihilation process, where two gamma photons are emitted into opposite directions, energy and momentum conservation dictates that the energy of the each photon is  $E_\gamma = m_0c^2 \pm \frac{1}{2}p_{//}c$  in the laboratory frame, where  $m_0c^2$  is 511 keV and  $p_{//}$  represents the momentum component of the electron-positron pair parallel to one of the gamma rays. Given that the momentum of the thermalized positron is relatively low (energy of a few tens of meV), the Doppler broadening of the 511 keV annihilation line is mostly determined by the momentum of the annihilation electrons.

In DB-PAS, the shape parameter (S-parameter) and the wing parameter (W-parameter) are used to represent the low-momentum and high-momentum regions of the positron-electron momentum distribution. For the DB-PAS instrument VEP at TU Delft [63], the low momentum S-parameter and high momentum W-parameter were defined as, respectively, the number of annihilation events (1) in the central area with an energy window of  $|E| < 0.77$  keV (or electron momentum  $|p| < 3.0 \times 10^{-3} m_0c$ ) and (2) in the area with a energy window of  $2 \text{ keV} < |E| < 6 \text{ keV}$  ( $8.2 \times 10^{-3} m_0c < |p| < 23.4 \times 10^{-3} m_0c$ ), divided by the total annihilation events under the gamma photopeak around 511 keV. The definitions of the S-parameter and W-parameter are illustrated in a representative energy spectrum of gamma rays emitted from positron-electron annihilation near  $\sim 511$  keV, as shown in Fig. 1.3.

Typically the annihilation of positrons with valence and conduction electrons contributes to the S-parameter due to the low localization (low momentum) characteristic of these electrons. Furthermore, as shown in Fig. 1.3, the presence of open-volume defects results in a higher S-parameter compared with that for the defect-free lattice region. This increase occurs because the probability of annihilation of the localized positron at a vacancy with a low-momentum valence electron is higher, owing to the strong reduced overlap of the positron wave function with (semi)core electrons of the neighbouring atoms. On the other hand, primarily the annihilation of positrons with high-momentum (semi)core electrons (inner shell of electrons in atoms) contributes to the W-parameter. Hence, the W-parameter is sensitive to the local chemical environment of surrounding atoms at the positron annihilation site. The presence of atomic nanoclusters with a different electronic structure than the embedding matrix could change the S and W parameters significantly, assuming that those clusters can effectively trap positrons.

The variable-energy slow positron beam (0.1-30 keV) used in DB-PAS allows us to probe thin-film samples with thicknesses of up to a few micrometer. The mean implantation depth  $\bar{z}$  in nm in a material with density  $\rho$  in g/cm<sup>3</sup> can be calculated as a function of positron implantation energy  $E$  in keV according to  $\bar{z}(E) = \frac{AE^n}{\rho}$ , and we used  $n=1.6$  and  $A=4 \mu\text{g cm}^{-2}$  keV<sup>-n</sup> [64,65]. By varying the positron implantation energy, one can obtain a depth profile for the film sample. The S and W parameter, measured as a function of positron implantation energy can be analyzed using VEPFIT [66]. This program solves the equations for positron implantation and diffusion of thermalized positrons, enabling the extraction of parameters such as the S and W parameter and the positron diffusion length  $L_+$  for each layer in a multi-layered sample.

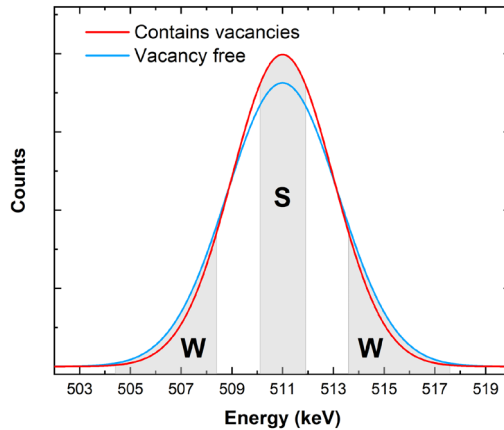


**Figure 1.3** Energy distribution of the annihilation gamma rays for a vacancy-free sample (blue line) and a vacancy-containing material (red line) and the representative energy windows for the S-parameter and the W-parameter.

## PALS

PALS is a powerful technique for identifying and quantifying open-volume defects in solid, providing detailed information on their size and the concentration. The positron lifetime depends solely on the local electron density encountered by the positron, described by  $\tau = \frac{1}{\lambda}$  and  $\lambda = \pi r_0^2 c n_e$ , where  $\lambda$  is the corresponding annihilation rate,  $r_0$  is the classical electron radius,  $n_e$  is the electron density, and  $c$  is the speed of light [53]. The positron bulk lifetime refers to the lifetime value of positrons annihilating in defect-free regions of a material. Longer lifetime components indicate positron annihilation in regions with a lower electron density, such as vacancies or voids. In addition, the positron lifetime increases with the size of vacancy defects, due to the reduced local electron density. A representative example of theoretically calculated positron lifetimes for bulk (defect-free) crystalline silicon (c-Si) and for vacancy clusters in c-Si is shown in Fig. 1.4 [67]. In defect-free c-Si, the positron bulk lifetime is  $\sim 220$  ps, and the positron lifetime increases from  $\sim 250$  ps for monovacancies to  $\sim 420$  ps for  $V_{10}$ , after which positron lifetime tends to saturate.

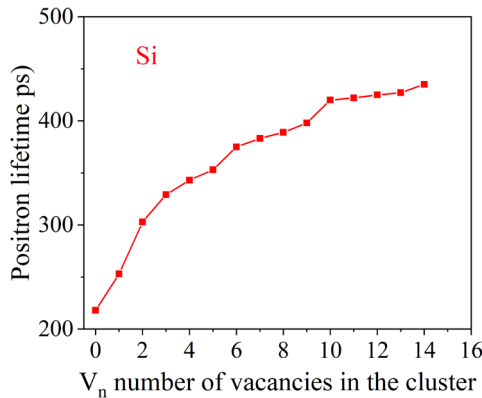


**Figure 1.4** The calculated positron lifetime versus the number of vacancies in a vacancy cluster in c-Si, data extracted from ref. [67].

The concentration of vacancy defects can be determined using a defect trapping model, provided that the concentration of vacancy defects is above  $\sim 10^{-7}$  and positron saturation trapping does not occur, i.e. the concentration does not exceed  $\sim 10^{-4}$  [53]. The positron trapping rate  $k_d$  is proportional to the vacancy concentration  $C_d$ , following  $k_d = \mu_d C_d$ , where  $\mu_d$  is the trapping coefficient. In the defect trapping model,  $k_{di}$  for the number of defects  $i$  can be calculated by solving the rate equations, assuming that the open-volume defects are non-interacting [53]. For example, in the single-defect trapping model (only one type of vacancy is present),  $k_d$  is given by  $k_d = I_2(\frac{1}{\tau_1} - \frac{1}{\tau_2})$ . Hence, the concentration of vacancies can be estimated from their respective positron lifetime parameters, as typically the  $\mu_d$  at negatively charged vacancies is approximately  $10^{15}$  to  $10^{16} \text{ s}^{-1}$  at 300 K and the  $\mu_d$  at neutral vacancies

is  $\sim 10^{14}$ - $10^{15} \text{ s}^{-1}$ , independent of temperature [49,53]. More details on the defect trapping model and the calculation of the concentration of vacancy defects can be found in ref. [53].

Therefore, in this thesis both DB-PAS and PALS are applied to explore the nature and the evolution of metallic domains and open-volume defects in  $\text{REH}_x\text{O}_y$  films by measuring Doppler broadening of annihilation radiation and positron lifetimes.

### 1.3.2 Spectroscopic ellipsometry

Spectroscopic ellipsometry is a non-destructive and non-invasive optical technique used to determine the optical parameters, thickness and roughness of thin films by measuring changes in polarization state and intensity of light upon reflection from the film. Spectroscopic ellipsometry has been widely used in inorganic, organic, composite and even biological materials [68-70].

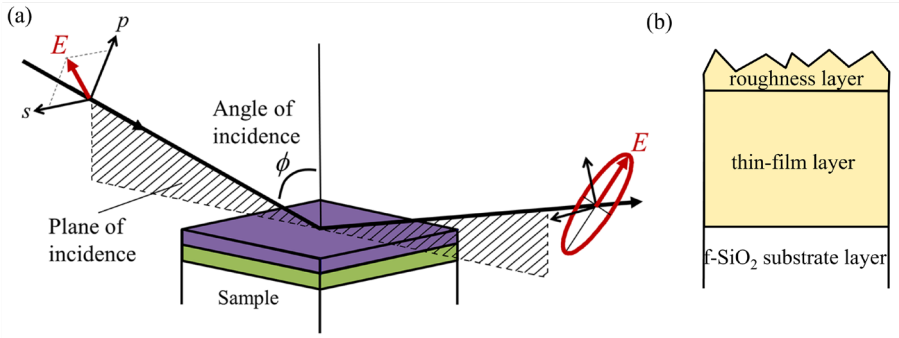


**Figure 1.5** (a) Schematics of the basic principle ellipsometry. Reprinted from [71], (b) Schematics for a representative three-layer model applied to this thesis.

Fig. 1.5 (a) illustrates the basic principle of ellipsometry. Incident light, containing two orthogonal electromagnetic waves in the p (parallel) and s (“senkrecht”, perpendicular) directions to the incidence of plane, hits the sample at an angle of incidence ( $\phi$ ). Upon reflection, the light undergoes changes in its polarization state due to interactions with the material (including reflection, transmission and absorption). These light-material interactions are determined by the optical parameters (the refractive index  $n$  and the extinction coefficient  $k$ ), the thickness and roughness of the film and the optical properties of the substrate, causing the light to become elliptically polarized. These changes are quantified by two ellipsometry parameters, psi ( $\Psi$ ) and delta ( $\Delta$ ), described by the equation  $\rho = \frac{r_p}{r_s} = \tan(\Psi) e^{i\Delta}$ , where  $r_p$  and  $r_s$  are the Fresnel reflection coefficient for the p-wave and s-wave.  $\Psi$  reflects the change in relative amplitude of both the p-wave and s-wave after reflection, which is defined as  $\tan(\Psi) = \frac{|r_p|}{|r_s|}$ .  $\Delta$  reflects the phase shifts of both waves, defined as  $\Delta = \delta_1 - \delta_2$ , where  $\delta_1$  denotes the phase difference between the p-wave and s-wave after polarization, and  $\delta_2$

denotes the phase difference of the p-wave and s-wave after reflection from the sample surface.  $\Psi$  and  $\Delta$  are two quantities that ellipsometry measures as a function of the wavelength  $\lambda$  of the applied light source.

The measured  $\Psi(\lambda)$  and  $\Delta(\lambda)$  can be analyzed and fitted by building an layered model. For example, for a homogenous transparent  $\text{YH}_x\text{O}_y$  film deposited on a f-SiO<sub>2</sub> substrate, a three-layer model can be constructed (Fig. 1.5 (b)), consisting of a roughness layer, a  $\text{YH}_x\text{O}_y$  layer and a substrate layer. The roughness layer is fitted using an in-built Bruggeman effective medium approximation model, assuming that this roughness layer consists of a mixed layer with 50% oxyhydride and 50% air ( $n = 1$ ,  $k = 0$ ). The remaining layers can be fitted employing selected mathematical equations such as the Cauchy dispersion equation ( $n(\lambda) = A + B/\lambda^2 + C/\lambda^4$ ), which is valid for wavelength regions below the bandgap of a transparent film [72]. Through iterative fitting, optical parameters can be obtained.

In addition, the development of in-situ ellipsometry enables the characterization of films under various conditions, such as during film deposition [73], heating and cooling [74], and under UV illumination [75]. In this thesis, in-situ illumination above the bandgap is used to monitor the variation in the optical parameters of RE oxyhydride films during photodarkening and bleaching.

## 1.4 Thesis outline

In this thesis, in-situ above bandgap illumination PAS and spectroscopic ellipsometry are employed to investigate the nature and evolution of microstructural and (opto-)electronic structure changes of rare-earth oxyhydride films on a nanometer scale during photodarkening-bleaching cycles, and to explore their possible relationship with the photochromic effect and the memory effect.

In Chapter 2, we systematically investigate the formation of metallic-like domains and open-volume defects by in-situ illumination DB-PAS during one photodarkening-bleaching cycle in both  $\text{YH}_x\text{O}_y$  and  $\text{GdH}_x\text{O}_y$  films. Under illumination, clear shifts of the Doppler parameters toward those of dihydrides are observed that partially recover back during bleaching. Accordingly, we propose two types of metallic-like domains to explain the photochromic effect, including (i) phase-segregated hydrogen-rich metallic domains, and (ii) Anderson-Mott insulator-to-metal transition in certain domains of the film. In addition, the irreversible part of the shifts in S and W parameters observed after bleaching suggests that divacancy-like defects are formed, as PALS on as-prepared films shows that yttrium monovacancies are the dominant positron trapping vacancies in the as-prepared oxyhydride films.

In Chapter 3, we further explore the evolution of open-volume defects and metallic-like domains upon six photodarkening-bleaching cycles in  $\text{YH}_x\text{O}_y$  and  $\text{GdH}_x\text{O}_y$  films employing in-situ DB-PAS and investigate whether and how these microstructural and electronic

changes relate to the evolution of photochromic transmittance. For the first three cycles, a strong correlation between the increase in S-parameter after each cycle and the slower bleaching rate (known as the memory effect) is observed. This increase in the S-parameter is attributed to vacancy agglomeration of the preexisted yttrium monovacancies with hydrogen vacancies, and the growth of vacancy clusters, as revealed by PALS measurements before and after one cycle. Furthermore, we propose several possibilities to understand the memory effect and corresponding systematic slowing down of the bleaching rate from an microscopic perspective. For the second three cycles, the observed reversible shifts in Doppler parameters in every cycle reinforce the hypothesis of the formation of metallic-like domains during photodarkening for explaining the photochromic effect.

In Chapter 4, we employ in-situ illumination PALS measurements on two yttrium oxyhydride films to monitor the time-dependent evolution of open-volume defects and metallic-like domains on the nanometer scale and their correlation with the photochromic effect. We observed distinct dynamic changes in the positron lifetime and intensity for each of the three observed lifetime components during photodarkening and bleaching processes. Accordingly, we provide a schematic illustration depicting the dynamic changes of open-volume defects and metallic domains before illumination, during the first fast phase of  $\sim 3$  min and the subsequent gradual phase of  $\sim 2$  h of photodarkening, and during two subsequent bleaching phases (I and II) in yttrium oxyhydride films, as revealed by PALS. Notably, a strong correlation is found between the shortest positron lifetime and the photochromic contrast during these two bleaching phases in both samples. This study deepens our microscopic understanding of the photochromism and the memory effect in yttrium oxyhydride films.

In Chapter 5, we further examine the nature of metallic-like domains formed during photodarkening in yttrium oxyhydride films from an optical perspective using spectroscopic ellipsometry. We report on the optical constants of as-prepared  $\text{YH}_x\text{O}_y$  and  $\text{YH}_{-2}$ ,  $\text{YH}_x$  and Y films. By applying a Bruggeman effective medium approximation model to the ellipsometry data obtained in the photodarkened state of the  $\text{YH}_x\text{O}_y$  film, we assess whether the formation of phase-segregated Y or Y hydride metallic domains in a semiconducting  $\text{YH}_x\text{O}_y$  matrix can explain the photochromic effect. Alternatively, we utilize a Kramers-Kronig consistent basic-spline approach to fit the ellipsometry data and determine the dielectric function and absorption coefficient of the photodarkened  $\text{YH}_x\text{O}_y$  film. Based on these optical parameters, we examine the potential formation of metallic domains related to hydrogen vacancies-induced Anderson-Mott insulator-to-metal transition as the basic mechanism of the photochromism. Finally, the possibility of the formation of Y monoxide-like domains in the semiconducting  $\text{YH}_x\text{O}_y$  matrix is assessed, based on the derived feature of the optical absorption coefficient  $\alpha(\lambda)$  during photodarkening.

## References

- [1] J. Fritzsche, Photochromism of tetracene, *Comptes Rendus. Acad. Sci. Paris* **69**, 1035 (1867).
- [2] E. Y. Fischer, Y. Hirshberg-in memoriam, *J. of Chem. Edu.* **40**, 1035 (1963).
- [3] X. Dong, Y. R. Lu, X. H. Liu, L. H. Zhang, and Y. D. Tong, Nanostructured tungsten oxide as photochromic material for smart devices, energy conversion, and environmental remediation, *J. Photoch. Photobio. C* **53** (2022).
- [4] W. H. Armistead and S. D. Stookey, Photochromic silicate glasses sensitized by silver halides - their characteristic of changing color reversibly in combination with other properties suggests many uses, *Science* **144**, 150 (1964).
- [5] A. B. Kayani, S. Kuriakose, M. Monshipouri, F. A. Khalid, S. Walia, S. Sriram, and M. Bhaskaran, UV photochromism in transition metal oxides and hybrid materials, *Small* **17** (2021).
- [6] Y. Badour, V. Jubera, I. Andron, C. Frayret, and M. Gaudon, Photochromism in inorganic crystallised compounds, *Optical Materials: X* **12** (2021).
- [7] R. Pardo, M. Zayat, and D. Levy, Photochromic organic-inorganic hybrid materials, *Chem. Soc. Rev.* **40**, 672 (2011).
- [8] G. K. Megla, Optical properties and applications of photochromic glass, *Appl. Optics* **5**, 945 (1966).
- [9] S. Glaus and G. Calzaferri, The band structures of the silver halides AgF, AgCl, and AgBr: A comparative study, *Photoch. Photobio. Sci.* **2**, 398 (2003).
- [10] G. P. Smith, Photochromic glasses: Properties and applications, *J. Mater. Sci.* **2**, 139 (1967).
- [11] T. P. Seward, Coloration and optical anisotropy in silver-containing glasses, *J. Non-Cryst. Solids* **40**, 499 (1980).
- [12] M. Zayat, PhD thesis, Hebrew University of Jerusalem, Jerusalem, Israel, 1997.
- [13] R. C. Jin, Y. W. Cao, C. A. Mirkin, K. L. Kelly, G. C. Schatz, and J. G. Zheng, Photoinduced conversion of silver nanospheres to nanoprisms, *Science* **294**, 1901 (2001).
- [14] R. Y. Han, X. T. Zhang, L. L. Wang, R. Dai, and Y. C. Liu, Size-dependent photochromism-based holographic storage of Ag/TiO<sub>2</sub> nanocomposite film, *Appl. Phys. Lett.* **98** (2011).
- [15] C. G. Granqvist, Electrochromic tungsten oxide films: Review of progress 1993-1998, *Sol. Energy Mater. Sol. Cells* **60**, 201 (2000).
- [16] V. R. Buch, A. K. Chawla, and S. K. Rawal, Review on electrochromic property for WO<sub>3</sub> thin films using different deposition techniques, *Mater. Today-Proc.* **3**, 1429 (2016).

- [17] S. K. Deb, Optical and photoelectric properties and color centers in thin-films of tungsten oxide, *Philos. Mag.* **27**, 801 (1973).
- [18] B. W. Faughnan, R. S. Crandall, and P. M. Heyman, Electrochromism in  $\text{WO}_3$  amorphous films, *Rca Rev* **36**, 177 (1975).
- [19] F. Rauch, W. Wagner, and K. Bange, Nuclear-reaction analysis of hydrogen in optically-active coatings on glass, *Nucl. Instrum. Meth. B* **42**, 264 (1989).
- [20] J. G. Zhang, D. K. Benson, C. E. Tracy, S. K. Deb, A. W. Czanderna, and C. Bechinger, Chromic mechanism in amorphous  $\text{WO}_3$  films, *J. Electrochem. Soc.* **144**, 2022 (1997).
- [21] A. I. Gavriluk, Aging of the nanosized photochromic  $\text{WO}_3$  films and the role of adsorbed water in the photochromism, *Appl. Surf. Sci.* **364**, 498 (2016).
- [22] Y. J. Ke, J. W. Chen, C. J. Lin, S. C. Wang, Y. Zhou, J. Yin, P. S. Lee, and Y. Long, Smart windows: Electro-, thermo-, mechano-, photochromics, and beyond, *Adv. Energy Mater.* **9**, 1902066 (2019).
- [23] Z. F. Huang, J. J. Song, L. Pan, X. W. Zhang, L. Wang, and J. J. Zou, Tungsten oxides for photocatalysis, electrochemistry, and phototherapy, *Adv. Mater.* **27**, 5309 (2015).
- [24] T. D. Chen, B. A. Xu, M. Zhu, J. Z. Zhang, W. W. Sun, and J. Han, Advanced functional photochromic wearables with fast photo-responsivity, long color-retention, and multi-environmental stability, *Chem. Eng. J.* **490** (2024).
- [25] T. Mongstad, C. Platzer-Bjorkman, J. P. Maehlen, L. P. A. Mooij, Y. Pivak, B. Dam, E. S. Marstein, B. C. Hauback, and S. Z. Karazhanov, A new thin film photochromic material: Oxygen-containing yttrium hydride, *Sol. Energy Mater. Sol. Cells* **95**, 3596 (2011).
- [26] F. Nafezarefi, H. Schreuders, B. Dam, and S. Cornelius, Photochromism of rare-earth metal-oxy-hydrides, *Appl. Phys. Lett.* **111**, 103903 (2017).
- [27] S. Cornelius, G. Colombi, F. Nafezarefi, H. Schreuders, R. Heller, F. Munnik, and B. Dam, Oxyhydride nature of rare-earth-based photochromic thin films, *J. Phys. Chem. Lett.* **10**, 1342 (2019).
- [28] S. M. Adalsteinsson, M. V. Moro, D. Moldarev, S. Droulias, M. Wolff, and D. Primetzhofner, Correlating chemical composition and optical properties of photochromic rare-earth oxyhydrides using ion beam analysis, *Nucl. Instrum. Meth. B* **485**, 36 (2020).
- [29] D. Chaykina, F. Nafezarefi, G. Colombi, S. Cornelius, L. J. Bannenberg, H. Schreuders, and B. Dam, Influence of crystal structure, encapsulation, and annealing on photochromism in Nd oxyhydride thin films, *J. Phys. Chem. Lett.* **126**, 2276 (2022).
- [30] D. Chaykina, G. Colombi, H. Schreuders, and B. Dam, Photochromic samarium oxyhydride thin films, *AIP Adv.* **13**, 055211 (2023).
- [31] B. Dam, F. Nafezarefi, D. Chaykina, G. Colombi, Z. Wu, S. W.H. Eijt, S. Banerjee, G. A. de Wijs, A. Kentgens, Perspective on the photochromic and photoconductive properties of rare-earth oxyhydride thin films, *Sol. Energy Mater. Sol. Cells* **273**, 112921 (2024).



- [32] G. Colombi, T. De Krom, D. Chaykina, S. Cornelius, S. W. H. Eijt, and B. Dam, Influence of cation (RE = Sc, Y, Gd) and O/H anion ratio on the photochromic properties of  $\text{REO}_x\text{H}_{3-2x}$  thin films, *ACS Photonics* **8**, 709 (2021).
- [33] G. Colombi, S. Cornelius, A. Longo, and B. Dam, Structure model for anion-disordered photochromic gadolinium oxyhydride thin films, *J. Phys. Chem. C* **124**, 13541 (2020).
- [34] C. C. You, T. Mongstad, J. P. Maehlen, and S. Karazhanov, Engineering of the band gap and optical properties of thin films of yttrium hydride, *Appl. Phys. Lett.* **105** (2014).
- [35] D. Chaykina, I. Usman, G. Colombi, H. Schreuders, B. Tyburska-Pueschel, Z. Wu, S. W. H. Eijt, L. J. Bannenberg, G. A. de Wijs, and B. Dam, Aliovalent calcium doping of yttrium oxyhydride thin films and implications for photochromism, *J. Phys. Chem. C* **126**, 14742 (2022).
- [36] T. Yamasaki, R. Takaoka, S. Iimura, J. Kim, H. Hiramatsu, and H. Hosono, Characteristic resistive switching of rare-earth oxyhydrides by hydride ion insertion and extraction, *ACS Appl. Mater. Inter.* **14**, 19766 (2022).
- [37] L. Andronic, D. Moldarev, D. Deribew, E. Moons, and S. Z. Karazhanov, Photocatalytic self-cleaning properties of thin films of photochromic yttrium oxyhydride, *J. Solid State Chem.* **316** (2022).
- [38] J. Montero, F. A. Martinsen, M. Garcia-Tecedor, S. Z. Karazhanov, D. Maestre, B. Hauback, and E. S. Marstein, Photochromic mechanism in oxygen-containing yttrium hydride thin films: An optical perspective, *Phys. Rev. B* **95**, 201301(R) (2017).
- [39] M. P. Plokker, S. W. H. Eijt, F. Naziris, H. Schut, F. Nafezarefi, H. Schreuders, S. Cornelius, and B. Dam, Electronic structure and vacancy formation in photochromic yttrium oxy-hydride thin films studied by positron annihilation, *Sol. Energy Mater. Sol. Cells* **177**, 97 (2018).
- [40] S. W. H. Eijt, T. De Krom, D. Chaykina, H. Schut, G. Colombi, S. Cornerlius, W. Egger, M. Dickmann, C. Hugenschmidt, and B. Dam, Photochromic  $\text{YO}_x\text{H}_y$  thin films examined by in situ positron annihilation spectroscopy, *Acta Phys. Pol. A* **137**, 205 (2020).
- [41] J. Montero-Amenedo, Photochromism in rare earth oxyhydrides for large-area transmittance control, *Sol. Energy Mater. Sol. Cells* **272** (2024).
- [42] P. A. M. Dirac, On the quantum theory of electrons, *Physikalische Zeitschrift* **29**, 561 (1928).
- [43] C. D. Anderson, The positive electron, *Phys. Rev.* **43**, 491 (1933).
- [44] H. F. Waung, W. Brandt, and P. W. Levy, Color-center studies in NaCl crystals by positron annihilation, *Bulletin Am. Phys. Soc.* **13**, 1473 (1968).
- [45] P. J. Schultz and K. G. Lynn, Interaction of positron beams with surfaces, thin-films, and interfaces, *Rev. Mod. Phys.* **60**, 701 (1988).
- [46] M. J. Puska and R. M. Nieminen, Theory of positrons in solids and on solid-surfaces, *Rev. Mod. Phys.* **66**, 841 (1994).

- [47] K. Saarinen, P. Hautojärvi, and C. Corbel, Positron annihilation spectroscopy of defects in semiconductors, *Semiconduct. Semimet.* **51**, 209 (1998).
- [48] R. Krause-Rehberg, H. S. Leipner, T. Abgarjan, and A. Polity, Review of defect investigations by means of positron annihilation in II-VI compound semiconductors, *Appl. Phys. A-Mater.* **66**, 599 (1998).
- [49] F. Tuomisto and I. Makkonen, Defect identification in semiconductors with positron annihilation: Experiment and theory, *Rev. Mod. Phys.* **85**, 1583 (2013).
- [50] J. Cizek, Characterization of lattice defects in metallic materials by positron annihilation spectroscopy: A review, *J. Mater. Sci. Technol.* **34**, 577 (2018).
- [51] K. O. Jensen and A. B. Walker, Positron thermalization and nonthermal trapping in metals, *J. Phys-Condens Mat.* **2**, 9757 (1990).
- [52] H. H. Jorch, K. G. Lynn, and T. McMullen, Positron diffusion in germanium, *Phys. Rev. B* **30**, 93 (1984).
- [53] R. Krause-Rehberg, H. S. Leipner, *Positron annihilation in semiconductors - defect studies* (Springer-Verlag Berlin Heidelberg, 1999), 127.
- [54] M. A. van Huis, A. van Veen, H. Schut, C. V. Falub, S. W. H. Eijt, P. E. Mijnders, and J. Kuriplach, Positron confinement in embedded lithium nanoclusters, *Phys. Rev. B* **65** (2002).
- [55] V. L. Sedov, V. A. Teimurazova, and K. Berndt, Interaction of positrons with precipitations in a diluted Al-Zn alloy, *Phys. Lett. A* **33**, 319 (1970).
- [56] A. Dupasquier, P. Folegati, N. de Diego, and A. Somoza, Current positron studies of structural modifications in age-hardenable metallic systems, *J. Phys-Condens Mat.* **10**, 10409 (1998).
- [57] A. Somoza and A. Dupasquier, Positron studies of solute aggregation in age-hardenable aluminum alloys, *J. Mater. Process Tech.* **135**, 83 (2003).
- [58] Y. Nagai, T. Chiba, Z. Tang, T. Akahane, T. Kanai, M. Hasegawa, M. Takenaka, and E. Kuramoto, Fermi surface of nanocrystalline embedded particles in materials: Bcc Cu in Fe, *Phys. Rev. Lett.* **87**, 176402 (2001).
- [59] C. V. Falub, P. E. Mijnders, S. W. H. Eijt, M. A. van Huis, A. van Veen, and H. Schut, Electronic structure and orientation relationship of Li nanoclusters embedded in MgO studied by depth-selective positron annihilation two-dimensional angular correlation, *Phys. Rev. B* **66**, 075426 (2002).
- [60] J. Xu, J. Moxom, B. Somieski, C. W. White, A. P. Mills, R. Suzuki, and S. Ishibashi, Positronic probe of vacancy defects on surfaces of Au nanoparticles embedded in MgO, *Phys. Rev. B* **64**, 113404 (2001).
- [61] M. A. van Huis, A. van Veen, H. Schut, B. J. Kooi, and J. T. M. De Hosson, Formation of solid Kr nanoclusters in MgO, *Phys. Rev. B* **67**, 235409 (2003).

- [62] G. H. Dai, Q. J. Yan, Y. Wang, and Q. S. Liu, Li-doped MgO as catalysts for oxidative coupling of methane - a positron-annihilation study, *Chem. Phys.* **155**, 275 (1991).
- [63] H. Schut, A Variable Energy Positron Beam Facility with Applications in Materials Science, PhD thesis, Delft University of Technology, Delft, the Netherlands, 1990.
- [64] V. J. Ghosh, Positron implantation profiles in elemental and multilayer systems, *Appl. Surf. Sci.* **85**, 187 (1995).
- [65] A. Zubiaga, J. A. Garcia, F. Plazaola, F. Tuomisto, J. Zuniga-Perez, and V. Munoz-Sanjose, Positron annihilation spectroscopy for the determination of thickness and defect profile in thin semiconductor layers, *Phys. Rev. B* **75** (2007).
- [66] A. van Veen, H. Schut, J. Devries, R. A. Hakvoort, and M. R. Ijpma, Analysis of positron profiling data by means of Vepfit, *AIP Conf. Proc.* **218**, 171 (1990).
- [67] T. E. M. Staab, M. Haugk, A. Sieck, T. Frauenheim, and H. S. Leipner, Magic number vacancy aggregates in Si and GaAs - structure and positron lifetime studies, *Physica B* **273-274**, 501 (1999).
- [68] H. H. Li, C. C. Cui, X. P. Xu, S. B. Bian, C. Ngaojampa, P. Ruankham, and A. P. Jaroenjittchai, A review of characterization of perovskite film in solar cells by spectroscopic ellipsometry, *Sol. Energy* **212**, 48 (2020).
- [69] W. Ogieglo, H. Wormeester, K. J. Eichhorn, M. Wessling, and N. E. Benes, In situ ellipsometry studies on swelling of thin polymer films: A review, *Prog. Polym. Sci.* **42**, 42 (2015).
- [70] H. Arwin, Spectroscopic ellipsometry and biology: Recent developments and challenges, *Thin Solid Films* **313**, 764 (1998).
- [71] H. G. H. Tompkins, J. N. Hilfiker, *Spectroscopic ellipsometry-practical application to thin film characterization* (Momentum Press, 2016).
- [72] CompleteEASE software manual, J. A. Woollam, 2020.
- [73] E. Langereis, S. B. S. Heil, H. C. M. Knoop, W. Keuning, M. C. M. van de Sanden, and W. M. M. Kessels, Spectroscopic ellipsometry as a versatile tool for studying atomic layer deposition, *J. Phys. D Appl. Phys.* **42** (2009).
- [74] S. Zollner, F. Abadizaman, C. Emminger, and N. Samarasingha, Spectroscopic ellipsometry from 10 to 700 K, *Adv. Opt. Technol.* **11**, 117 (2022).
- [75] H. Camirand, B. Baloukas, J. E. Klemberg-Sapieha, and L. Martinu, Spectroscopic ellipsometry of electrochromic amorphous tungsten oxide films, *Sol. Energy Mater. Sol. Cells* **140**, 77 (2015).



## **2. Formation of vacancies and metallic-like domains in photochromic rare-earth oxyhydride thin films studied by in-situ illumination positron annihilation spectroscopy**

This chapter is based on Z. Wu, T. de Krom, G. Colombi, D. Chaykina, G. van Hattem, H. Schut, M. Dickmann, W. Egger, C. Hugenschmidt, E. Brück, B. Dam, and S. W. H. Eijt, Formation of vacancies and metallic-like domains in photochromic rare-earth oxyhydride thin films studied by in-situ illumination positron annihilation spectroscopy, *Phys. Rev. Mater.* 6, 065201 (2022).

## Abstract

Rare-earth oxyhydride thin films show a color-neutral, reversible photochromic effect at ambient conditions. The origin of the photochromism is topic of current investigations. Here, we investigated the lattice defects, electronic structure, and crystal structure of photochromic  $\text{YH}_x\text{O}_y$  and  $\text{GdH}_x\text{O}_y$  thin films deposited by magnetron sputtering using positron annihilation techniques and X-ray diffraction, in comparison with Y,  $\text{YH}_{-1.9}$ ,  $\text{Y}_2\text{O}_3$  and Gd,  $\text{GdH}_{-1.8}$ ,  $\text{Gd}_2\text{O}_3$  films. Positron annihilation lifetime spectroscopy (PALS) reveals the presence of cation mono-vacancies in the as-deposited Y and  $\text{YH}_{-1.9}$  films at concentrations of  $\sim 10^{-5}$  per cation. In addition, vacancy clusters and nanopores are found in the as-prepared  $\text{YH}_x\text{O}_y$  and  $\text{Y}_2\text{O}_3$  films. Doppler broadening positron annihilation spectroscopy (DB-PAS) of the Y-based and Gd-based films reflects the transition from a metallic to an insulating nature of the rare-earth (RE) metal, metal hydride, semiconducting oxyhydride and insulating oxide films. *In-situ* illumination DB-PAS shows the irreversible formation predominantly of di-vacancies, as PALS showed that cation mono-vacancies are already abundantly present in the as-prepared films. The formation of di-vacancies supports conjectures that  $\text{H}^-$  (and/or  $\text{O}^{2-}$ ) ions become mobile upon illumination, as these will leave anion vacancies behind, some of which may subsequently cluster with cation vacancies present. In addition, in RE oxyhydride films, partially reversible shifts in the Doppler parameters are observed that correlate with the photochromic effect and point to the formation of metallic domains in the semiconducting films. Two processes are discussed that may explain the formation of these metallic domains and the changes in optical properties associated with the photochromic effect. The first process considers the reversible formation of metallic nano-domains with reduced O:H composition by transport of light-induced mobile hydrogen and local oxygen displacements. The second process considers metallic nano-domains resulting from the trapping of photo-excited electrons in an  $e_g$  orbital at the yttrium ions surrounding positively charged hydrogen vacancies, that are formed by light-induced removal of hydrogen atoms from octahedral sites. When a sufficiently large concentration, on the order of  $\sim 10\%$ , is reached in a certain domain of the film, band formation of the  $e_g$  electrons may occur, leading to an Anderson-Mott insulator-metal transition similar to the case of yttrium trihydride in these domains.

## 2.1 Introduction

Inorganic photochromic materials have attracted extensive interest because they possess a higher physico-chemical stability compared to organic photochromic materials. They are promising for applications in the fields of energy-saving smart windows [1], adaptive eyewear lenses [2] and sensors [3]. Traditional inorganic photochromic materials include transition metal oxides and doped metal halides, e.g. tungsten oxide [4] and copper doped silver halide [5]. The photochromism of yttrium oxyhydride thin films ( $\text{YH}_x\text{O}_y$ ), where oxygen is incorporated into  $\text{YH}_{2-x}$  metal hydride films by *ex-situ* oxidation, was discovered in 2011 [6]. Other rare-earth metal oxyhydride films, based on Gd, Er, Dy and Sc, also showed similar photochromic properties, characterized by a strong reduction in the optical transmission below the band gap energy in a broad wavelength range in the visible and near-IR upon UV illumination [7, 8]. These photochromic oxyhydride films were prepared by reactive magnetron sputtering of metal dihydride films in an argon/hydrogen atmosphere above a specific critical deposition pressure, followed by exposure to air. The incorporation of oxygen into the rare-earth metal hydride films during post-oxidation does not induce a phase transition, but the crystal lattice expands and maintains an fcc-like structure similar to the dihydride films [7]. The bandgap, optical properties and electrical properties of oxyhydride films can be modified by tailoring the chemical composition ( $\text{O}^{2-}$  and  $\text{H}^-$  contents) by varying the deposition pressure [8-12].

However, the mechanism of photochromism in rare-earth oxyhydride films is still unclarified. The photochromic mechanism of the well-known inorganic photochromic material Cu-doped AgCl is associated with the formation of metallic silver clusters due to the light-induced electron generation and transport that induces a change in the valence state of Ag ions according to  $\text{Ag}^+ + \text{e}^- \rightarrow \text{Ag}^0$  [13]. The  $\text{Ag}^0$  atoms move to interstitial sites and cluster to form metallic regions, leading to pronounced photo-darkening of the material. A similar mechanism may be involved in rare-earth oxyhydride films. Based on spectroscopic ellipsometry, Montero *et al.* [14] proposed that the photo-darkening of  $\text{YH}_x\text{O}_y$  films is related to the formation of metallic domains, since the optical transmittance of  $\text{YH}_x\text{O}_y$  under illumination could be modelled well by the formation of a small fraction of up to 6 vol.% of metallic domains. The domains were supposed to be  $\text{YH}_2$ -like, but it remained unclear how they formed. Based on solid state Nuclear Magnetic Resonance (NMR), Chandran *et al.* [15] showed that a rearrangement of mobile hydrogen species occurs during illumination of  $\text{YH}_x\text{O}_y$ , that reverses during bleaching, correlating with the photochromic changes. Our previous positron annihilation studies [8, 16] showed that the UV illumination induces the formation of vacancies, providing additional (indirect) support for ion mobility during photo-darkening. In that study, the formation of vacancies appeared irreversible during the subsequent bleaching phase, suggesting that the vacancies observed by positron annihilation are not directly responsible for the photochromic effect.

In this study, we further clarify the formation of vacancies during photo-darkening. Moreover, we monitored the changes in electronic structure during illumination and subsequent bleaching, and found that these are (at least partially) reversible in character. Positron annihilation lifetime spectroscopy (PALS) was used to identify the sizes of vacancy-like defects and concentrations of vacancies in as-prepared  $\text{Y}/\text{YH}_{-1.9}/\text{YH}_x\text{O}_y/\text{Y}_2\text{O}_3$  films. X-Ray Diffraction (XRD) and Doppler broadening positron annihilation spectroscopy (DB-PAS) were employed to investigate the crystal structure and electronic structure via detection of electronic momentum distributions of as-deposited Gd-based and Y-based films. In addition, *in-situ* illumination DB-PAS was used to probe the evolution of vacancies and electronic structure properties of the oxyhydride films during UV illumination and subsequent bleaching in the dark. We describe and discuss two different possible mechanisms for the photo-darkening of the rare-earth metal oxyhydride films consistent with the reversible changes observed in the *in-situ* illumination positron studies. The first mechanism involves the formation of H-rich domains that exhibit a metallic-like electronic structure, enabled by photo-induced transport of hydrogen. Modelling based on diffusion-limited positron trapping in such H-rich domains suggests that the characteristic sizes of these domains are in the range of  $\sim 1\text{--}20$  nm. The second mechanism involves the formation of positively charged hydrogen vacancies at octahedral sites with a localized charge-compensating electron in an  $e_g$ -state orbital at the surrounding yttrium ions. At sufficiently high concentrations, overlap between the  $e_g$ -state orbitals of these localized electrons may occur, leading to band formation and a local metallic behaviour in the respective domains in the  $\text{YH}_x\text{O}_y$  film, similar to what has been proposed for the Anderson-Mott insulator-to-metal transition of yttrium trihydride at a composition of  $\text{YH}_{-2.7}$ .

## 2.2 Experiment

### 2.2.1 Sample preparation

The rare-earth metal dihydride and oxyhydride films were deposited on unheated UV-grade fused silica ( $\text{f-SiO}_2$ ) substrates by reactive direct current (DC) magnetron sputtering of yttrium or gadolinium targets (with 99.9% purity) in an  $\text{Ar}/\text{H}_2$  gas mixture. The DC power supplied to the Y and Gd target was 200 W and 180 W, respectively. The sputtered metal dihydride films were deposited under a pressure of 0.3 Pa, while the oxyhydride films were obtained from the post-oxidation of metal dihydride films deposited above the critical pressure of around 0.4 Pa for  $\text{YH}_x\text{O}_y$  and 0.6 Pa for  $\text{GdH}_x\text{O}_y$  films, respectively [7], at room temperature. A second type of rare-earth metal dihydride films was prepared by post-hydrogenation of sputtered Y or Gd films capped with a thin Pd layer. The Pd layer not only protects the film from oxidation and but also catalyzes the hydrogenation process [17]. Some of the oxyhydride films were capped by a thin aluminum (Al) layer after exposure of the reactively sputtered dihydride films to air for around 3 hours. The Al layer was used to



prevent interaction of the oxyhydride films with the ambient (or vacuum) environment during the experiments. The Y and Gd metal films were deposited in an Argon atmosphere under a pressure of 0.3 Pa, while the  $Y_2O_3$  and  $Gd_2O_3$  metal oxide films were made in an Ar/ $O_2$  atmosphere under a pressure of 0.3 Pa via pulsed DC reactive magnetron sputtering. Detailed information about the deposition method can be found in Ref. [8]. All the samples used are listed in Table 2.1 and Table S2.1 (see Supplemental material [18]).

Table 2.1: List of main samples, deposition pressures and experiments.

Samples	Deposition pressure	measurements
Y	0.3 Pa	PALS, DB-PAS, XRD
YH <sub>-1.9</sub> //Pd	0.3 Pa (hydrogenation)	PALS, DB-PAS, XRD
YH <sub>x</sub> O <sub>y</sub> -1	0.5 Pa	PALS, DB-PAS, XRD, <i>In-situ</i> illumination DB-PAS
YH <sub>x</sub> O <sub>y</sub> -2	0.5 Pa	PALS
YH <sub>x</sub> O <sub>y</sub> //Al	0.5 Pa	DB-PAS, XRD, <i>In-situ</i> illumination DB-PAS
Y <sub>2</sub> O <sub>3</sub>	0.3 Pa	PALS, DB-PAS
Gd	0.3 Pa	DB-PAS
GdH <sub>-1.8</sub> //Pd	0.3 Pa (hydrogenation)	DB-PAS, XRD
GdH <sub>2</sub>	0.3 Pa	DB-PAS, XRD
GdH <sub>x</sub> O <sub>y</sub>	0.8 Pa	DB-PAS, XRD
GdH <sub>x</sub> O <sub>y</sub> //Al	0.8 Pa	DB-PAS, XRD
GdH <sub>x</sub> O <sub>y</sub>	0.9 Pa	DB-PAS, XRD, <i>In-situ</i> illumination DB-PAS
GdH <sub>x</sub> O <sub>y</sub> //Al	0.9 Pa	DB-PAS, XRD, <i>In-situ</i> illumination DB-PAS
Gd <sub>2</sub> O <sub>3</sub>	0.3 Pa	DB-PAS

### 2.2.2 Characterization

Grazing-incidence XRD measurements were performed on a PANalytical X-pert Pro diffractometer with a Cu  $K\alpha$  source ( $\lambda = 1.54 \text{ \AA}$ ) at room temperature and the angle of incidence was fixed at  $\omega = 2^\circ$  for all measurements. The XRD patterns were analyzed by the Rietveld refinement method using the Fullprof Suite [19, 20]. The crystal structures of the various films deduced from the Rietveld refinement are in agreement with previous findings [8, 9], with a hexagonal close-packed (hcp) structure and space group of  $P6_3/mmc$  for the Y and Gd films, and a face-centered-cubic (fcc) structure and space group  $Fm\bar{3}m$  for the rare-earth metal dihydride and oxyhydride thin films. Yttrium oxide ( $Y_2O_3$ ) crystallizes in a body-centered-cubic (bcc) structure with space group  $Ia\bar{3}$  [21]. Detailed information on the Rietveld refinement analysis of the films, including the crystal structures, lattice parameters and volume per Y (or Gd) atom, is given in the Supplemental Material [18].

PALS studies were performed using the pulsed low-energy positron lifetime spectrometer (PLEPS) of the neutron-induced positron source (NEPOMUC) facility at the Heinz Maier-Leibnitz Zentrum (MLZ) research reactor in Garching [22, 23, 24]. For each lifetime spectrum,  $4 \times 10^6$  counts were collected. The instrument time resolution function, determined

by PALS measurements on a reference p-doped SiC sample at each positron implantation energy, was taken into account when decomposing the experimental positron annihilation lifetime spectra. The extracted time resolution was approximately 180 ps. The lifetime spectra of eight samples, collected at various positron implantation energies in the range of 0.5-16 keV, were fitted by the POSWIN program [25, 26].

DB-PAS was employed to study the electronic structure and vacancy-type defects in Y-based and Gd-based thin films. DB-PAS depth profiles of the films were measured at room temperature with positron implantation energies ranging from 0.1 keV to 20 keV, using the variable energy positron beam (VEP) facility at the Reactor Institute Delft [27]. A high purity Ge (HPGe) detector cooled by liquid-nitrogen with the energy resolution of 1.2 keV was used to detect the energy distribution of the  $\sim 511$  keV  $\gamma$ -rays produced by the annihilation of positrons and electrons. The intensity of the low energy positron beam at the sample position is around  $10^4$  e<sup>+</sup>/s and the FWHM of the beam diameter is around 8 mm. The depth-profiles of the extracted shape (S) and wing (W) parameters were fitted by the VEPFIT program [28]. The S-parameter represents positron annihilation with valence electrons, which provides sensitivity to the electronic structure and open volume defects such as vacancies or vacancy clusters, while the W-parameter reflects positron annihilation with (semi-)core electrons, which provides information on the local chemical environment of the positron trapping site. Momentum windows of  $|p| < 3.0 \times 10^{-3} m_0c$  and  $8.2 \times 10^{-3} m_0c < |p| < 23.4 \times 10^{-3} m_0c$  were used for determining the S- and W-parameter, respectively.

Optical transmittance measurements were performed in a custom-built setup equipped with a white source (DH-2000BAL, Ocean Optics) and a silicon CCD array spectrometer (HR4000, Ocean Optics). The light source triggering the photochromic effect of oxyhydride films used in the transmittance measurements was a narrow wavelength LED (385 nm, I  $\sim 75$  mW/cm<sup>2</sup>). In the *in-situ* illumination DB-PAS experiments, the same LED equipped with a Köhler lens system is placed  $\sim 45$  cm behind the sample, with an intensity of  $\sim 33$  mW/cm<sup>2</sup> at the position of the sample.

## 2.3 Results and discussion

### 2.3.1 Open-volume defects in Y-based thin films examined by PALS

In order to examine the nature of the positron annihilation sites and presence of vacancy-related defects in the as-deposited films, positron annihilation lifetime spectroscopy (PALS) experiments were performed on various yttrium-based films. This PALS study enabled us to probe the sizes and concentrations of vacancy-related defects in the films. Representative spectra obtained for the YH<sub>-1.9</sub>/Pd and YH<sub>x</sub>O<sub>y</sub>-1 films, collected at a positron implantation energy of 4 keV are shown in Fig. 2.1, together with best-fits obtained using POSWIN analysis. In order to reliably extract the lifetime parameters for each film, we considered the PALS spectra collected at 3 and 4 keV, since at these positron implantation energies the

largest fraction of positrons ( $\sim 91\text{--}96\%$  for  $\text{YH}_{-1.9}/\text{Pd}$  and  $\sim 94\text{--}98\%$  for  $\text{YH}_x\text{O}_y$ -1) annihilate inside the film, according to VEPFIT analysis [28], as presented in Fig. S2.3 of the Supplemental Material [18]. The positron lifetime spectra of all Y-based thin films at 3 and 4 keV are shown in Fig. S2.4, Supplemental Material [18]. The spectra of the metallic Y and  $\text{YH}_{2-x}$  films decay according to a sum of exponential decay components too close to the background level beyond  $\sim 6$  ns. In contrast, a component with a long exponential decay is observed in the PALS spectra of  $\text{YH}_x\text{O}_y$  and  $\text{Y}_2\text{O}_3$  films. This shows that ortho-positronium (o-Ps) pick-off annihilation is present in the  $\text{YH}_x\text{O}_y$  and  $\text{Y}_2\text{O}_3$  films, while it is absent in the metallic Y and  $\text{YH}_{2-x}$  films. Positronium (Ps) is a hydrogen-like bound state of a positron and an electron. Ortho-positronium (o-Ps) has spin  $S=1$  and a long self-annihilation lifetime in vacuum of  $\sim 142$  ns due to annihilation into 3 gamma-ray photons, and can be formed in sufficient large open space, for instance, nanopores present in a material. The self-annihilation lifetime of  $\sim 142$  ns can be reduced substantially by so-called pick-off annihilation, in which the positron of o-Ps annihilates with an electron of opposite spin of the surrounding material under emission of 2 gamma quanta. The formation of o-Ps in the  $\text{YH}_x\text{O}_y$  and  $\text{Y}_2\text{O}_3$  films therefore indicates the presence of nanopores. However, o-Ps formation is likely inhibited in the metal and metal hydride films due to their metallic character.

The PALS spectra of the Y and  $\text{YH}_{2-x}$  films were satisfactorily fitted by a three-lifetime-component analysis, while the spectra of  $\text{YH}_x\text{O}_y$  and  $\text{Y}_2\text{O}_3$  films were satisfactorily fitted by a four-lifetime-component analysis using the POSWIN analysis program [25, 26]. For all Y-based films, the lifetime of the first component extracted in the analysis (Table 2.2, and Table S2.3 in the Supplemental Material [18]) is significantly shorter than typical values for the positron bulk lifetime characteristic for annihilation in defect-free materials [29]. We attribute this first component to positron annihilation in a defect-free local environment in our vacancy-containing films, that only occurs at short timescales before these positrons had the chance to find and trap into vacancy-related point defects in the films. The lifetime of the first component is reduced with respect to the positron bulk lifetime by the competitive process of positron trapping in vacancy-related open volume defects, which provides additional decay channels that add to the decay rate of the first component [29]. The other two lifetime components, which are linked to positron annihilation in open volume defects, have a lifetime that is characteristic for the size of the vacancy-related defect, vacancy cluster or nanopore involved, while their intensity is associated with the concentration of the respective open volume defect. As we will discuss further on, the second component with observed positron lifetimes in the range of 260 to 295 ps is related to positron trapping in mono-vacancies, while the third component with a lifetime  $\tau_3$  in the range of 500-700 ps may originate from larger vacancy clusters. The fourth component seen for  $\text{YH}_x\text{O}_y$  and  $\text{Y}_2\text{O}_3$  films with long lifetimes in the range of 1.5-3.2 ns corresponds to pick-off annihilation of o-Ps formed in nanopores in the films. The best-fit parameters of lifetimes ( $\tau_i$ ), intensities ( $I_i$ ) and average lifetimes ( $\tau_{av}$ ) of all Y-based films at 4 keV and 3 keV are presented in Table 2.2 and Table S2.3 (see Supplemental Material [18]), respectively.

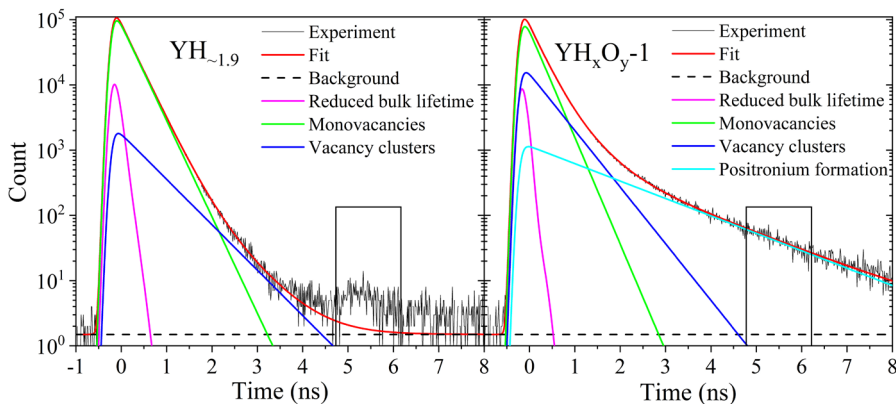


**Figure 2.1:** PALS spectra collected at a positron implantation energy of 4 keV of (a)  $\text{YH}_{-1.9}/\text{Pd}$  with 3-component best-fit analysis and (b)  $\text{YH}_x\text{O}_y-1$  with 4-component best-fit analysis using the POSWIN program. The peaks in the rectangular region in the spectra are excluded in the analysis, since they correspond to back-scattered positrons that annihilate at a different location in the sample chamber of the PLEPS spectrometer.

Table 2.2: Positron lifetimes ( $\tau_i$ ), intensities ( $I_i$ ), average lifetimes ( $\tau_{\text{av}}$ ) for the PALS spectra of Y-based thin films collected at 4 keV as deduced from POSWIN best-fit analysis.

samples	$\tau_1$ (ps)	$\tau_2$ (ps)	$\tau_3$ (ps)	$\tau_4$ (ns)	$I_1$ (%)	$I_2$ (%)	$I_3$ (%)	$I_4$ (%)	$\tau_{\text{av}}$ (ps)
Y	$65 \pm 3$	$279 \pm 1$	$683 \pm 22$	-	$6 \pm 0.2$	$92 \pm 0.2$	$1.5 \pm 0.2$	-	$272 \pm 1$
$\text{YH}_{-1.9}/\text{Pd}$	$73 \pm 5$	$294 \pm 1$	$624 \pm 17$	-	$5 \pm 0.2$	$92 \pm 0.2$	$3 \pm 0.3$	-	$293 \pm 3$
$\text{YH}_x\text{O}_y-1$	$47 \pm 5$	$266 \pm 4$	$500 \pm 20$	$1.63 \pm 0.03$	$3.8 \pm 0.2$	$71 \pm 2$	$22 \pm 2$	$4.2 \pm 0.2$	$365 \pm 17$
$\text{YH}_x\text{O}_y-2$	$60 \pm 4$	$281 \pm 3$	$638 \pm 29$	$2.16 \pm 0.05$	$5.2 \pm 0.3$	$78 \pm 1$	$13 \pm 1$	$4.2 \pm 0.2$	$395 \pm 9$
$\text{Y}_2\text{O}_3$	$58 \pm 5$	$276 \pm 4$	$539 \pm 16$	$3.03 \pm 0.06$	$5.1 \pm 0.3$	$71 \pm 2$	$21 \pm 2$	$3.4 \pm 0.1$	$412 \pm 13$

### Two-defect positron trapping model

In order to elucidate the size and concentration of the vacancy-related defects, a two-defect positron trapping model [29] was applied to extract the bulk lifetime ( $\tau_b$ ), positron trapping rate ( $k_i$ ) and defect concentrations ( $C_i$ ) of all samples. In the two-defect positron trapping model, we consider that positrons may be trapped and annihilate in two different types of vacancy-related defects independently. We neglect de-trapping of positrons from either of the vacancy-related traps. Besides, positrons may annihilate in defect-free regions of the material (bulk annihilation) if they do not get trapped in either type of defect before annihilation. According to this model, the lifetime of the first component  $\tau_1$  corresponds the reduced bulk lifetime, that satisfies  $\frac{1}{\tau_1} = \frac{1}{\tau_b} + k_1 + k_2$ , with  $k_1$  and  $k_2$  the trapping rates in the two types of defects. As will be explained further on, the second component  $\tau_2$  for the series of films studied here is a signature of cation mono-vacancies and  $\tau_3$  is a signature of vacancy

clusters. The minor contributions from the long lifetime o-Ps components (< 5%) in the lifetime spectra of  $\text{YH}_x\text{O}_y$  and  $\text{Y}_2\text{O}_3$  were ignored when using this two-defect positron trapping model. The intensities of the other three components were rescaled accordingly in order to ensure  $\sum_{i=1}^3 I_i = 1$ , as required for application of the two-defect positron trapping model. The main equations of this model

$$k_1 = \mu C_1 = I_2 \left( \frac{1}{\tau_1} - \frac{1}{\tau_2} \right) \quad (2.1)$$

$$k_2 = \mu C_2 = I_3 \left( \frac{1}{\tau_1} - \frac{1}{\tau_3} \right) \quad (2.2)$$

$$\tau_b = \left( \frac{I_1}{\tau_1} + \frac{I_2}{\tau_2} + \frac{I_3}{\tau_3} \right)^{-1} \quad (2.3)$$

are used to derive the positron trapping rates  $k_1$  and  $k_2$  in the two types of defects and the positron bulk lifetime  $\tau_b$  from the lifetimes  $\tau_i$  and intensities  $I_i$  ( $i=1,2,3$ ) extracted from the positron lifetime spectra. The trapping coefficient  $\mu$  for single vacancies in solids is generally on the order of  $10^{15} \text{ s}^{-1}$  [29, 30]. Since empirical or theoretical values for the trapping coefficients for defects in the Y-based films are not available, we set  $\mu=10^{15} \text{ s}^{-1}$  for mono-vacancies in our analysis. The trapping coefficient will be approximately proportional to the number of vacancies  $n$  for small vacancy clusters  $V_n$  ( $n \leq 5$ ), according to the equation  $\mu_n = n\mu$ , while it will saturate at a high value for larger vacancy clusters, since the trapping coefficient will be limited by the positron mobility [29]. Correspondingly, we included a multiplication factor of 5 in the estimation of the trapping coefficient for  $V_5$ -clusters, and a factor of 7-8 for  $V_{10}$ -clusters [29]. The  $\tau_b$ ,  $k_i$  and  $C_i$  for Y-based thin films determined from the average of the respective values as extracted at 3 and 4 keV are shown in Table 2.3. The expressions used to derive the standard deviations in these parameters are given in the Supplemental Material [18].

Table 2.3: Positron bulk lifetime  $\tau_b$ , positron trapping rates  $k_i$  ( $i=1,2$ ) and defect concentrations  $C_i$  ( $i=1,2$ ) for Y-based thin films obtained from the average of the respective values extracted from PALS spectra collected at 3 and 4 keV. The error ranges correspond to the standard deviations.

Samples	$\tau_b$ (ps)	$k_1$ ( $10^{10} \text{ s}^{-1}$ )	$k_2$ ( $10^{10} \text{ s}^{-1}$ )	$C_1$ ( $10^{-6}$ )	$C_2$ ( $10^{-6}$ )
Y	235±4	1.0±0.1	0.02±0.001	10±1	<0.1
YH <sub>-1.9</sub> /Pd	260±6	0.8±0.1	0.03±0.003	8±1	<0.1
YH <sub>x</sub> O <sub>y</sub> -1	238±6	1.5±0.3	0.5±0.1	15±3	1±0.5
YH <sub>x</sub> O <sub>y</sub> -2	242±4	1.2±0.2	0.33±0.05	12±2	0.4±0.2
Y <sub>2</sub> O <sub>3</sub>	256±4	0.9±0.1	0.27±0.03	9±1	0.3±0.1

The extracted bulk lifetime for the hcp Y thin film of 235±4 ps is comparable to previous studies that report an experimental bulk lifetime of 249 ps and a calculated bulk lifetime of 215 ps for hcp Y [31], indicating that the two-defect trapping model is valid for the Y thin film. The dominant second component, with an intensity ~92%, has a lifetime of 279 ps

which is about 19% larger than the positron bulk lifetime in hcp Y. Such an increase in lifetime is comparable to the case of  $V_{\text{Mg}}$  mono-vacancies in Mg, where Mg crystallizes in an hcp structure with the same space group ( $P6_3/mmc$ ) as Y. The positron lifetime related to the Mg mono-vacancies was  $\sim 13\%$  larger than the positron bulk lifetime in defect-free Mg [32, 33]. This suggests that the second component for the Y film can be attributed to yttrium mono-vacancies ( $V_Y$ ). Since the increase of  $\sim 19\%$  is, on the other hand, significantly lower than for Mg di-vacancies in hcp Mg (with a positron lifetime that is 39% larger than the positron bulk lifetime) [32, 33], Y di-vacancies are not present in the film at detectable concentrations. The concentration of cation mono-vacancies extracted from the two-defect trapping model is  $\sim 10 \times 10^{-6}$  (Table 2.3), which means that 1 out of approximately  $10^5$  Y sites is vacant in the as-deposited Y film. The observed third lifetime component with a lifetime  $\tau_3 \sim 680$  ps is a signature of vacancy clusters that are present at a very small amount, while o-Ps formation in the yttrium film is not seen, as can be understood in view the high density of conduction electrons in the metallic phase that will effectively screen the positron charge, prohibiting Ps formation.

The two-defect trapping model is applied to the  $\text{YH}_{-1.9}$  and  $\text{YH}_x\text{O}_y$  films as well. The extracted positron bulk lifetime  $\tau_b$  for the palladium capped  $\text{YH}_{-1.9}$  ( $\text{YH}_{-1.9}/\text{Pd}$ ) thin film is  $\sim 260$  ps, which is about 10% larger than that for the hcp Y film. To the best of our knowledge, no positron lifetime experiments or calculations on yttrium dihydride nor  $\text{YH}_x\text{O}_y$  are reported in the literature, meaning that no reference values for the positron lifetime in defect-free regions (bulk annihilation) are available. Nevertheless, the observed increase of  $\sim 10\%$  in the extracted positron bulk lifetime for  $\text{YH}_{-1.9}$  compared to Y can be understood, as it can be attributed to the increase in the lattice volume per Y atom of  $\sim 6\%$  in  $\text{YH}_{-1.9}$  compared to Y (as extracted from our XRD results presented in Table S2.2 in the Supplemental Material [18]), leading to larger interstitial space, while the concentration of delocalized conduction electrons is also smaller in  $\text{YH}_{-1.9}$  compared to Y. Furthermore, the extracted bulk positron lifetime  $\tau_b$  for  $\text{YH}_{-1.9}$  is also compatible with the estimated value for the positron bulk lifetime of  $\sim 256$  ps based on an empirical equation for the dependence of  $\tau_b$  on lattice volume for similar metal dihydrides, derived from ab-initio calculations for defect-free  $\text{TiH}_2$  and  $\text{MgH}_2$  [33]. The dominant second component with a lifetime  $\tau_2$  of  $\sim 294$  ps is  $\sim 14\%$  larger than the bulk positron lifetime, and can therefore be assigned to  $V_Y$  mono-vacancies with an extracted concentration of  $\sim 8 \times 10^{-6}$  (Table 2.3). The low intensity third lifetime component arises from a very small amount of larger open volume defects such as vacancy clusters, similar to the case of Y.

Two  $\text{YH}_x\text{O}_y$  thin films,  $\text{YH}_x\text{O}_y-1$  and  $\text{YH}_x\text{O}_y-2$ , were examined in the positron lifetime measurements. The average extracted bulk lifetime for these films is  $\sim 240$  ps. The lifetime of the dominant second component  $\tau_2$  for  $\text{YH}_x\text{O}_y-1$  is  $\sim 11\%$  larger than the bulk positron lifetime  $\tau_b$ , which again can be attributed to  $V_Y$  mono-vacancies. The concentration of cation vacancies in the as-prepared  $\text{YH}_x\text{O}_y$  films is similar to those in the Y and  $\text{YH}_2$  films. The lifetime of the third component of  $\tau_3 \sim 500$  ps is characteristic for vacancy clusters. These

vacancy clusters, at concentrations of about one third to one fourth of the concentration of cation vacancies, are much more abundant than in the Y and  $\text{YH}_{1.9}$  films. The lifetime of  $\tau_3 \sim 500$  ps suggests that the number of vacancies in the cluster is more than five. Namely, we may compare this value to the positron lifetime  $\sim 450$  ps observed for semiconducting GeSn and phosphorus doped Ge (with bulk lifetimes of  $\sim 225$  ps) that is associated with vacancy clusters formed by more than five vacancies [34, 35]. Finally, the long lifetime of  $\sim 1.6$  ns of the fourth component for  $\text{YH}_x\text{O}_y$ -1 indicates that o-Ps is formed in the oxyhydride films, which may occur in nanopores. The estimated average radius of these nanopores is  $\sim 0.25$  nm according to the Tao-Eldrup (TE) model [36, 37] that relates the o-Ps pick-off annihilation lifetime to the size of nanopores, assuming that they are spherical in shape. This pore size corresponds to about seven atoms missing in one unit cell of  $\text{YH}_x\text{O}_y$  ( $\sim V_7$  vacancy cluster). We notice that such vacancy clusters with an average size of  $V_7$  could (in principle) also be responsible for the third lifetime component, if both positron annihilation as well as Ps formation and annihilation occur in the same type of vacancy clusters. The  $\text{YH}_x\text{O}_y$ -2 film shows similar lifetimes and intensities as  $\text{YH}_x\text{O}_y$ -1, indicating that the dominant second lifetime component of  $\text{YH}_x\text{O}_y$ -2 can also be assigned to  $V_Y$  mono-vacancies, while the fourth lifetime component with  $\tau_4$  of  $\sim 2.2$  ns indicates the presence of nanopores with an average radius of  $\sim 0.29$  nm, corresponding to  $\sim V_{10}$  clusters, *i.e.* somewhat larger than in the  $\text{YH}_x\text{O}_y$ -1 film.

The bulk lifetime of the  $\text{Y}_2\text{O}_3$  thin film extracted from the two-defect positron trapping model is  $\sim 256$  ps, which is a bit larger than the lifetime of 239 ps observed in  $\text{Y}_2\text{O}_3$  powders [38]. On the other hand, an experimental lifetime of about 200 ps for sintered  $\text{Y}_2\text{O}_3$  has also been reported [39], while first-principles calculations using the parameter-free generalized gradient approximation indicate a theoretical bulk lifetime of  $\sim 174$  ps [40]. Assuming, nevertheless, that the two-defect positron trapping model is applicable, our study suggests that  $V_Y$  mono-vacancies are present in the  $\text{Y}_2\text{O}_3$  film, together with vacancy clusters. The concentrations of these two types of open-volume defects are of the same order as for the  $\text{YH}_x\text{O}_y$  films. Moreover, the presence of a long lifetime component with  $\tau_4 \approx 3.0$  ns indicates that o-Ps is formed in nanopores, with an average radius of  $\sim 0.37$  nm according to the Tao-Eldrup model assuming a spherical shape. This suggests that  $\sim 14$  atoms are locally missing in the lattice ( $\sim V_{14}$  cluster), showing that the  $\text{Y}_2\text{O}_3$  film contains larger nanopores than the  $\text{YH}_x\text{O}_y$  films.

Summarizing the results of our PALS study,  $V_Y$  cation mono-vacancies are present in all of the sputtered films at similar concentrations of the order of  $10^{-5}$ , leading to near-saturation trapping of positrons and a dominant second lifetime component in the PALS spectra. In addition, vacancy clusters are observed in the yttrium oxyhydride and oxide films at a concentration that is about 15 to 30 times lower than the concentration of the mono-vacancies. Furthermore, o-Ps pick-off annihilation in the yttrium oxyhydride and oxide films is seen, indicating the presence of nanopores with an average diameter in the range of  $\sim 0.5$ - $0.7$  nm. The extracted bulk positron lifetimes for Y,  $\text{YH}_2$  and  $\text{Y}_2\text{O}_3$  are in line with the results

of previous studies, supporting the validity of the two-defect positron trapping model used to analyze the PALS results obtained for the magnetron sputtered Y-based thin films. Furthermore, the information extracted by PALS on the vacancies present in the as-prepared yttrium oxyhydride films aids to elucidate the relationship between the changes in DB-PAS parameters observed during illumination and the microstructural changes that cause the photochromic effect (see section C).

### 2.3.2 Evolution of the electronic structure of Y-based and Gd-based thin films observed by DB-PAS

In this section, we describe our investigation of the variation in electronic structure of the Y-based and Gd-based thin films, that ranges from metal and semiconductor to insulator behaviour, via detection of key aspects of their electron momentum distributions (EMDs) as seen by positrons in DB-PAS. The S- and W-parameters extracted from VEPFIT analysis of the depth-profiles for the Y-based and Gd-based metal, metal hydride, oxyhydride and oxide thin films are presented in the S-W diagrams shown in Fig. 2.2. A systematic decrease of the S-parameter and increase of the W-parameter occurs going from the Y or Gd metal to the metal hydride and metal oxide films, which follows the same trend as previously reported for these types of Y-based films in Refs. [16] and [8], induced by the variation in their electronic structure [16]. Both Gd and Y metal thin films possess the highest values for the S-parameter due to their relatively narrow electron momentum distributions, reflecting the contributions of electrons in a free-electron-like conduction band. The incorporation of H into the lattice of Y or Gd leads to a reduction in S-parameter and increase in W-parameter, indicating a broader positron-electron momentum distribution (PEMD) of the rare-earth (RE) dihydride films compared to the RE films [16]. This is in line with previous positron angular correction of annihilation radiation (ACAR) studies and theoretical models for Y and  $\text{YH}_2$  [41, 42]. The broadening in part stems from localization of some of the conduction electron states in orbitals associated with the H, involving the formation of covalent-ionic Y-H bonds. Detailed insights into the shape of the PEMD and its evolution upon hydrogenation of Y could be obtained by ACAR experiments [43] and/or by ab-initio calculations [44], that are beyond the scope of the present study. The low S-parameter and high W-parameter observed for the insulating RE metal oxide films can also be understood, as this is induced by the strongly localized valence electron orbitals centred around the electronegative oxygen atoms, leading to a correspondingly broad PEMD [45, 46].

If we now compare the S- and W-parameters for the Gd,  $\text{GdH}_2$  and  $\text{Gd}_2\text{O}_3$  films with those of the corresponding Y-based films in Fig. 2.2, very similar trends are observed, while a clear systematic shift towards higher W-parameters and lower S-parameters is apparent. The higher W-parameters of the Gd-based films as compared to the corresponding Y-based films can be attributed to electrons in the confined 4f-orbital of Gd, leading to a broader momentum distribution.



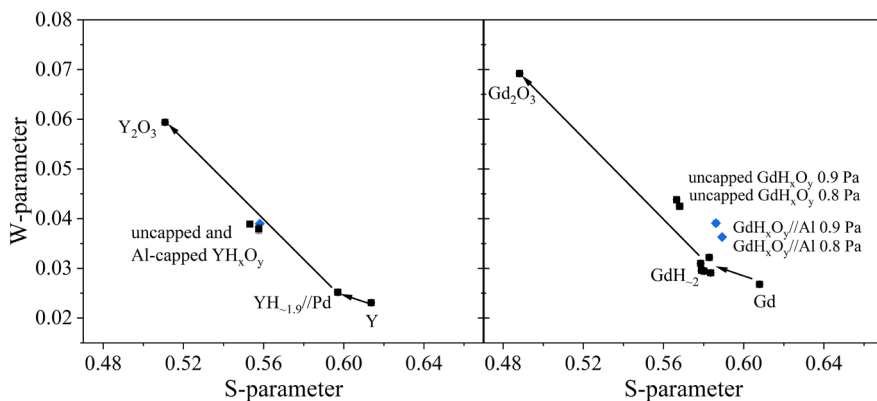


**Figure 2.2:** S-W diagrams of Y-based and Gd-based thin films. The Al capped oxyhydride films are marked with blue colour.

Fig. 2.2 shows that the semiconducting  $\text{YH}_x\text{O}_y$  and  $\text{GdH}_x\text{O}_y$  metal oxyhydride films have S- and W-parameters that lie in-between those of the respective RE metals and RE oxide, reflecting their intermediate composition and ionicity. The S-W points of  $\text{YH}_x\text{O}_y$  films are almost on the line in the S-W diagram connecting  $\text{Y}_2\text{O}_3$  and  $\text{YH}_{-1.9}$ . Clearly, the S-W points of  $\text{GdH}_x\text{O}_y$  films are shifted to higher S values compared to the line from  $\text{Gd}_2\text{O}_3$  to  $\text{GdH}_2$ , suggesting that as-prepared  $\text{GdH}_x\text{O}_y$  films have more and/or larger vacancies that trap positrons compared to  $\text{YH}_x\text{O}_y$  films. This could be related to a more porous structure of the  $\text{GdH}_x\text{O}_y$  films, as these are deposited at higher pressures (0.8 Pa and 0.9 Pa) compared to the  $\text{YH}_x\text{O}_y$  films (0.5 Pa).

The S-W points for the uncapped and capped  $\text{YH}_x\text{O}_y$  films (0.5 Pa) are close together and consistent with our previous results [8, 16]. The S-W points of the uncapped  $\text{GdH}_x\text{O}_y$  films on the other hand are shifted compared to the S-W points of the Al-capped  $\text{GdH}_x\text{O}_y$  films, in the direction towards the S-W point of the  $\text{Gd}_2\text{O}_3$  film. This suggests that these uncapped  $\text{GdH}_x\text{O}_y$  films have a higher O:H ratio compared to the Al-capped films, which could be the result of continued incorporation of O into the lattice of the films for prolonged exposure to ambient air. Apparently, in the films investigated in this study, the air exposure time seems to have a noticeable effect on the oxygen content in  $\text{GdH}_x\text{O}_y$ , while the effect in  $\text{YH}_x\text{O}_y$  is negligible, again pointing to a more porous structure of the  $\text{GdH}_x\text{O}_y$  films.

### 2.3.3 *In-situ* illumination positron Doppler study of the nanostructural evolution of photochromic $\text{YH}_x\text{O}_y$ and $\text{GdH}_x\text{O}_y$ films during photo-darkening and bleaching

#### A. Optical properties

The optical transmittance of  $\text{YH}_x\text{O}_y$  and  $\text{GdH}_x\text{O}_y$  films was measured in order to extract their optical indirect bandgap by Tauc analysis [47] as shown in Fig. S2.5 in Supplemental material [18]. The band gaps of the three  $\text{YH}_x\text{O}_y$  (0.5 Pa) thin films are similar, with an average band gap  $2.53 \pm 0.08$  eV, while the band gaps for the  $\text{GdH}_x\text{O}_y$  (0.8 Pa) and  $\text{GdH}_x\text{O}_y$  (0.9 Pa) films

of  $2.36 \pm 0.05$  eV and  $2.51 \pm 0.06$  eV, respectively, are slightly lower than that for the  $\text{YH}_x\text{O}_y$  films. The increase in band gap for the  $\text{GdH}_x\text{O}_y$  film deposited at higher pressure is presumably related to the larger degree of oxidation that increases the ionicity of the film, as found in our previous studies [8, 9].

The  $\text{YH}_x\text{O}_y$  and  $\text{GdH}_x\text{O}_y$  films show a high transmittance window in the visible and near-IR range (see Fig. S2.5 in the Supplemental Material [18]). The change of the average optical transmittance in the wavelength range of 450-1000 nm between the virgin and the photo-darkened state is used to define the photochromic contrast. Fig. 2.3 shows the time dependence of the average transmittance of  $\text{YH}_x\text{O}_y$  and  $\text{GdH}_x\text{O}_y$  films before illumination, during photo-darkening and during bleaching, normalized to the transmittance of the as-prepared films. Both  $\text{YH}_x\text{O}_y$  and  $\text{GdH}_x\text{O}_y$  films show a clear reduction in sub-bandgap transmittance upon UV illumination at 385 nm, *i.e.* with a photon energy of 3.22 eV, larger than the band gap. The transmittance of the films nearly fully recovers after stopping illumination and subsequent bleaching for several hours. The change in transmittance nearly saturates after  $\sim 1$  h illumination for the  $\text{YH}_x\text{O}_y$  (0.5 Pa) and  $\sim 0.5$  h illumination for the  $\text{GdH}_x\text{O}_y$  (0.8 Pa) sample. The photochromic contrast is  $\sim 40\%$  for the  $\text{YH}_x\text{O}_y$  film, and  $\sim 55\%$  (0.8 Pa) and  $>35\%$  (0.9 Pa) for the  $\text{GdH}_x\text{O}_y$  films.

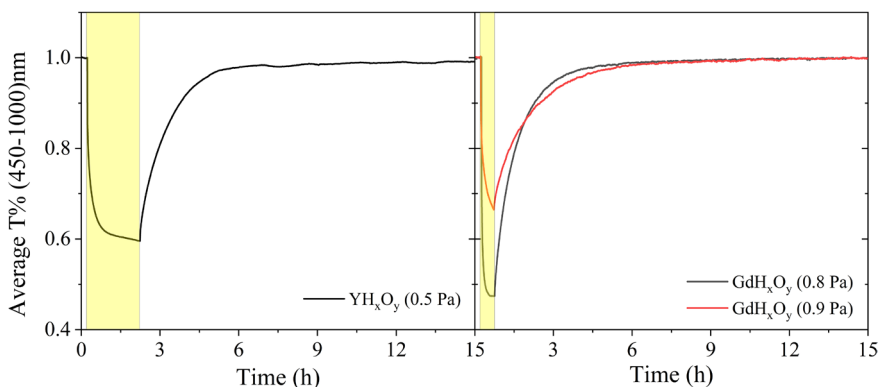


**Figure 2.3:** Normalized transmittance (averaged over the wavelength range of 450-1000 nm) for representative  $\text{YH}_x\text{O}_y$  and  $\text{GdH}_x\text{O}_y$  films during UV illumination (yellow regions) at 385 nm, followed by bleaching in the dark.

### ***B. In-situ Positron Doppler experiments during UV illumination***

*In-situ* illumination DB-PAS measurements were performed on four oxyhydride film samples, namely Al-capped  $\text{YH}_x\text{O}_y$  (0.5 Pa), uncapped  $\text{YH}_x\text{O}_y$  (0.5 Pa), Al-capped  $\text{GdH}_x\text{O}_y$  (0.9 Pa) and uncapped  $\text{GdH}_x\text{O}_y$  (0.9 Pa), in order to investigate the evolution of open-volume defects and electronic structure of the oxyhydride films during photo-darkening and subsequent bleaching. In order to ensure saturation of photo-darkening, an illumination time

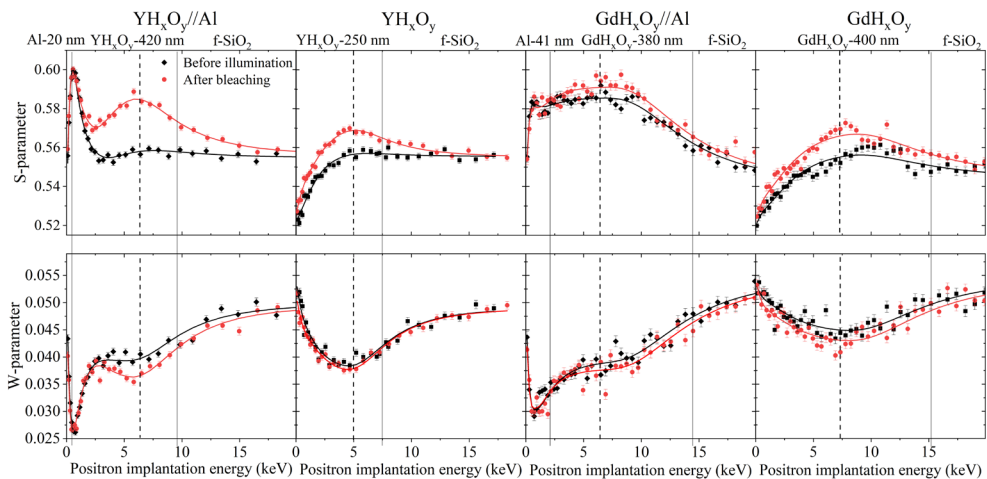


**Figure 2.4:** S- and W-parameter positron Doppler broadening depth profiles of  $\text{YH}_x\text{O}_y//\text{Al}$  (0.5 Pa),  $\text{YH}_x\text{O}_y$  (0.5 Pa),  $\text{GdH}_x\text{O}_y//\text{Al}$  (0.9 Pa) and  $\text{GdH}_x\text{O}_y$  (0.9 Pa), thin films before illumination (black symbols and lines), and after 2.5 h illumination and bleaching for  $\sim 38$  h (red circles and lines). The dashed lines indicate the positron implantation energy for the *in-situ* illumination DB-PAS measurements shown in Figure 2.5. The vertical solid lines indicate the boundaries between adjacent layers based on the VEPFIT analyses.

of 2.5 h was used for all oxyhydride films, while the bleaching phase was monitored for  $\sim 38$  hours, *i.e.* well beyond the time required to achieve full bleaching.

Fig. 2.4 shows the S- and W-parameter depth profiles extracted from the DB-PAS measurements for the four samples before illumination, and after full bleaching of the darkened state, respectively. The clear increase in S-parameter and modest reduction in W-parameter indicate that some of the nanostructural modifications of the oxyhydride films induced by the illumination do not fully recover after bleaching. The changes in the S- and W-depth profiles are qualitatively similar to those observed in our previous study on Al-capped  $\text{YH}_x\text{O}_y$  films [8], where they were attributed to the formation of  $\text{V}_\text{Y}$  cation vacancies or small vacancy clusters such as  $\text{V}_\text{Y}-\text{V}_\text{H}$  or  $\text{V}_\text{Y}-\text{V}_\text{O}$  di-vacancies, suggesting that some of the  $\text{H}^-$  and/or  $\text{O}^{2-}$  ions are removed from their lattice positions during the illumination. More insights are gained by including the results of our current PALS study, which shows that as-prepared  $\text{YH}_x\text{O}_y$  films already contain a large concentration of cation vacancies of  $\sim 12\text{--}15 \times 10^{-6}$  [48] ( $I_2 \sim 71\text{--}78\%$ ) and vacancy clusters of  $\sim 0.4\text{--}1 \times 10^{-6}$  ( $I_3 \sim 13\text{--}22\%$ ), leading to near-saturation trapping of positrons in these vacancy-related defects ( $I_2 + I_3 \sim 91\text{--}95\%$ ) [29, 49]. Therefore, we can exclude that the formation of more cation mono-vacancies plays a dominant role in the observed significant changes in the positron Doppler broadening S-parameter after illumination and bleaching. However, the observed changes may originate from light-induced formation of anion vacancies ( $\text{V}_\text{H}$ ,  $\text{V}_\text{O}$ ) that are created by  $\text{H}^-$  or  $\text{O}^{2-}$  released from their lattice positions. The formed anion vacancies may subsequently cluster

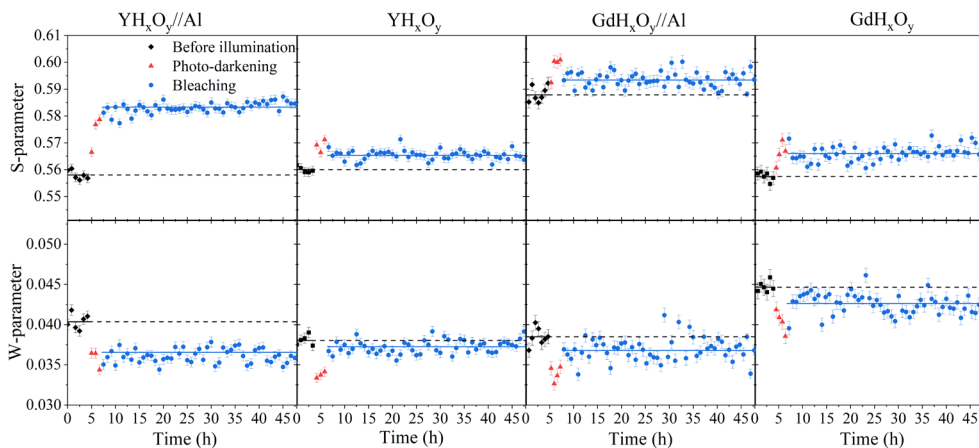


**Figure 2.5:** Time dependence of the S and W Doppler broadening parameters collected in *in-situ* DB-PAS measurements on  $\text{YH}_x\text{O}_y//\text{Al}$ , uncapped  $\text{YH}_x\text{O}_y$ ,  $\text{GdH}_x\text{O}_y//\text{Al}$  and uncapped  $\text{GdH}_x\text{O}_y$  films before UV illumination (black symbols), under 2.5 h illumination (photo-darkening, red triangles) and during  $\sim 38$  h of bleaching (blue circles) collected at a positron implantation energy of 6.4, 5, 6.4 and 7.2 keV, respectively.

with cation mono-vacancies to form  $\text{V}_\text{Y}-\text{V}_\text{H}$  or  $\text{V}_\text{Y}-\text{V}_\text{O}$  di-vacancies, or small vacancy clusters [16], leading to positron trapping and annihilation in these larger vacancy defects. Since the changes in S- and W-parameter systematically occur in all films, we infer that in general the optical excitation of electron-hole pairs induces the release of  $\text{H}^-$  or  $\text{O}^{2-}$  ions from their lattice positions. Such a (possibly local) displacement of anions may play a role in the mechanism of the photochromic effect for both rare-earth oxyhydride systems, as suggested previously in Refs. [8, 50].

More insights into the evolution of the nanostructure of the oxyhydride layers were gained from the time dependence of the S- and W-parameter of the  $\text{YH}_x\text{O}_y//\text{Al}$ , uncapped  $\text{YH}_x\text{O}_y$ ,  $\text{GdH}_x\text{O}_y//\text{Al}$  and uncapped  $\text{GdH}_x\text{O}_y$  films before illumination, during UV photo-darkening and during subsequent bleaching, collected at a fixed positron implantation energy of 6.4, 5, 6.4 and 7.2 keV, respectively, as shown in Fig. 2.5. These positron implantation energies were selected in order to ensure that most of the positrons annihilate in the oxyhydride layer. For all samples, the S-parameter shows a substantial increase during illumination, while the W-parameter decreases strongly. In the case of the Al-capped  $\text{YH}_x\text{O}_y$  film, the S- and W-parameter do not change further during bleaching, demonstrating that irreversible changes take place that persist on a time scale of at least 38 h, *i.e.* long after optical transparency of the film has returned, in line with the corresponding depth profiles and as reported in Ref. [8]. In contrast, the S- and W-parameters of the other three samples show a partially reversed behavior once the illumination is stopped, as the S- and W-values are seen to move back into the direction of their initial values, suggesting that the nanostructural properties of the films

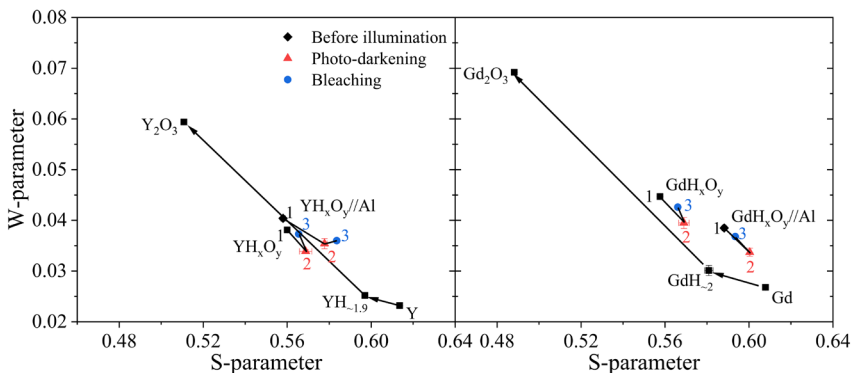


**Figure 2.6:** S and W values for  $\text{YH}_x\text{O}_y//\text{Al}$ , uncapped  $\text{YH}_x\text{O}_y$ ,  $\text{GdH}_x\text{O}_y//\text{Al}$  and uncapped  $\text{GdH}_x\text{O}_y$  films before illumination (1, black symbols), upon illumination for 1.5-2.5 hours (2, red triangles) and after illumination in the bleaching state (3, blue circles) according to the *in-situ* illumination DB-PAS measurements, compared to the (S,W)-points of the as-deposited Y, Gd metal,  $\text{YH}_{-1.9}$ ,  $\text{GdH}_{-2}$  metal hydride and  $\text{YH}_2\text{O}_3$ ,  $\text{Gd}_2\text{O}_3$  metal oxide films.

partially return towards the initial state. Nevertheless, permanent changes are also seen for these samples, with shifted S- and W-parameters that remain stable during bleaching for ~38 hours, consistent with the depth profiles in Fig. 2.4. As discussed, these permanent changes are related to the formation of stable di-vacancies (or small vacancy clusters) during illumination. It is remarkable that the Doppler broadening parameters, in particular the W-parameter, show large changes during illumination which partially shift back to the original state upon bleaching in the uncapped  $\text{YH}_x\text{O}_y$ , Al-capped  $\text{GdH}_x\text{O}_y//\text{Al}$  and uncapped  $\text{GdH}_x\text{O}_y$  films. This strongly suggests that a second type of nanostructural changes occurs during illumination, which recovers during bleaching.

In order to gain more insights into the origin of the changes in S and W during illumination, we compare the evolution of the S and W parameters in an S-W diagram with those of the as-deposited metal, metal hydride and metal oxide films, Y,  $\text{YH}_{-1.9}$ ,  $\text{Y}_2\text{O}_3$  and Gd,  $\text{GdH}_{-2}$ ,  $\text{Gd}_2\text{O}_3$ , respectively. In Fig. 2.6, the S-W points are presented for  $\text{YH}_x\text{O}_y//\text{Al}$ , uncapped  $\text{YH}_x\text{O}_y$ ,  $\text{GdH}_x\text{O}_y//\text{Al}$  and uncapped  $\text{GdH}_x\text{O}_y$  films before illumination (1), upon 1.5 to 2.5 hours of illumination (2) and after illumination in the bleached state (3) extracted from the time-dependence measurements at fixed positron implantation energy (Fig. 2.5), together with those of the as-deposited metal, metal hydride and oxide films. The values of the S- and W-parameters are also given in Table S2.4 in the Supplemental Material [18]. The shifts in the (S,W) points of the  $\text{YH}_x\text{O}_y$ ,  $\text{GdH}_x\text{O}_y//\text{Al}$ , and  $\text{GdH}_x\text{O}_y$  films during illumination (process 1→2) clearly are parallel to the line connecting the (S,W) points of the metal oxide  $\text{RE}_2\text{O}_3$  and metal hydride  $\text{REH}_2$  phases. The corresponding quantitative values of the parameter  $R = \frac{\Delta S}{\Delta W}$ , with  $\Delta S$  and  $\Delta W$  the change in respectively the S- and W-parameter induced by the illumination, for the oxyhydride films of  $R = -2.0 \pm 0.5$  ( $\text{YH}_x\text{O}_y$ ),  $-2.5 \pm 0.5$  ( $\text{GdH}_x\text{O}_y//\text{Al}$ ) and

$-2.2 \pm 0.7$  ( $\text{GdH}_x\text{O}_y$ ) are close to  $R = -2.5 \pm 0.1$  for the line that connects the Y or Gd metal oxide and metal hydride. After the illumination is stopped and bleaching sets in, the shifts in the S-W diagram are partially reversed (process 2 $\rightarrow$ 3), suggesting that part of the illumination-induced nanostructural transformations is reversible, possibly related to formation and disappearance of metallic domains. In contrast, the illumination-induced shift in S-W for the Al-capped  $\text{YH}_x\text{O}_y$  film, with  $R = -4 \pm 1$ , is not exactly parallel to the line connecting the S-W points of  $\text{Y}_2\text{O}_3$  and  $\text{YH}_{-1.9}$ . Furthermore, in the bleaching phase, no sign of reversibility is observed for this sample, in line with Ref. [8]. This could be due to a larger concentration of di-vacancies induced in this sample by the illumination, leading to a relatively large increase in S compared to the other samples. During bleaching, the metallic domains disappear, causing even more positrons to trap in di-vacancies during bleaching compared to the photodarkening state. In this case, the irreversible formation of di-vacancies (or small vacancy clusters) that act as positron trapping centers appears to be the dominant process. The increase in S-parameter indicates that the S-parameter for di-vacancies is higher than for the metallic domains.

We note that the irreversible formation of di-vacancies occurs for all samples, as the  $R$ -values obtained from a comparison of the as-prepared state with the state of the films after bleaching (1 $\rightarrow$ 3) of  $R = -7 \pm 1$  ( $\text{YH}_x\text{O}_y/\text{Al}$ ),  $R = -6.9 \pm 2.5$  ( $\text{YH}_x\text{O}_y$ ),  $R = -3.1 \pm 0.9$  ( $\text{GdH}_x\text{O}_y/\text{Al}$ ), and  $R = -4.0 \pm 0.8$  ( $\text{GdH}_x\text{O}_y$ ) are larger than for the shifts in (S,W) observed during photo-darkening. In view of the photochromism, the partially reversible behaviour observed during bleaching for the latter three samples is significant and points to a second, reversible nanostructural process induced by the illumination, besides the formation of vacancies and irreversible formation of di-vacancies. Below we will discuss two proposed mechanisms that may contribute to the photo-darkening and at the same time could also explain the observed reversible part of the changes in the positron Doppler broadening S and W parameters. These two proposed mechanisms are schematically illustrated in Fig. 2.7.

### ***Proposed mechanism 1: the formation of hydrogen-rich metallic-like nanodomains***

The observed shift of the S-W points for the oxyhydride films during UV illumination into the direction of the S-W point of the metal hydride suggests that the illumination leads to the formation of domains with lower O:H ratios (lower ionicity). Indeed, in our previous study [8], we found that  $\text{YH}_x\text{O}_y$  films synthesized at lower deposition pressure contain more hydrogen (lower O:H ratio) and exhibit systematically higher S- and lower W-parameters [8]. If we assume that the difference in (S,W) point for  $\text{YH}_x\text{O}_y$  with respect to the (S,W) point of the metal oxide  $\text{Y}_2\text{O}_3$  phase is proportional to its hydrogen fraction, and that  $\text{YH}_x\text{O}_y$  deposited at 0.4 Pa (near the boundary pressure beyond which the films gain full optical transparency) corresponds to a composition close to  $\text{YH}_2\text{O}_{0.5}$ , the composition of the film deposited at 0.5 Pa would approximately correspond to  $\text{YH}_{-1.7}\text{O}_{-0.65}$ . Upon illumination, the

## 2

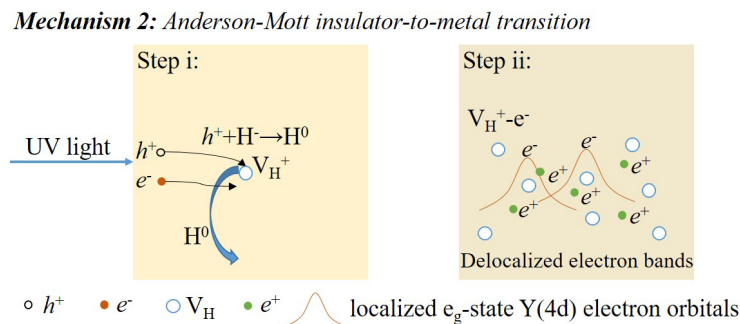
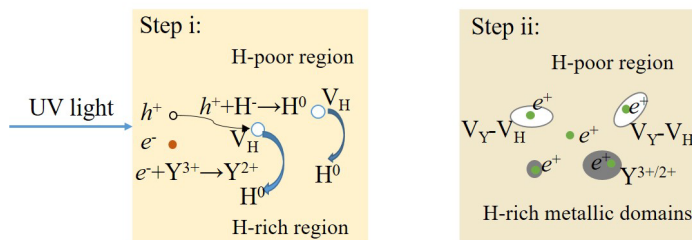


**Figure 2.7:** Schematic illustration of the two proposed mechanisms 1 and 2.

(S,W) point of the 0.5 Pa sample approaches that of the as-prepared 0.4 Pa sample, suggesting that the domains probed by the positrons contain an hydrogen-enriched composition that is, on the average, close to that of  $\text{YH}_2\text{O}_{0.5}$ . The picture, thus, emerges that during UV illumination some hydrogen ions are released from their lattice positions, possibly from the energetically less favourable octahedral sites [51, 52], due to the light-induced formation of mobile neutral hydrogen by the excitation of electron-hole pairs with  $\text{H}^- + h^+ \rightarrow \text{H}^0$ . Subsequently, the mobile neutral hydrogen ions move towards a local environment with lower oxygen content and form hydrogen-enriched domains. If the local composition reaches an O:H ratio below that of  $\text{YH}_2\text{O}_{0.5}$ , in particular  $\text{YH}_2\text{O}_x$  with  $x < 0.5$ , a mixed valence character of the Y cations sets in, with part of the  $\text{Y}^{3+}$  replaced by  $\text{Y}^{2+}$ , and the electronic structure becomes metallic-like for a sufficiently high local concentration of  $\text{Y}^{2+}$ . Alternatively, the mentioned removal of hydrogen atoms in combination with a local displacement of an oxygen ion to the site of one out of two removed hydrogen atoms can lead to local phase segregation into a hydrogen-poor area and a metallic hydrogen-rich area with a local composition of  $\text{YH}_2\text{O}_x$  ( $x < 0.5$ ), for example according to  $2 \text{Y}_4\text{H}_8\text{O}_2 \rightarrow \text{Y}_4\text{H}_8\text{O}_2 + \text{Y}_4\text{H}_6\text{O}_2 + 2 \text{H}^0 \rightarrow \text{Y}_4\text{H}_8\text{O} + \text{Y}_4\text{H}_6\text{O}_3 + 2 \text{H}^0$ , with the resulting  $\text{YH}_2\text{O}_{0.25}$  in a mixed  $\text{Y}^{2+}/\text{Y}^{3+}$  valence state, while the hydrogen-poor  $\text{YH}_{1.5}\text{O}_{0.75}$  fully retains the  $\text{Y}^{3+}$  valence state. Both mentioned options suggest that phase-segregated domains with a metallic-like character are formed during illumination, enabled by mobility of light-induced interstitial hydrogen (supported also by the observation of release of a small amount of hydrogen molecules from

$\text{YH}_x\text{O}_y$  films during UV illumination [53]), and local displacements of oxygen ions. Indeed, molecular dynamics simulations suggest hopping mobility primarily of hydrogen located at octahedral sites, but a small hopping mobility of oxygen is also seen [52]. The occurrence of the phase segregation process is supported by previous spectroscopic ellipsometry studies that suggested that metallic domains at a volume fraction of up to ~6 vol. % are formed during the illumination [14], leading to pronounced changes in the dielectric function in the near-infrared and visible range. NMR studies on  $\text{YH}_x\text{O}_y$  films suggest relocation of the hydrogen in the lattice during the illumination, reporting the disappearance of a ~3% mobile hydrogen fraction seen in  $^1\text{H}$  MAS (magic angle spinning), that recovers after bleaching in the dark [15]. The formation of such metallic-like domains in an otherwise semiconducting (transparent) matrix may explain the reduction in optical transmission over a large sub-band gap wavelength range [14], characteristic for the photochromic effect in this class of rare-earth oxyhydrides. Remarkably, such changes in the optical properties also occur by modification of the composition to  $\text{Y}_{1-z}\text{Zr}_z\text{H}_x\text{O}_y$  by co-sputtering of Y and Zr [54]. For these mixed cation oxyhydride films, the addition of Zr leads to a strong reduction in the optical transmission in the sub-band gap wavelength range ( $T \sim 86\%$  for  $z = 0$  to  $T \sim 62\%$  for  $z = 0.5$ ), while the reflectivity  $R$  stays relatively small ( $R \sim 12\%$  for  $z = 0$  to  $R \sim 15\%$  for  $z = 0.5$ ; with  $R \sim 12\%$  for  $\text{YO}_x\text{H}_y$  films mainly related to the index of refraction in the range of  $n \sim 1.9 - 2.2$  [14, 55]) and the sub-band gap optical absorption is increased, attributed to the presence of not fully oxidized metallic  $\text{ZrH}_2$  clusters in the otherwise semiconducting  $\text{Y}_{1-z}\text{Zr}_z\text{H}_x\text{O}_y$  films (with band gaps in the range of 2.2-2.8 eV) [54].

We note that the observed remarkably large change in the positron Doppler broadening  $W$ -parameter (~12%) and the corresponding clear shift in the  $S$ -parameter in these films upon illumination can be attributed within this proposed mechanism to either a high concentration of H-rich domains, or a high fraction of positrons annihilating in H-rich domains. Since the formation of H-rich domains is necessarily accompanied by the formation of H-poor domains (as we assume no H enters or diffuses out of the film), one could expect that the values for  $S$  and  $W$  averaged over the volume of the oxyhydride film do not change much. Therefore, the large reversible part of the changes in  $S$  and  $W$  observed during illumination requires that a high fraction of positrons after diffusion in the film traps and annihilates in the H-rich domains. Such preferential trapping of positrons can be caused by a larger positron affinity for H-rich regions compared to H-poor regions, and can have a pronounced effect on the positron signal even when only a relatively small amount of nano-sized H-rich domains is present. For instance, in previous positron Doppler broadening and 2D-ACAR studies of metallic Li nanoclusters embedded in crystalline MgO [56], a positron trapping fraction in the Li nanoclusters as high as ~92% was observed with only ~3 vol. % of Li nanoclusters present in the MgO matrix [56]. In that study, the preferred positron trapping in the Li nano-domains was caused by the large difference in the positron affinity for Li compared to MgO (~1.8-2.8 eV) deduced from ab-initio calculations [56, 46]. We should note that, in the present case, during illumination not only H-rich domains are formed, but also cation-anion di-



vacancies such as  $V_Y$ - $V_H$  in the H-poor oxyhydride matrix. Thus, during illumination preferential trapping of positron not only occurs at H-rich metallic domains, but also at  $V_Y$ - $V_H$  in the H-poor regions (Fig. 2.8). Both processes contribute to the observed changes in S and W during illumination. For simplicity, we did not include the process of di-vacancy formation in the oxyhydride matrix, which might reduce the positron diffusion length, in our simulations.

A similar amplifying effect of the positron signal from embedded metallic nano-domains could also take place for the photo-darkened oxyhydrides, provided that (1) the average distance between H-enriched domains that appear during illumination are of the same order of magnitude or less than the diffusion length of positrons in the surrounding H-poor oxyhydride matrix, and (2) the difference in positron affinity is sufficiently large, i.e. at least several tenths of eV to prevent significant thermal de-trapping.

In order to assess the implications of preferred positron trapping quantitatively, we present simulations on the fraction of positrons that annihilate in such H-enriched domains following the diffusion-limited trapping model used in Refs. [56, 57]. This model assumes that the domains are spherical in shape and homogeneously distributed in the matrix. We assume that all positrons that reach H-rich domains are trapped, and that de-trapping of positrons from the domains can be neglected. The fraction of positrons that are initially stopped in the matrix and subsequently trap in H-rich domains  $f_{\text{domains}}$  is then given by equations (4) and (5) [56, 57]:

$$f_{\text{domains}} = \frac{\kappa}{\kappa + \lambda_{\text{matrix}}} = \frac{4\pi r D_+ c}{4\pi r D_+ c + \lambda_{\text{matrix}}} = \frac{4\pi r L_+^2 c}{4\pi r L_+^2 c + 1} \quad (2.4)$$

$$L_+ = \sqrt{D_+ / \lambda_{\text{matrix}}} \quad (2.5)$$

where  $\kappa$  is the positron trapping rate in the hydrogen-rich metallic-like domains ( $\text{s}^{-1}$ ),  $\lambda_{\text{matrix}}$  is the effective annihilation rate in the oxyhydride matrix surrounding the domains ( $\text{s}^{-1}$ ),  $r$  is the radius of the domains (m),  $c$  is the concentration of the domains ( $\text{m}^{-3}$ ),  $D_+$  and  $L_+$  are, respectively, the positron diffusion coefficient ( $\text{m}^2 \text{s}^{-1}$ ) and positron diffusion length in the oxyhydride matrix (m). Equation (4) can be rewritten in terms of the volume fraction of metallic domains  $f_V$ , the radius of a metallic domain  $r$  and the positron diffusion length  $L_+$ ,

$$\text{according to } f_{\text{domains}}(r) = \frac{f_V \cdot 3L_+^2}{f_V \cdot 3L_+^2 + r^2}.$$

While the size of the H-rich domains formed in the oxyhydride films is not known, their size must be larger than  $\sim 0.5$  nm since the positrons cannot trap if the domain size is too small, as the difference in positron affinity with the surrounding matrix will disappear due to the increase in the energy of the quantum confined positron state with reduced domain size [56]. On the other hand, if the size of the H-rich domains is large at a low (constant) volume fraction of H-rich domains, the concentration of domains will be small. The probability of positron trapping in the domains will be low in that case due to the large average distance between the H-rich domains. This distance then becomes much larger than the positron

diffusion length in the H-poor oxyhydride matrix, and only a small fraction of positrons will be able to reach the H-rich domains and annihilate there instead of the surrounding matrix.

As an example of our simulations, we first consider the case of H-rich domains with a radius of 1 nm occupying a volume fraction of 6 vol. % of the oxyhydride. The concentration of the domains will then be  $\sim 1.4 \times 10^{25} \text{ m}^{-3}$ , corresponding to an average inter-domain distance of around 4 nm. We assume that the diffusion length  $L_+$  in oxyhydride films is 20 nm, since the experimental diffusion length extracted from the VEPFIT analysis of the oxyhydride films ranges from  $\sim 10$  to  $\sim 40$  nm (Table S2.5 in Supplemental Material [18]), i.e. reduced with respect to the estimated diffusion length of  $\sim 150$  nm for defect-free yttrium oxyhydride by positron trapping in vacancies with a concentrations of  $\sim 10^{-4}$  [48] (see Supplemental Material [18]). These parameters yield a very high fraction of  $\sim 99\%$  of positrons that trap and annihilate in domains with a radius of 1 nm. This illustrates that, despite a low volume fraction, the positron signal can be dominated by annihilation in H-rich domains. We note that in this model, the fraction of positrons trapping in the H-rich domains is significantly affected by the average distance between the domains (that scales proportional to the size of the domains for a given volume fraction) and by the positron diffusion length in the H-poor matrix. If we take into account that a fraction of the implanted positrons will be stopped inside of the metallic domains instead of the matrix, the full expression for the fraction of positrons annihilating in the metallic domains is  $f_{\text{domains}}(r) = (1-f_V) \cdot \frac{f_V \cdot 3L_+^2}{f_V \cdot 3L_+^2 + r^2} + f_V$ , assuming that the mass density of the domains and the matrix are comparable.

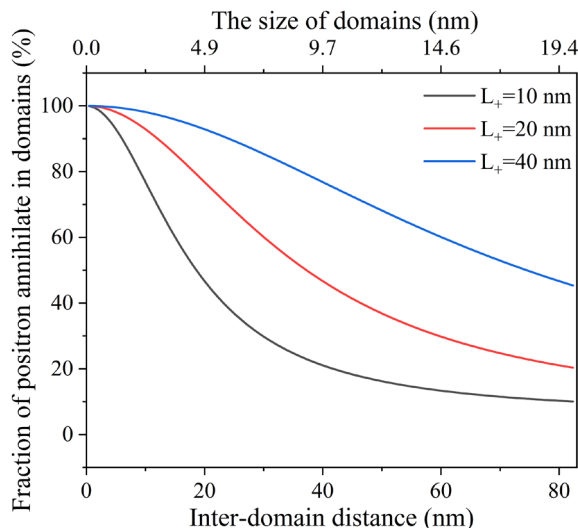


**Figure 2.8:** Simulated positron annihilation fractions in H-rich domains as a function of average distance between the domains at a positron diffusion length of 10, 20 and 40 nm, respectively. A volume fraction of 6 vol.% of spherically-shaped domains was assumed.

In Fig. 2.8, we therefore show the simulated dependence of the fraction of positrons that annihilate in the H-rich domains  $f_{\text{domains}}$  on the average distance between (and size of) these domains, for three different positron diffusion lengths of 10, 20 and 40 nm, respectively, for a volume fraction  $f_v = 0.06$  (6 vol.%) of H-rich domains with radius  $r$ .

The positron annihilation fractions in the H-rich domains are much higher in most areas of Fig. 2.8 compared to what would be expected solely on the basis of a volume fraction of  $\sim 6$  vol. % of these domains. This shows that H-rich domains at a small volume fraction can dominate the positron signal in certain parameter regions. Our simulations suggest that the average size of the H-rich domains (at a volume fraction of 6 vol.%) should be in the range of  $\sim 0.5$  nm to  $\sim 20$  nm in case that the observed shifts in (S,W) parameters (Fig. 2.6) are caused by the formation of H-rich domains in a H-reduced  $\text{YO}_x\text{H}_y$  matrix.

***Proposed mechanism 2: Anderson-Mott insulator-to-metal transition in domains related to electron states localized near formed hydrogen vacancies***

A second possible mechanism that we discuss here is inspired by the insulator-to-metal transition in yttrium trihydride and lanthanum trihydride, which exhibit large changes in the optical properties and conductivity upon release of hydrogen when a composition of respectively  $\text{YH}_{-2.7}$  and  $\text{LaH}_{-2.8}$  is reached. According to Ng *et al.*, the insulator-to-metal transition is induced by the formation of hydrogen vacancies at octahedral sites ( $V_{\text{H}}^+$ ), where charge-compensating electrons are localized in an  $e_g$ -state Y(4d) electron orbital at the surrounding Y ions. When the concentration of these localized electrons is sufficient high, their orbitals overlap, leading to the formation of a delocalized electron band and the occurrence of the insulator-to-metal transition [58].

We assume that a similar scenario may play a role in the photochromism of the rare-earth oxyhydride films. When such oxyhydride films are exposed to UV light with photon energy above the band gap, electron-hole ( $e^-h^+$ ) pairs are generated. The positively charged holes may be trapped by  $\text{H}^-$  anions and formed neutral hydrogen ( $\text{H}^0$ ) according to  $\text{H}^- + h^+ \rightarrow \text{H}^0$ . The neutral hydrogen will subsequently be released from its lattice position. Since hydrogen atoms are less strongly bound at the octahedral sites [51, 52], this process will occur predominantly for octahedral site hydrogen, and hydrogen vacancies are formed at octahedral sites, similar to the case of  $\text{YH}_3$  and  $\text{LaH}_3$ , carrying a positive charge,  $V_{\text{H}}^+$ .

The released  $\text{H}^0$  might stay at interstitial positions, or get trapped at the vacancy clusters or nanopores inside the films, or, similar to what occurs in  $\text{YH}_3$  and  $\text{LaH}_3$ , even effuse out of the films. Simultaneously, the photo-excited electrons present in the conduction band of the  $\text{REH}_x\text{O}_y$  will sense the Coulomb force of the positively charged  $V_{\text{H}}^+$  centers, and may get trapped in a localized  $e_g$ -Y(4d) orbital of the Y ions surrounding a hydrogen vacancy, as this will constitute a strongly bonded state with binding energies of the order of several eV [58]. Progressive illumination will lead to continuous creation of  $e^-h^+$  pairs. As a consequence, the concentration of  $V_{\text{H}}^+$  vacancies will gradually increase in time. When the concentration of

octahedral  $V_H^+$  in a certain domain of the  $YH_xO_y$  film is sufficient large, say of the order of  $\sim 10\%$  of the hydrogen present in the domains (as required for yttrium trihydride,  $YH_3$ ), one can expect the orbitals of the trapped charge-compensating localized  $e_g$ -state  $Y(4d)$  electrons to overlap. This will lead to the formation of an electron band and a metallic-like electronic structure of the respective domains in the  $YH_xO_y$  film, inducing the Anderson-Mott insulator-to-metal transition in these domains in the rare-earth oxyhydride films under illumination. We note in addition, that such a high concentration of delocalized electrons is observable in positron Doppler broadening, which would lead to a shift in (S,W) to higher S and lower W parameters approximately towards the direction of the (S,W) point of the metallic dihydride.

It is interesting to discuss the implications of this proposed mechanism for the time scale of the photo-darkening process in a semi-quantitative manner. If we assume that, in order to induce photo-darkening, a significant fraction of neutral charge H atoms need to be removed from octahedral sites of, for example,  $YH_2O_{0.5}$ , according to  $Y_4H_8O_{0.5} \rightarrow Y_4H_7O_{0.5} + H^0$  ( $\sim 12.5\%$  of the hydrogen removed),  $\sim 1$  hydrogen vacancy will be formed on the average in a cubic unit cell with lattice parameter of  $\sim 0.54$  nm. Following this, a required hydrogen vacancy density of  $\sim 6.4 \times 10^{21} \text{ cm}^{-3}$  can be estimated. On the other hand, the photon flux of the LED used in the present *in-situ* illumination DB-PAS studies is  $\sim 6.6 \times 10^{16} \text{ photons/cm}^2/\text{s}$ . Assuming that all incident photons are absorbed in the  $\sim 300$  nm thick  $YH_xO_y$  film, one can estimate an average density of absorbed photons per second of  $\sim 2.2 \times 10^{21} \text{ photons/cm}^3/\text{s}$ . If each photon is converted into an electron-hole pair and leads to the generation of a hydrogen vacancy-localized electron pair at 100% conversion efficiency, one can estimate that a time on the order of a few seconds would be required to induce the insulator-to-metal transition. This estimated time scale needed for photo-darkening of the films is clearly much longer than typical for photo-excited carrier processes in opto-electric materials such as solar cells (on the order of nanoseconds to microseconds) [59]. The initial stages of the photo-darkening in the rare-earth oxyhydride films indeed take place at a seconds timescale, but slows down in the process towards saturation. For instance, about one-third of the total change in transmittance upon UV illumination of both  $YH_xO_y$  and  $GdH_xO_y$  films (Fig. 2.4) occurs within the first 30 seconds. Clearly, therefore, the observed time scales for photo-darkening in these rare-earth oxyhydride films, which in the initial phase are an order of magnitude larger than the theoretical estimate, can be understood well within this proposed mechanism, since most of the above-mentioned processes will likely not be highly efficient.

The above-mentioned parameters can also be used to give a qualitative insight into the optical properties associated with the photo-darkening phenomenon in oxyhydride films, in which a substantial reduction in the transmittance in a broad sub-band-gap wavelength range (above  $\sim 400$  nm) is observed after illumination, related to a strong increase in absorption. In simple free-electron metals, strong increase in reflectance is primarily caused by prohibition of propagation of light waves within the metal at frequencies around and below plasma frequency  $\omega_p$  since the index of refraction becomes predominantly imaginary, and collision

losses of conduction electrons may lead to strong absorption [60, 61]. The plasma frequency  $\omega_p$  is given by  $\omega_p = \sqrt{\frac{ne^2}{\epsilon_0 m^*}}$ , where  $n$  is density of electrons,  $e$  the electron charge,  $\epsilon_0$  the dielectric permittivity of the vacuum, and  $m^*$  is the effective electron mass, respectively. Accordingly, the plasma wavelength  $\lambda_p$  is given by  $\lambda_p = \frac{2\pi c}{\omega_p}$ , where  $c$  is the velocity of light in the vacuum. We assume, in this simple free-electron (Drude-like) picture, that the effective electron mass is equal to its rest mass. Based on the assumption that a delocalized electron band is formed in domains of the  $\text{YH}_x\text{O}_y$  film when the local electron density reaches  $\sim 6.4 \times 10^{21} \text{ cm}^{-3}$  (i.e. for the case of 12.5% hydrogen vacancies in  $\text{YH}_2\text{O}_{0.5}$ ), a plasma frequency  $\omega_p$  and a plasma wavelength  $\lambda_p$  of  $\sim 4.5 \times 10^{15} \text{ s}^{-1}$  and  $\sim 420 \text{ nm}$ , respectively, can be estimated. For a macroscopic, free-electron metal, such plasma resonance results in a high reflectivity  $R \sim 1$  for wavelengths longer than the plasma wavelength. However, in case of a metallic domain of size smaller or comparable to the incident wavelength, the confinement in space of the free electron gas leads to a more complex situation better described by the Mie theory [62, 63]. Here, as the oscillating electromagnetic field drives the electron gas against the surfaces of the metallic domain, an oscillating dipole/multipole is induced, and a fraction of the incoming radiation energy is absorbed in the polarization of the metal/dielectric interface. A further fraction of the incoming energy is scattered as radiation from the oscillating dipole/multipole. The presence of domains with a metallic-like character in the illuminated rare-earth oxyhydride films may explain their largely changed optical properties in the photo-darkened state, e.g. the large reduction in optical transmission in a wide sub-band gap wavelength range (above  $\sim 400 \text{ nm}$ ). Future studies are required to simulate the optical properties of metallic domains embedded in a semiconducting  $\text{YH}_x\text{O}_y$  medium, which may include plasmonic resonances that depend on the size and shape of the domains, as well as on their electron concentration. In particular also, ab-initio calculations of the electronic structure of the formed electron band are a promising future research direction to gain advanced insights into the mechanism proposed in this section.

Finally, we note that this proposed mechanism is also in line with the observed gradual reduction in the photochromic contrast with increased O:H ratio, for compositions of  $x \sim 0.5$  to  $x \sim 1$  for magnetron-sputtered  $\text{YH}_{3-2x}\text{O}_x$  films [8]. In this composition range, a systematic decrease occurs in the number of hydrogen atoms located at octahedral sites. This leads to a reduction in the (maximum) concentration of octahedral vacancies that can be generated by the illumination. Consequently, this reduces the probability that, in a certain nanoscale area, the threshold concentration of electrons is reached required for the formation of the (free-)electron band that, within this proposed mechanism, underlies the (local) insulator-to-metal transition and corresponding changes in the optical properties of the film under illumination.

## 2.4 Conclusions

The sizes and concentrations of open volume defects in as-prepared magnetron sputtered  $\text{YH}_x\text{O}_y$ , Y,  $\text{YH}_{-1.9}$ , and  $\text{Y}_2\text{O}_3$  thin films were studied by positron annihilation lifetime spectroscopy. It was found that yttrium cation mono-vacancies dominate the positron annihilation signal in Y and Y dihydride thin films at concentrations on the order of  $10^{-5}$  per Y atom. The concentration of mono-vacancies extracted by DB-PAS is on the order of  $10^{-4}$ . Thus, we conclude that the concentration of mono-vacancies is in the range of  $10^{-5}$ - $10^{-4}$ . Furthermore, larger vacancy clusters are also present at lower concentrations. In addition, the formation of positronium (Ps) in the  $\text{YH}_x\text{O}_y$  and  $\text{Y}_2\text{O}_3$  thin films is observed, revealing the presence of nanopores. The systematic changes of electronic structure of RE metal, metal dihydride, semiconducting metal oxyhydride, and insulating metal oxide films upon varying the O and H contents of the films were seen in the S-W diagrams extracted from positron Doppler broadening experiments. The nanostructural evolution in photochromic Al-capped and uncapped Y/Gd oxyhydride films upon illumination is studied by *in-situ* DB-PAS. For the  $\text{YO}_x\text{H}_y/\text{Al}$  film, a pronounced increase in S-parameter and decrease in W-parameter results from the 2.5 h illumination and remain stable during ~38 h bleaching. This indicates that UV illumination induces the formation of anion vacancies by releasing anions from their lattice positions. Part of the anion vacancies cluster subsequently with  $V_Y$  mono-vacancies in an irreversible manner, resulting in the formation of stable di-vacancies. For the  $\text{YO}_x\text{H}_y$ ,  $\text{GdO}_x\text{H}_y/\text{Al}$  and  $\text{GdO}_x\text{H}_y$  films, partially reversible shifts of their S-W points in the direction of the S-W point of the rare-earth metal hydride were observed during photo-darkening, indicating the formation of metallic domains. Two proposed mechanisms for the formation of metallic domains in these rare-earth oxyhydride films during illumination are discussed. The first proposed mechanism suggests the formation of phase-segregated H-rich domains, enabled by hydrogen liberated from their lattice positions during illumination, and possibly local oxygen displacement. The strong shifts in the S and W parameters can be explained by preferred trapping of positrons in the phase-segregated nano-sized H-rich metallic-like domains, as supported by our simulations using a diffusion-limited trapping model. This supports proposed mechanisms for the photochromic effect in these rare-earth oxyhydrides based on the formation of metallic-like nano-sized domains. The second proposed mechanism is based on the formation of positively charged hydrogen vacancies at octahedral sites enabled by hydrogen liberated during illumination, with charge-compensating Y(4d)  $e_g$ -state electrons localized at the surrounding Y ions. When the concentration of these  $e_g$ -state electrons in certain domains in the  $\text{REH}_x\text{O}_y$  film is sufficiently high, their orbitals overlap and a (free-)electron band is formed, causing metallicity of these domains, resulting in photo-darkening of the film. This mechanism can qualitatively explain the timescale of photo-darkening, the reduction in optical transmission over a large sub-band gap wavelength interval, and the systematic reduction in photochromic contrast for compositions with increased O:H ratios.

## References

- [1] Y. J. Ke, J. W. Chen, C. J. Lin, S. C. Wang, Y. Zhou, J. Yin, P. S. Lee, and Y. Long, Smart windows: Electro-, thermo-, mechano-, photochromics, and beyond, *Adv. Energy Mater.* **9**, 1902066 (2019).
- [2] A. D. Towns, in *Applied Photochemistry: When Light Meets Molecules*, edited by G. Bergamini, and S. Silvi (Springer International Publishing, Cham, 2016), pp. 227.
- [3] K. Yoshimura, C. Langhammer, and B. Dam, Metal hydrides for smart window and sensor applications, *MRS Bull.* **38**, 495 (2013).
- [4] S. F. Wang, W. R. Fan, Z. C. Liu, A. B. Yu, and X. C. Jiang, Advances on tungsten oxide based photochromic materials: Strategies to improve their photochromic properties, *J. Mater. Chem. C* **6**, 191 (2018).
- [5] G. P. Smith, Photochromic Glasses: Properties and Applications, *J. Mater. Sci.* **2**, 139 (1967).
- [6] T. Mongstad, C. Platzer-Bjorkman, J. P. Maehlen, L. P. A. Mooij, Y. Pivak, B. Dam, E. S. Marstein, B. C. Hauback, and S. Z. Karazhanov, A new thin film photochromic material: Oxygen-containing yttrium hydride, *Sol. Energy Mat. Sol. Cells* **95**, 3596 (2011).
- [7] F. Nafezarefi, H. Schreuders, B. Dam, and S. Cornelius, Photochromism of rare-earth metal-oxy-hydrides, *Appl. Phys. Lett.* **111**, 103903 (2017).
- [8] G. Colombi, T. De Krom, D. Chaykina, S. Cornelius, S. W. H. Eijt, and B. Dam, Influence of cation (RE = Sc, Y, Gd) and O/H anion ratio on the photochromic properties of  $\text{REO}_x\text{H}_{3-2x}$  thin films, *ACS Photonics* **8**, 709 (2021).
- [9] S. Cornelius, G. Colombi, F. Nafezarefi, H. Schreuders, R. Heller, F. Munnik, and B. Dam, Oxyhydride nature of rare-earth-based photochromic thin films, *J. Phys. Chem. Lett.* **10**, 1342 (2019).
- [10] C. C. You, T. Mongstad, E. S. Marstein, and S. Z. Karazhanov, The dependence of structural, electrical and optical properties on the composition of photochromic yttrium oxyhydride thin films, *Materialia* **6**, 100307 (2019).
- [11] C. C. You, T. Mongstad, J. P. Maehlen, and S. Karazhanov, Engineering of the band gap and optical properties of thin films of yttrium hydride, *Appl. Phys. Lett.* **105**, 031910 (2014).
- [12] D. Moldarev, M. V. Moro, C. C. You, E. M. Baba, S. Z. Karazhanov, M. Wolff, and D. Primetzhofner, Yttrium oxyhydrides for photochromic applications: Correlating composition and optical response, *Phys. Rev. Mat.* **2**, 115203 (2018).
- [13] H. J. Hoffmann, *Photochromic glasses*, The properties of Optical Glass (Springer, Berlin, Heidelberg, Berlin, 1998).
- [14] J. Montero, F. A. Martinsen, M. Garcia-Tecedor, S. Z. Karazhanov, D. Maestre, B. Hauback, and E. S. Marstein, Photochromic mechanism in oxygen-containing yttrium hydride thin films: An optical perspective, *Phys. Rev. B* **95**, 201301(R) (2017).

- [15] C. V. Chandran, H. Schreuders, B. Dam, J. W. G. Janssen, J. Bart, A. P. M. Kentgens, and P. J. M. van Bentum, Solid-State NMR Studies of the Photochromic Effects of Thin Films of Oxygen-Containing Yttrium Hydride, *J. Phys. Chem. C* **118**, 22935 (2014).
- [16] M. P. Plokker, S. W. H. Eijt, F. Naziris, H. Schut, F. Nafezarefi, H. Schreuders, S. Cornelius, and B. Dam, Electronic structure and vacancy formation in photochromic yttrium oxy-hydride thin films studied by positron annihilation, *Sol. Energy Mat. Sol. Cells* **177**, 97 (2018).
- [17] J. N. Huiberts, R. Griessen, J. H. Rector, R. J. Wijngaarden, J. P. Dekker, D. G. de Groot, and N. J. Koeman, Yttrium and lanthanum hydride films with switchable optical properties, *Nature* **380**, 231 (1996).
- [18] See Supplemental Material for the list of additional samples, X-ray diffraction, positron annihilation fractions for each layer as a function of implantation energy, positron annihilation lifetime spectra, positron lifetime parameters, optical transmittance spectra and Tauc plot analysis of the optical band gap, the S and W values from Doppler broadening positron annihilation experiments.
- [19] H. M. Rietveld, A profile refinement method for nuclear and magnetic structures, *J. Appl. Crystallogr.* **2**, 65 (1969).
- [20] J. Rodriguez-Carvajal, FULLPROF: a program for Rietveld refinement and pattern matching analysis, satellite meeting on powder diffraction of the XV congress of the IUCr (Toulouse, France, 1990).
- [21] M. Zhang, M. A. Farid, H. Zhang, J. L. Sun, G. B. Li, F. H. Liao, and J. H. Lin, Superconductivity of perovskite  $\text{Ba}_{1-x}\text{Y}_x(\text{Bi}_{0.2}\text{Pb}_{0.8})\text{O}_{3-\delta}$ , *J. Supercond. Nov. Magn.* **30**, 1705 (2017).
- [22] P. Sperr, W. Egger, G. Kögel, G. Dollinger, C. Hugenschmidt, R. Repper, and C. Piochacz, Status of the pulsed low energy positron beam system (PLEPS) at the Munich Research Reactor FRM-II, *Appl. Surf. Sci.* **255**, 35 (2008).
- [23] C. Hugenschmidt, B. Löwe, J. Mayer, C. Piochacz, P. Pikart, R. Repper, M. Stadlbauer, and K. Schreckenbach, Unprecedented intensity of a low-energy positron beam, *Nucl. Instrum. Meth. A* **593**, 614 (2008).
- [24] C. Hugenschmidt, C. Piochacz, M. Reiner, and K. Schreckenbach, The NEPOMUC upgrade and advanced positron beam experiments, *New J. Phys.* **14**, 055027 (2012).
- [25] D. Bochert, Optimierte Analyse von Lebenszeitspektren aus Positronenstrahlsystemen, Diplom Arbeit, Universität der Bundeswehr München, München, Germany, 2004.
- [26] W. Egger, P. Sperr, G. Kögel, M. Wetzel, and H. J. Gudladt, Investigations of epoxy-based adhesives with PLEPS, *Appl. Surf. Sci.* **255**, 209 (2008).
- [27] H. Schut, A Variable Energy Positron Beam Facility with Applications in Materials Science, PhD thesis, Delft University of Technology, Delft, the Netherlands, 1990.
- [28] A. van Veen, H. Schut, J. Devries, R. A. Hakvoort, and M. R. Ijpma, Analysis of positron profiling data by means of Vepfit, *AIP Conf. Proc.* **218**, 171 (1990).



- [29] Reinhard Krause-Rehberg, Hartmut S. Leipner, *Positron Annihilation in Semiconductors - Defect Studies* (Springer-Verlag, Berlin, 1999).
- [30] M. J. Puska, C. Corbel, and R. M. Nieminen, Positron trapping in semiconductors, *Phys. Rev. B* **41**, 9980 (1990).
- [31] J. M. C. Robles, E. Ogando, and F. Plazaola, Positron lifetime calculation for the elements of the periodic table, *J. Phys.-Condens. Mat.* **19**, 176222 (2007).
- [32] H. Leegwater, H. Schut, W. Egger, A. Baldi, B. Dam, and S. W. H. Eijt, Divacancies and the hydrogenation of Mg-Ti films with short range chemical order, *Appl. Phys. Lett.* **96**, 121902 (2010).
- [33] A. Anastasopol, S. W. H. Eijt, H. Schut, F. M. Mulder, F. Plazaola, and B. Dam, Thermal stability of  $\text{Mg}_y\text{Ti}_{1-y}$  thin films investigated by positron annihilation spectroscopy, *Phys. Procedia* **35**, 16 (2012).
- [34] S. Assali, M. Elsayed, J. Nicolas, M. O. Liedke, A. Wagner, M. Butterling, R. Krause-Rehberg, and O. Moutanabbir, Vacancy complexes in nonequilibrium germanium-tin semiconductors, *Appl. Phys. Lett.* **114**, 251907 (2019).
- [35] M. Elsayed, N. Y. Arutyunov, R. Krause-Rehberg, G. A. Oganessian, and V. V. Kozlovski, Formation and annealing of vacancy-P complexes in proton-irradiated germanium, *Acta Mater.* **100**, 1 (2015).
- [36] M. Eldrup, D. Lightbody, and J. N. Sherwood, The temperature-dependence of positron lifetimes in solid pivalic acid, *Chem. Phys.* **63**, 51 (1981).
- [37] S. J. Tao, Positronium annihilation in molecular substances, *J. Chem. Phys.* **56**, 5499 (1972).
- [38] L. C. Damonte, M. A. Taylor, J. Desimoni, and J. Runco, PALS study on the defect structure of yttria-stabilized zirconia, *Radiat. Phys. Chem.* **76**, 248 (2007).
- [39] J. Brown, P. Mascher, and A. H. Kitai, Positron lifetime spectroscopy and cathodoluminescence of polycrystalline terbium-doped yttria, *J. Electrochem. Soc.* **142**, 958 (1995).
- [40] J. Kuriplach and B. Barbiellini, Parameter-free gradient correction for positron states in oxides, *Defect Diffus. Forum* **373**, 35 (2017).
- [41] B. Rozenfeld and Debowska, E., Investigation of the electronic structure of yttrium hydrides by positron annihilation, *Acta Phys. Pol. A* **47**, 37 (1975).
- [42] I. Y. Dekhtyar and V. I. Shevchenko, Positron-annihilation in hydrides of transition-metals, *Phys. Status Solidi B* **83**, 323 (1977).
- [43] W. J. Legerstee, J. de Roode, A. Anastasopol, C. V. Falub, and S. W. H. Eijt, In-situ hydrogen sorption 2D-ACAR facility for the study of metal hydrides for hydrogen storage, *Physcs. Proc.* **35**, 22 (2012).

[44] A. Karjalainen, V. Prozheeva, K. Simula, I. Makkonen, V. Callewaert, J. B. Varley, and F. Tuomisto, Split Ga vacancies and the unusually strong anisotropy of positron annihilation spectra in  $\beta$ -Ga<sub>2</sub>O<sub>3</sub>, *Phys. Rev. B* **102**, 195207 (2020).

[45] J. Heikinheimo, S. Ortner, I. Makkonen, J. Kujala, M. Blackmur, and F. Tuomisto, Positron annihilation analysis of the atomic scale changes in oxidized zircaloy-4 samples, *J. Nucl. Mater.* **495**, 172 (2017).

[46] C. V. Falub, P. E. Mijnders, S. W. H. Eijt, M. A. van Huis, A. van Veen and H. Schut, Electronic structure and orientation relationship of Li nanoclusters embedded in MgO studied by depth selective positron annihilation two-dimensional angular correlation, *Phys. Rev. B* **66**, 075426 (2002).

[47] J. Tauc, R. Grigorovici, and A. Vancu, Optical properties and electronic structure of amorphous germanium, *Phys. Status Solidi B* **15**, 627 (1966).

[48] We note that vacancy concentrations in the uncapped YH<sub>x</sub>O<sub>y</sub> film extracted from the diffusion length  $L_+$  from DB-PAS depth profiling gives the mono-vacancy concentration in the range of  $\sim 6 \times 10^{-5}$  -  $1.5 \times 10^{-4}$ , which is an order of magnitude larger than the values extracted by PALS. This could stem from either the closeness to saturation trapping in PALS or from the fact that the fitted positron diffusion length can be affected by, e.g., compositional or defect gradients. In view of the lower accuracy offered by using the diffusion length as a parameter to extract concentrations, we conclude that the concentration of mono-vacancies is in the range of  $10^{-5}$  -  $10^{-4}$  [49]. The detailed calculation of vacancy concentrations extracted using positron diffusion lengths  $L_+$  determined in the VEPFIT analysis can be found in Supplemental Materials.

[49] J. Cizek, F. Lukac, I. Prochazka, R. Kuzel, Y. Jiraskova, D. Janickovic, W. Anwand, and G. Brauer, Characterization of quenched-in vacancies in Fe-Al alloys, *Physica B* **407**, 2659 (2012).

[50] D. Chaykina, T. de Krom, G. Colombi, H. Schreuders, A. Suter, T. Prokscha, B. Dam, and S. Eijt, Structural properties and anion dynamics of yttrium dihydride and photochromic oxyhydride thin films examined by in situ  $\mu^+$ SR, *Phys. Rev. B* **103**, 224106 (2021).

[51] G. Colombi, S. Cornelius, A. Longo, and B. Dam, Structure model for anion-disordered photochromic gadolinium oxyhydride thin films, *J. Phys. Chem. C* **124**, 13541 (2020).

[52] R. Stigter, A computational investigation on the structure of yttrium oxyhydride compounds and their anion mobility, MSc thesis, Delft University of Technology, Delft, the Netherlands, 2020.

[53] D. Moldarev, L. Stolz, M. V. Moro, S. M. Adalsteinsson, I. A. Chioar, S. Z. Karazhanov, D. Primetzhofer, and M. Wolff, Environmental dependence of the photochromic effect of oxygen-containing rare-earth metal hydrides, *J. Appl. Phys.* **129**, 153101 (2021).

[54] F. Nafezarefi, S. Cornelius, J. Nijskens, H. Schreuders, B. Dam, Effects of the addition of zirconium on the photochromic properties of yttrium oxy-hydride, *Sol. Energy Mater. Sol. Cells* **200**, 109923 (2019).

- [55] G. Colombi, R. Stigter, D. Chaykina, S. Banerjee, A. P. M. Kentgens, S.W. H. Eijt, B. Dam, and G. A. de Wijs, Energy, metastability, and optical properties of anion-disordered  $\text{REO}_x\text{H}_{3-2x}$  (RE=Y,La) oxyhydrides: a computational study, *Phys. Rev. B* **105**, 054208 (2022).
- [56] M. A. van Huis, A. van Veen, H. Schut, C. V. Falub, S. W. H. Eijt, P. E. Mijnders, and J. Kuriplach, Positron confinement in embedded lithium nanoclusters, *Phys. Rev. B* **65**, 085416 (2002).
- [57] A. Dupasquier and A. Mills Jr, *Positron spectroscopy of solids* (IOS press, 1995), Vol. 125.
- [58] K. K. Ng, F. C. Zhang, V. I. Anisimov, and T. M. Rice, Electronic structure of lanthanum hydrides with switchable optical properties, *Phys. Rev. Lett.* **78**, 1311 (1997).
- [59] J. J. Shi, Y. M. Li, Y. S. Li, D. M. Li, Y. H. Luo, H. J. Wu, and Q. B. Meng, From ultrafast to ultraslow: charge-carrier dynamics of perovskite solar cells, *Joule* **2**, 879 (2018).
- [60] N. W. Ashcroft and N. D. Mermin, *Solid State Physics* (Holt, Rinehart and Winston, New York, 1976).
- [61] A. Zangwill, *Modern Electrodynamics* (Cambridge University Press, Cambridge, UK, 2013).
- [62] H.C. van de Hulst, *Light Scattering by Small Particles* (Dover Publ., London, 1981).
- [63] S. A. Maier, *Plasmonics: Fundamentals and Applications* (Springer, New York, 2007).



## Supplementary information for Chapter 2

### List of other samples

Table S2.1: List of additional samples used in this study.

Samples	Deposition pressure	measurements
GdH <sub>x</sub> O <sub>y</sub> //Ti	0.8 Pa	DB-PAS, XRD
GdH <sub>x</sub> O <sub>y</sub> //Pd	0.8 Pa	DB-PAS, XRD
GdH <sub>x</sub> O <sub>y</sub> //Ti	0.9 Pa	DB-PAS, XRD
GdH <sub>x</sub> O <sub>y</sub> //Pd	0.9 Pa	DB-PAS, XRD

### X-ray diffraction

In this section, the XRD patterns of all Y-based and Gd-based films are shown in Fig. S2.1. The information of crystal structures of all films were obtained from the Rietveld refinements of the XRD patterns by the Fullprof program. The refinements of XRD patterns are acceptable since the calculated patterns fit with the measured patterns with agreement factors that are acceptable, i.e.  $R_p$ ,  $R_{wp}$  and  $chi2$  are below 10. Representative refined XRD patterns of Al capped YH<sub>x</sub>O<sub>y</sub> (YH<sub>x</sub>O<sub>y</sub>//Al) film deposited at 0.5 Pa and Al capped GdH<sub>x</sub>O<sub>y</sub> (GdH<sub>x</sub>O<sub>y</sub>//Al) film deposited at 0.9 Pa are shown in Fig. S2.2 (a) and (b), respectively. The refined lattice parameters and accordingly derived lattice volumes of the Y-based and Gd-based thin films are listed in Table S2.2.

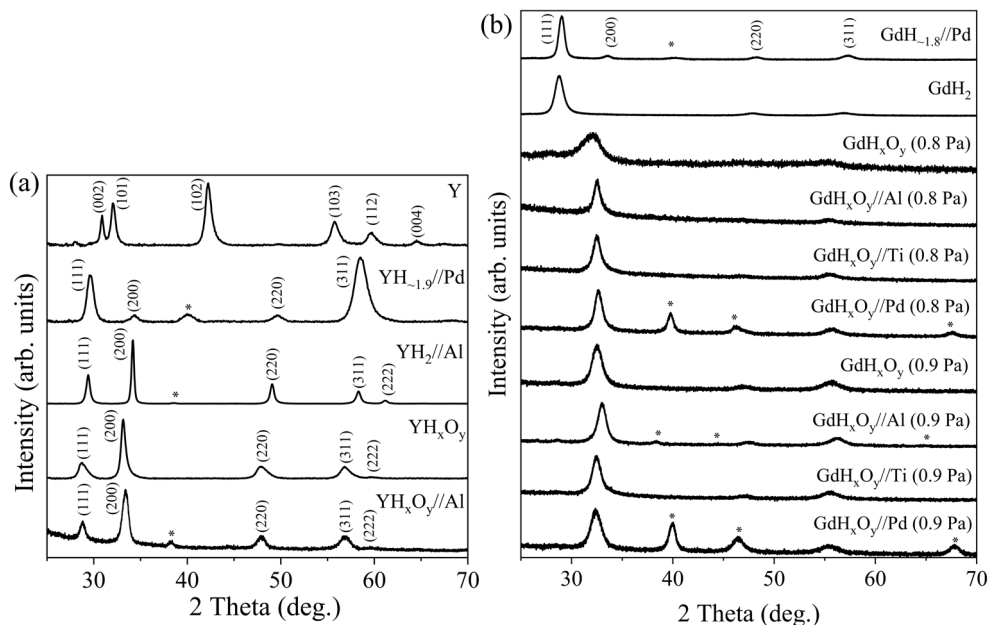


Figure S2.1: XRD patterns of (a) Y-based thin films and (b) Gd-based thin films.

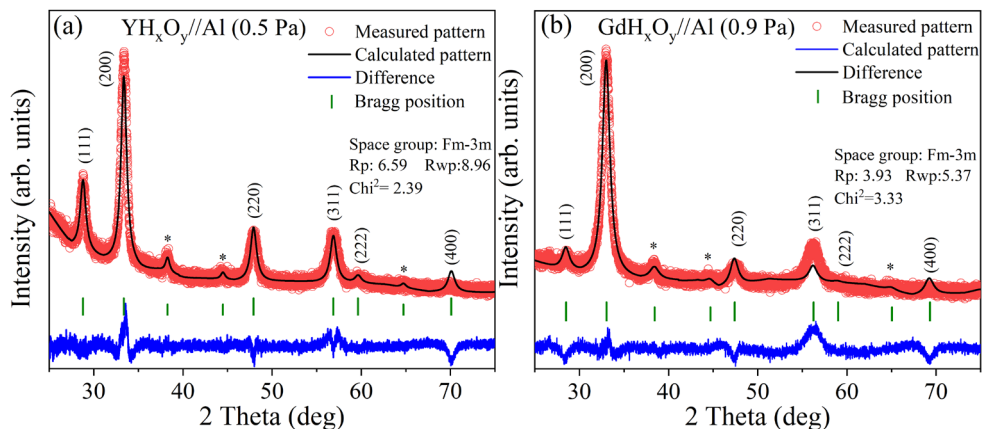


Figure S2.2: Representative Rietveld refinements of the XRD patterns of  $\text{YH}_x\text{O}_y$  and  $\text{GdH}_x\text{O}_y$  films with the  $Fm\bar{3}m$  crystal symmetry. The marked stars stand for the diffraction signals from the Al capping layer.

Table S2.2: Crystal structure, lattice parameter and volume per Y or Gd atom from Rietveld refinement of the XRD patterns of all thin films.

Sample	Crystal structure	Lattice parameter ( $\text{\AA}$ )	Volume per Y or Gd ( $\text{\AA}^3$ )
Y	$P6_3/mmc$ (hcp)	$3.675 \pm 0.003$ $5.785 \pm 0.006$	33.8
$\text{YH}_{-1.9}/\text{Pd}$	$Fm\bar{3}m$ (fcc)	$5.222 \pm 0.002$	35.6
$\text{YH}_x\text{O}_y$ -1	$Fm\bar{3}m$ (fcc)	$5.395 \pm 0.010$	39.3
$\text{YH}_x\text{O}_y$ -2	$Fm\bar{3}m$ (fcc)	$5.397 \pm 0.009$	39.3
$\text{YH}_x\text{O}_y//\text{Al}$	$Fm\bar{3}m$ (fcc)	$5.393 \pm 0.001$	39.2
$\text{GdH}_{-1.8}/\text{Pd}$	$Fm\bar{3}m$ (fcc)	$5.3268 \pm 0.0001$	37.8
$\text{GdH}_2$	$Fm\bar{3}m$ (fcc)	$5.3667 \pm 0.0002$	38.6
$\text{GdH}_x\text{O}_y$ (0.8Pa)	$Fm\bar{3}m$ (fcc)	$5.6989 \pm 0.0007$	46.3
$\text{GdH}_x\text{O}_y//\text{Al}$ (0.8Pa)	$Fm\bar{3}m$ (fcc)	$5.5034 \pm 0.0003$	41.7
$\text{GdH}_x\text{O}_y//\text{Ti}$ (0.8Pa)	$Fm\bar{3}m$ (fcc)	$5.5034 \pm 0.0003$	41.7
$\text{GdH}_x\text{O}_y//\text{Pd}$ (0.8Pa)	$Fm\bar{3}m$ (fcc)	$5.4788 \pm 0.0002$	41.1
$\text{GdH}_x\text{O}_y$ (0.9Pa)	$Fm\bar{3}m$ (fcc)	$5.5018 \pm 0.0003$	41.6
$\text{GdH}_x\text{O}_y//\text{Al}$ (0.9Pa)	$Fm\bar{3}m$ (fcc)	$5.4242 \pm 0.0002$	39.9
$\text{GdH}_x\text{O}_y//\text{Ti}$ (0.9Pa)	$Fm\bar{3}m$ (fcc)	$5.5081 \pm 0.0003$	41.8
$\text{GdH}_x\text{O}_y//\text{Pd}$ (0.9Pa)	$Fm\bar{3}m$ (fcc)	$5.5210 \pm 0.0003$	42.1

### Positron fractions as a function of implantation energy for $\text{YH}_{-1.9}/\text{Pd}$ and $\text{YH}_x\text{O}_y-1$ films

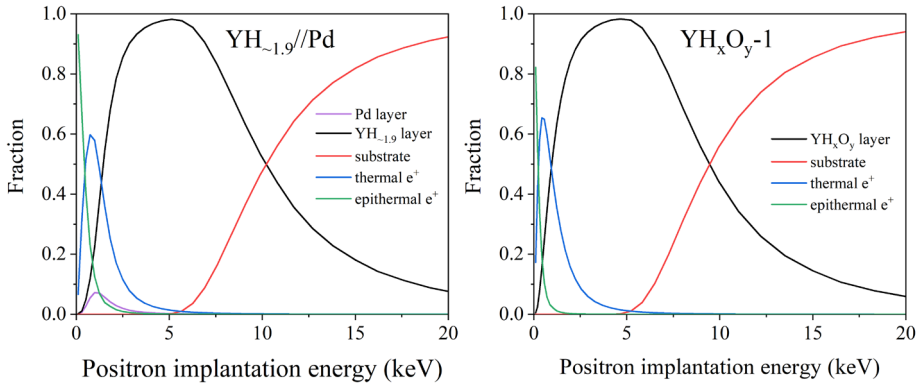


Figure S2.3: The fraction of positrons annihilating in each layer in the  $\text{YH}_{-1.9}/\text{Pd}$  and  $\text{YH}_x\text{O}_y-1$  films as a function of positron implantation energy, as derived by VEPFIT analysis.

### Positron annihilation lifetime spectra and best-fit parameters obtained by POSWIN analysis

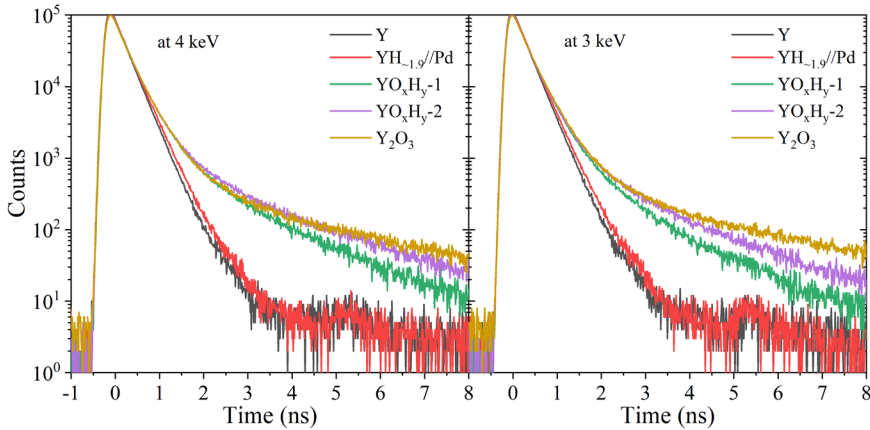


Figure S2.4: The positron lifetime spectra of all Y-based thin films collected at an implantation energy of 4 keV (left) and 3 keV (right).

Table S2.3: Positron lifetimes ( $\tau_i$ ), intensities ( $I_i$ ), average lifetimes ( $\tau_{av}$ ) for Y-based thin films at 3 keV fitted by POSWIN.

samples	$\tau_1$ (ps)	$\tau_2$ (ps)	$\tau_3$ (ps)	$\tau_4$ (ns)	$I_1$ (%)	$I_2$ (%)	$I_3$ (%)	$I_4$ (%)	$\tau_{av}$ (ps)
Y	75 $\pm$ 3	283 $\pm$ 1	823 $\pm$ 29	-	7 $\pm$ 0.2	92 $\pm$ 0.2	0.8 $\pm$ 0.1	-	272 $\pm$ 1
$\text{YH}_{-1.9}/\text{Pd}$	72 $\pm$ 4	292 $\pm$ 1	584 $\pm$ 16	-	5.4 $\pm$ 0.3	91 $\pm$ 0.3	3.6 $\pm$ 0.4	-	291 $\pm$ 4
$\text{YO}_x\text{H}_y-1$	38 $\pm$ 4	263 $\pm$ 4	500 $\pm$ 18	1.51 $\pm$ 0.03	4 $\pm$ 0.2	71 $\pm$ 2	22 $\pm$ 2	3.2 $\pm$ 0.2	346 $\pm$ 15
$\text{YO}_x\text{H}_y-2$	44 $\pm$ 4	263 $\pm$ 4	506 $\pm$ 16	1.91 $\pm$ 0.02	4.5 $\pm$ 0.2	69 $\pm$ 2	22 $\pm$ 2	4.1 $\pm$ 0.1	375 $\pm$ 14
$\text{Y}_2\text{O}_3$	74 $\pm$ 5	290 $\pm$ 4	592 $\pm$ 23	3.22 $\pm$ 0.08	6.4 $\pm$ 0.4	74 $\pm$ 1	16 $\pm$ 2	3.5 $\pm$ 0.1	427 $\pm$ 13

**Expressions used to derive the standard deviations for  $\tau_b$ ,  $k_i$  ( $i=1,2$ ) and  $C_i$  ( $i=1,2$ ) in the two-defect positron trapping model**

$$\sigma_{\tau_b} = \sqrt{(\tau_b)^4 \sum_{j=1}^k \left( \frac{\sigma_{I_j}^2}{\tau_j^2} + \frac{I_j^2 \sigma_{\tau_j}^2}{\tau_j^4} \right)} \quad (\text{S2.1})$$

$$\sigma_{k_1} = \frac{1}{\tau_1^4} (I_2^2 \sigma_{I_2}^2 + I_2^2 \sigma_{\tau_1}^2) + \frac{1}{\tau_2^4} (I_2^2 \sigma_{I_2}^2 + I_2^2 \sigma_{\tau_2}^2) \quad (\text{S2.2})$$

$$\sigma_{k_2} = \frac{1}{\tau_1^4} (I_3^2 \sigma_{I_3}^2 + I_3^2 \sigma_{\tau_1}^2) + \frac{1}{\tau_3^4} (I_3^2 \sigma_{I_3}^2 + I_3^2 \sigma_{\tau_3}^2) \quad (\text{S2.3})$$

$$\sigma_{C_i} = \frac{\sigma_{k_i}}{|\mu|} \quad (\text{S2.4})$$

2

### The transmittance and optical bandgap of $\text{YH}_x\text{O}_y$ and $\text{GdH}_x\text{O}_y$ films

The relationship between the transmission  $T(\lambda)$  and absorption coefficient  $\alpha(\lambda)$  is given by  $T(\lambda) = (1-R)\exp[-\alpha(\lambda)d]$ , where  $R$  and  $d$  are optical reflectivity and the thickness of the film, respectively. As an approximation, the reflectance was neglected and the absorption coefficient was calculated from the transmittance spectra using the expression  $\alpha(\lambda) = -\ln[-T(\lambda)]/d$ . The indirect optical band gap  $E_g$  of all rare-earth oxyhydride films was determined by extrapolating the linear part of the plots of  $(\alpha h\nu)^{1/2}$  versus  $h\nu$ .

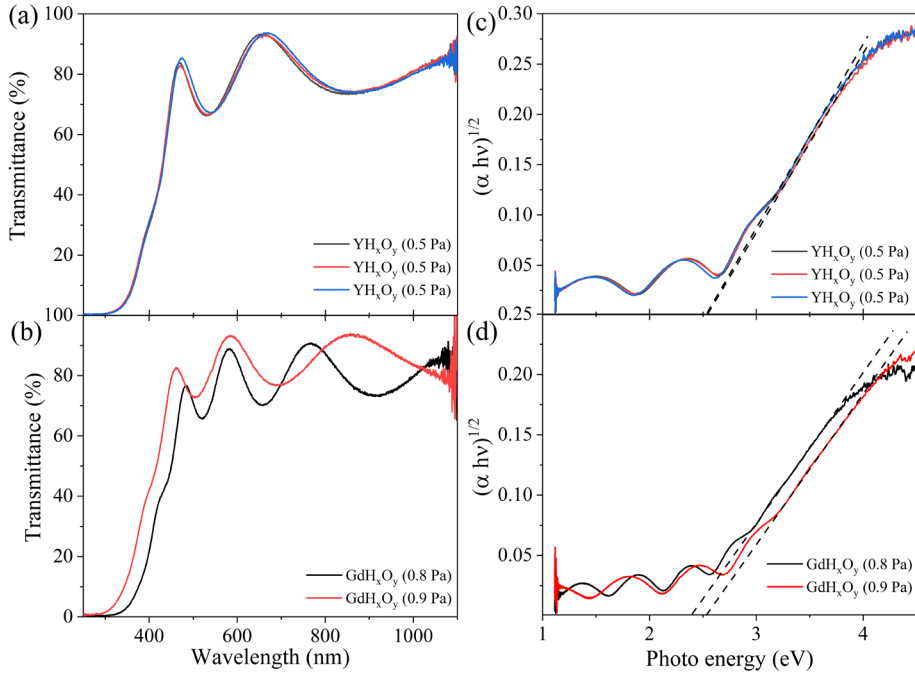


Figure S2.5: The transmittance and optical bandgap of three  $\text{YH}_x\text{O}_y$  and two  $\text{GdH}_x\text{O}_y$  films.



## The S and W values extracted from the Doppler broadening positron annihilation experiments

Table S2.4: S and W values for  $\text{YH}_x\text{O}_y//\text{Al}$ , uncapped  $\text{YH}_x\text{O}_y$ ,  $\text{GdH}_x\text{O}_y//\text{Al}$  and uncapped  $\text{GdH}_x\text{O}_y$  films before illumination, upon illumination for 1.5-2.5 hours and after illumination in the bleaching state according to the *in-situ* illumination DB-PAS measurements. The S- and W-parameters were collected at a positron implantation energy of 6.4, 5, 6.4 and 7.2 keV, respectively.

Samples	States	S-parameter	W-parameter
$\text{YH}_x\text{O}_y//\text{Al}$	Before illumination	$0.5580 \pm 0.0007$	$0.0404 \pm 0.0004$
	During illumination	$0.5778 \pm 0.0012$	$0.0354 \pm 0.0013$
	Bleaching	$0.5836 \pm 0.0002$	$0.0368 \pm 0.0002$
$\text{YH}_x\text{O}_y$	Before illumination	$0.5600 \pm 0.0005$	$0.0381 \pm 0.0003$
	During illumination	$0.5689 \pm 0.0020$	$0.0337 \pm 0.0003$
	Bleaching	$0.5655 \pm 0.0002$	$0.0373 \pm 0.0001$
$\text{GdH}_x\text{O}_y//\text{Al}$	Before illumination	$0.5882 \pm 0.0011$	$0.0385 \pm 0.0004$
	During illumination	$0.6004 \pm 0.0004$	$0.0337 \pm 0.0008$
	Bleaching	$0.5935 \pm 0.0004$	$0.0368 \pm 0.0002$
$\text{GdH}_x\text{O}_y$	Before illumination	$0.5576 \pm 0.0007$	$0.0447 \pm 0.0003$
	During illumination	$0.5690 \pm 0.0025$	$0.0395 \pm 0.0011$
	Bleaching	$0.5661 \pm 0.0003$	$0.0426 \pm 0.0002$

Table S2.5: S and W values for  $\text{YH}_x\text{O}_y//\text{Al}$ , uncapped  $\text{YH}_x\text{O}_y$ ,  $\text{GdH}_x\text{O}_y//\text{Al}$  and uncapped  $\text{GdH}_x\text{O}_y$  films before illumination and after 2.5 h illumination (photo-darkening) and ~38 h of bleaching extracted from the depth profile measurements by VEPFIT analysis.

Samples	States	S-parameter	W-parameter	Diffusion length (nm)
$\text{YH}_x\text{O}_y//\text{Al}$	Before illumination	$0.5630 \pm 0.0020$	$0.0372 \pm 0.0007$	$40 \pm 11$
	After bleaching	$0.5918 \pm 0.0015$	$0.0347 \pm 0.0006$	$22 \pm 6$
$\text{YH}_x\text{O}_y$	Before illumination	$0.5587 \pm 0.0005$	$0.0373 \pm 0.0003$	$24 \pm 1$
	After bleaching	$0.5744 \pm 0.0006$	$0.0359 \pm 0.0004$	$37 \pm 1$
$\text{GdH}_x\text{O}_y//\text{Al}$	Before illumination	$0.5861 \pm 0.0003$	$0.0395 \pm 0.0003$	$20 \pm 3$
	After bleaching	$0.5916 \pm 0.0006$	$0.0379 \pm 0.0002$	$10 \pm 3$
$\text{GdH}_x\text{O}_y$	Before illumination	$0.5586 \pm 0.0007$	$0.0445 \pm 0.0003$	$40 \pm 10$
	After bleaching	$0.5708 \pm 0.0007$	$0.0427 \pm 0.0003$	$40 \pm 10$

Table S2.6: The best-fit parameters for  $\text{YH}_x\text{O}_y//\text{Al}$  film before illumination and after 2.5 h illumination and ~38 h of bleaching extracted from the DB-PAS depth profiles by VEPFIT analysis.

Before illumination:

Layer	Density ( $\text{g}/\text{cm}^3$ )	Layer width (nm)	Diffusion length (nm)	S-parameter	W-parameter
Al	2.7	20	10	0.5783	0.0310
$\text{YH}_x\text{O}_y$	4.3	80	$15 \pm 1$	$0.5439 \pm 0.0016$	$0.0432 \pm 0.0006$
$\text{YH}_x\text{O}_y$	4.3	340	$40 \pm 11$	$0.5630 \pm 0.0020$	$0.0372 \pm 0.0007$
f-SiO <sub>2</sub>	2.2	-	25	$0.5550 \pm 0.0012$	$0.0499 \pm 0.0005$

After 2.5 h illumination (photo-darkening) and ~38 h of bleaching bleaching:

Layer	Density (g/cm <sup>3</sup> )	Layer width (nm)	Diffusion length (nm)	S-parameter	W-parameter
Al	2.7	20	10	0.5783	0.0310
YH <sub>x</sub> O <sub>y</sub>	4.3	80	14±2	0.5632±0.0016	0.0414±0.0006
YH <sub>x</sub> O <sub>y</sub>	4.3	340	22±6	0.5918±0.0015	0.0347±0.0006
f-SiO <sub>2</sub>	2.2	-	25	0.5554±0.0020	0.0496±0.0005

Table S2.7: The best-fit parameters for YH<sub>x</sub>O<sub>y</sub> film before illumination and after 2.5 h illumination and ~38 h of bleaching extracted from the DB-PAS depth profiles by VEPFIT analysis.

Before illumination :

Layer	Density (g/cm <sup>3</sup> )	Layer width (nm)	Diffusion length (nm)	S-parameter	W-parameter
YH <sub>x</sub> O <sub>y</sub>	4.3	250	24±1	0.5587±0.0005	0.0373±0.0003
f-SiO <sub>2</sub>	2.2	-	25	0.5554±0.0006	0.0492±0.0003

After 2.5 h illumination (photo-darkening) and ~38 h of bleaching:

Layer	Density (g/cm <sup>3</sup> )	Layer width (nm)	Diffusion length (nm)	S-parameter	W-parameter
YH <sub>x</sub> O <sub>y</sub>	4.3	250±10	37±1	0.5744±0.0006	0.0359±0.0004
f-SiO <sub>2</sub>	2.2	-	25	0.5550±0.0006	0.0491±0.0003

Table S2.8: The best-fit parameters for GdH<sub>x</sub>O<sub>y</sub>//Al film before illumination and after 2.5 h illumination and ~38 h of bleaching extracted from the DB-PAS depth profiles by VEPFIT analysis.

Before illumination:

Layer	Density (g/cm <sup>3</sup> )	Layer width (nm)	Diffusion length (nm)	S-parameter	W-parameter
Al	2.7	41	10	0.5783	0.0310
GdH <sub>x</sub> O <sub>y</sub>	7.2	380±10	20±3	0.5861±0.0003	0.0395±0.0003
f-SiO <sub>2</sub>	2.2	-	25	0.5397±0.0004	0.0550±0.0004

After 2.5 h illumination (photo-darkening) and ~38 h of bleaching bleaching:

Layer	Density (g/cm <sup>3</sup> )	Layer width (nm)	Diffusion length (nm)	S-parameter	W-parameter
Al	2.7	41	10	0.5783	0.0310
GdH <sub>x</sub> O <sub>y</sub>	7.2	380	10±3	0.5916±0.0006	0.0379±0.0002
f-SiO <sub>2</sub>	2.2	-	25	0.5408±0.0009	0.0547±0.0004

Table S2.9: The best-fit parameters for  $\text{GdH}_x\text{O}_y$  film before illumination and after 2.5 h illumination and  $\sim 38$  h of bleaching extracted from the DB-PAS depth profiles by VEPFIT analysis.

Before illumination:

Layer	Density ( $\text{g}/\text{cm}^3$ )	Layer width (nm)	Diffusion length (nm)	S-parameter	W-parameter
$\text{GdH}_x\text{O}_y$	7.2	$400 \pm 30$	$40 \pm 10$	$0.5586 \pm 0.0007$	$0.0445 \pm 0.0003$
f- $\text{SiO}_2$	2.2	-	25	$0.5425 \pm 0.0011$	$0.0555 \pm 0.0005$

After 2.5 h illumination (photo-darkening) and  $\sim 38$  h of bleaching:

Layer	Density ( $\text{g}/\text{cm}^3$ )	Layer width (nm)	Diffusion length (nm)	S-parameter	W-parameter
$\text{GdH}_x\text{O}_y$	7.2	400	$40 \pm 10$	$0.5708 \pm 0.0007$	$0.0427 \pm 0.0003$
f- $\text{SiO}_2$	2.2	-	25	$0.5424 \pm 0.0011$	$0.0551 \pm 0.0005$

The fused- $\text{SiO}_2$  substrates for depositing Al,  $\text{YH}_x\text{O}_y$  and  $\text{YH}_x\text{O}_y/\text{Al}$  films are from the same commercially obtained batch of substrates, and show S and W parameters that are similar to each other. In contrast, the fused- $\text{SiO}_2$  substrates in  $\text{GdH}_x\text{O}_y$  and  $\text{GdH}_x\text{O}_y/\text{Al}$  films from another batch show different S-/W- parameters.

In order to obtain the S-/W- parameters for Al capping layer, that were kept fixed during the VEPFIT fit analysis for the Al-capped oxyhydride samples, a magnetron sputtered Al film was produced by magnetron sputtering at an Ar pressure of 0.3 Pa, *i.e.* at the same pressure as applied for the Al-capped oxyhydride films. The S- and W-parameter depth profiles for this sample and the best-fit parameters from VEPFIT analysis are shown in Fig. S2.6 and in Table S2.10, respectively.

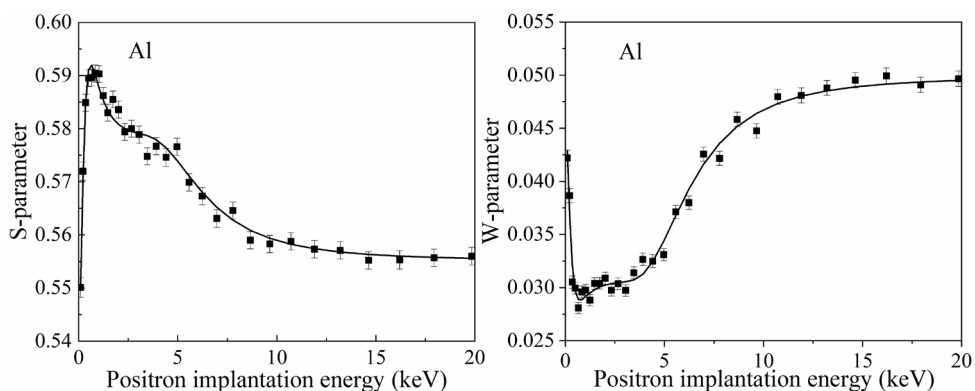


Figure S2.6: S- and W-parameter depth profiles of a magnetron sputtered Al film.

Table S2.10: The best-fit parameters for a magnetron sputtered Al film extracted from the DB-PAS depth profiles by VEPFIT analysis.

Layer	Density (g/cm <sup>3</sup> )	Layer width (nm)	Diffusion length (nm)	S-parameter	W-parameter
YH <sub>x</sub> O <sub>y</sub>	2.7	262±6	10	0.5783±0.0004	0.0310±0.0003
f-SiO <sub>2</sub>	2.2	-	25	0.5552±0.0004	0.0499±0.0003

### Calculation of vacancy concentrations using the positron diffusion length $L_+$ (DB-PAS)

The positron diffusion length  $L_+$  extracted from the DB-PAS measurements can be used to estimate the positron trapping rate  $k$ , according to the equation  $k = D_+ \left( \frac{1}{L_+^2} - \frac{1}{L_{\text{bulk}}^2} \right)$ . When assuming a reasonable value for the positron diffusion coefficient  $D_+$  of  $\sim 1 \text{ cm}^2/\text{s}$  [29], and taking into account the bulk positron lifetime of  $\tau_{\text{bulk}} \sim 240 \text{ ps}$  in the YH<sub>x</sub>O<sub>y</sub> films, the bulk positron diffusion length  $L_{\text{bulk}}$  for defect-free YH<sub>x</sub>O<sub>y</sub> can be estimated, according to  $L_{\text{bulk}} = \sqrt{D_+ \tau_{\text{bulk}}} \approx 150 \text{ nm}$ . Based on the experimental diffusion lengths of  $\sim 25 \text{ nm}$  and  $\sim 40 \text{ nm}$  in uncapped YH<sub>x</sub>O<sub>y</sub> film, one arrives at positron trapping rates  $k$  of  $1.5 \times 10^{11} \text{ s}^{-1}$  and  $6 \times 10^{10} \text{ s}^{-1}$ , respectively, and vacancy concentrations in the range of  $\sim 6 \times 10^{-5}$ - $1.5 \times 10^{-4}$ .

### **3. The memory effect in photochromic rare-earth oxyhydride thin films studied by in-situ positron annihilation spectroscopy upon photodarkening-bleaching cycling**

This chapter is based on Z. Wu, L. de Wit, M. Beek, G. Colombi, D. Chaykina, H. Schreuder, H. Schut, M. O. Liedke, M. Butterling, A. Wagner, M. Dickmann, E. Brück, B. Dam, and S. W.H. Eijt, The memory effect in photochromic rare-earth oxyhydride thin films studied by in-situ positron annihilation spectroscopy upon photodarkening-bleaching cycling, *Phys. Rev. Mater.* **8**, 045201 (2024).

## Abstract

Cycling stability of the photochromic effect in rare-earth oxyhydride thin films is of great importance for long-term applications such as smart windows. However, an increasingly slower bleaching rate upon photochromic cycling was found in yttrium oxyhydride thin films; the origin of this memory effect is yet unclear. In this work, the microstructural changes under six photodarkening-bleaching cycles in  $\text{YH}_x\text{O}_y$  and  $\text{GdH}_x\text{O}_y$  thin films are investigated by *in-situ* illumination Doppler broadening positron annihilation spectroscopy (DB-PAS), complemented by positron annihilation lifetime spectroscopy (PALS) investigations on  $\text{YH}_x\text{O}_y$  films before and after one cycle. For the first three cycles, the Doppler broadening S-parameter after bleaching increases systematically with photodarkening-bleaching cycle, and correlates with the bleaching time constant extracted from optical transmittance measurements. This suggests that the microstructural evolution that leads to progressively slower bleaching involves vacancy creation and agglomeration. PALS suggests that, during a photodarkening-bleaching cycle, divacancies are formed that are possibly composed of illumination-induced hydrogen vacancies and pre-existing yttrium monovacancies, and vacancy clusters grow, which might be due to local removal of hydrogen. If bleaching is a diffusion-related process, the formed vacancy defects induced by illumination might affect the diffusion time by reducing the diffusion coefficient. Hydrogen loss could also be a key factor in the reduced bleaching kinetics. Other microstructural origins including domain growth, or formation of  $\text{OH}^-$  hydroxide groups are also discussed with respect to the slower bleaching kinetics. During the fourth to sixth photodarkening-bleaching cycle, reversible shifts in the Doppler S and W parameters are seen that are consistent with the reversible formation of metallic-like domains, previously proposed as a key factor in the mechanism for the photochromic effect.

### 3.1 Introduction

Rare-earth oxyhydride thin films have gained increasing interest due to their color-neutral photochromic effect at room temperature. Their photochromic performance in terms of contrast and bleaching speed can be modified by different strategies, such as adjusting the type of cation, tuning the deposition pressure, thermal annealing, and doping, making them promising for applications in smart windows and photochromic sunglasses [1-5]. A stable photochromic performance during photodarkening-bleaching cycles and fast switching kinetics is required for long-term practical applications. However, a progressively slower bleaching kinetics upon photochromic cycling was observed in yttrium oxyhydride ( $\text{YH}_x\text{O}_y$ ) thin films [6]. This is the so-called memory effect, which is induced by the illumination. This memory effect remains for time scales on the order of at least a few weeks in  $\text{YH}_x\text{O}_y$  [6]. The memory effect is therefore a major concern in view of practical applications, and understanding its origin is of great importance.

However, the microscopic origins of the memory effect have not been unravelled yet. Many previous studies have focused on the nature of the reversible processes and optical phenomena linked to the photochromism, while the link of light-induced irreversible changes to the memory effect has rarely been reported. Moldarev *et al.* [7] observed the release of hydrogen gas during illumination for the first two cycles and their results suggest that the removal of hydrogen may be related to the memory effect. Our previous positron annihilation studies during one photodarkening-bleaching cycle showed irreversible shifts in Doppler broadening parameters that maintained after full bleaching in both  $\text{YH}_x\text{O}_y$  and  $\text{GdH}_x\text{O}_y$  films, suggesting that stable or weakly metastable vacancy-related defects are formed, that may contribute to the memory effect and/or are related to the microscopic origins of the memory effect [8-10]. In order to gain understanding of the memory effect, further exploration of the microstructural changes upon cycling is required.

Positron annihilation spectroscopy (PAS) is a well-established non-destructive tool to characterize open-volume defects on a nanometer scale in solids [11-14]. The neutral and negatively-charged open-volume defects are often effective positron traps due to the lack of positive ion cores. By measuring the Doppler shifts of the positron-electron annihilation photopeak, one can obtain information on changes in the local valence electron states via the positron-electron momentum distribution caused by changes in open-volume defects and electronic structure. This technique is known as Doppler-Broadening Positron Annihilation Spectroscopy (DB-PAS). Another well-known positron annihilation technique is Positron Annihilation Lifetime Spectroscopy (PALS), which can quantify and identify open-volume defects to provide information on the type and concentration of vacancy defects. Namely, the lifetime of a positron in an open volume defect will be longer than in the defect-free material, since the electron density in the open volume defect is lower, leading to a reduction in the positron-electron annihilation rate.

In this work, the photochromic performance of  $\text{YH}_x\text{O}_y$  and  $\text{GdH}_x\text{O}_y$  thin films under six photodarkening-bleaching cycles is monitored by *in-situ* transmittance measurements, and the microstructural changes under the same six cycles are examined by *in-situ* illumination DB-PAS, complemented by PALS investigations on  $\text{YH}_x\text{O}_y$  thin films before and after one cycle. The *in-situ* DB-PAS study demonstrates that the increase of the bleaching time constant upon cycling is accompanied by an increase of the S-parameter after bleaching, revealing a strong correlation between these parameters. The observed increase in S-parameter is attributed to vacancy agglomeration of light-induced hydrogen vacancies with yttrium monovacancies and growth of vacancy clusters present in the as-deposited films, as revealed by PALS measurements before and after one photodarkening-bleaching cycle. These findings suggest that incomplete refilling of the light-created hydrogen vacancies with hydrogen could be a key ingredient of the microscopic origin of the memory effect.

## 3.2 Experimental

### 3.2.1 Sample preparation

A total of eight yttrium oxyhydride films and eight gadolinium oxyhydride thin films were prepared by two steps. First, metal hydride films were deposited on fused-silica substrates by reactive magnetron sputtering with a constant  $\text{Ar}/\text{H}_2$  flow (7:1) at room temperature. The deposition power supplied to the yttrium and gadolinium targets is 100 W and 165 W, respectively. The total pressure was maintained at 0.5 Pa for  $\text{YH}_x\text{O}_y$  and at 0.8 Pa for  $\text{GdH}_x\text{O}_y$ , respectively, which exceeded the critical pressure necessary to induce sufficient porosity of the metal hydride films, enabling the subsequent formation of the semiconducting  $\text{YH}_x\text{O}_y$  and  $\text{GdH}_x\text{O}_y$  oxyhydride phase during post-oxidation [1]. This post-oxidation process occurs by exposure of the metal hydride films to ambient environment, in which an oxidation time of  $\sim 10$  days is sufficient to achieve a stable composition. After that, half of the yttrium oxyhydride and gadolinium oxyhydride thin film samples of each batch were stored in ambient air (noted as YHO-air and GdHO-air), while the others were stored under a vacuum pressure of  $10^{-2}$  mbar (noted as YHO-vac and GdHO-vac). The thickness of the  $\text{YH}_x\text{O}_y$  and  $\text{GdH}_x\text{O}_y$  films was determined by profilometry to be 420 nm and 570 nm, respectively, within  $\sim 10\%$  accuracy. For the PALS measurements, one additional thin film  $\text{YH}_x\text{O}_y$  sample was made by the same recipe while the other was deposited at 200 W. The thickness of the two additional  $\text{YH}_x\text{O}_y$  films was determined to be  $\sim 370$  nm. Table 1 summarizes the different types of rare-earth oxyhydride thin films studied in this work as well as the corresponding deposition parameters, thickness and storage environment.



Table 3.1: List of the main parameters and measurements of rare-earth oxyhydride thin film samples studied in this work

Sample type	Total deposition pressure (Pa)	Deposition power (W)	Thickness (nm)	Storage environment	Measurements
YHO-air	0.5	100	420	Air	Transmittance, DB-PAS, XRD
YHO-vac	0.5	100	420	Vacuum	Transmittance, DB-PAS
GdHO-air	0.8	165	570	Air	Transmittance, DB-PAS, XRD
GdHO-vac	0.8	165	570	Vacuum	Transmittance, DB-PAS
YHO-1	0.5	100	370	Air	PALS
YHO-2	0.5	200	370	Air	PALS

### 3.2.2 Characterization

The transmittance spectra of the yttrium and gadolinium oxyhydride film samples were acquired in the range of 230-1120 nm on a custom-built optical fiber-based spectrometer [2]. The optical properties of the vacuum-stored samples were measured under a vacuum condition of 8-9 Pa. The photochromic effect of oxyhydride films was triggered by a narrow wavelength LED (385 nm) with an intensity of  $\sim 30 \text{ mW/cm}^2$ . The same light source equipped with a Köhler lens system was used to illuminate the sample for the *ex-situ* illumination X-ray diffraction (XRD) and the *in-situ* illumination DB-PAS experiments. For all photodarkening-bleaching cycles, the illumination time and the monitoring time during bleaching were set at respectively 2.5 h and 20 h, for both the optical and DB-PAS measurements, meaning that a full photodarkening-bleaching cycle corresponded to 22.5 h. The grazing-incidence X-ray diffraction (GIXRD) patterns were collected on a PANalytical X'Pert PRO diffractometer at an incident angle of  $2^\circ$  with a Cu  $K\alpha$  source ( $\lambda = 1.54 \text{ \AA}$ ) at room temperature.

DB-PAS experiments were carried out using the variable energy positron (VEP) beam setup at the TU Delft Reactor Institute [15]. The intensity of the positron beam at sample position is around  $10^4 \text{ e}^+/\text{s}$  and the FWHM of the beam diameter is around 8 mm. The low momentum shape (S-) and high momentum wing (W-) parameter were defined as, the annihilation events (1) in the central area with an energy window of  $|E| < 0.77 \text{ keV}$  (or electron momentum  $|p| < 3.0 \times 10^{-3} m_0c$ ) and (2) the area with a energy window of  $2 \text{ keV} < |E| < 6 \text{ keV}$  ( $8.2 \times 10^{-3} m_0c < |p| < 23.4 \times 10^{-3} m_0c$ ), divided by the total annihilation events under the gamma ray photopeak around 511 keV. The S-parameter reflects the annihilation with primarily valence electrons, providing sensitivity to the electronic structure and the presence of vacancies, while the W-parameter represents positron annihilation with semicore electrons, providing sensitivity to the local chemical surrounding of the positron trapping site. The collected depth-profiles with implantation energies of 0.1-25 keV were fitted by

VEPFIT to extract the S- and W-parameter of the rare-earth oxyhydride layer [16]. For the time-dependent *in-situ* DB-PAS measurements under multiple illumination cycles, the implantation energy of positrons is fixed at 5.5 keV and 10 keV for  $\text{YH}_x\text{O}_y$  and  $\text{GdH}_x\text{O}_y$ , respectively, to ensure that most of the positrons annihilate in the oxyhydride layer ( $> 95\%$  for  $\text{YH}_x\text{O}_y$  and  $> 90\%$  for  $\text{GdH}_x\text{O}_y$ ) rather than in the substrate or at the surface. The fractions of positrons annihilating in each layer of  $\text{YH}_x\text{O}_y$  and  $\text{GdH}_x\text{O}_y$  extracted from the VEPFIT analyses are shown in the Supplemental Material, Fig. S1. The positron implantation depth distribution is assumed to follow a Makhovian implantation profile. The calculated Makhovian implantation profiles for an implantation energy of 5.5 keV for  $\text{YH}_x\text{O}_y$  and of 10 keV for  $\text{GdH}_x\text{O}_y$  are plotted in Fig. 3.1, which demonstrates that these implantation profiles fit well within the thickness of the layers (see Table 3.1). The positron implantation profiles in a material with density  $\rho$  in  $\text{g/cm}^3$  are described by

$$P(z, E) = \frac{mz^{m-1}}{z_0^m} \exp\left[-\left(\frac{z}{z_0}\right)^m\right] \quad (3.1)$$

with  $m=2$ ,  $z$  the implantation depth, and  $z_0=1.13\bar{z}$ , with  $\bar{z}$  the mean implantation depth in nm, is a function of the positron implantation energy  $E$  in keV according to  $z_0(E)=\frac{AE^n}{\rho}$ , and we used  $n=1.6$  and  $A=4 \mu\text{g cm}^{-2} \text{keV}^{-n}$  [17, 18], and  $\rho=4.3 \text{ g/cm}^3$  for  $\text{YH}_x\text{O}_y$  and  $\rho=7.2 \text{ g/cm}^3$  for  $\text{GdH}_x\text{O}_y$ , respectively.

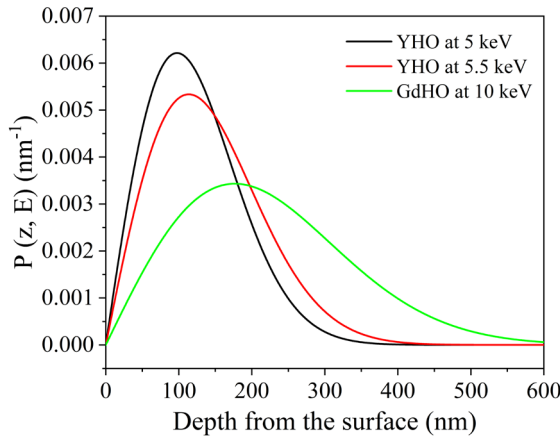


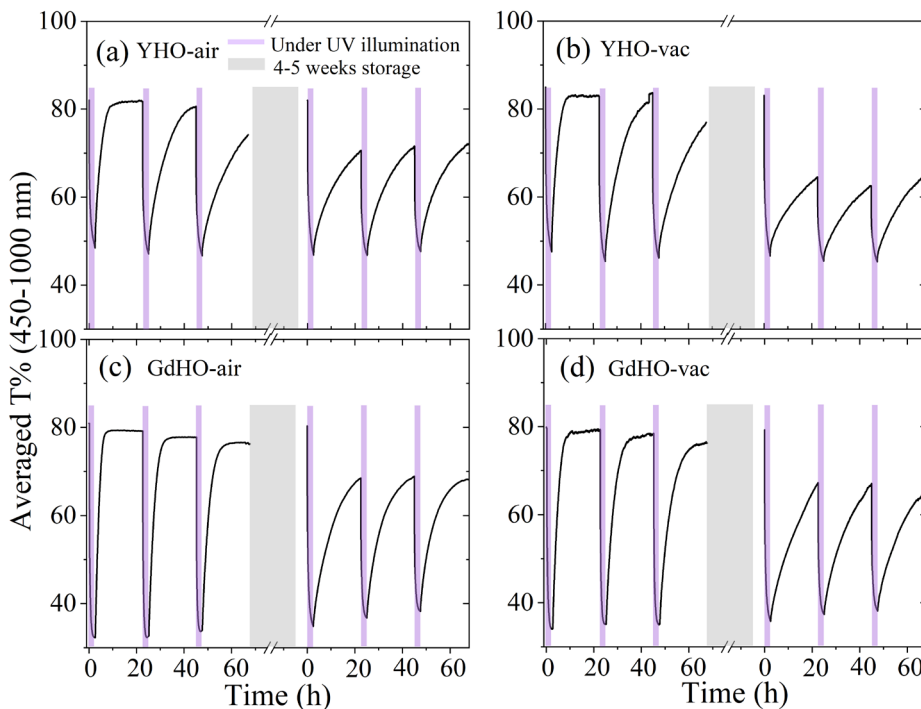
**Figure 3.1:** Positron implantation profiles for implantation energies of 5 and 5.5 keV in  $\text{YH}_x\text{O}_y$ , and 10 keV in  $\text{GdH}_x\text{O}_y$ .

PALS measurements were performed using the Mono-energetic Positron Spectroscopy (MePS) setup at the ELBE (Electron Linac for beams with high Brilliance and low Emittance) facility at the Helmholtz-Zentrum Dresden-Rossendorf (HZDR), Germany [19]. Approximately  $10^7$  counts were collected for each spectrum. A  $\text{CeBr}_3$  scintillator detector

coupled to a Hamamatsu R13089-100 photomultiplier (PMT) tube was utilized for gamma quanta acquisition and the signals were processed by the SPDevices ADQ14DC-2X digitizer (14 bit vertical resolution and 2 GS/s horizontal resolution) [20]. The time resolution was estimated to be  $\sim 250$  ps by determination of the PALS spectrum of a reference amorphous Yttria stabilized zirconia (YSZ) sample with two lifetime components. Since the thickness of the  $\text{YH}_x\text{O}_y$  films ( $\sim 370$  nm) examined in the PALS study was slightly less than the thickness of the  $\text{YH}_x\text{O}_y$  films studied in the DB-PAS experiments, the positron implantation energy was fixed to 5 keV before illumination and during the photodarkening-bleaching cycle. The corresponding calculated Makhovian positron implantation profile is shown in Fig. 3.1. The program PALSfit3 was used to analyse the positron lifetime spectra [21].

### 3.3 Results

#### 3.3.1 Photochromic responses upon cycling



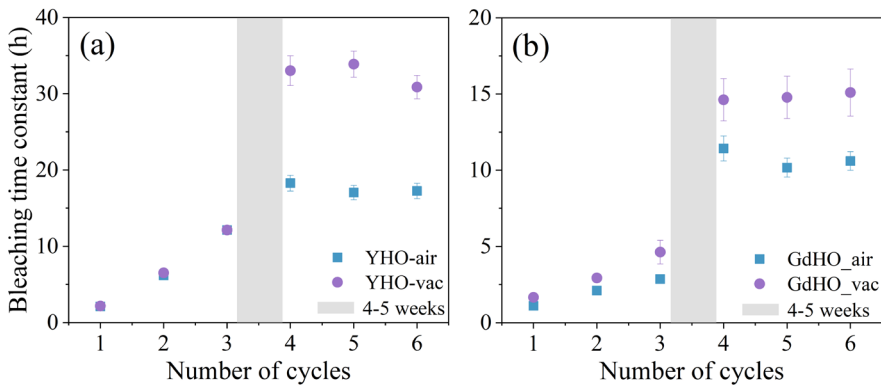
**Figure 3.2:** Time dependence of average transmittance in the range of 450-1000 nm of (a) YHO-air, (b) YHO-vac, (c) GdHO-air, and (d) GdHO-vac thin films during six photodarkening(bleaching)-bleaching cycles including an intermediate period of 4-5 weeks of storage in air or vacuum (shaded with a rectangular grey area).

Fig. 3.2 shows the transmittance averaged over the wavelength range of 450 nm to 1000 nm as a function of time upon six consecutive photodarkening-bleaching cycles for four thin film samples, YHO-air, YHO-vac, GdHO-air, and GdHO-vac. The transmittance in the photodarkened state after each illumination period of 2.5 h is fairly constant for the six cycles for each film, and there is no significant difference in transmittance between air-stored and vacuum-stored films, as can be seen comparing Figs. 3.2(a) to 3.2(b) and 3.2(c) to 3.2(d), respectively. However, the bleaching process becomes progressively slower with subsequent photodarkening-bleaching cycle, i.e., longer time is needed to reverse back to the bleached (transparent) state for the first four cycles, after which the bleaching rate stabilizes. This process of increasingly slower bleaching kinetics in  $\text{YH}_x\text{O}_y$  films upon photochromic cycling is known as the memory effect [6]. Quantitatively, the bleaching process can be evaluated by the bleaching time constant ( $\tau_{\text{bleach}}$ ), which can be determined according to equation (2), assuming first-order kinetics for the bleaching process [4]. The corresponding fits are shown in Fig. S3.2 in the Supplemental Material and the extracting values for bleaching time constant for each cycle are shown in Fig. 3.3.

$$\ln\left(-\ln\left(\frac{T(t)}{T_0}\right)\right) = -\frac{1}{\tau_{\text{bleach}}}t + \ln\left(-\ln\left(\frac{T_{\text{dark}}}{T_0}\right)\right) \quad (3.2)$$

where  $T_0$  is the initial average transmittance before illumination,  $T_{\text{dark}}$  is the transmittance of the photodarkened state at the end of the illumination period and  $T(t)$  is the transmittance after a time  $t$  of bleaching.

As shown in Fig. 3.3,  $\tau_{\text{bleach}}$  increases almost linearly for the first three cycles for all samples, in which  $\tau_{\text{bleach}}$  shows an increase by a factor of  $\sim 6$  and  $\sim 2$  for  $\text{YH}_x\text{O}_y$  and  $\text{GdH}_x\text{O}_y$ , respectively. After the storage under dark conditions for 4-5 weeks and the subsequent fourth



**Figure 3.3:** The bleaching time constant  $\tau_{\text{bleach}}$  extracted from the optical transmittance measurements according to equation (1) for the (a)  $\text{YH}_x\text{O}_y$  and (b)  $\text{GdH}_x\text{O}_y$  films with the number of cycles.

illumination, the bleaching process is even slower (larger  $\tau_{\text{bleach}}$ ) compared to the previous cycle, demonstrating that the memory effect remains present for at least 4-5 weeks of storage, both under ambient or vacuum conditions. After the fourth photodarkening-bleaching cycle, the bleaching time  $\tau_{\text{bleach}}$  remains constant on subsequent cycling. Clearly, faster bleaching is observed in the  $\text{GdH}_x\text{O}_y$  films compared to the  $\text{YH}_x\text{O}_y$  films, consistent with previous studies, that connected the faster bleaching kinetics to the larger ionic radius of Gd compared to Y and Sc [2]. In addition, the similarity of the evolution of the photochromic effect observed in the oxyhydride films stored and measured in air and in vacuum, as shown in Figs. 3.2 and 3.3, indicates that an ambient environment is not a crucial factor for the photochromic effect, consistent with Ref. [7] where it was shown that  $\text{YH}_x\text{O}_y$  bleaches under ultra-high vacuum conditions. However, we do observe that both  $\text{YH}_x\text{O}_y$  and  $\text{GdH}_x\text{O}_y$  films bleach slower after four weeks of storage under vacuum compared to four weeks of storage in air.

### 3.3.2 Microstructural changes investigated by in-situ illumination positron annihilation

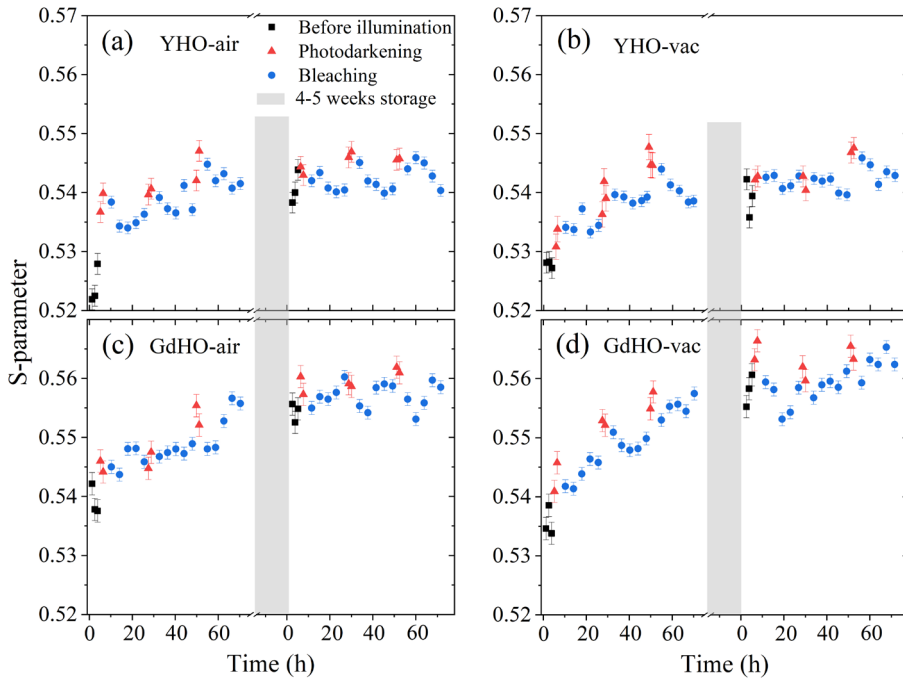


**Figure 3.4:** Time evolution of the S-parameter at a positron implantation energy of 5.5 keV for samples (a) YHO-air and (b) YHO-vac, and at a positron implantation energy of 10 keV for samples (c) GdHO-air, and (d) GdHO-vac before illumination (black points) and under six photodarkening (red points) -bleaching (blue points) cycles, including an intermediate storage period of 4-5 weeks (grey region).

In order to gain an understanding of the origin of the memory effect from a microstructural perspective, in-situ DB-PAS measurements were conducted during six photodarkening-bleaching cycles with time intervals for illumination and for monitoring during bleaching that are the same as for the transmittance measurements reported in Section III.A. The evolution of the line shape parameter  $S$  as a function of time for six photodarkening-bleaching cycles for  $\text{YHxO}_y$  and  $\text{GdHxO}_y$  is shown in Fig. 3.4 (a-b) and Fig. 3.4 (c-d), respectively. The corresponding changes in the wing parameter  $W$  are shown in Fig. S3.3 in the Supplemental Material. The results show that the  $S$ -parameter increases upon illumination and it decreases partially reversibly during bleaching for both the  $\text{YHxO}_y$  and  $\text{GdHxO}_y$  films, consistent with our previous DB-PAS study [10]. During the first three cycles, in addition to the reversible part of the shifts in  $S$ -parameter with photodarkening and bleaching, the  $S$ -parameter after each photodarkening-bleaching cycle increases successively. The nature of this irreversible increase in the  $S$ -parameter is discussed in more details further on. For the second three cycles, the increase in  $S$ -parameter under illumination is nearly fully reversed after bleaching. The  $S$ - $W$  diagrams presented in Fig. 3.5 show that the corresponding  $(S, W)$  values shift back-and-forth between the  $(S, W)$  value for the photodarkened state and

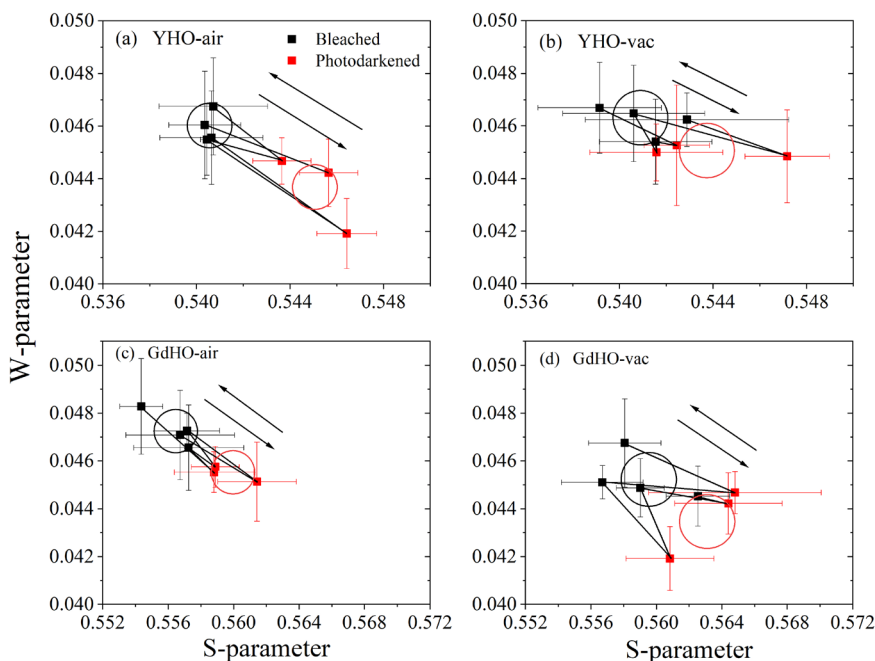


**Figure 3.5:**  $S$ - $W$  plots of the second three photodarkening-bleaching cycles for the bleached state (black points) and photodarkened state (red points) for (a) YHO-air, (b) YHO-vac, (c) GdHO-air, and (d) GdHO-vac. The circles and arrows are a guide for the eyes. The center of each circle is located at the average value of each bleached and photodarkening state.

the (S,W) value for the bleached state with a lower S- and higher W-parameter. These reversible shifts of the positron Doppler broadening S and W parameters occur systematically for each of the second three cycles for all oxyhydride films, and correlate with the reversible changes in the transmittance upon photodarkening and bleaching. As discussed in our previous study, the reversible changes in the Doppler parameters and in the optical transmittance during photodarkening and bleaching can be explained by reversible formation and disappearance of metallic-like nanodomains in the semiconducting oxyhydride matrix [10]. Indeed, the reversible shifts of the Doppler parameters to a larger S-parameter and a smaller W-parameter point in the direction of the (S,W) value of the rare-earth dihydride [10], in line with the reversible formation of metallic-like nanodomains. In [10], two types of mechanisms for the formation of metallic-like domains were proposed, that both involve liberation of hydrogen atoms from their lattice positions by the illumination, namely (i) the formation of hydrogen-rich domains enabled by local transport of hydrogen and oxygen ions, which might acquire a metallic-like character due to a mixed  $Y^{2+}/Y^{3+}$  valence state (e.g.  $YH_2O_x$  with  $x < 0.5$ ), and (ii) the occurrence of an Anderson-Mott insulator-to-metal transition in domains of the film, induced by the formation of a sufficiently high local concentration (above ~30%) of hydrogen vacancies at the octahedral sites and subsequent band formation of photo-excited electrons that occupy Y(4d) orbitals surrounding the hydrogen vacancies [10].

In addition to the reversible shifts of the S-parameter, Fig. 3.4 clearly shows that the S-parameter after each photodarkening-bleaching cycle (blue symbols) increases successively for the first three cycles for all samples. Quantitatively, the S-parameter after these photodarkening-bleaching cycles has increased by ~3% and 5-6% for  $YH_xO_y$  and  $GdH_xO_y$ , respectively, compared to the initial S-parameter before the first illumination. These increments are similar to the changes extracted from VEPFIT analysis of the DB-PAS depth profiles before and after the first three cycles (in the Supplemental Material, Fig. S3.4 and Table S5.1-5.4). Simultaneously, the W-parameter shows a decrease by ~4% and ~7% for the  $YH_xO_y$  and  $GdH_xO_y$  samples, respectively. After 4-5 weeks of storage, the S-parameter is still high, suggesting that the microstructural changes induced in the photodarkening-bleaching cycles are stable. During the second set of three photodarkening-bleaching cycles, the S-parameter after bleaching remains nearly constant with subsequent cycles for each oxyhydride film. This saturation of the S-parameter after bleaching could be due to either (i) the concentration and size of open-volume defects do not noticeably increase anymore with the photodarkening-bleaching cycling, or (ii) the concentration of vacancy defects still increases but exceeds the sensitivity of DB-PAS due to saturation trapping of positrons in these defects, that will occur when concentrations of order  $\sim 10^{-4}$  or higher are reached [12, 22].

These trends in the S and W parameters upon photochromic cycling are further illustrated in the corresponding S-W diagrams of Fig. 3.6 (a-b) and Fig. 3.6 (c-d) for the Y-based and Gd-based oxyhydride films, that reveal the systematic increase in S-parameter and decrease

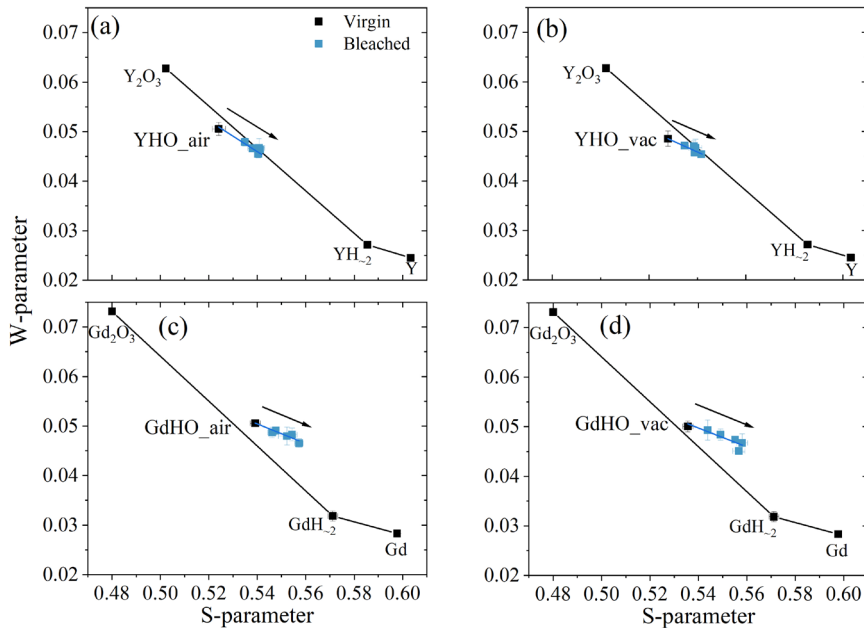


**Figure 3.6:** S-W values of (a-b) Y-based and (c-d) Gd-based oxyhydride films in the virgin state and in the bleached state upon cycling extracted from the *in-situ* illumination DB-PAS measurements, compared with the (S,W) values of the Y-based or Gd-based metal, metal hydride and oxide films [10]. The arrows are a guide for the eyes, showing the trends for the six cycles.

in W-parameter in the bleached states upon photochromic cycling, together with a comparison to the (S,W) values of the respective yttrium and gadolinium rare-earth metal, metal hydride and oxide films determined in our previous studies [2, 10]. It is found that upon photochromic cycling for the first three cycles, the (S,W) values after bleaching for each cycle progressively shift in the same direction towards higher S and lower W, with a slope that is smaller than the line connecting the (S,W) values of the rare-earth metal oxyhydride and rare-earth metal hydride films. These observed linear shifts of the (S,W) values are in line with either a systematic increase in the concentration of open-volume defects formed during photochromic cycling or a progressive systematic increase in the size of the vacancy defects.

### 3.3.3 Correlation between photochromic responses and microstructural changes

The previous sections showed a systematic increase in the positron Doppler broadening S-parameter after bleaching as well as in the time scale of bleaching,  $\tau_{bleach}$ , with photodarkening-bleaching cycling. This suggests that the microstructural changes corresponding to the changes in S-parameter may correlate with the memory effect. In order



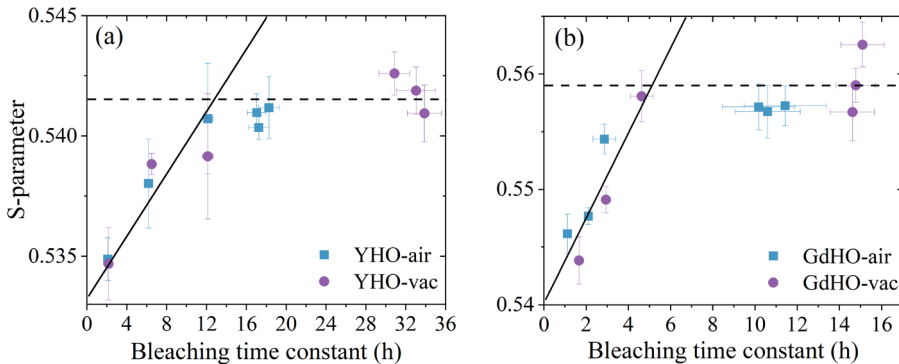


**Figure 3.7:** The averaged S-parameter after bleaching versus the bleaching time constant  $\tau_{\text{bleach}}$ , according to the time-dependent DB-PAS measurements and the optical transmittance measurements for YHO-air, YHO-vac, GdHO-air and GdHO-vac samples. The solid tilted lines are a guide for the eyes for the first three cycles (suggesting a linear correlation for the first three cycles) and the dashed horizontal lines are a guide for the eyes for the second three cycles.

to examine this correlation, the averaged S-parameter after each photodarkening-bleaching cycle is plotted in Fig. 3.7 versus  $\tau_{\text{bleach}}$  for each cycle. For the first three cycles, S-parameter rises almost linearly with increasing bleaching time,  $\tau_{\text{bleach}}$ . This strong correlation suggests that the progressively slower bleaching kinetics upon cycling is accompanied by an increased concentration or size of open-volume defects. Our study thus clearly points to a relationship between bleaching kinetics ( $\tau_{\text{bleach}}$ ) and formed vacancy structure. After the third illumination and bleaching cycle, the S-parameter stays nearly constant. This could be due to the formation of a stable composition of vacancies, or to positron saturation trapping at open-volume defects, meaning that additionally formed vacancies do not induce an observable change in S-parameter. After the fourth photodarkening-bleaching cycle, the bleaching time  $\tau_{\text{bleach}}$  also remains constant.

### 3.3.4 Nature of the vacancy-related defects induced by cycling investigated by PALS

To gain more insights into the origin of the irreversible systematic increase in S-parameter and decrease in W-parameter observed upon photodarkening-bleaching cycling, two  $\text{YH}_x\text{O}_y$  films were measured in the virgin state and in the bleached state after one photodarkening-bleaching cycle by *in-situ* PALS at HZDR. All positron lifetime spectra were decomposed by a three-component analysis, shown in Fig. 3.8.

The extracted lifetimes and the corresponding intensities are shown in Table 3.2. The first and second positron lifetimes in both films are larger than the reported bulk lifetime ( $\sim 240$  ps) extracted from a two-defect trapping model in our previous study [10]. The reported bulk

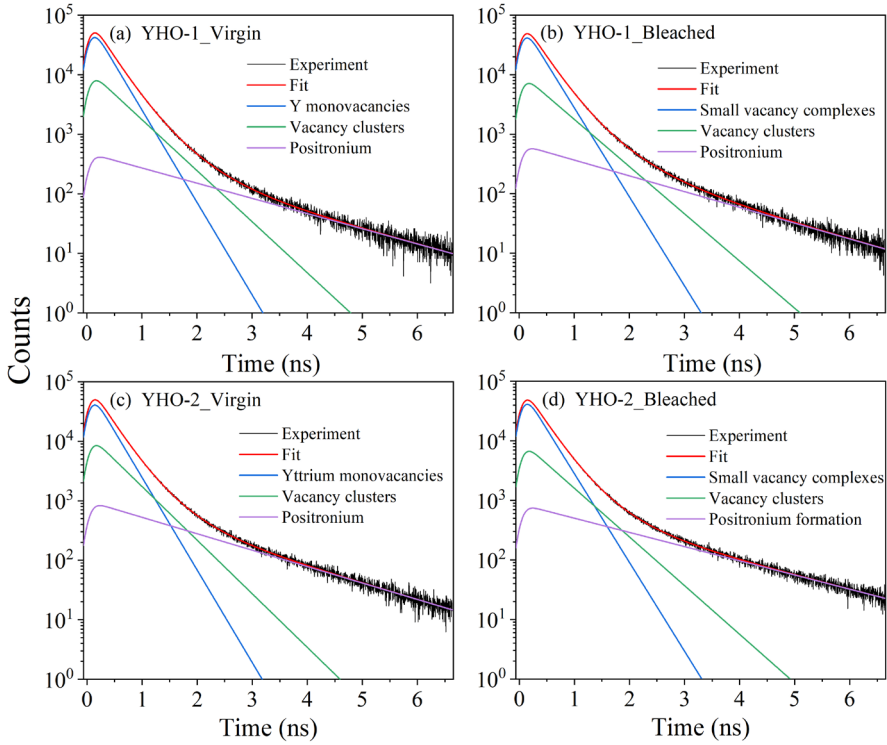


**Figure 3.8:** Positron lifetime spectra collected at an implantation energy of 5 keV of (a) YHO-1 in the virgin state and (b) the bleached state after one cycle, and (c) YHO-2 in the virgin state and (d) the bleached state after one cycle, and the corresponding three-component analyses. The background was less than 1 for all fits.

Table 3.2: Time-averaged positron lifetimes ( $\tau_i$ ) and intensities ( $I_i$ ) for two  $\text{YH}_x\text{O}_y$  films in the virgin state and in the bleached state after one photodarkening-bleaching cycle, extracted from PALS spectra collected at 5 keV.

sample	Status	$\tau_1$ (ps)	$\tau_2$ (ps)	$\tau_3$ (ns)	$I_1$ (%)	$I_2$ (%)	$I_3$ (%)
YHO-1	Virgin state	279 $\pm$ 2	506 $\pm$ 12	1.71 $\pm$ 0.03	76 $\pm$ 2	21 $\pm$ 1	2.9 $\pm$ 0.1
	Bleached state after one cycle	290 $\pm$ 2	546 $\pm$ 15	1.66 $\pm$ 0.03	76 $\pm$ 1	21 $\pm$ 1	3.8 $\pm$ 0.2
YHO-2	Virgin state	280 $\pm$ 2	484 $\pm$ 16	1.57 $\pm$ 0.02	73 $\pm$ 2	21 $\pm$ 2	5.4 $\pm$ 0.1
	Bleached state after one cycle	291 $\pm$ 2	532 $\pm$ 18	1.81 $\pm$ 0.03	76 $\pm$ 2	18 $\pm$ 2	5.5 $\pm$ 0.1

lifetime is close to the theoretical bulk lifetimes of  $\sim 231$  ps and  $\sim 241$  ps in  $\text{YH}_{2.5}\text{O}_{0.25}$  calculated using the two-component density functional theory within the local density approximation (LDA) and generalized gradient approximation (GGA) framework, respectively. More details on the methods employed in the DFT calculation can be found in

Appendix E. The reason of using the composition  $\text{YH}_{2.5}\text{O}_{0.25}$  for the theoretical positron lifetime calculation is that a recent DFT study showed that  $\text{YH}_{2.5}\text{O}_{0.25}$  and YHO have a lower total energy compared to the intermediate compositions, and therefore  $\text{YH}_{2.5}\text{O}_{0.25}$  could be the main component of our hydrogen-rich oxyhydride films [23]. The large lifetimes and the intensities of the experimental first and second positron lifetime components together with the absence of a (reduced) bulk lifetime component indicate positron saturation trapping for these samples due to a high vacancy concentration of the order of  $10^{-4}$  or higher, i.e., almost all (>99%) implanted positrons are trapped and annihilate at vacancy-type defects. In the virgin state of both films, the first lifetime component with  $\tau_1$  of  $\sim 280$  ps is close to the calculated values  $\sim 290$  ps (LDA) and  $\sim 324$  ps (GGA) for yttrium monovacancies, therefore this component could be assigned to yttrium monovacancies ( $V_Y$ ) present in the as-deposited films. We note here that we cannot strictly exclude the possibility of hydrogen-decorated metal vacancies, as have been observed in the niobium, nickel and tungsten systems [24-27]. These studies showed that the decoration of a metal vacancy with one hydrogen atom can decrease the positron lifetime at a cation monovacancy by 10-20 ps. However, yttrium oxyhydride is different from the above-mentioned transition metals in the sense of its mostly ionic binding of the metal cation ( $\text{Y}^{3+}$ ) and the hydrogen ( $\text{H}^-$ ) and oxygen ( $\text{O}^{2-}$ ) anions, leading to a high stability of the formed oxyhydride phase [28]. For yttrium oxyhydride films, it is likely that during the reactive magnetron sputtering process and subsequent post-oxidation, hydrogen atoms strongly prefer anion (tetrahedral and octahedral) lattice sites of the stable oxyhydride phase, rather than vacant cation lattice sites (cation monovacancies). Similarly, no hydrogen-decorated small vacancies were found in hydrogenated MgTi-based ionic compounds [29]. The relatively high intensity  $I_1$  ( $\sim 73$ -76 %) indicates that these vacancies are dominant positron trapping sites. The longer lifetime of the second component  $\tau_2$  of  $\sim 500$  ps with an intensity of 21% stems from annihilation in large vacancy clusters (consisting of > 5 vacancies [10]), while the third component with the longest lifetime  $\tau_3$  in the range of  $\sim 1.6$ -1.7 ns is a characteristic of ortho-Positronium (o-Ps) formed in nanoscale open volume (such as nanopores) present in the films. Assuming pores that are spherically shaped, the diameter can be estimated to be around 0.50 nm according to Tao-Eldrup model [30,31]. Both positron annihilation and ortho-positronium formation might therefore occur in the same type of vacancy clusters [10].

After  $\sim 2$  h illumination and 2-3 h of bleaching in the dark, both  $\tau_1$  and  $\tau_2$  have increased in the same manner for both samples, indicating growth of the corresponding vacancies and vacancy clusters. The first lifetime  $\tau_1$  increases to  $\sim 290$  ps, which can be attributed to the formation of divacancies or small multi-vacancy complexes, involving Y monovacancies present in the as-deposited films and light-induced hydrogen vacancies. Local hydrogen (hopping) mobility has been proposed to be a key element of photochromism in rare-earth oxyhydride films [32-34]. This can be understood, since under the photo-excitation of charge carriers across the bandgap, hydrogen ions at octahedral sites may capture photo-generated holes ( $\text{H}^+ + h^+ \rightarrow \text{H}^0$ ) and leave their lattice positions, producing hydrogen vacant sites in the

lattice. Some of these hydrogen vacancies may aggregate with yttrium monovacancies to form divacancies  $V_Y-V_H$ , or perhaps even small vacancy complexes consisting of  $V_Y$  and a few hydrogen vacancies. In principle, the formation of  $V_Y-V_O$  is also possible, although O is considered to be less mobile than H due to its lower polarity and larger mass, and liberation from its lattice position is less probable [28, 35]. Notably, the increase in  $\tau_1$  after bleaching is  $\sim 4\%$ , and therefore clearly smaller than the typical increase in lifetimes ( $>10\%$ ) going from monovacancies to divacancies in semiconductors such as Si, GaAs and SiC [36, 37]. This suggests that only part of the yttrium monovacancies turn into divacancy-like defects, meaning that a mixture of monovacancies and divacancy-like defects is present in the films after one photodarkening-bleaching cycle. Such a transformation from monovacancies to divacancy-like defects for only part of the Y monovacancies present is understandable. If we assume that the mobility of hydrogen vacancies is small,  $V_Y$  and  $V_H$  can only aggregate when a hydrogen vacancy is created on a lattice site adjacent to the yttrium vacancy. Considering now the concentration of hydrogen vacancies at octahedral sites that are formed during the first photodarkening (we assume an average concentration of octahedral hydrogen vacancies of the order of  $\sim 10\%$  of all octahedral hydrogen in the film, which would be a reasonable value in the framework of the Anderson-Mott model) and the concentration of pre-existing yttrium vacancies  $V_Y$  (of the order of  $10^{-4}$ ) [10], one can estimate that the probability of formation of a hydrogen vacancy adjacent to an Y monovacancy is on the order of  $\sim 25\%$  [38]. Therefore, we can expect a concentration of formed divacancy-like defects of the order of  $10^{-5}$ , i.e. somewhat smaller than the concentration of  $V_Y$  and likely below the concentration threshold for saturation trapping of positrons. The increase in the lifetime of the second component  $\tau_2$  of 40-50 ps after one cycle is rather large, and could be due to the release of loosely-bonded hydrogen atoms from the walls of the large vacancy clusters or of dihydrogen molecules from these vacancy clusters [7]. The changes in the third component varies from sample to sample. Overall, the increase in S-parameter after one photodarkening-bleaching cycle could be the result of the clustering of hydrogen vacancies (created by the illumination) with the pre-existing Y monovacancies, forming divacancies (or small vacancy complexes), and of hydrogen liberated from vacancy clusters, as inferred from the PALS study, in combination with incomplete refilling of hydrogen vacancies during the bleaching process. Alternatively, a small amount of nanoscale metallic-like domains that possibly remain present after bleaching may also lead to an irreversible increase in the S-parameter. This process cannot be completely ruled out from the PALS measurements of this study, since the lifetime of positrons that trap and annihilate in the metallic-like domains and the exact nature of the metallic-like domains is yet unknown. However, we note here that the reported positron bulk lifetime of metallic yttrium dihydride of  $\sim 260$  ps [10] is smaller than that of the lifetime of the first component of the yttrium oxyhydride samples both in the as-deposited state ( $\sim 280$  ps) and after a full photodarkening-bleaching cycle ( $\sim 290$  ps, i.e. *increased* by  $\sim 10$  ps), making this alternative explanation less probable.

Finally, we note here that, since the PALS measurements after one photodarkening-bleaching cycle suggest that only part of the initially present Y monovacancies transform into divacancy-like defects, it is likely that more divacancy-like defects will be formed in the subsequent cycles. Clearly, this may explain the systematic increase in S-parameter in the bleached state observed during the first three photochromic cycles.

### 3.4 Discussion

Our studies show that both yttrium and gadolinium oxyhydride thin films exhibit a reversible photochromic effect upon six consecutive photodarkening-bleaching cycles, in which the transmittance is able to recover back to its original state after bleaching. However, the bleaching kinetics becomes increasingly slower upon cycling for the first four cycles, after which the bleaching rate stabilizes. Interestingly, our studies reveal a clear correlation between the progressively larger bleaching time constants and the evolution of the positron Doppler S-parameter as detected after each photodarkening-bleaching cycle. In combination with the PALS results, this suggests that the slower bleaching process upon cycling is accompanied by an increased concentration of divacancy-like defects and growth of vacancy clusters due to hydrogen liberated from their (lattice) positions. In order to gain further understanding of the memory effect from such a microscopic perspective, we propose and discuss a number of possibilities in the context of this positron study.

#### A. Increase in diffusion time

The slow bleaching kinetics of the order of hours for both yttrium and gadolinium oxyhydride films, as depicted in Fig. 3.2, could be caused by diffusion of hydrogen anions acting as a rate-limiting process for the return of the film to the transparent state. This hypothesis of hydrogen diffusion can be evaluated in the context of proposed mechanisms for the photochromism that involve the formation of metallic domains, such as (i) phase-segregated hydrogen-rich domains enabled by local transport of hydrogen and oxygen ions liberated during illumination, which might acquire a metallic-like character due to a mixed  $Y^{2+}/Y^{3+}$  valence state (e.g.  $YH_2O_x$  with  $x < 0.5$ ), in a hydrogen-poor transparent matrix, and (ii) Anderson-Mott transition in certain domains of the yttrium oxyhydride films where the concentration of illumination-induced hydrogen vacancies and subsequently nearby trapped electrons localized in Y(4d) orbitals is sufficiently high to lead to electron band formation and local metallicity [10,32,39]. Indeed, high hydrogen anion conduction is observed in powder La and Nd oxyhydrides, albeit that other rare-earth oxyhydrides show substantially lower macroscopic hydrogen diffusion [40, 41].

For a diffusion process, the diffusion time  $\tau_{\text{diff}}$  is proportional to the square of the diffusion distance  $L$  and is inversely proportional to the diffusion coefficient  $D$ , according to

$\tau_{\text{diff}} \sim \frac{L^2}{D}$  [42]. Therefore an increase in the diffusion distance  $L$  can lead to an increase in the diffusion time. For example, if hydrogen-rich metallic domains become systematically larger upon cycling during photodarkening, the diffusion distance for hydrogen anions to travel out of the domains will become larger, leading to a longer diffusion time and thus, slower bleaching kinetics. Secondly, the diffusion coefficient  $D$  can be influenced by multiple factors, for instance, vacancy defects [43, 44]. The increase in concentration of vacancy defects in oxyhydride films upon cycling, as observed in this study, may provide more hydrogen anion trapping sites, resulting in a smaller diffusion coefficient and a longer diffusion time. Such trapping of hydrogen in vacancies was observed in for example monoclinic zirconia, which decreased the diffusion coefficient and slowed down the hydrogen diffusion [43].

### B. Loss of hydrogen

Another possible cause for the gradual slowdown of bleaching kinetics upon cycling could be the loss of hydrogen, since the local hydrogen composition is expected to be important in regaining transparency. Previous studies into the nature of the photochromism provided indications that hydrogen is a key element in the photochromic effect in rare-earth oxyhydride films [10,32,39].

Within the Anderson-Mott insulator-to-metal transition proposed in [10] and briefly discussed here in section III.B, the bleaching process requires the refilling with hydrogen of a sufficient amount of hydrogen vacancies in order to reduce the concentration of trapped electrons near such hydrogen vacancies to below the threshold concentration for metallicity in a domain and reach the original semiconductor (transparent) state. However, hydrogen may get lost due to trapping at (for example) grain boundaries, or/and due to out-diffusion of hydrogen to the environment. Indeed, Moldarev *et al.* [7] observed hydrogen effusion in yttrium oxyhydride films for the first and second photodarkening-bleaching cycles [7]. The loss of hydrogen will reduce the amount of mobile hydrogen with respect to the amount of hydrogen liberated from lattice positions in the film during photodarkening. This may result in a slower bleaching kinetics, since some of the hydrogen required to refill the hydrogen vacancies in the metallic areas will need to come from a larger distance.

Indeed, the case of hydrogen loss seems to be in line with the irreversible formation of di-vacancies observed in our positron annihilation study, since hydrogen atoms that leave their lattice positions during photodarkening and are lost from the film will cause irreversible creation of hydrogen vacancies. Some of these hydrogen vacancies may aggregate with the pre-existing yttrium monovacancies, explaining the increase in the lifetime of the first component  $\tau_1$  and the increase in the S-parameter after bleaching. Also, hydrogen removal from the larger vacancy clusters will lead to growth in the open volume of these clusters, in line with the observed increase in  $\tau_2$ . Furthermore, the progressive increase in the S-parameter

after bleaching upon cycling can be naturally explained when the hydrogen loss occurs primarily in the first three cycles, in line with the observations by Molderav *et al.* [7].

### C. Grain growth

Komatsu *et al.* demonstrated that epitaxially grown yttrium oxyhydride films exhibit an extremely slow bleaching rate, as the high conductivity of the photo-induced metallic state hardly changes during the ~50 h long observation time after the UV illumination had stopped [33]. Hence, the systematic reduction in bleaching kinetics of the yttrium oxyhydride films studied here might be ascribed to a gradual structural transformation from the polycrystalline state in the direction towards epitaxially grown films, which may have larger grain sizes and less grain interfaces [45, 46].

However, in both our yttrium and gadolinium oxyhydride samples, the speculation of grain growth is not supported by the *ex-situ* XRD results, as the grain size estimated from the peak width of the strongest diffraction peak at  $\sim 33^\circ$  using the Scherrer equation does not change within error bars after illumination of  $\sim 2.5$  h for both samples (see the Supplemental Material, Fig. S3.5).

### D. Formation of hydroxide (OH<sup>-</sup>)

A mechanism for the photochromic effect in yttrium oxyhydride films that does not rely on diffusion was proposed in [32, 33]. This mechanism involves the local formation of OH<sup>-</sup> hydroxyl groups, as has been previously observed in mayenite [47-49]. In this scenario, large polarons are created in the yttrium oxyhydride structure due to the release of electrons according to the local reaction  $\text{O}^{2-} + \text{H}^+ + h\nu \rightarrow \text{OH}^- + 2\text{e}^-$  during illumination [33]. When the concentration of such polarons is large enough, meaning an average distance between polarons below about 7 Å, the localized electron orbitals overlap and form delocalized electron bands. The threshold fraction of formed OH<sup>-</sup> hydroxide bonds to induce metallic conductivity within this polaron mechanism was estimated to be  $\sim 2.2\%$  according to percolation theory [33]. Indeed, the formation of such a concentration of metallic areas under illumination can be observed by positrons [10] and is consistent with the observed increase in S-parameter during illumination (Fig. 3.4). However, in Ref. [33] it was reported that the transparent state could only be recovered when annealing the photodarkened sample to a high temperature of 125 °C, which would point to a high activation barrier for the reverse reaction  $\text{OH}^- + 2\text{e}^- \rightarrow \text{O}^{2-} + \text{H}^+$  [33]. This suggests that, if such local polaron formation is the sole actor in the mechanism in photodarkening and bleaching process, it is hard to explain the much faster bleaching observed in our oxyhydride films.

### 3.5 Conclusions

A stable cycling performance is of great importance for applications of photochromic  $\text{YH}_x\text{O}_y$  and  $\text{GdH}_x\text{O}_y$  thin films. We investigated the optical responses of photochromic  $\text{YH}_x\text{O}_y$  and  $\text{GdH}_x\text{O}_y$  thin films under six photodarkening-bleaching cycles by *in-situ* illumination transmittance measurements. In both systems, the transmittance recovers after each photodarkening-bleaching cycle, while a slowing down of the bleaching kinetics is observed upon cycling (the memory effect). The microstructural evolution in both  $\text{YH}_x\text{O}_y$  and  $\text{GdH}_x\text{O}_y$  films under the same six photodarkening-bleaching cycles is investigated by *in-situ* illumination DB-PAS and by PALS after one cycle. For the first three cycles, DB-PAS shows a systematic increase in the S-parameter after bleaching upon cycling, and a strong correlation between the S-parameter and the bleaching time constant is observed. This correlation suggests that the microstructural changes corresponding to the slower bleaching upon cycling involve vacancy aggregation, supported by PALS studies that show the formation of divacancies and growth of vacancy clusters. The change in the open-volume defects may affect the diffusion time by reducing the diffusion coefficient, supposing bleaching is a diffusion-related process. Moreover, hydrogen vacancies that cannot be refilled due to hydrogen loss may also contribute to a slower bleaching kinetics. For the second three cycles, the reversible shifts in the Doppler parameters back-and-forth between the photodarkened state and the bleached state could be due to the reversible formation of metallic-like domains, pointing to previously proposed mechanisms of the photochromism.



## References

- [1] F. Nafezarefi, H. Schreuders, B. Dam, and S. Cornelius, Photochromism of rare-earth metal-oxy-hydrides, *Appl. Phys. Lett.* **111**, 103903 (2017).
- [2] G. Colombi, T. De Krom, D. Chaykina, S. Cornelius, S. W. H. Eijt, and B. Dam, Influence of cation (RE = Sc, Y, Gd) and O/H anion ratio on the photochromic properties of  $\text{REO}_x\text{H}_{3-2x}$  thin films, *ACS Photonics* **8**, 709 (2021).
- [3] C. C. You and S. Z. Karazhanov, Effect of temperature and illumination conditions on the photochromic performance of yttrium oxyhydride thin films, *J. Appl. Phys.* **128**, 013106 (2020).
- [4] F. Nafezarefi, S. Cornelius, J. Nijskens, H. Schreuders, and B. Dam, Effect of the addition of zirconium on the photochromic properties of yttrium oxy-hydride, *Sol. Energy Mater. Sol. Cells* **200**, 109923 (2019).
- [5] D. Chaykina, I. Usman, G. Colombi, H. Schreuders, B. Tyburska-Pueschel, Z. Wu, S. W. H. Eijt, L. J. Bannenbergh, G. A. de Wijs, and B. Dam, Aliovalent calcium doping of yttrium oxyhydride thin films and implications for photochromism, *J. Phys. Chem. C* **126**, 14742 (2022).
- [6] T. Mongstad, C. Platzer-Bjorkman, J. P. Maehlen, L. P. A. Mooij, Y. Pivak, B. Dam, E. S. Marstein, B. C. Hauback, and S. Z. Karazhanov, A new thin film photochromic material: Oxygen-containing yttrium hydride, *Sol. Energy Mater. Sol. Cells* **95**, 3596 (2011).
- [7] D. Moldarev, L. Stolz, M. V. Moro, S. M. Adalsteinsson, I. A. Chioar, S. Z. Karazhanov, D. Primetzhofer, and M. Wolff, Environmental dependence of the photochromic effect of oxygen-containing rare-earth metal hydrides, *J. Appl. Phys.* **129**, 153101 (2021).
- [8] M. P. Plokker, S. W. H. Eijt, F. Naziris, H. Schut, F. Nafezarefi, H. Schreuders, S. Cornelius, and B. Dam, Electronic structure and vacancy formation in photochromic yttrium oxy-hydride thin films studied by positron annihilation, *Sol. Energy Mater. Sol. Cells* **177**, 97 (2018).
- [9] S. W. H. Eijt, T.W.H. de Krom, D. Chaykina, H. Schut, G. Colombi, S. Cornelius, W. Egger, M. Dickmann, C. Hugenschmidt, B. Dam, Photochromic  $\text{YO}_x\text{H}_y$  thin films examined by *in situ* positron annihilation spectroscopy, *Acta Phys. Pol. A* **137**, 205 (2020).
- [10] Z. Wu, T. de Krom, G. Colombi, D. Chaykina, G. van Hattem, H. Schut, M. Dickmann, W. Egger, C. Hugenschmidt, E. Brück, B. Dam, and S. W. H. Eijt, Formation of vacancies and metallic-like domains in photochromic rare-earth oxyhydride thin films studied by *in-situ* illumination positron annihilation spectroscopy, *Phys. Rev. Mater.* **6**, 065201 (2022).
- [11] F. Tuomisto, I. Makkonen, Defect identification in semiconductors with positron annihilation: Experiment and theory, *Rev. Mod. Phys.*, **85**, 1583 (2013).
- [12] M.J. Puska and R.M. Nieminen, Theory of positrons in solids and on solid surfaces, *Rev. Mod. Phys.*, **66**, 841 (1994).
- [13] C. Hugenschmidt, Positrons in surface physics, *Surf. Sci. Reports* **71**, 547 (2016).

- [14] J. Cizek, Characterization of lattice defects in metallic materials by positronannihilation spectroscopy: A review, *J. Mater. Sci. & Tech.* **34**, 577 (2018).
- [15] H. Schut, A Variable Energy Positron Beam Facility with Applications in Materials Science, Ph.D. thesis, Delft University of Technology, Delft, 1990.
- [16] A. van Veen, H. Schut, J. Devries, R. A. Hakvoort, and M. R. Ijpma, Analysis of positron profiling data by means of VEPFIT, *AIP Conf. Proc.* **218**, 171 (1990).
- [17] V.J. Ghosh, Positron implantation profiles in elemental and multilayer systems, *Appl. Surf. Sci.* **85**, 187 (1995).
- [18] A. Zubiaga, J. A. Garcia, F. Plazaola, F. Tuomisto, J. Zuniga-Perez, and V. Munoz-SanJose, Positron annihilation spectroscopy for the determination of thickness and defect profile in thin semiconductor layers, *Phys. Rev. B* **75**, 205305 (2007).
- [19] A. Wagner, M. Butterling, M. O. Liedke, K. Potzger, and R. Krause-Rehberg, Positron annihilation lifetime and doppler broadening spectroscopy at the ELBE facility, *AIP Conf. Proc.* **1970**, 040003 (2018).
- [20] E. Hirschmann, M. Butterling, U. H. Acosta, M. O. Liedke, A. G. Attallah, P. Petring, M. Görler, R. Krause-Rehberg, and A. Wagner, A new system for real-time data acquisition and pulse parameterization for digital positron annihilation lifetime spectrometers with high repetition rates, *J. Instrum.* **16**, P08001 (2021).
- [21] J. V. Olsen, P. Kirkegaard, and M. Eldrup, Analysis of positron lifetime spectra using the PALSfit3 program, *AIP Conf. Proc.* **2182**, 040005 (2019).
- [22] Reinhard Krause-Rehberg, Hartmut S. Leipner, *Positron Annihilation in Semiconductors - Defect Studies* (Springer-Verlag, Berlin, 1999).
- [23] S. Banerjee, D. Chaykina, R. Stigter, G. Colombi, S. W. H. Eijt, B. Dam, G. A. de Wijs, and A. P. M. Kentgens, Exploring multi-anion chemistry in yttrium oxyhydrides: Solid-state NMR studies and DFT calculations, *J. Phys. Chem. C* **127**, 14303 (2023).
- [24] J. Cízek, I. Procházka, F. Becvár, R. Kuzel, M. Cieslar, G. Brauer, W. Anwand, R. Kirchheim, and A. Pundt, Hydrogen-induced defects in bulk niobium, *Phys. Rev. B* **69**, 224106 (2004).
- [25] J. Cízek, I. Procházka, S. Daniš, G. Brauer and W. Anwand, R. Gemma, E. Nikitin, R. Kirchheim, A. Pundt, R.K. Islamgaliev, Hydrogen-vacancy complexes in electron-irradiated niobium, *Phys. Rev. B* **79**, 054108 (2009).
- [26] B. L. Shivachev, T. Troev, and T. Yoshiie, Positron lifetime computations of defects in nickel containing hydrogen or helium, *J. Nucl. Mater.* **306**, 105 (2002).
- [27] K. Sato, A. Hirozako, K. Ishibashi, Y. Miura, Q. Xu, M. Onoue, Y. Fukutoku, T. Onitsuka, M. Hatakeyama, S. Sunada, T. Yoshiie, Quantitative evaluation of hydrogen atoms trapped at single vacancies in tungsten using positron annihilation lifetime measurements: Experiments and theoretical calculations, *J. Nucl. Mater.* **496**, 9 (2017).

- [28] G. Colombi, R. Stigter, D. Chaykina, S. Banerjee, A. P.M. Kentgens, S. W.H. Eijt, B. Dam, and G. de Wijs, Energy, metastability, and optical properties of anion-disordered  $\text{REO}_x\text{H}_{3-2x}$  (RE = Y, La) oxyhydrides: a computational study, *Phys. Rev. B* **105**, 054208 (2022).
- [29] H. Leegwater, H. Schut, W. Egger, A. Baldi, B. Dam, and S. W. H. Eijt, Divacancies and the hydrogenation of mg-ti films with short range chemical order, *Appl. Phys. Lett.* **96**, 121902 (2010).
- [30] S. J. Tao, Positronium annihilation in molecular substances, *J. Chem. Phys.* **56**, 5499 (1972).
- [31] M. Eldrup, D. Lightbody, and J. N. Sherwood, The temperature-dependence of positron lifetimes in solid pivalic acid, *Chem. Phys.* **63**, 51 (1981).
- [32] D. Chaykina, T. de Krom, G. Colombi, H. Schreuders, A. Suter, T. Prokscha, B. Dam, and S. Eijt, Structural properties and anion dynamics of yttrium dihydride and photochromic oxyhydride thin films examined by *in situ*  $\mu^+\text{SR}$ , *Phys. Rev. B* **103**, 224106 (2021).
- [33] Y. Komatsu, R. Shimizu, R. Sato, M. Wilde, K. Nishio, T. Katase, D. Matsumura, H. Saitoh, M. Miyauchi, J. R. Adelman, R. M. L. McFadden, D. Fujimoto, J. O. Ticknor, M. Stachura, I. McKenzie, G.D. Morris, W. Andrew MacFarlane, J. Sugiyama, K. Fukutani, S. Tsuneyuki, and T. Hitosugi, Repeatable photoinduced insulator-to-metal transition in yttrium oxyhydride epitaxial thin films, *Chem. Mater.* **34**, 3616 (2022).
- [34] J. Chai, Z. Shao, H. Wang, C. Ming, W. Oh, T. Ye, Y. Zhang, X. Cao, P. Jin, S. Zhang, Y. Sun, Ultrafast processes in photochromic material  $\text{YH}_x\text{O}_y$  studied by excited-state density functional theory simulation, *Sci. China Mater.* **63**, 1579 (2020).
- [35] R. Stigter, A Computational Investigation on the Structure of Yttrium Oxyhydride Compounds and Their Anion Mobility, MSc thesis, Delft University of Technology, Delft, the Netherlands, 2020.
- [36] P. Hautojarvi, Defects in semiconductors-recent progress in positron experiments, *Mater. Sci. Forum* **175**, 47 (1995).
- [37] G. Brauer, W. Anwand, P. G. Coleman, J. Stormer, F. Plazaola, J. M. Campillo, Y. Pacaud, and W. Skorupa, Post-implantation annealing of SiC studied by slow-positron spectroscopies, *J. Phys.-Condens Mat.* **10**, 1147 (1998).
- [38] This value is calculated based on the composition  $\text{YH}_2\text{O}_{0.5}$ . In this composition, three of the six closest octahedral sites of yttrium are occupied by hydrogen. Assuming that 10% of the octahedral hydrogen from all previously occupied octahedral sites is removed, the probability of removing one of the three hydrogen atoms from the nearest neighbour octahedral sites of the yttrium is approximately 25% ( $1 - 0.9^3 \approx 0.27$ ).
- [39] J. Montero, F. A. Martinsen, M. Garcia-Tecedor, S. Z. Karazhanov, D. Maestre, B. Hauback, and E. S. Marstein, Photochromic mechanism in oxygen-containing yttrium hydride thin films: An optical perspective, *Phys. Rev. B* **95**, 201301(R) (2017).

- [40] K. Fukui, S. Limura, T. Tada, S. Fujitsu, M. Sasase, H. Tamatsukuri, T. Honda, K. Ikeda, T. Otomo, H. Hosono, Characteristic fast H ion conduction in oxygen-substituted lanthanum hydride, *Nat. Commun.* **10**, 2578 (2019).
- [41] K. Fukui, S. Imura, J. J. Wang, T. Tada, T. Honda, K. Ikeda, T. Otomo, and H. Hosono, Stabilization factor of anion-excess fluorite phase for fast anion conduction, *Chem. Mater.* **33**, 1867 (2021).
- [42] J. Crank, *The mathematics of diffusion* (Oxford University Press, London, 1975), second edition.
- [43] E. Haurat, J. P. Crocombette, T. Schuler, and M. Tupin, Hydrogen diffusion coefficient in monoclinic zirconia in presence of oxygen vacancies, *Int. J. Hydrogen Energy* **47**, 33517 (2022).
- [44] N. Fernandez, Y. Ferro, and D. Kato, Hydrogen diffusion and vacancies formation in tungsten: Density functional theory calculations and statistical models, *Acta Mater.* **94**, 307 (2015).
- [45] A. Bikowski and K. Ellmer, A comparative study of electronic and structural properties of polycrystalline and epitaxial magnetron-sputtered ZnO:Al and  $\text{Zn}_{1-x}\text{Mg}_x\text{O:Al}$  films-Origin of the grain barrier traps, *J. Appl. Phys.* **114**, 063709 (2013).
- [46] C. Mitra, P. Raychaudhuri, J. John, S. K. Dhar, A. K. Nigam, and R. Pinto, Growth of epitaxial and polycrystalline thin films of the electron doped system  $\text{La}_{1-x}\text{Ce}_x\text{MnO}_3$  through pulsed laser deposition, *J. Appl. Phys.* **89**, 524 (2001).
- [47] K. Hayashi, Kinetics of electron decay in hydride ion-doped mayenite, *J. Phys. Chem. C* **115**, 11003 (2011).
- [48] K. Hayashi, P. V. Sushko, Y. Hashimoto, A. L. Shluger, and H. Hosono, Hydride ions in oxide hosts hidden by hydroxide ions, *Nat. Commun.* **5**, 3515 (2014).
- [49] K. Hayashi, S. Matsuishi, T. Kamiya, M. Hirano, and H. Hosono, Light-induced conversion of an insulating refractory oxide into a persistent electronic conductor, *Nature* **419**, 462 (2002).

## Supplementary information for Chapter 3

### Positron fractions as a function of implantation energy for $\text{YH}_x\text{O}_y$ and $\text{GdH}_x\text{O}_y$ films

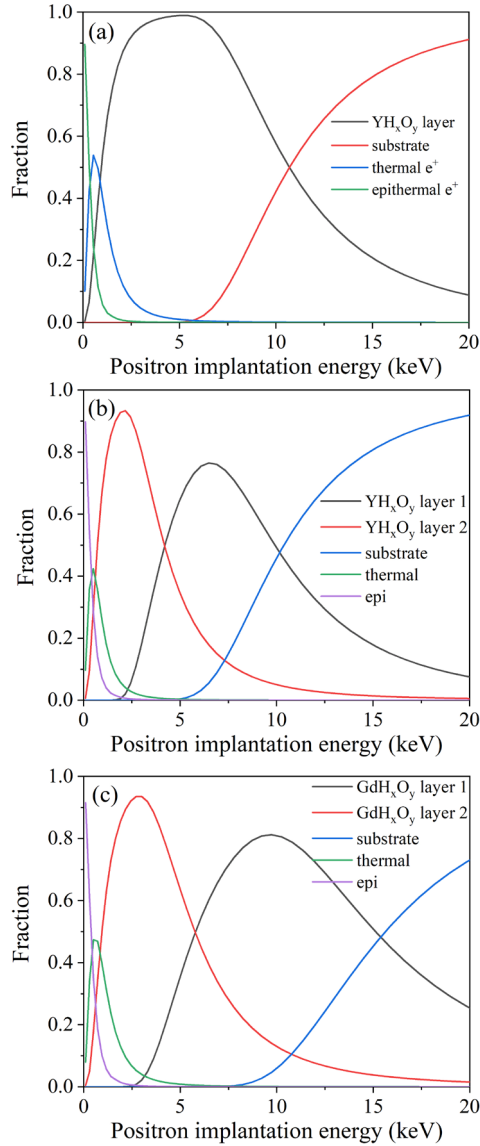


Figure S3.1: The fractions of positrons annihilating in each layer in the  $\text{YH}_x\text{O}_y$  and  $\text{GdH}_x\text{O}_y$  films as a function of positron implantation energy derived by VEPFIT analysis, using a (a) one-layer or (b) two-layer model for  $\text{YH}_x\text{O}_y$  layer, and (c) a two-layer model for  $\text{GdH}_x\text{O}_y$  layer.

### Derivation of the bleaching time constant

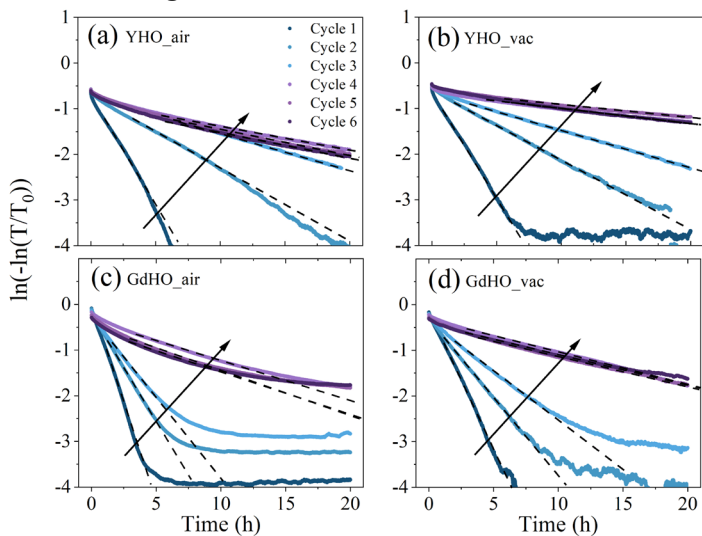


Figure S3.2: The natural logarithm of the negative natural logarithm of the normalized optical transmittance as a function of bleaching time, and corresponding linear best fits (dashed lines) used to derive the bleaching time constant according to equation (2).

### Time evolution of the W-parameter upon photodarkening-bleaching cycling

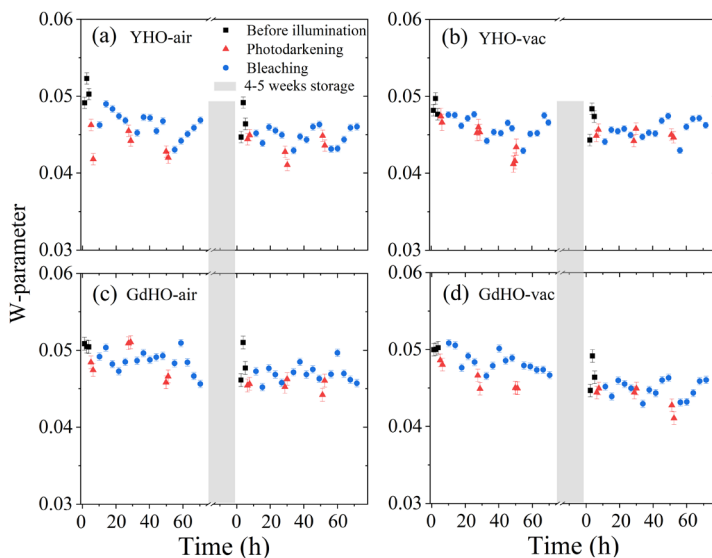


Figure S3.3: Time evolution of W-parameter at a positron implantation energy of 5.5 keV for (a) YHO-air and (b) YHO-vac, and at a positron implantation energy of 10 keV for (c) GdHO-air, and (d) GdHO-vac under six photodarkening(red)-bleaching(blue) cycles, including an intermediate storage period of 4-5 weeks under ambient or vacuum conditions (grey region).

## DB-PAS depth profiles and VEPFIT analyses

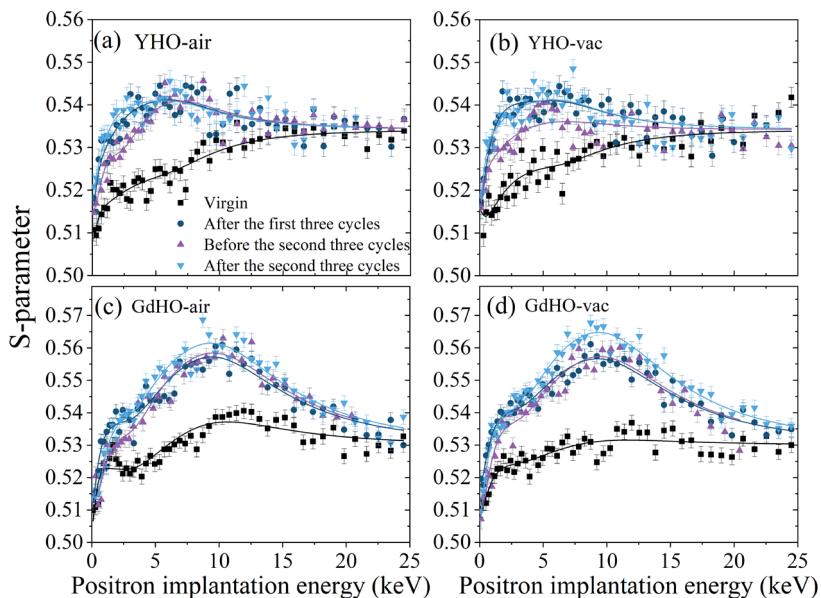


Figure S3.4: DB-PAS depth profiles of (a) YHO-air, (b) YHO-vac, (c) GdHO-air and (d) GdHO-vac in the virgin state (black color), after the first three photodarkening-bleaching cycles (dark blue color), before the second three cycles (purple color) and after the second three cycles (light blue color).

Fig. S3.4 shows the DB-PAS S-parameter depth profiles for all four samples (a) YHO-air, (b) YHO-vac, (c) GdHO-air, and (d) GdHO-vac in the virgin state, after the first three cycles, before the second three cycles, and after the second three cycles. In order to minimize the number of fit parameters, the S-parameter, W-parameter of the fused-SiO<sub>2</sub> substrate layer were fixed to 0.5325, 0.059, as extracted from the high implantation energy range (20-25 keV). The density and diffusion length ( $L_d$ ) of the fused-SiO<sub>2</sub> substrate layer were fixed to 2.2 g/cm<sup>3</sup>, and 25 nm. According to VEPFIT analysis of the depth profiles after the first three cycles, the thickness ( $d$ ) of the oxyhydride layer of the YH<sub>x</sub>O<sub>y</sub> samples is 360 nm, so the layer thicknesses were fixed at this value for the depth profiles collected at the other stages of cycling. For the YHO-air sample before the second three cycles, the S-parameter of the bulk oxyhydride layer (at 5 keV) seems to be unchanged while the S-parameter of the oxyhydride layer near the surface region decreases, so an additional near-surface layer was added to the model. The thicknesses of the near-surface oxyhydride layer and bulk oxyhydride layer are noted as  $d_1$  and  $d_2$ , respectively. For the GdH<sub>x</sub>O<sub>y</sub> samples, in addition to the bulk oxyhydride layer (at 10 keV), an additional much thinner oxyhydride layer near the surface region below 5 keV for each depth profile is seen, therefore a two-layer model for the

Gadolinium oxyhydride layer is utilized. According to VEPFIT analysis of the depth profile after the first three cycles, the thickness of the near-surface and bulk oxyhydride layer of the  $\text{GdH}_x\text{O}_y$  samples are 60 nm and 360 nm, so the total thickness is 420 nm. The layer thicknesses were fixed at these values for the rest of the depth profiles of  $\text{GdH}_x\text{O}_y$  samples, assuming the thickness of the near-surface layer remains the same at other stages of cycling. A density of  $4.3 \text{ g/cm}^3$  and  $7.2 \text{ g/cm}^3$  was used for the  $\text{YH}_x\text{O}_y$  and  $\text{GdH}_x\text{O}_y$  oxyhydride layers, respectively. A two- or three-layer model (including one layer for the semi-infinite substrate layer) was used in the VEPFIT analysis. The corresponding results of the best-fit analysis are shown in Table S3.1-S3.4.

Table S3.1: The best-fit parameters of DB-PAS depth profiles for the oxyhydride layer of YHO-air in the virgin state, after the first three cycles, before the second three cycles and after the second three cycles.

State	Near-surface oxyhydride layer			Bulk oxyhydride layer			
	$d1$ (nm)	S1	W1	$d2$ (nm)	S2	W2	$L_{d2}$ (nm)
Virgin state	-	-	-	360	0.525 (1)	0.0478 (5)	60 (3)
After the first 3 cycles	-	-	-	360	0.542 (1)	0.0458 (3)	30 (2)
Before the second 3 cycles	60 (5)	0.529 (1)	0.0504 (3)	300	0.544 (1)	0.0431 (3)	30 (3)
After the second 3 cycles	-	-	-	360	0.541 (1)	0.0468 (3)	15 (1)

Table S3.2: The best-fit parameters of DB-PAS depth profiles for the oxyhydride layer of YHO-vac in the virgin state, after the first three cycles, before the second three cycles and after the second three cycles.

State	$d$ (nm)	S	W	$L_d$ (nm)
Virgin state	360	0.526 (1)	0.0480 (5)	30 (2)
After the first 3 cycles	360	0.541 (1)	0.0461 (3)	10 (1)
Before the second 3 cycles	360	0.537 (1)	0.0475 (2)	37 (3)
After the second 3 cycles	360	0.542 (1)	0.0484 (3)	30 (1)

Table S3.3: The best-fit parameters of DB-PAS depth profiles for the oxyhydride layer of  $\text{GdHO}$ -air in the virgin state, after the first three cycles, before the second three cycles and after the second three cycles.

State	Near-surface oxyhydride layer			Bulk oxyhydride layer			
	$d1$ (nm)	S1	W1	$d2$ (nm)	S2	W2	$L_{d2}$ (nm)
Virgin state	60	0.522 (1)	0.0551 (3)	360	0.545 (1)	0.0460 (5)	70 (3)
After the first 3 cycles	60	0.538 (1)	0.0505 (3)	360	0.565 (1)	0.0433 (3)	45 (2)
Before the second 3 cycles	60	0.534 (1)	0.0503 (3)	360	0.564 (1)	0.0436 (3)	30 (2)
After the second 3 cycles	60	0.540 (1)	0.0502 (3)	360	0.567 (1)	0.0451 (3)	30 (2)



Table S3.4: The best-fit parameters of DB-PAS depth profiles for the oxyhydride layer of GdHO-vac in the virgin state, after the first three cycles, before the second three cycles and after the second three cycles.

State	Near-surface oxyhydride layer			Bulk oxyhydride layer			$L_{d2}$ (nm)
	$d1$ (nm)	S1	W1	$d2$ (nm)	S2	W2	
Virgin state	60	0.525 (1)	0.0533 (3)	360	0.534 (1)	0.0486 (3)	60 (5)
After the first 3 cycles	60	0.539 (1)	0.0489 (3)	360	0.565 (1)	0.0454 (3)	48 (2)
Before the second 3 cycles	60	0.542 (1)	0.0504 (3)	360	0.563 (1)	0.0447 (3)	48 (2)
After the second 3 cycles	60	0.542 (1)	0.0506 (3)	360	0.571 (1)	0.0441 (3)	33 (2)

When assuming a (reasonable) value for the positron diffusion coefficient  $D_+$  of  $\sim 1 \text{ cm}^2/\text{s}$  at room temperature [1,2], and taking into account the bulk positron lifetime of  $\tau_{\text{bulk}} \sim 240 \text{ ps}$  in the  $\text{YH}_x\text{O}_y$  films [2], the bulk positron diffusion length  $L_{\text{bulk}}$  in defect-free  $\text{YH}_x\text{O}_y$  can be estimated, according to  $L_{\text{bulk}} = \sqrt{D_+ \tau_{\text{bulk}}} = \sqrt{1 \times 240 \times 10^{-12} \times 10^7} \text{ nm} \approx 150 \text{ nm}$  [3]. If the vacancy concentration  $C_d$  is near the upper limit of saturated trapping, e.g. on the order of  $10^{-4}$  [2-4], the effective positron diffusion length  $L_+$  can be estimated to be around 30 nm, according to  $k_d = \mu C_d = D_+ \left( \frac{1}{L_+^2} - \frac{1}{L_{\text{bulk}}^2} \right)$ , assuming the positron trapping coefficient  $\mu$  is  $1 \times 10^{15} \text{ s}^{-1}$  [2,3].

### Positron lifetime calculation methods

We employed the self-consistent two-component density functional theory (TCDFT) calculations in the open-source ABINIT package to calculate the positron bulk lifetime and the positron lifetime of yttrium monovacancies in  $\text{YH}_{2.5}\text{O}_{0.25}$  [5,6]. The positron lifetime of yttrium vacancies were calculated after complete lattice relaxation. Calculations were performed with the  $Fm\bar{3}m$  structure of  $\text{YH}_{2.5}\text{O}_{0.25}$  using a  $2 \times 2 \times 2$  supercell containing 120 atoms. The atomic configurations were produced using the ATOMPAW code [7]. The ground states of electrons and the positron were calculated by the projector augmented wave (PAW) method. The exchange-correlation interactions were described by the local density approximation (LDA) and the generalized gradient approximation (GGA). For LDA, we employed the Teter-Pade parametrization [8] and the Zero-positron density limit of Arponen and Pajanne, as implemented by Boronski and Nieminen [9]. For the GGA calculations, the Perdew-Burke-Ernzerhof functional [10] was combined with the same exchange-correlation functionals as we used for LDA, supplemented by correction terms provided by Barbiellini et al. [8]. All positron lifetimes were calculated using the enhancement factor given by Boronski and Nieminen in the random phase approximation (RPA) limit [9].

## X-ray diffraction

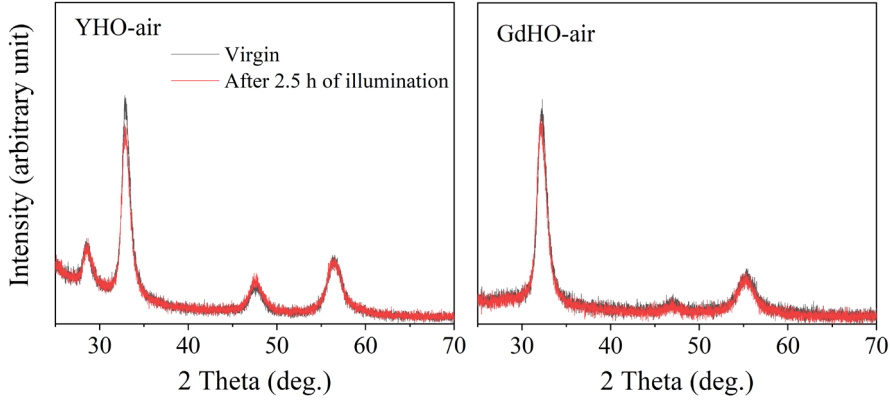


Figure S3.5: X-ray diffraction patterns of the YHO-air and GdHO-air samples before and after illumination for 2.5 h.

3

The average size of grains was estimated from the peak width of an x-ray diffraction peak using Scherrer's equation  $d_{\text{grain}} = \frac{k\lambda}{\beta_{\text{sample}} \cos \theta}$  and  $\beta_{\text{sample}} = \sqrt{\beta_{\text{total}}^2 - \beta_{\text{instrument}}^2}$ , where  $d_{\text{grain}}$  is the average grain size in nm,  $\lambda$  is the x-ray wavelength in nm,  $\theta$  is the diffraction angle, and  $k$  is the Scherrer's constant, here we used 0.94 for a cubic structure,  $\beta_{\text{total}}$  is the full width half maximum (FWHM, in radians) of the diffraction peak at  $\sim 33^\circ$  (200) in our case,  $\beta_{\text{instrument}}$  is extracted from an independent XRD measurement on a single crystal silicon sample. The average grain size for the YHO-air sample in the virgin state and the state right after 2.5 h illumination is  $8 \pm 0.5$  nm and  $8 \pm 0.5$  nm. The average grain size for the GdHO-air sample in the virgin state and the state immediately after 2.5 h illumination is  $7 \pm 0.5$  nm and  $7 \pm 0.5$  nm. In this analysis, other factors that may also cause the peak broadening, for instance, strain are not included.

## References

- [1] F. Tuomisto, I. Makkonen, Defect identification in semiconductors with positron annihilation: Experiment and theory, *Rev. Mod. Phys.*, **85**, 1583 (2013).
- [2] Z. Wu, T. de Krom, G. Colombi, D. Chaykina, G. van Hattem, H. Schut, M. Dickmann, W. Egger, C. Hugenschmidt, E. Brück, B. Dam, and S. W. H. Eijt, Formation of vacancies and metallic-like domains in photochromic rare-earth oxyhydride thin films studied by *in-situ* illumination positron annihilation spectroscopy, *Phys. Rev. Mater.* **6**, 065201 (2022).
- [3] Reinhard Krause-Rehberg, Hartmut S. Leipner, *Positron Annihilation in Semiconductors - Defect Studies* (Springer-Verlag, Berlin, 1999).
- [4] M.J. Puska and R.M. Nieminen, Theory of positrons in solids and on solid surfaces, *Rev. Mod. Phys.*, **66**, 841 (1994).
- [5] M. Torrent, F. Jollet, F. Bottin, G. Zérah, X. Gonze, Implementation of the projector augmented-wave method in the ABINIT code: Application to the study of iron under pressure, *Comput. Mater. Sci.*, **42**, 337 (2008).
- [6] B. Barbiellini, M. J. Puska, T. Torsti, and R. M. Nieminen, Gradient correction for positron states in solids, *Phys. Rev. B* **51**, 7341 (1995).
- [7] N. A. W. Holzwarth, A. R. Tackett, and G. E. Matthews, A Projector Augmented Wave (PAW) code for electronic structure calculations, Part I: atompaw for generating atom-centered functions, *Comput. Phys. Commun.* **135**, 329 (2001).
- [8] S. Goedecker, M. Teter, and J. Hutter, Separable dual-space gaussian pseudopotentials, *Phys. Rev. B* **54**, 1703 (1996).
- [9] E. Boronski and R. M. Nieminen, Electron-positron density-functional theory, *Phys. Rev. B* **34**, 3820 (1986).
- [10] J. P. Perdew, K. Burke, and M. Ernzerhof, Generalized gradient approximation made simple, *Phys. Rev. Lett.* **77**, 3865 (1996).



**4. Time dependent evolution of vacancies and metallic domains and their correlation with the photochromic effect in yttrium oxyhydride films revealed by in-situ illumination positron annihilation lifetime spectroscopy**

## Abstract

The photodarkening and bleaching processes in photochromic yttrium oxyhydride thin films were studied by in-situ UV illumination positron annihilation lifetime spectroscopy (PALS) in order to gain insights into the time evolution of open-volume defects and metallic domains. The PALS depth profiles before and after a photodarkening-bleaching cycle revealed a light-induced increase in open-volume defects, that occurs homogeneously throughout the oxyhydride layer. The time-dependent PALS measurements show that upon photodarkening, a fast initial formation of metallic domains occurs, as well as a fast release of loosely-bounded hydrogen from vacancy clusters and nanopores. During further photodarkening, the concentration of divacancy-like defects gradually increases due to the aggregation of light-induced hydrogen vacancies with pre-existing yttrium monovacancies. After the UV illumination is stopped, two subsequent bleaching phases are observed. During the first bleaching phase, a strong correlation between the shortest positron lifetime  $\tau_1$  and the photochromic contrast is seen in both samples, suggesting that metallic domains disappear and, correspondingly, that positron trapping at yttrium monovacancies and divacancy-like defects increases. During the second bleaching phase, a subsequent correlation between  $\tau_1$  and the photochromic contrast is observed in the more H-rich sample, related to the disappearance of larger metallic domains. After bleaching, most of the metallic domains and the photoexcited electrons in the matrix have disappeared, while the formed small vacancy complexes and larger vacancies remain stable.

## 4.1 Introduction

Yttrium oxyhydride ( $\text{YH}_x\text{O}_y$ ) thin films have attained increasing attention because of their color-neutral photochromic effect at ambient conditions, since the first report of the photochromism in yttrium oxyhydride thin films in 2011 [1].  $\text{YH}_x\text{O}_y$  films are transparent semiconductors, they can be darkened when subjected to photons with above-bandgap energies, causing a reduction in the transmittance in a broad range from visible to near IR. When the light is switched off, the transmittance bleaches back to its original state. So far, rare-earth (RE) including Y, Gd, Sc, Nd, Dy, Er, and Sm oxyhydride thin films have been discovered to exhibit the photochromic effect [2-7]. The tuneable photochromic properties, adjustable bandgap and the presence of photoconductivity make these photochromic films promising for applications in smart windows [7,8], memory devices [9], and photo-catalysts [10].

However, the mechanism of the photochromic effect is still not fully clarified and a comprehensive understanding of the corresponding microstructural and electronic structure changes during photodarkening and bleaching is still lacking. By modelling optical spectroscopic ellipsometry data, Montero et al. [11] proposed that hydride-like metallic domains are formed in a semiconducting  $\text{YH}_x\text{O}_y$  matrix with a volume fraction of up to 6 % upon illumination. The formation of metallic domains was supported by a magnetic susceptibility study on Gd oxyhydride films in [12], where a reversible increase in the Curie-Weiss temperature for the photodarkened state was observed. In addition, a nuclear magnetic resonance study on RE oxyhydride films (RE = Y and Sc) suggested that the photodarkening process is accompanied by a reduction of  $\text{RE}^{3+}$  to  $\text{RE}^{2+}$  [13]. Indeed, a previous positron annihilation study [14] showed (partially) reversible shifts in the positron Doppler-broadening S-W values in the direction towards the metal dihydride upon illumination in both  $\text{YH}_x\text{O}_y$  and  $\text{GdH}_x\text{O}_y$  films, suggesting the reversible formation of metallic nanodomains with a valence change from  $\text{RE}^{3+}$  to  $\text{RE}^{2+}$ . On the other hand, irreversible shifts in S-parameters to a higher value and W-parameter to a lower value after a photodarkening-bleaching cycle were also observed in both  $\text{YH}_x\text{O}_y$  and  $\text{GdH}_x\text{O}_y$  [14]. These irreversible shifts in S-parameter were found to correlate strongly with the bleaching time constant extracted from optical transmittance upon photodarkening-bleaching cycling, particularly for the first three cycles, suggesting that the microstructural changes corresponding to the slower bleaching upon cycling involve vacancy aggregation [15]. This was supported by PALS measurements before and after one cycle that suggests the irreversible formation of divacancy-like defects and growth of vacancy clusters due to the aggregation of light-induced hydrogen vacancies with the preexisting yttrium monovacancies and vacancy clusters [15]. The formation of vacancies is consistent with the observed release of hydrogen gas from  $\text{YH}_x\text{O}_y$  films during illumination, supporting the mobility of hydrogen liberated by the illumination [16]. However, it remains largely unknown how microstructure and electronic structure evolve in time during photodarkening and bleaching in RE oxyhydride films.

Positron annihilation lifetime spectroscopy (PALS) is a well-known non-destructive tool to identify and quantify open-volume defects at a nanometer-sized scale, providing information on the size and the concentration of open-volume defects. Due to the capability of relative fast measurement (in the order of minutes), PALS has been employed to investigate vacancy dynamics in niobium during thermal annealing [17] and in hydrogen-charged nickel during aging at room temperature [18], and to examine the kinetics of vacancy clustering and precipitation during natural aging in Al-Mg-Si alloys [19]. It has also been applied to study the dynamic changes of the charge state of vacancy clusters after switching off the illumination in diamond [20]. In addition, our previous Doppler broadening positron annihilation spectroscopy (DB-PAS) study suggested that preferred positron trapping at metallic nanodomains occurs during illumination [14]. Indeed, if the positron affinity of the metallic nanodomains is different from the matrix, preferential positron trapping at nanometallic domains could occur, as has been observed in Li, Au, and Kr nanoclusters embedded in MgO [21-24], and in Cu nanoparticles embedded in Fe [25]. The preferential trapping at nanodomains could potentially increase the intensity of the corresponding positron lifetime component. For instance, in the Li-doped MgO system, the trapping rate and the intensity of positron annihilation at  $\text{Li}_2\text{CO}_3$  precipitates increases almost linearly with the doping concentration of Li [26]. If the positron lifetime in a metallic domain is different from that of the surrounding matrix, the formation of metallic domains will change the positron lifetime. Therefore, PALS may provide essential information on the evolution of metallic domains and open-volume defects during photodarkening and bleaching.

In this study, we employed in-situ illumination PALS measurements on two photochromic yttrium oxyhydride films to investigate 1) the time-evolution of the metallic domains and open-volume defects before illumination, during photodarkening and subsequent bleaching; 2) the presence and nature of vacancy defects as a function of implantation energy (mean positron probe depth) before illumination and after bleaching. The PALS depth profiles show that there is no significant depth dependence of the vacancy defect distribution in the oxyhydride layer. The time-dependent PALS demonstrates a distinct behaviour of the positron lifetime and intensity of each annihilation component in the PALS spectra during photodarkening and bleaching, providing key insights into the evolution of open-volume defects and metallic domains. This study deepens our understanding of the photochromism and the memory effect in yttrium oxyhydride films, and provides a method to study light-induced local structural changes at a nanometer scale and electronic changes in other photochromic polycrystalline films.

## 4.2 Experimental

### 4.2.1 Sample preparation



Two types of yttrium dihydride thin films (YHO-1 and YHO-2) were deposited on unheated fused silica substrates ( $1 \times 1 \text{ cm}^2$ ) by reactive magnetron sputtering in an  $\text{Ar}/\text{H}_2$  (at a ratio of 7:1) atmosphere and the deposition pressure was maintained at 0.5 Pa during sputtering [2]. The direct current power supplied to a yttrium target was 100 W and 200 W for YHO-1 and YHO-2 thin-film samples, respectively. The as-deposited yttrium dihydride thin films were then oxidized by exposure to an ambient environment. An oxyhydride phase was formed during the post-oxidation process, in which at least five days were given to reach a stable composition [27]. The thickness of the oxyhydride layer in YHO-1 and YHO-2 samples was determined by profilometry to be 400 and 420 nm, with an uncertainty of  $\sim 10\%$ . The same deposition method as for the YHO-1 samples was used with a second yttrium target for preparing YHO-a film samples employed in the second PALS measurement at HZDR. The thickness of the oxyhydride layer in the YHO-a film samples was  $\sim 350 \text{ nm}$ .

#### 4.2.2 Optical properties

The optical transmittance of the yttrium oxyhydride film samples was measured in the wavelength range of 230–1120 nm using a custom-built optical fiber-based spectrometer [27]. A narrow band LED (385 nm,  $I = 30 \text{ mW/cm}^2$ ) was employed as the light source to trigger the photochromic effect. The indirect optical bandgap energy of YHO-1, YHO-2, and YHO-a film samples was determined to be 2.49, 2.42, and 2.49 eV using a Tauc-plot method [27, 28].

#### 4.2.3 Positron annihilation lifetime spectroscopy (PALS)

When implanted into a solid, a positron will collide with the atoms and lose its kinetic energy via electron excitations and interactions with the lattice. After a few picoseconds, the positron is thermalized with an energy of a few tens of meV. The thermalized positron diffuses through the host lattice until annihilation occurs in a defect-free environment or until it finds an open-volume defect. Open-volume defects such as negatively charged or neutral vacancies preferentially trap positrons due to the lack of Coulomb repulsion of the ion cores. If the size of open-volume defects is sufficiently large, positronium, a bound state of a positron and an electron, can form. The positron lifetime depends on the local electron density at the annihilation site. The lifetime of a positron annihilating in the defect-free bulk state can vary from about 140 to 280 ps in semiconductors [29,30]. An increase in the size of open-volume defects will decrease the local electron density and thus increase the positron lifetime. The lifetime of ortho-positronium (a bound state of an electron and a positron, with spin  $S=1$ ) in semiconductors is typically in the order of nanoseconds due to pick-off annihilation [30]. PALS can therefore be applied to examine the presence of open volume defects and their size.

PALS measurements were performed at the Mono-energetic Positron Source (MePS) beamline, which is one of the end stations of the ELBE (Electron Linac for beams with high Brilliance and low Emittance) facility at Helmholtz-Zentrum Dresden-Rossendorf, Germany

[31]. Approximately  $10^7$  counts were collected for each spectrum. Thanks to the high flux low energy positron beam, the acquisition time for one spectrum is about three minutes, enabling monitoring the microstructural changes at this time resolution. A CeBr<sub>3</sub> scintillator detector coupled to a Hamamatsu R13089-100 photomultiplier (PMT) tube was utilized for gamma quanta acquisition and the signals were processed by the SPDevices ADQ14DC-2X digitizer (14-bit vertical resolution and 2 GS/s horizontal resolution) [32]. The instrument time resolution was estimated to be  $\sim 250$  ps by determination of the PALS spectrum of a reference amorphous Yttria stabilized zirconia (YSZ) sample with a single well-defined lifetime component. The positron lifetime spectra were analyzed by the convolution between

the sum of  $N$  exponential decays  $\sum_{i=1}^N \frac{I_i}{\tau_i} \exp(-t / \tau_i)$  and the time resolution function  $R(t)$  of the spectrometer superimposed onto a constant background  $bkg$ , namely:

$$Z(t) = R(t) \otimes \sum_{i=1}^N \frac{I_i}{\tau_i} \exp(-t / \tau_i) + bkg$$

where  $\tau_i$  is the positron lifetime in state  $i$  and  $I_i$  is the corresponding intensity.

A three-component analysis was applied to decompose all positron lifetime spectra using the PALSfit3 program [33]. The average lifetime  $\tau_{ave}$  is calculated as follows:

$$\tau_{ave} = \sum_{i=1}^N \tau_i I_i (i = 3), \quad I_1 + I_2 + I_3 = 1$$

When the average lifetime exceeds the positron lifetime in the (defect-free) bulk material, it indicates the presence of open volume defects.

For the in-situ illumination PALS measurements, an ultraviolet (UV) laser source ( $\sim 375$  nm) with a comparable intensity to the abovementioned LED was utilized. Using a custom-built beam expander consisting of three optical lenses, the diameter of the UV spot at the sample position was around 1.5 cm.

## 4.3 Results and discussion

### 4.3.1 Photochromic properties

The photochromic properties of YHO-1 and YHO-2 thin-film samples were examined by illuminating the film with UV light (3.2 eV) for 2 h. Fig. 4.1 shows the transmittance  $T$  (averaged from 450 to 1000 nm) before illumination, during 2 h UV illumination (photodarkening), and the subsequent bleaching, normalized to the initial averaged transmittance  $T_0$ . For both yttrium oxyhydride thin-film samples, the transmittance reduces significantly during the first few minutes upon photodarkening and tends to stabilize with longer illumination time. The difference between the transmittance in virgin state  $T_0$  and the

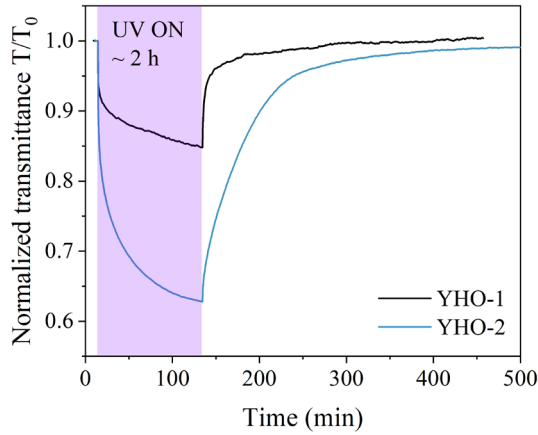


**Figure 4.1:** Optical transmittance normalized to the initial transmittance ( $T/T_0$ ), averaged in the wavelength range of 450-1000 nm before illumination, during ~2 h ultraviolet (UV) illumination (purple shaded region), and during subsequent bleaching for YHO-1 and YHO-2 thin-film samples.

transmittance at a time  $T$ , with respect to  $T_0$ , is defined as the photochromic contrast  $((T_0 - T)/T_0)$ . After 2 h of UV illumination, the photochromic contrast reaches 15% and 37% for YHO-1 and YHO-2 samples, respectively. When the UV light is switched off, the transmittance starts to increase, and it can fully recover after bleaching for several hours. Comparing the two thin-film samples, a lower contrast and a faster bleaching rate were found for the YHO-1 sample. It is likely that compared to the YHO-2 sample, the dihydride phase of the YHO-1 sample deposited at a lower deposition power has a higher porosity [34], enabling the absorption of more oxygen into the film during air oxidation, thus resulting in a higher O:H ratio in the YHO-1 sample. Indeed, the higher O:H ratio could explain the higher bandgap of the YHO-1 sample [27]. Furthermore, according to an ideal (model) face-center-cubic motif of yttrium oxyhydrides, the film with a higher O:H ratio has fewer hydrogen atoms at the octahedral sites [3], which is responsible for the lower contrast and faster bleaching of the YHO-1 sample [27,35], supposing that the release of octahedral hydrogen from its lattice position is a key factor for the photochromic effect.

#### 4.3.2 In-situ illumination positron lifetime experiments

In-situ illumination PALS measurements were performed on YHO-1 and YHO-2 thin-film samples to investigate the evolution of open-volume defects and metallic domains during a photodarkening-bleaching cycle. Here, the UV illumination time for both samples is the same as in the transmittance measurements, i.e. 2 h. For the YHO-1 sample, the time monitoring the bleaching process is around 2.8 h, when the photodarkened film is nearly fully bleached.

For the YHO-2 sample, the bleaching monitoring time for in-situ PALS is 1.5 h, where photochromic contrast recovers by more than 80%.

#### 4.3.2.1 PALS depth profiles before illumination and after photodarkening and bleaching

PALS depth profiles were collected in a positron implantation energy range from 0.5 up to 9 keV to monitor the open-volume defects as a function of positron implantation energy in YHO-1 and in YHO-2 thin-film samples before illumination and after bleaching.  $\tau_{\text{ave}}$  is a robust parameter and rather insensitive to fitting procedures, leading to an accuracy within about 1 ps. Fig. 4.2 (a) and (b) show the average positron lifetime ( $\tau_{\text{ave}}$ ) as a function of positron implantation energy for both samples before illumination (grey squares), extracted

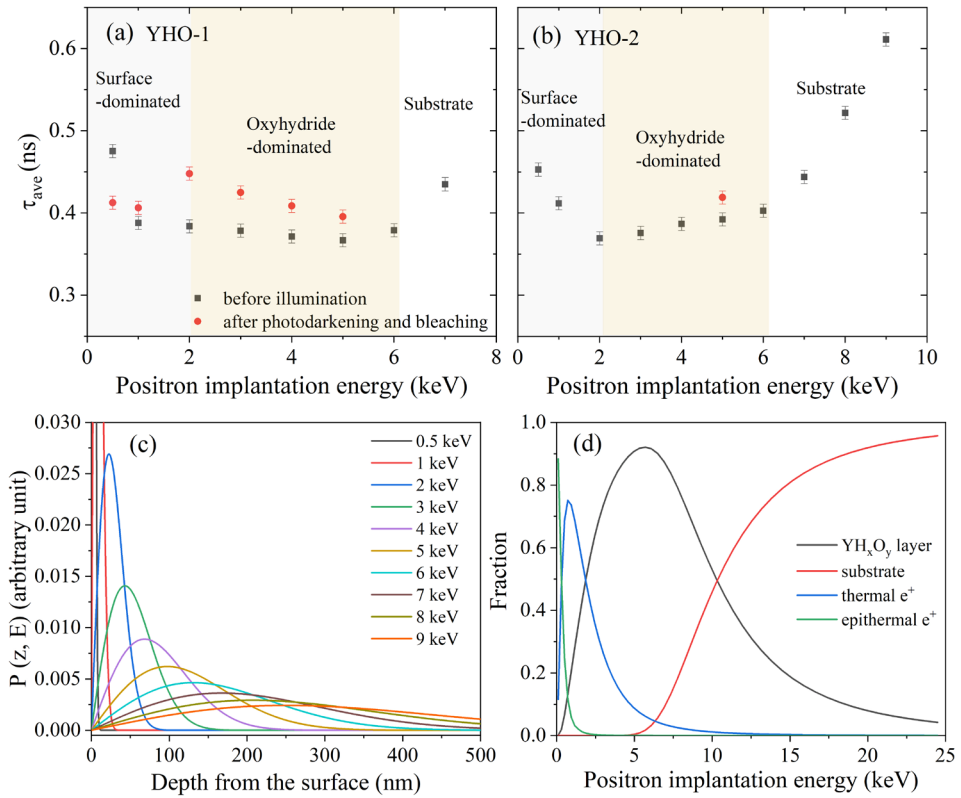


**Figure 4.2:** The average positron lifetimes ( $\tau_{\text{ave}}$ ) as a function of positron implantation energy for (a) YHO-1 and (b) YHO-2 thin-film samples before illumination (grey squares) as well as after 2 h photodarkening and  $\sim 2.8$  h bleaching for the YHO-1 sample and  $\sim 1.5$  h bleaching for the YHO-2 sample (red circles), as well as (c) Makhovian positron implantation profiles for implantation energies from 0.5 keV to 9 keV for both  $\text{YH}_x\text{O}_y$  samples, and (d) the fractions of positrons annihilating in each layer for the YHO-1 film sample as a function of positron implantation energy derived by VEPFIT analysis.

from a three-component analysis of the positron lifetime spectra collected in PALS depth profiling measurements. Fig. 4.2 (a) also shows the  $\tau_{\text{ave}}$  a function of positron implantation energy after bleaching (red circles) for the YHO-1 sample, while in Fig. 4.2 (b) the data point of  $\tau_{\text{ave}}$  at 5 keV after bleaching (red circle) for the YHO-2 sample is shown for comparison, extracted from the time-dependent measurement performed at 5 keV (see section 4.3.2.2).

Before illumination, the  $\tau_{\text{ave}}$  values for both films are fairly constant in the range of 2-6 keV, while the values below 2 keV and above 6 keV are typically higher. Positrons with a higher energy can probe deeper into the materials. The positron implantation profiles in a material with density  $\rho$  in  $\text{g/cm}^3$  are described by Makhovian implantation profiles:

$$P(z, E) = \frac{mz^{m-1}}{z_0^m} \exp \left[ - \left( \frac{z}{z_0} \right)^m \right] \quad (4.1)$$

with  $m=2$ ,  $z$  the implantation depth, and  $z_0=1.13\bar{z}$ , with  $\bar{z}$  the mean implantation depth in nm, is a function of the positron implantation energy  $E$  in keV according to  $z_0(E)=\frac{AE^n}{\rho}$ , and we used  $n=1.6$  and  $A=4 \mu\text{g cm}^{-2} \text{keV}^{-n}$  [36,37], and  $\rho=4.3 \text{ g/cm}^3$  for  $\text{YH}_x\text{O}_y$ , respectively.

As seen in Fig. 4.2 (c), positrons at an implantation energy of about 6 keV starts to probe the region deeper than 400 nm. Hence, with increasing implantation energy above 6 keV, the increase in the average lifetime steadily results from the increased contribution from the substrate ( $> \sim 400$  nm). This is consistent with the VEPFIT analysis of the DB-PAS depth profiles for the YHO-1 sample: Fig. 4.2 (d) shows that the derived fraction of positrons annihilating in the substrate layer starts to increase essentially above 6 keV. The fraction of positrons annihilating in each layer for the YHO-2 sample is similar to that for the YHO-1 sample (see Fig. S4.1 in the Supplementary Material (SM)). More details on the experimental DB-PAS depth profiles and the corresponding best-fit parameters for both samples can be found in Fig. S4.2 and Table S4.1 (see SM). The higher  $\tau_{\text{ave}}$  below 2 keV comes from the increased positron annihilation at the surface, which is supported by Fig. 4.2 (d) which shows that the total fraction of positron annihilation from thermal and epithermal positrons increases with decreasing positron implantation energy below  $\sim 2$  keV. Therefore, the positron lifetimes in the range of 2-6 keV dominantly arise from the bulk oxyhydride layer. The  $\tau_{\text{ave}}$  values above  $\sim 360$  ps of this bulk oxyhydride layer before illumination are much larger than the calculated and experimental defect-free bulk lifetime values of  $\sim 240$  ps reported in our previous studies, indicating the presence of open-volume defects [14,15] throughout the layer.

To provide more insights into the nature of open-volume defects in the samples before illumination, we continue here with a discussion of the lifetimes and intensities extracted from the three-component analysis of the respective positron lifetime spectra. Representative positron lifetime spectra collected at a positron implantation energy of 5 keV of YHO-1 and YHO-2 thin-film samples before illumination and the corresponding fits are shown in Fig 4.3. The fairly constant  $\tau_{\text{ave}}$  values in the range of 2-6 keV (Fig. 4.2a and 4.2b) as well as the corresponding positron lifetimes and intensities of the bulk oxyhydride layer (see SM, Figs.

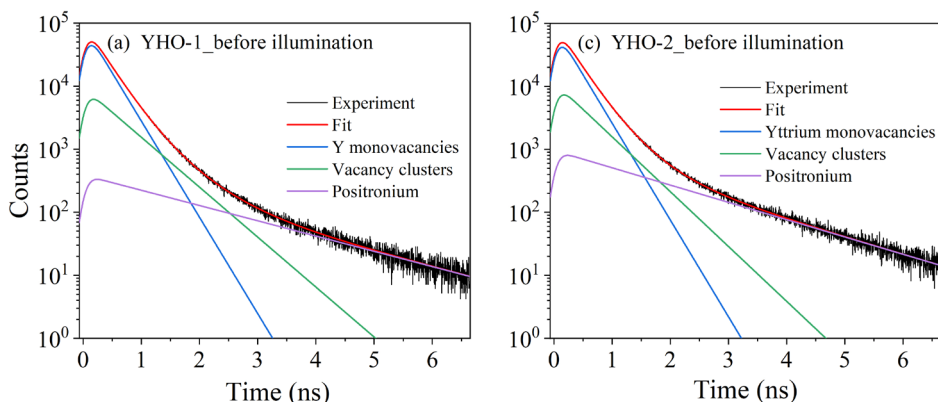


**Figure 4.3:** Positron lifetime spectra collected at an implantation energy of 5 keV of (a) YHO-1 and (b) YHO-2 thin-film samples before illumination, and the corresponding three-component analyses. The background was fitted to be less than 1 for all fits.

Table 4.1: Positron lifetimes ( $\tau_i$ ) and intensities ( $I_i$ ) for the YHO-1 and YHO-2 thin-film samples before illumination, obtained from the average of the respective values extracted from the PALS spectra collected at 3-5 keV.

Sample	Status	$\tau_1$ (ps)	$\tau_2$ (ps)	$\tau_3$ (ns)	$I_1$ (%)	$I_2$ (%)	$I_3$ (%)
YHO-1	Before illumination	276 $\pm$ 2	498 $\pm$ 11	1.93 $\pm$ 0.04	74 $\pm$ 2	24 $\pm$ 1	2.7 $\pm$ 0.1
YHO-2	Before illumination	277 $\pm$ 2	480 $\pm$ 15	1.54 $\pm$ 0.02	72 $\pm$ 2	23 $\pm$ 2	4.9 $\pm$ 0.1

S4.4 and S4.5) indicate that there is no significant depth-dependence in the defect distribution in both samples. The depth-dependence of the positron lifetimes and corresponding intensities obtained from a three-component analysis for YHO-1 and YHO-2 film samples in the collected positron implantation energy range can be found in Figs. S4.4 and S4.5 (see SM). The positron lifetimes and corresponding intensities of the three components averaged in the energy range of 3-5 keV for both YHO-1 and YHO-2 samples before illumination are shown in Table 4.1.

The first shortest positron lifetime  $\tau_1$  of  $\sim 277$  ps is  $\sim 13\%$  larger than the experimental and calculated bulk lifetime values ( $\sim 240$  ps) and is close to the calculated lifetime values for yttrium monovacancies ( $\sim 290$  ps for LDA and  $\sim 324$  for GGA), so this first lifetime could be ascribed to yttrium monovacancies [14,15]. The corresponding intensity  $I_1$  above 70% indicates that yttrium monovacancies are the dominant open-volume defects and positron trapping sites in both samples. The second lifetime in the range of 480-500 ps with an intermediate intensity (23-24%) arises from large vacancy clusters, and the size is likely larger than about five vacancies [14]. The longest positron lifetime values, that are larger than  $\sim 1.5$  ns indicate the formation of ortho-positronium (o-Ps) in nanopores. The lifetime of o-Ps in vacuum is 142 ns, which can be reduced to a few nanoseconds by picking up and annihilating with one electron of opposite spin from the wall of the nanopore, which is known

as the pick-off annihilation process [38-40]. Assuming a spherical shape, the averaged radius of pores can be estimated to be 0.29 nm and 0.25 nm in the oxyhydride layer of YHO-1 and YHO-2 samples using the Tao-Eldrup model [41,42]. These relatively large open-volume defects can be formed at grain boundaries and inside grains. The first and the second positron lifetimes of both films are larger than the reported experimental ( $\sim 240$  ps) and theoretical bulk lifetime of  $\text{YH}_{2.5}\text{O}_{0.25}$  ( $\sim 231$  ps for LDA and  $\sim 241$  for GGA) [15], and the sum of  $I_1$  and  $I_2$  is larger than 95%, indicating the presence of positron saturated trapping due to a higher concentration of open-volume defects (typically  $>10^{-4}$ ). Indeed, no reduced (first) bulk lifetime component was observed for these samples.

After 2 h photodarkening and fully bleaching, Fig. 4.2 (a) shows that in the YHO-1 film sample  $\tau_{\text{ave}}$  increases over a broad range of positron implantation energies from 2 to 5 keV, suggesting that the changes in open-volume defects occur throughout the whole oxyhydride layer. In addition, the increase in  $\tau_{\text{ave}}$  at 5 keV in the YHO-2 sample is the same as the YHO-1 sample, i.e., about 27 ps. This is due to an increase in the size and/or concentration of open-volume defects as a result of the photodarkening-bleaching cycle [15].

#### 4.3.2.2 Time-dependent positron lifetime experiments at 5 keV

Time-dependent PALS measurements were performed at the selected implantation energy of 5 keV to investigate the evolution of microstructural and electronic structure changes during photodarkening and the subsequent bleaching. An implantation energy of 5 keV was selected, as at this implantation energy nearly all positrons are annihilating in the oxyhydride layer (Fig. 4.2 (d)). Fig. 4.4 shows the  $\tau_{\text{ave}}$  as a function of time before illumination, during photodarkening and bleaching in YHO-1 and YHO-2 thin-film samples.  $\tau_{\text{ave}}$  is fairly constant for both samples before illumination, while it shows dynamic changes during photodarkening and bleaching. Upon photodarkening within the data collection time for one spectrum, i.e.  $\sim 3$  min,  $\tau_{\text{ave}}$  abruptly increases by 8 ps for the YHO-1 sample, while it decreases abruptly by 4 ps for the YHO-2 sample. The abrupt change in  $\tau_{\text{ave}}$  indicates the occurrence of rapid microstructural and/or electronic structure changes, while the trend in  $\tau_{\text{ave}}$  depends on the sample. During longer photodarkening,  $\tau_{\text{ave}}$  changes slowly. Compared to the  $\tau_{\text{ave}}$  at the beginning of photodarkening,  $\tau_{\text{ave}}$  decreases by 1-2 ps after photodarkening of  $\sim 2$  h. After the UV illumination is stopped, during bleaching  $\tau_{\text{ave}}$  starts to increase significantly and tends to saturate on a time scale that is similar to that of the optical transmittance shown in Fig. 4.1. The similar time dependence of  $\tau_{\text{ave}}$  to that of the transmittance during bleaching in both samples suggests that the increase in  $\tau_{\text{ave}}$  during bleaching is related to the disappearance of the photodarkened state. The average lifetime  $\tau_{\text{ave}}$  at the end of bleaching has increased by 25 ps and 27 ps for YHO-1 and YHO-2 samples compared to the values before illumination, which is consistent with the increments of  $\tau_{\text{ave}}$  at 5 keV in depth profiling PALS measurements in section 4.3.2.1. In addition, the stabilization of  $\tau_{\text{ave}}$  at these increased values indicates that the light-induced microstructural changes after bleaching are rather stable.

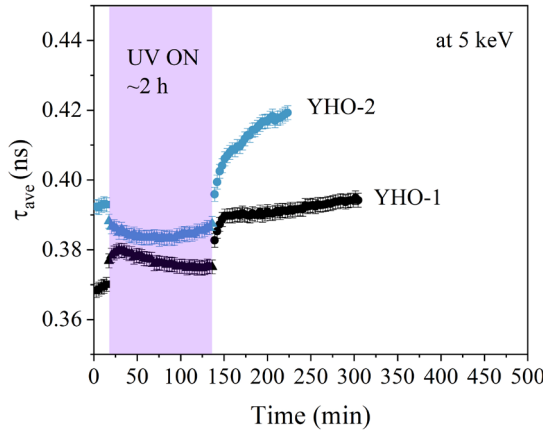


**Figure 4.4:** Time dependence of the average positron lifetime ( $\tau_{\text{ave}}$ ) for YHO-1 and YHO-2 thin-film samples, extracted from the lifetime spectra collected at 5 keV during in-situ illumination PALS measurements before illumination (squares), during photodarkening ( $\sim 2$  h, triangles, purple shaded area) and the subsequent bleaching (circles).

In order to unravel the nature of microstructural changes and their evolution during photodarkening and bleaching, we now consider the time evolution of the three individual positron lifetimes and corresponding intensities from the three-component analysis. To reduce the statistical scattering in the fitting,  $I_2$  was fixed to the averaged values either (1) before illumination or (2) during photodarkening and bleaching, as  $I_2$  is nearly unchanged in these two time windows. The unfixed  $I_2$  together with the positron lifetimes ( $\tau_i$ ) and other intensities ( $I_i$ ) obtained from the fits after fixing  $I_2$  are shown in Fig. 5 as a function of time before illumination, and during photodarkening and the subsequent bleaching for YHO-1 and YHO-2 thin-film samples at an implantation energy of 5 keV.

#### A. Time-evolution of the first positron lifetime component

As discussed in section 4.3.2.1, before illumination the dominant shortest lifetime  $\tau_1$  of around 279 ps shown in Fig. 4.5 (a) and Table 4.2 can be attributed to yttrium monovacancies. Upon photodarkening within  $\sim 3$  min,  $\tau_1$  abruptly drops by 4-6 ps. The lifetime parameters of the first PALS spectrum upon photodarkening reflect the average of the first 3 min, i.e. approximately the status of the film at around 1.5 min, as the first positron lifetime spectrum was collected in the period of 0-3 min after the UV light was switched on. The rapid drop in  $\tau_1$  may be related to the microstructural and electronic structure changes causing photodarkening, since the photochromic contrast initially reduces rapidly by more than 40% after illumination of 1.5 min for photodarkening. A first possible cause of the rapid decrease in  $\tau_1$  can be the formation of metallic domains, that was proposed to be the origin of the photochromic effect [11,14,43]. In previous in-situ illumination DB-PAS studies, two types



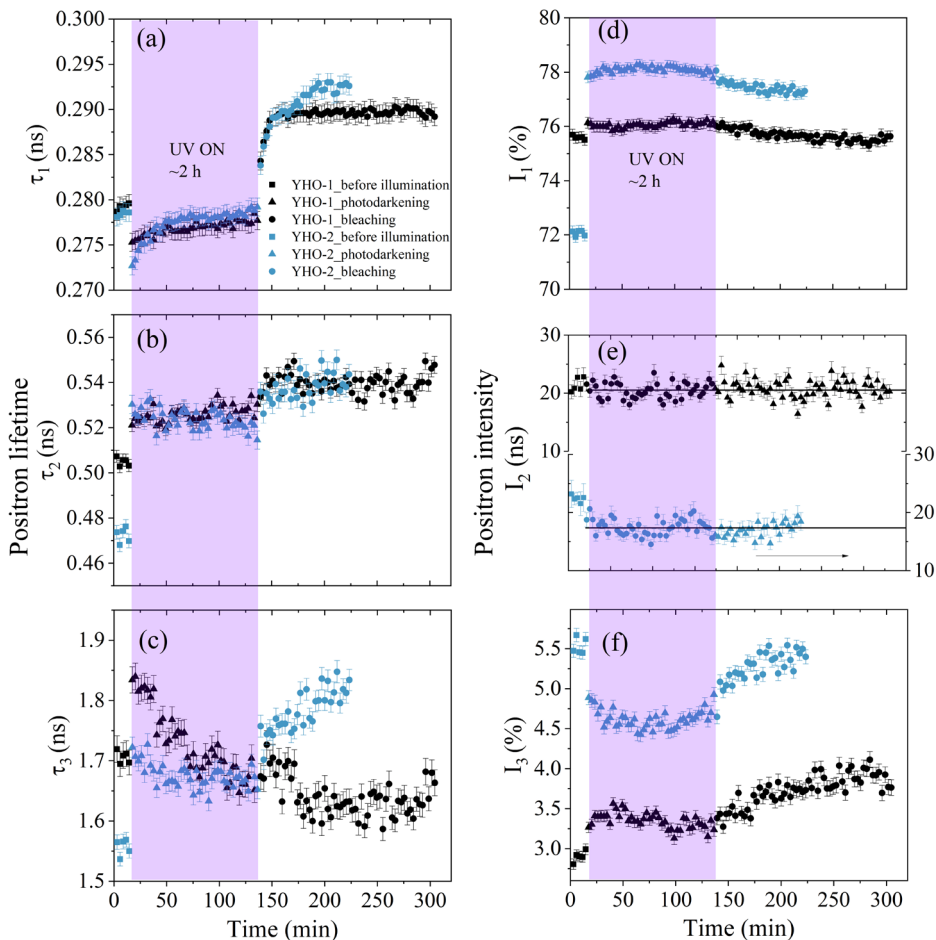


**Figure 4.5:** Time dependence of the positron lifetimes ( $\tau_i$ ) and the corresponding intensities ( $I_i$ ) extracted from the lifetime spectra collected at 5 keV during in-situ illumination PALS measurements for both YHO-1 and YHO-2 thin-film samples before illumination (squares), during photodarkening ( $\sim 2$  h, triangles, purple shaded area) and the subsequent bleaching (circles).

of metallic domains were proposed as possible alternative explanations for the photochromic effect, based on the reversible shifts in Doppler parameters and transmittance [14]. The first type involves the formation of phase-segregated hydrogen-rich metallic domains with a local composition of  $\text{YH}_2\text{O}_x$  ( $x < 0.5$ ) in a mixed  $\text{Y}^{2+}/\text{Y}^{3+}$  valence state, due to local rearrangements of both hydrogen and oxygen in the semiconducting oxyhydride matrix. For example, according to  $2 \text{YH}_2\text{O}_{0.5} \rightarrow \text{YH}_2\text{O}_{0.25} + \text{YH}_{1.5}\text{O}_{0.75} + 0.5 \text{H}^0$ , the resulting phase-segregated metallic  $\text{YH}_2\text{O}_{0.25}$  has a mixed  $\text{Y}^{2+}/\text{Y}^{3+}$  valence, while the more H-poor  $\text{YH}_{1.5}\text{O}_{0.75}$  retains the  $\text{Y}^{3+}$  valence. This is similar to what has been reported in a spectroscopic ellipsometry study

[11], where the ellipsometry data under illumination are successfully modelled by the formation of yttrium hydride-like metallic domains in a semiconducting matrix, and 2% of such metallic domains could explain a reduction in transmittance of  $\sim 30\%$ . We furthermore note that the calculated positron bulk lifetime of  $\text{YH}_{1.9}$  is 225 ps and 229 ps in the framework of LDA and GGA, and the experimental bulk lifetime of  $\text{YH}_{1.9}$  of  $\sim 260$  ps is also smaller than the value before illumination (279 ps) [14]. More details on ab calculation methods can be found in the SM. If hydride-like metallic domains are formed and trap positrons upon photodarkening, a reduction in  $\tau_1$  as observed in the first  $\sim 3$  min would therefore indeed be expected. The second type of metallic domains proposed are formed by a hydrogen vacancies-induced Anderson-Mott insulator-to-metal transition, which was inspired by the well-known insulator-to-metal transition from yttrium trihydrides to dihydrides [14,44]. In this scenario, electron-hole pairs are generated under illumination. Subsequently, some of the  $\text{H}^-$  anions at the octahedral sites capture a photo-excited hole and form  $\text{H}^0$  atoms ( $\text{H}^- + h^+ \rightarrow \text{H}^0$ ), which become mobile and leave their lattice positions, while some of the photo-excited electrons may localize at Y (4d) orbitals around the positively charged hydrogen vacancies due to charge compensation. When the concentration of such Y (4d) electrons at the octahedral sites is sufficiently large, these electron orbitals start to overlap and form an electron band. Compared to the phase-segregated H-rich metallic domains, the formation of hydrogen vacancies-induced metallic domains is more easily achieved chemically since it only requires the removal of hydrogen from octahedral sites, for instance, according to  $2 \text{YH}_2\text{O}_{0.5} \rightarrow 2 \text{YH}_{1.75}\text{O}_{0.5} + 0.5 \text{H}^0$ . Therefore, we believe that the second type of metallic domains are formed rather than the first type, in line with what was previously concluded in ref. [7]. The formed positively charged hydrogen vacancies essentially will not influence the positron lifetime as they repel positrons. However, the formation of electron bands in metallic domains due to the overlapping of electron orbitals at Y 4d around hydrogen vacancies will significantly increase the electron density locally. This may cause a decrease in the shortest lifetime if part of positrons annihilate at those metallic domains. Note that the positron lifetime associated with annihilation in such Anderson-Mott type of metallic domains is unknown, and would require further ab initio calculations to gain insights into its exact value. Overall, the formation of metallic domains may well explain the abrupt drop of  $\tau_1$  and the substantial reduction of transmittance.

An alternative explanation for the sudden decrease in  $\tau_1$  may consist of a change in the charge state of monovacancies due to capturing of photo-excited electrons, e.g., from  $\text{V}^+$  to  $\text{V}^0$ . A transition of the charge state of vacancies was previously observed in the photon-illuminated GaN [45], diamond [17], GaAs [46,47], *n*-type SiC [48], and Si [49] systems. For example, the study on GaAs showed that the positron lifetime of the photo-induced negatively charged As monovacancies  $\text{V}_{\text{As}}$  is 28 ps smaller than that of the respective neutral vacancies in GaAs, caused by the increased electron density at the vacancies [46]. A previous study showed that the as-prepared Gd oxyhydride films are *p*-type semiconductors, and the hole density is on the order of  $\sim 10^{11}$ - $10^{12} \text{ cm}^{-3}$ , indicating a mild doping level [50]. Assuming

a similar case for Y oxyhydride films, the p-type character of the film will lead to a position of the Fermi level close to the valence band maximum, and part of yttrium monovacancies might capture holes and turn into a charge-neutral state  $V_Y^0$ . Upon photodarkening, the n-type characteristic become dominant [50], and neutral yttrium monovacancies could easily capture a photo-excited electron and become negatively charged ( $V_Y^0 + e^- \rightarrow V_Y^-$ ). This transition may lead to a fast reduction of  $\tau_1$  in  $YH_xO_y$ . We further note that, in some cases, it was observed that the change of charge state of vacancy defects in GaN [45], diamond [17], 6H-SiC [46], and Si [49] significantly affects the trapping rate rather than the lifetime of the respective defects. Therefore, the transition from  $V_Y^0$  to  $V_Y^-$  might explain the increase in  $I_1$  as well as the reduction in  $\tau_1$ . Note however, that the extent of the possible presence of  $V_Y^0$  is not determined in the as-prepared  $YH_xO_y$  films, and possibly occurring changes in the charge state of Y monovacancies would need further detailed investigation, for instance, of the involved vacancy formation energies and determination of the position of the Fermi energy level of the as-deposited films and during photodarkening. A second option of the change in the charge state of vacancies that could occur in  $YH_xO_y$  upon photodarkening would be from  $V_H^+$  to  $V_H^0$  or  $V_H^-$ . The positively charged anion vacancies cannot trap positrons but the neutral or negatively charged anion vacancies might trap positrons. For instance, the neutral As vacancies and O vacancies have been detected by PAS in GaAs and  $LaSrCoO_3$ , respectively [46,51]. Therefore,  $V_H^0$  or  $V_H^-$  might trap positrons, but the positron lifetime at such vacancies is unknown. Further investigations on the charge state of vacancies would need temperature-dependent PALS measurements [49,52-54] and/or theoretical ab initio positron lifetime calculations. Note here that in this case, there would be a competition between the change in the charge state of hydrogen vacancies by capturing photo-excited electrons and the localization of electrons at Y (4d) orbitals around hydrogen vacancies as suggested by the Anderson-Mott insulator-to-metal related mechanism. This could be unravelled by calculating the binding energy of electrons with hydrogen vacancies and at Y (4d) orbitals.

During further photodarkening, in contrast to the initial abrupt drop,  $\tau_1$  increases gradually for at least the first 30 min, after which it tends to stabilize at 278-279 ps. It is expected that in this timeframe additional metallic domains are gradually formed, leading to the further decrease in transmittance. If more trapping of positrons at metallic domains occurs, one would expect a continual decrease in  $\tau_1$ . However, the increase in  $\tau_1$  suggests the occurrence of an additional microstructural change, for instance, the formation of divacancies. Namely, under photodarkening, some of the hydrogen vacancies created by UV illumination could aggregate with the pre-existing yttrium monovacancies and form divacancies  $V_Y-V_H$  or small vacancy complexes consisting of  $V_Y$  and a few neighbouring hydrogen vacancies when the hydrogen vacancies are creating in the vicinity of an yttrium monovacancy. The gradual increase in  $\tau_1$  during further photodarkening indicates increased positron trapping at such divacancy-like defects due to an increase in the concentration of those defects that are continuously created by the UV-illumination. At the end of photodarkening,  $\tau_1$  tends to

stabilize in parallel with the transmittance, which implies that positron trapping at the divacancy-like defects, pre-existing yttrium monovacancies, metallic domains, and possibly at charged cation and/or anion monovacancies in the semiconducting  $\text{YH}_x\text{O}_y$  matrix reaches an equilibrium state in the presence of UV illumination due to the stabilization of the light-induced microstructural and electronic structure changes.

After the UV illumination was stopped,  $\tau_1$  during bleaching increases on a time scale similar to the increase in the optical transmittance until it stabilizes at  $\sim 289$  ps for the YHO-1 sample and at  $\sim 293$  ps for the YHO-2 sample. At the end of bleaching, the transmittance is largely recovered as a result of the disappearance of metallic domains, meaning that the high  $\tau_1$  values of  $\sim 289$  ps and  $\sim 293$  ps at the end of bleaching can be attributed to the light-induced formation of divacancy-like defects or small vacancy complexes in the  $\text{YH}_x\text{O}_y$  semiconductor. Noticeably, compared to the value before illumination,  $\tau_1$  after bleaching has increased by  $\sim 4\%$  and  $5\%$  for YHO-1 and YHO-2 samples. This is smaller than the typical increment in lifetime ( $>10\%$ ) from monovacancies to divacancies in Si, GaAs and SiC [55,56], and suggests that only part of the yttrium monovacancies are transformed into divacancies or small vacancy complexes [15]. The larger increase in  $\tau_1$  in the YHO-2 sample compared with the YHO-1 sample could be due to the formation of more divacancy-like defects due to the larger photochromic contrast, suggesting that more microstructural changes take place during illumination for this more H-rich sample.

## B. Correlation of the first positron lifetime component with photochromic contrast during bleaching

During bleaching, the gradual increase in  $\tau_1$  for both samples is understandable, since the decrease in positron trapping at metallic domains (and possibly at charged monovacancies) due to the gradual disappearance of the metallic domains and photo-generated charge carriers will lead to an increase in positron trapping at the pre-existing yttrium monovacancies and at the illumination-induced divacancy-like defects, and increase  $\tau_1$ . Noteworthy, the time-dependence of both  $\tau_{\text{ave}}$  and  $\tau_1$  during bleaching (Fig. 4.4 and 4.5(a)) is similar to the photochromic contrast (Fig. 4.1). The time evolution of the photochromic contrast during bleaching is shown in Fig. 4.6 (a), while the correlation diagrams of  $\tau_{\text{ave}}$  and  $\tau_1$  versus the photochromic contrast in YHO-1 and YHO-2 thin-film samples during bleaching are plotted in Fig. 4.6 (b-e). Clearly, for both samples, during the initial period of  $\sim 15$  min in the bleaching phase,  $\tau_{\text{ave}}$  and  $\tau_1$  increase almost linearly with decreasing photochromic contrast. Quantitatively, during this period,  $\tau_1$  increases by 11 ps with an decrease in photochromic contrast of 11% in the YHO-1 sample, while in sample YHO-2 the increase in  $\tau_1$  and the decrease in photochromic contrast are 10 ps and 11%. This strong correlation between  $\tau_1$  and the photochromic contrast in these two samples suggests that the quantity of metallic domains that disappear during this first fast bleaching phase (I) and the correspondingly increased fraction of positron trapping at yttrium monovacancies and divacancy-like defects are quantitatively very similar in both samples. During further bleaching,  $\tau_1$  for the YHO-1

sample tends to stabilize at around 289 ps when the contrast still decreases  $\sim 4\%$ . It is likely that during this second bleaching phase (II) in the YHO-1 sample, positron saturation trapping at yttrium monovacancies and divacancy-like defects occurs while the positron trapping at metallic domains is tiny due to the small concentration and/or size of metallic domains (resulting in a small contrast  $\sim 4\%$ ), so the disappearance of metallic domains does not noticeably increase the positron trapping at yttrium monovacancies and divacancy-like defects, resulting in a relatively stable  $\tau_1$ .

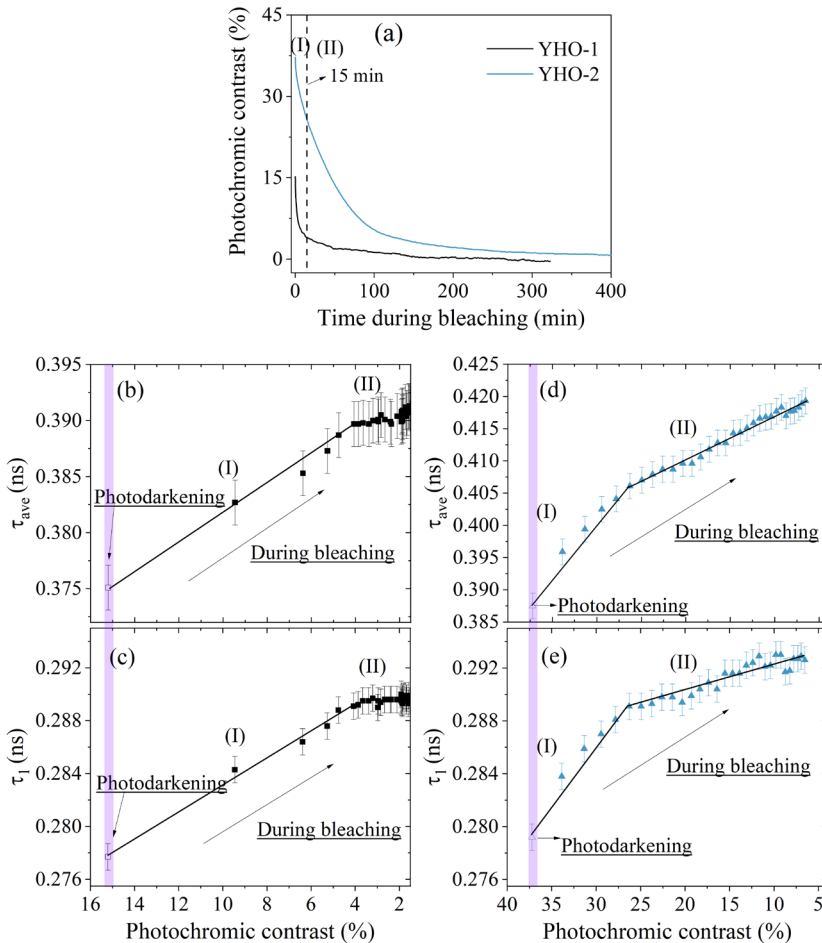


**Figure 4.6:** Photochromic contrast as a function of time during bleaching (a), as well as the relationship between  $\tau_{ave}$  respectively  $\tau_1$  with the photochromic contrast in YHO-1 (b and c) and YHO-2 (d and e) thin-film samples at the end of photodarkening and during bleaching. The solid lines are a guide for the eyes, with bleaching phase (I) corresponding to the first  $\sim 15$  min of bleaching for both samples and bleaching phase (II) corresponding to the time interval after  $\sim 15$  min of bleaching.

However, during further bleaching in the YHO-2 sample,  $\tau_1$  increases further by 4 ps with decrease in contrast of  $\sim 20\%$ . The second correlation between  $\tau_1$  and the photochromic contrast during this second bleaching phase (II) in the YHO-2 sample indicates a continued decrease in positron trapping at metallic domains due to the disappearance of metallic domains and correspondingly increased positron trapping at yttrium monovacancies and divacancy-like defects, but with slower kinetics. The fact that after 2 h of photodarkening a much higher contrast in the YHO-2 sample is reached compared to the YHO-1 sample suggests that more and possibly larger metallic domains are formed in sample YHO-2. Indeed, if larger metallic domains are formed in the YHO-2 sample, the disappearance of larger metallic domains would require longer bleaching time due to the longer diffusion distance of hydrogen anions [15,57]. Therefore, the slower increase in  $\tau_1$  with decreasing photochromic contrast during the second bleaching phase (II) in the YHO-2 sample could be caused by the slower disappearance of those metallic domains that are originally large in size, while the similar first bleaching phase (I) may correspond to the disappearance of metallic domains that are smaller in size.

Table 4.2: Positron lifetimes ( $\tau_i$ ) and intensities ( $I_i$ ) for the YHO-1 and YHO-2 thin-film samples averaged from five PALS spectra before illumination, at the end of photodarkening and at the end of bleaching, collected at 5 keV in the time-dependent PALS measurements.

sample	Status	$\tau_1$ (ps)	$\tau_2$ (ps)	$\tau_3$ (ns)	$I_1$ (%)	$I_2$ (%)	$I_3$ (%)
YHO-1	Before illumination	279 $\pm$ 1	505 $\pm$ 2	1.71 $\pm$ 0.01	75.5 $\pm$ 0.2	22	2.9 $\pm$ 0.1
	At the end of illumination	278 $\pm$ 1	529 $\pm$ 2	1.67 $\pm$ 0.01	76 $\pm$ 0.2	21	3.3 $\pm$ 0.1
	After bleaching	290 $\pm$ 1	542 $\pm$ 2	1.64 $\pm$ 0.01	75.5 $\pm$ 0.2	21	3.9 $\pm$ 0.1
YHO-2	Virgin state	278 $\pm$ 1	472 $\pm$ 2	1.56 $\pm$ 0.01	72 $\pm$ 0.2	22	5.5 $\pm$ 0.1
	At the end of illumination	279 $\pm$ 1	519 $\pm$ 2	1.68 $\pm$ 0.01	78 $\pm$ 0.2	17	4.7 $\pm$ 0.1
	After bleaching	293 $\pm$ 1	541 $\pm$ 2	1.82 $\pm$ 0.01	77 $\pm$ 0.2	17	5.4 $\pm$ 0.1

### C. Time evolution of the second and third positron lifetime components

For the second lifetime  $\tau_2$ , the value before illumination of around 470 and 500 ps in Fig. 4.5 (b) and Table 4.2 arises from vacancy clusters ( $V_n$ ,  $n \geq 5$ ). Upon photodarkening for the first  $\sim 3$  min, the observed fast increase in  $\tau_2$  to  $\sim 520$ -530 ps could be a consequence of fast release of loosely-bounded hydrogen atoms from the walls of the vacancy clusters and/or hydrogen molecules from the vacancy clusters [14,15]. Indeed, Moldarev et al. showed that the partial hydrogen pressure reaches the highest value during the first  $\sim 5$  min of UV illumination of a photochromic  $\text{YH}_x\text{O}_y$  film, suggesting the presence of a fast process of hydrogen release [16]. During illumination for longer times,  $\tau_2$  hardly changes, while during bleaching it increases up to about 540 ps within  $\sim 20$  min (the YHO-1 sample) to  $\sim 40$  min (the YHO-2 sample). The increase in lifetime during bleaching indicates the detection of vacancies with a larger size. However, vacancy formation and aggregation are likely to occur only during illumination, when the photo-generated charge carriers liberate hydrogen and create hydrogen vacancies.

Therefore, it is possible that during photodarkening, the light-induced anion vacancies aggregate with the pre-existing vacancy clusters and form larger open-volume defects, similar to the formation of divacancy-like defects from the yttrium monovacancies. Vacancy formation and aggregation would induce an increase in the positron lifetime, however,  $\tau_2$  is fairly constant during photodarkening. The unchanged  $\tau_2$  suggests the presence of other processes during photodarkening that can reduce  $\tau_2$  and compensate for the increase. If some metallic domains are formed in the vicinity of vacancy clusters,  $\tau_2$  can be reduced due to the locally increased electron density. In addition, the increased concentration of photo-excited electrons in the semiconducting matrix might increase the electron density around vacancy clusters as well and reduce  $\tau_2$ . During bleaching, metallic domains at the boundaries of vacancy clusters and photo-excited electrons in the semiconducting matrix gradually disappear, leading to a gradual decrease in the electron density around the grown vacancy clusters, and thus causing a gradual increase in  $\tau_2$  on a timescale that is quite similar to that of the optical transmittance (Fig. 4.6 (a)). The  $\tau_2$  values of  $\sim 540$  ps at the end of the bleaching phase for both samples suggest a similar size of the grown vacancy clusters after the photodarkening-bleaching cycle, which is consistent with the results in the previous PALS study [15].

The third positron lifetime  $\tau_3$  is fairly constant before illumination, and the value of above  $\sim 1.5$  ns (Fig. 4.5 (c)) is an indication of formation of ortho-positronium in nanopores. Upon photodarkening for the first 3 min,  $\tau_3$  rises abruptly by  $\sim 8\%$  up to 1.84 ns for the YHO-1 sample and by 10% up to 1.71 ns for the YHO-2 sample. The increase in  $\tau_3$  of 8-10% could be the result of an increased size of nanopores due to the release of hydrogen molecules from these nanopores [16]. During photodarkening,  $\tau_3$  reduces at least in the first 30 minutes due to the formation of metallic areas near the surface of nanopores (leading to faster pick-off annihilation) and tends to stabilize, while during bleaching it varies from sample to sample.

#### D. Time variation of positron trapping rates/intensities

Due to the presence of positron saturated trapping at open-volume defects in the films, the concentration of the defects cannot be determined. However, the changes of  $I_1$  and  $I_2$  during photodarkening and bleaching could reflect the changes in the corresponding positron trapping rates  $\kappa_1$  and  $\kappa_2$  at the sites associated with  $\tau_1$  and  $\tau_2$ , while  $I_3$  reflects the probability of forming o-Ps at a formation rate  $\kappa_3$ , which undergo pick-off annihilation in nanopores.

In the YHO-1 sample, upon photodarkening for the first  $\sim 3$  min, both  $I_1$  and  $I_3$  increase about 0.5% (Fig. 4.5), while  $I_2$  decreases  $\sim 1\%$  accordingly ( $I_1 + I_2 + I_3 = 1$ ). Upon photodarkening, based on the abrupt increase in the positron lifetime for vacancy clusters  $\tau_2$  ( $V_n$ ,  $n \geq 5$ ) due to the release of hydrogen, one would expect an increase in the corresponding trapping rate  $\kappa_2$ , via an increase in the trapping coefficient [30]. However, the decrease in  $I_2$  and the increase in  $I_1$  and  $I_3$  in the YHO-1 sample upon photodarkening for the first  $\sim 3$  min indicates that the relative fraction of positrons trapping at the vacancy clusters decreases due to the larger increase in  $\kappa_1$  and  $\kappa_3$  compared to  $\kappa_2$ . Indeed, the formed metallic domains could

act as new trapping sites and enhance the trapping rate  $\kappa_1$ , in line with the previous DB-PAS study that showed preferential positron trapping at metallic domains [14]. Furthermore, if some monovacancies are charged by the photo-excited electrons upon photodarkening, the trapping rate  $\kappa_1$  could also be increased by the enhanced attractive Coulomb force for positrons. Indeed, it was reported that the intensity of the positron lifetime associated with the  $V_{\text{Ga}}(V_{\text{N}})_n$  defects ( $n=2-4$ ) nearly doubles in GaN under illumination [45], which was assigned to the increase in the trapping rate due to the change in the charge state of vacancies by capturing photo-excited electrons. In addition, the aggregation of light-induced hydrogen vacancies with yttrium monovacancies may already appear at small concentrations, which could increase  $\kappa_1$  as well via increasing the trapping coefficient compared to the one for monovacancies [30]. Therefore, upon photodarkening for the first  $\sim 3$  min, the occurrence of new and more effective trapping sites leads to an increase in  $\kappa_1$  in the YHO-1 sample. On the other hand, the abrupt increase in  $I_3$  ( $\Delta I_3 \cong +0.5\%$ ) in the YHO-1 sample indicates an enhanced probability of forming o-Ps, which could be caused by hydrogen release from the nanopores. If some nanopores of comparable size contain hydrogen molecules before illumination, upon illumination the release of those hydrogen molecules could make the previously invisible nanopores detectable via o-Ps formation, thereby increasing  $I_3$ .

For the YHO-2 sample, upon photodarkening for the first 3 min, both  $I_2$  and  $I_3$  decreases, while only  $I_1$  increases. Upon photodarkening for the first 3 min, similar to the YHO-1 sample, the release of hydrogen from vacancy clusters and some nanopores that contain hydrogen molecules before illumination could also occur in sample YHO-2, which could potentially increase the positron trapping rate at vacancy clusters  $\kappa_2$  and the probability of forming o-Ps  $I_3$ . Nevertheless, the relatively large increase in  $I_1$  ( $\Delta I_1 \cong +6\%$ ) leads to a net reduction in both  $I_2$  and  $I_3$  in the YHO-2 sample. This indicates that upon photodarkening for the first 3 min, the relative positron trapping rate at vacancy clusters  $\kappa_2/\kappa_1$  and the relative probability of forming o-Ps  $\kappa_3/\kappa_1$  decrease, caused by the larger, more dominate increase in the positron trapping rate  $\kappa_1$  at the annihilation sites associated with  $\tau_1$ . As discussed, the formation of metallic domains and divacancies, as well as the change in the charge state of monovacancies could increase  $\kappa_1$  and  $I_1$ . Compared to the YHO-1 sample, the larger increase in  $\kappa_1$  and  $I_1$  in the YHO-2 sample could be due to more changes in microstructure and electronic structure upon photodarkening for the first 3 min. Indeed, the photochromic contrast after 1.5 min of UV illumination in sample YHO-2 is about twice that in the YHO-1 sample, indicating that more metallic domains are formed in this more H-rich YHO-2 sample. Also, more hydrogen vacancies will be formed with increasing concentration of metallic domains, which leads to an increase in the probability of forming divacancy-like defects and the corresponding trapping rate  $\kappa_1$ .

During further photodarkening,  $I_1$ ,  $I_2$ , and  $I_3$  for both samples remain nearly unchanged, indicating that positron trapping rates at the sites associated with  $\tau_1$  and  $\tau_2$ , and the probability of forming o-Ps remain balanced. During bleaching, for both samples  $I_2$  continues to remain nearly unchanged, while  $I_1$  decreases and  $I_3$  increases slightly over the whole bleaching



period. The correlation between  $\tau_1$  and the photochromic contrast during bleaching suggests that little or no positron trapping occurs at metallic domains anymore after 15 min in sample YHO-1. Therefore, the gradual changes in  $I_3$  and  $I_1$  during bleaching cannot be (solely) attributed to the reduced trapping at the independent metallic domains in the semiconducting matrix due to the disappearance of those metallic domains. However, the increase in  $I_3$  indicates that the probability of forming o-Ps increases. This could be the result of a decrease in the metallicity around nanopores, as it is well-known that a metallic environment is less effective in converting positron to positronium, compared to porous metal oxide insulators and semiconductors that can efficiently generate positronium [58,59].

In general, our in-situ illumination PALS experiments provide key insights into the evolution of open-volume defects and metallic domains in time with optical transmittance during photodarkening-bleaching processes. The dynamics of open-volume defects and metallic domains along with a corresponding change in film color before illumination, during photodarkening for the first  $\sim 3$  min and photodarkening  $\sim 2$  h, and subsequent two bleaching phases (I and II) in yttrium oxyhydride films is schematically sketched in Fig. 4.7.

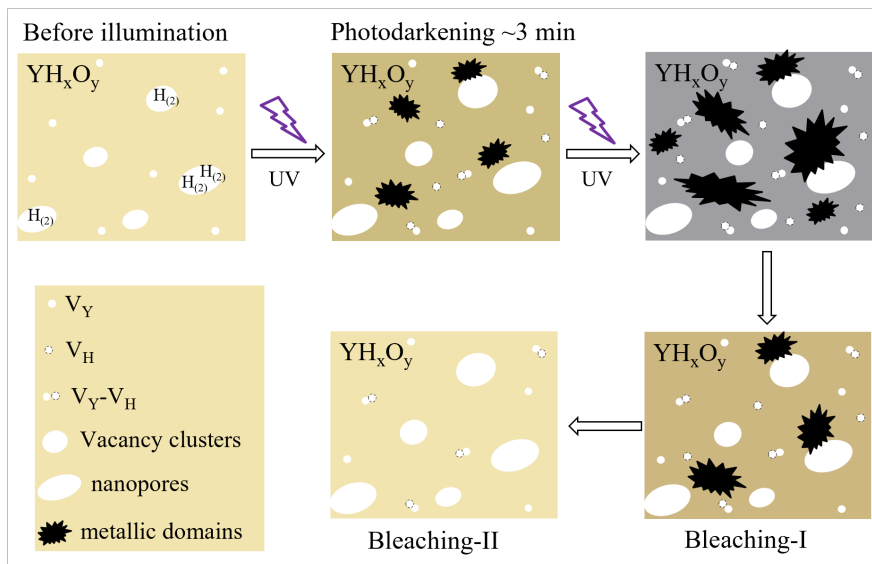


**Figure 4.7:** Schematics of the evolution of open-volume defects and metallic domains along with a corresponding change in film color before illumination, during photodarkening, and subsequent two bleaching phases in photochromic yttrium oxyhydride films.

#### 4.3.3 Second PALS experiment

Our previous DB-PAS study [15] on both  $\text{YH}_x\text{O}_y$  and  $\text{GdH}_x\text{O}_y$  thin-film samples under multiple photodarkening-bleaching cycles demonstrated that the S-parameter after bleaching

increases progressively upon cycling for the first three cycles and correlates with an increasingly slower bleaching rate. Combined with the results of PALS measurements before and after one cycle, this correlation suggests that the microstructural changes corresponding to the slower bleaching involve vacancy aggregation due to the release of hydrogen [15]. Indeed, both the depth-profile and time-dependent measurements show a significant increase in  $\tau_{\text{ave}}$  for both YHO-1 and YHO-2 samples after the photodarkening-bleaching cycle (Figs. 4.2 and 4.4), which is consistent with results in [15]. However, direct experimental evidence from positron lifetime spectroscopy on vacancy formation/aggregation upon photodarkening-bleaching cycling is important to gain more insights into the changes in open-volume defects upon multiple photochromic cycling. We therefore performed PALS measurements on an additional sample YHO-a, deposited the same way as the YHO-1 sample, during three photodarkening-bleaching cycles in a second PALS experiment at HZDR, in which each cycle included a short illumination time of  $\sim 9$  min. The statistical scattering and the minor changes in positron lifetime parameters made it difficult in this case to discern the separate changes in the positron lifetime parameters for the three individual components after each cycle. Therefore, we present in Fig. 4.8 the robust  $\tau_{\text{ave}}$  parameter collected at 4 keV as a function of time for the YHO-a sample during the three photodarkening-bleaching cycles. The positron implantation energy chosen in these time-dependent measurements for sample YHO-a was 4 keV, since the thickness of this film ( $\sim 350$  nm) was slightly less than the that of the YHO-1 sample. Note that bleaching times during the first and second cycles used in this experiment were sufficient to fully bleach the sample for the applied illumination time of  $\sim 9$  min (see SM, Fig. S4.6 for the corresponding time-dependence of the optical transmittance).

Fig. 4.8 shows that the average positron lifetime  $\tau_{\text{ave}}$  of the YHO-a sample increases progressively during these three photodarkening-bleaching cycles, which is in line with the increase in  $\tau_{\text{ave}}$  in YHO-1 and YHO-2 samples after one cycle (Fig. 4.4) and also with the successive increase in S-parameter upon multiple cycling reported in [15], suggesting that more and/or larger nanoscale open-volume defects are formed upon cycling. In addition, we notice that the increase in  $\tau_{\text{ave}}$  after the first cycle (4 ps) is larger than the increments of  $\tau_{\text{ave}}$  after bleaching for the following two cycles (about 3 ps in total). This is consistent with the behaviour of the S-parameter upon photochromic cycling, that reveal that the increase in the S-parameter after the first cycle is larger than the following two cycles in  $\text{YH}_x\text{O}_y$  films [15], suggesting that the changes in the open-volume defects are the largest for the first cycle. Indeed, the loosely-bonded hydrogen atoms and/or non-bonded hydrogen molecules in vacancy clusters and nanopores preferentially seem to be released during the first photodarkening [16], causing the largest change in  $\tau_{\text{ave}}$  and the S-parameter after the first cycle. Furthermore, compared to the increase in  $\tau_{\text{ave}}$  in YHO-1 and YHO-2 samples after photodarkening (2 h) and the subsequent bleaching of 25-27 ps as shown in Fig. 4.4, the much smaller increments in the YHO-a sample after each photodarkening-bleaching cycle

(2-4 ps) is likely related to the formation of fewer hydrogen vacancies due to the substantially shorter illumination time, leading to a lower probability of formation of vacancy complexes.

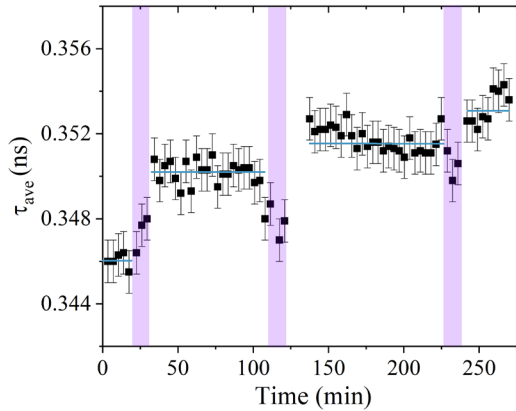


**Figure 4.8:** Time dependence of the average positron lifetime ( $\tau_{\text{ave}}$ ) for the YHO-a sample, extracted from the lifetime spectra collected at 4 keV during in-situ illumination PALS measurements before illumination and during three short photodarkening ( $\sim 9$  min, purple shaded area)-bleaching cycles.

## 4.4 Conclusions

In this study, yttrium oxyhydride thin-film samples deposited at two different sputtering power were investigated. The PALS depth profiles show that there is no significant depth-dependence in the distribution of open-volume defects in the bulk oxyhydride layer for both samples. After photodarkening and subsequent bleaching, the homogeneous increase in  $\tau_{\text{ave}}$  in the range of 2-5 keV suggests that an increase in the size/concentration of open-volume defects occurs throughout the whole oxyhydride layer.

In-situ illumination PALS measurements at 5 keV revealed the time evolution of open-volume defects and metallic domains of the oxyhydride layer for both YHO-1 and YHO-2 thin-film samples during photodarkening-bleaching processes. Upon photodarkening for the first 3 min, for both samples a sudden drop in the shortest positron lifetime  $\tau_1$  and a significant reduction in transmittance is observed, that results from the fast initial formation of metallic domains. In parallel, the occurrence of the sudden increase in  $\tau_2$  and  $\tau_3$  suggests the release of loosely-bounded hydrogen from vacancy clusters and nanopores. During further photodarkening, the gradual increase in  $\tau_1$  suggests that the concentration of divacancy-like defects in the semiconducting matrix increases. When the UV illumination is switched off, two subsequent bleaching phases are observed. During the first bleaching phase (I), a linear

relationship between  $\tau_1$  and the photochromic contrast is seen that is quantitatively similar for both samples, that suggests that the quantity of metallic domains that disappear during the first bleaching phase, and the correspondingly increased positron trapping at yttrium monovacancies and divacancy-like defects is similar in both samples. During the second bleaching phase (II), metallic domains continue to disappear, but the remaining small size or concentration of metallic domains prevents their detection by PALS in the YHO-1 sample with a small photochromic contrast ( $<4\%$ ), as indicated by a relatively stable  $\tau_1$ . In contrast, in the more H-rich sample YHO-2 a second linear relationship between  $\tau_1$  and the photochromic contrast is observed during the bleaching phase II, which could be due to the disappearance of those metallic domains that have grown larger during photodarkening. After bleaching, most of the metallic domains and the photoexcited charge carriers in the semiconducting matrix have disappeared, while the grown open-volume defects remain stable. This study deepens our understanding of the (nanoscale) structure-optical property relationship in photochromic yttrium oxyhydrides.

## References

- [1] T. Mongstad, C. Platzer-Bjorkman, J. P. Maehlen, L. P. A. Mooij, Y. Pivak, B. Dam, E. S. Marstein, B. C. Hauback, and S. Z. Karazhanov, A new thin film photochromic material: Oxygen-containing yttrium hydride, *Sol. Energy Mater. Sol. Cells* **95**, 3596 (2011).
- [2] F. Nafezarefi, H. Schreuders, B. Dam, and S. Cornelius, Photochromism of rare-earth metal-oxy-hydrides, *Appl. Phys. Lett.* **111**, 103903 (2017).
- [3] S. Cornelius, G. Colombi, F. Nafezarefi, H. Schreuders, R. Heller, F. Munnik, and B. Dam, Oxyhydride nature of rare-earth-based photochromic thin films, *J. Phys. Chem. Lett.* **10**, 1342 (2019).
- [4] S. M. Adalsteinsson, M. V. Moro, D. Moldarev, S. Droulias, M. Wolff, and D. Primetzhofer, Correlating chemical composition and optical properties of photochromic rare-earth oxyhydrides using ion beam analysis, *Nucl. Instrum. Meth. B* **485**, 36 (2020).
- [5] D. Chaykina, F. Nafezarefi, G. Colombi, S. Cornelius, L. J. Bannenberg, H. Schreuders, and B. Dam, Influence of crystal structure, encapsulation, and annealing on photochromism in Nd oxyhydride thin films, *J. Phys. Chem. Lett.* **126**, 2276 (2022).
- [6] D. Chaykina, G. Colombi, H. Schreuders, and B. Dam, Photochromic samarium oxyhydride thin films, *AIP Adv.* **13**, 055211 (2023).
- [7] B. Dam, F. Nafezarefi, D. Chaykina, G. Colombi, Z. Wu, S. W.H. Eijt, S. Banerjee, G. A. de Wijs, A. Kentgens, Perspective on the photochromic and photoconductive properties of rare-earth oxyhydride thin films, *Sol. Energy Mater. Sol. Cells* **273**, 112921 (2024).
- [8] Y. J. Ke, J. W. Chen, C. J. Lin, S. C. Wang, Y. Zhou, J. Yin, P. S. Lee, and Y. Long, Smart windows: Electro-, thermo-, mechano-, photochromics, and beyond, *Adv. Energy Mater.* **9**, 1902066 (2019).
- [9] T. Yamasaki, R. Takaoka, S. Iimura, J. Kim, H. Hiramatsu, and H. Hosono, Characteristic resistive switching of rare-earth oxyhydrides by hydride ion insertion and extraction, *Acs Appl. Mater. Inter.* **14**, 19766 (2022).
- [10] L. Andronic, D. Moldarev, D. Deribew, E. Moons, and S. Z. Karazhanov, Photocatalytic self-cleaning properties of thin films of photochromic yttrium oxyhydride, *J. Solid State Chem.* **316**, 123599 (2022).
- [11] J. Montero, F. A. Martinsen, M. Garcia-Tecedor, S. Z. Karazhanov, D. Maestre, B. Hauback, and E. S. Marstein, Photochromic mechanism in oxygen-containing yttrium hydride thin films: An optical perspective, *Phys. Rev. B* **95**, 201301(R) (2017).
- [12] J. Montero, P. Svedlindh, and L. Österlund, Photo-induced reversible modification of the Curie-Weiss temperature in paramagnetic gadolinium compounds, *Solid State Commun.* **378**, 115419 (2024).
- [13] S. Banerjee, D. Chaykina, G. Colombi, B. Dam, G. A. de Wijs, and A. P.M. Kentgens, Studying Photochromism in Scandium Oxyhydrides: Solid-state NMR Studies and DFT Calculations, to be published

- [14] Z. Wu, T. de Krom, G. Colombi, D. Chaykina, G. van Hattem, H. Schut, M. Dickmann, W. Egger, C. Hugenschmidt, E. Brück, B. Dam, and S. W. H. Eijt, Formation of vacancies and metallic-like domains in photochromic rare-earth oxyhydride thin films studied by in-situ illumination positron annihilation spectroscopy, *Phys. Rev. Mater.* **6**, 065201 (2022).
- [15] Z. Wu, L. de Wit, M. Beek, G. Colombi, D. Chaykina, H. Schreuder, H. Schut, M. O. Liedke, M. Butterling, A. Wagner, M. Dickmann, E. Brück, B. Dam, and S. W.H. Eijt, The memory effect in photochromic rare-earth oxyhydride thin films studied by in-situ positron annihilation spectroscopy upon photodarkening-bleaching cycling, *Phys. Rev. Mater.* **8**, 045201 (2024).
- [16] D. Moldarev, L. Stolz, M. V. Moro, S. M. Adalsteinsson, I. A. Chioar, S. Z. Karazhanov, D. Primetzhofer, and M. Wolff, Environmental dependence of the photochromic effect of oxygen-containing rare-earth metal hydrides, *J. Appl. Phys.* **129**, 153101 (2021).
- [17] M. Wenskat, J. Čížek, M. Oskar Liedke, M. Butterling, M. Stiehl, G. Dalla Lana Semione, C. Backes, C. Bate, O. Melikhova, E. Hirschmann, A. Wagner, H. Weise, A. Stierle, M. Aeschlimann, and W. Hillert, Vacancy dynamics in niobium and its native oxides and their potential implications for quantum computing and superconducting accelerators, *Phys. Rev. B* **106**, 094516 (2022).
- [18] L. Chiari, K. Kojima, Y. Endo, H. Teshigahara, M. Butterling, M. Oskar Liedke, E. Hirschmann, A. G. Attallah, A. Wagner, and M. Fujinami, Formation and time dynamics of hydrogen-induced vacancies in nickel, *Acta Mater.* **219**, 117264 (2021).
- [19] J. Banhart, M. D. H. Lay, C. S. T. Chang, and A. J. Hill, Kinetics of natural aging in Al-Mg-Si alloys studied by positron annihilation lifetime spectroscopy, *Phys. Rev. B* **83**, 014101 (2011).
- [20] J. M. Mäki, F. Tuomisto, A. Varpula, D. Fisher, R. U. A. Khan, and P. M. Martineau, Time dependence of charge transfer processes in diamond studied with positrons, *Phys. Rev. Lett.* **107**, 217403 (2011).
- [21] M. A. van Huis, A. van Veen, H. Schut, C. V. Falub, S. W. H. Eijt, P. E. Mijnders, and J. Kurplach, Positron confinement in embedded lithium nanoclusters, *Phys. Rev. B* **65**, 085416 (2002).
- [22] C. V. Falub, P. E. Mijnders, S. W. H. Eijt, M. A. van Huis, A. van Veen, and H. Schut, Electronic structure and orientation relationship of Li nanoclusters embedded in MgO studied by depth-selective positron annihilation two-dimensional angular correlation, *Phys. Rev. B* **66**, 075426 (2002).
- [23] J. Xu, J. Moxom, B. Somieski, C. W. White, A. P. Mills, R. Suzuki, and S. Ishibashi, Positronic probe of vacancy defects on surfaces of Au nanoparticles embedded in MgO, *Phys. Rev. B* **64**, 113404 (2001).
- [24] M. A. van Huis, A. van Veen, H. Schut, B. J. Kooi, and J. T. M. De Hosson, Formation of solid Kr nanoclusters in MgO, *Phys. Rev. B* **67**, 235409 (2003).

- [25] Y. Nagai, T. Chiba, Z. Tang, T. Akahane, T. Kanai, M. Hasegawa, M. Takenaka, and E. Kuramoto, Fermi surface of nanocrystalline embedded particles in materials: Bcc Cu in Fe, *Phys. Rev. Lett.* **87**, 176402 (2001).
- [26] G. H. Dai, Q. J. Yan, Y. Wang, and Q. S. Liu, Li-doped MgO as catalysts for oxidative coupling of methane - a positron-annihilation study, *Chem. Phys.* **155**, 275 (1991).
- [27] G. Colombi, T. De Krom, D. Chaykina, S. Cornelius, S. W. H. Eijt, and B. Dam, Influence of cation (re = Ssc, Y, Gd) and O/H anion ratio on the photochromic properties of  $\text{REO}_x\text{H}_{3-2x}$  thin films, *Acs Photonics* **8**, 709 (2021).
- [28] J. Tauc, R. Grigorovici, and A. Vancu, Optical properties and electronic structure of amorphous germanium, *Phys. Status Solidi.* **15**, 627 (1966).
- [29] B. Barbiellini, P. Genoud, and T. Jarlborg, Calculation of positron lifetimes in bulk materials, *J Phys-Condens Mat.* **3**, 7631 (1991).
- [30] Reinhard Krause-Rehberg, Hartmut S. Leipner, *Positron Annihilation in Semiconductors - Defect Studies* (Springer-Verlag, Berlin, 1999).
- [31] A. Wagner, M. Butterling, M. O. Liedke, K. Potzger, and R. Krause-Rehberg, Positron annihilation lifetime and doppler broadening spectroscopy at the ELBE facility, *AIP Conf. Proc.* **1970**, 040003 (2018).
- [32] E. Hirschmann, M. Butterling, U. H. Acosta, M. O. Liedke, A. G. Attallah, P. Petring, M. Görler, R. Krause-Rehberg, and A. Wagner, A new system for real-time data acquisition and pulse parameterization for digital positron annihilation lifetime spectrometers with high repetition rates, *J. Instrum.* **16**, P08001 (2021).
- [33] J. V. Olsen, P. Kirkegaard, and M. Eldrup, Analysis of positron lifetime spectra using the PALSfit3 program, *AIP Conf. Proc.* **2182**, 040005 (2019).
- [34] K. Eufinger, D. Poelman, H. Poelman, R. De Gryse, and G. B. Marin, Photocatalytic activity of dc magnetron sputter deposited amorphous  $\text{TiO}_2$  thin films, *Appl. Surf. Sci.* **254**, 148 (2007).
- [35] D. Chaykina, I. Usman, G. Colombi, H. Schreuders, B. Tyburska-Pueschel, Z. Wu, S. W. H. Eijt, L. J. Bannenberg, G. A. de Wijs, and B. Dam, Aliovalent calcium doping of yttrium oxyhydride thin films and implications for photochromism, *J. Phys. Chem. C* **126**, 14742 (2022).
- [36] V.J. Ghosh, Positron implantation profiles in elemental and multilayer systems, *Appl. Surf. Sci.* **85**, 187 (1995).
- [37] A. Zubiaga, J. A. Garcia, F. Plazaola, F. Tuomisto, J. Zuniga-Perez, and V. Munoz-Sanjose, Positron annihilation spectroscopy for the determination of thickness and defect profile in thin semiconductor layers, *Phys. Rev. B* **75**, 205305 (2007).
- [38] W. Brandt, S. Berko, and W. W. Walker, Positronium decay in molecular substances, *Phys. Rev.* **120**, 1289 (1960).

- [39] R. S. Vallery, P. W. Zitzewitz, and D. W. Gidley, Resolution of the orthopositronium-lifetime puzzle, *Phys. Rev. Lett.* **90**, 203402 (2003).
- [40] C. Hugenschmidt, Positrons in surface physics, *Surf. Sci. Rep.* **71**, 547 (2016).
- [41] S. J. Tao, Positronium annihilation in molecular substances, *J. Chem. Phys.* **56**, 5499 (1972).
- [42] M. Eldrup, D. Lightbody, and J. N. Sherwood, The temperature-dependence of positron lifetimes in solid pivalic acid, *Chem. Phys.* **63**, 51 (1981).
- [43] D. Chaykina, T. de Krom, G. Colombi, H. Schreuders, A. Suter, T. Prokscha, B. Dam, and S. Eijt, Structural properties and anion dynamics of yttrium dihydride and photochromic oxyhydride thin films examined by *in situ*  $\mu^+$ SR, *Phys. Rev. B* **103**, 224106 (2021).
- [44] K. K. Ng, F. C. Zhang, V. I. Anisimov, and T. M. Rice, Electronic structure of lanthanum hydrides with switchable optical properties, *Phys. Rev. Lett.* **78**, 1311 (1997).
- [45] A. Uedono, T. Tanaka, N. Ito, K. Nakahara, W. Egger, C. Hugenschmidt, S. Ishibashi, and M. Sumiya, Electron capture by-vacancy-type defects in carbon-doped GaN studied using monoenergetic positron beams, *Thin Solid Films* **639**, 78 (2017).
- [46] K. Saarinen, P. Hautojarvi, P. Lanki, and C. Corbel, Ionization levels of As vacancies in as-grown GaAs studied by positron-lifetime spectroscopy, *Phys. Rev. B* **44**, 10585 (1991).
- [47] S. Kuisma, K. Saarinen, P. Hautojarvi, C. Corbel, and C. LeBerre, Optical processes related to arsenic vacancies in semi-insulating GaAs studied by positron spectroscopy, *Phys. Rev. B* **53**, 9814 (1996).
- [48] S. Arpiainen, K. Saarinen, P. Hautojärvi, L. Henry, M. F. Barthe, and C. Corbel, Optical transitions of the silicon vacancy in 6H-SiC studied by positron annihilation spectroscopy, *Phys. Rev. B* **66**, 075206 (2002).
- [49] H. Kauppinen, C. Corbel, J. Nissila, K. Saarinen, and P. Hautojarvi, Photoionization of the silicon divacancy studied by positron-annihilation spectroscopy, *Phys. Rev. B* **57**, 12911 (1998).
- [50] G. Colombi, B. Boshuizen, D. Chaykina, L. Y. Hsu, H. Schreuders, T. J. Savenije, and B. Dam, Large polaron conduction, photoconductivity, and photochromism in  $\text{GdH}_x\text{O}_{3-2x}$  oxyhydride thin films, *Adv. Opt. Mater.* **11** 2202660 (2023).
- [51] T. Friessnegg, S. Madhukar, B. Nielsen, A. R. Moodenbaugh, S. Aggarwal, D. J. Keeble, E. H. Poindexter, P. Mascher, and R. Ramesh, Metal ion and oxygen vacancies in bulk and thin film  $\text{La}_x\text{Sr}_{1-x}\text{CoO}_3$ , *Phys. Rev. B* **59**, 13365 (1999).
- [52] M. J. Puska and R. M. Nieminen, Theory of positrons in solids and on solid-surfaces, *Rev. Mod. Phys.* **66**, 841 (1994).
- [53] D. J. Keeble, S. Singh, R. A. Mackie, M. Morozov, S. McGuire, and D. Damjanovic, Cation vacancies in ferroelectric  $\text{PbTiO}_3$  and  $\text{Pb}(\text{Zr,Ti})\text{O}_3$ : A positron annihilation lifetime spectroscopy study, *Phys. Rev. B* **76**, 144109 (2007).



- [54] J. Mahony and P. Mascher, Positron-annihilation study of vacancy defects in InAs, *Phys. Rev. B* **55**, 9637 (1997).
- [55] P. Hautojarvi, Defects in semiconductors - recent progress in positron experiments, *Mater. Sci. Forum* **175**, 47 (1995).
- [56] G. Brauer, W. Anwand, P. G. Coleman, J. Stormer, F. Plazaola, J. M. Campillo, Y. Pacaud, and W. Skorupa, Post-implantation annealing of SiC studied by slow-positron spectroscopies, *J. Phys.-Condens. Mat.* **10**, 1147 (1998).
- [57] J. Crank, *The mathematics of diffusion* (Oxford University Press, London, 1975), second edition.
- [58] D. B. Cassidy and A. P. Mills, The production of molecular positronium, *Nature* **449**, 195 (2007).
- [59] B. S. Cooper, A. M. Alonso, A. Deller, L. Liskay, and D. B. Cassidy, Positronium production in cryogenic environments, *Phys. Rev. B* **93**, 125305 (2016).



## Supplementary information for Chapter 4

### DB-PAS depth profiles and VEPFIT analysis

DB-PAS experiments were carried out using the variable energy positron (VEP) beam setup at the TU Delft Reactor Institute [1]. The intensity of the positron beam at sample position is around  $10^4$  e<sup>+</sup>/s and the FWHM of the beam diameter is around 8 mm. The momentum windows for the S- and W-parameter were set at  $|p| < 3.0 \times 10^{-3} m_0c$  and  $8.2 \times 10^{-3} m_0c < |p| < 23.4 \times 10^{-3} m_0c$ , respectively. The collected depth profiles with implantation energies of 0.1–25 keV were fitted by VEPFIT to extract the fractions of positrons annihilating in each layer and the Doppler parameters of the yttrium oxyhydride layer [2]. The fractions of positrons annihilating in each layer extracted from the VEPFIT analyses of the depth profiles for the YHO-2 sample before illumination is shown in Fig. S4.1.

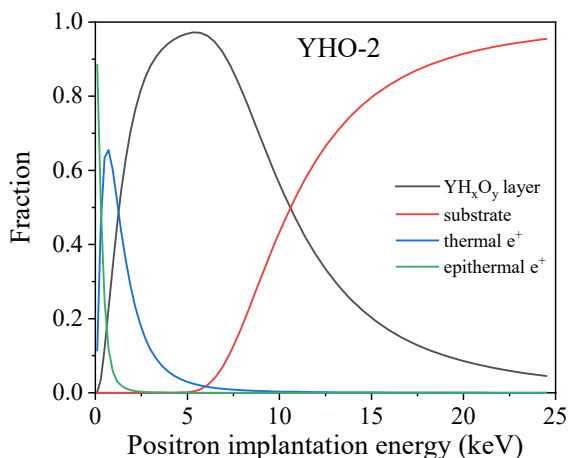


Figure S4.1: The fractions of positrons annihilating in each layer for the YHO-2 thin-film sample as a function of positron implantation energy derived by VEPFIT analysis.

The DB-PAS S- and W- parameter depth profiles for YHO-1 and YHO-2 thin-film samples before illumination and after the photodarkening-bleaching cycle are shown in Figure S4.2 and S4.3, respectively. The same light source as in the transmittance measurement equipped with a Köhler lens system was used to illuminate the sample for the DB-PAS experiments. A two-layer model including a oxyhydride layer and a semi-infinite fused silica substrate layer was used to fit depth profiles. A density of  $4.3 \text{ g/cm}^3$  and  $2.2 \text{ g/cm}^3$  was used for the  $\text{YH}_x\text{O}_y$  and the substrate layer, respectively. In order to minimize the number of fit parameters, the thickness ( $d$ ) of the oxyhydride layer of the  $\text{YH}_x\text{O}_y$  samples was fixed to 360 nm. For the substrate layer, the positron diffusion length ( $L_d$ ) of the fused- $\text{SiO}_2$  substrate layer was fixed to 25 nm, and the S-parameter and W-parameter were fixed to

0.526 and 0.062, respectively, as extracted from the high implantation energy range (20-25 keV). The corresponding results of the best-fit analysis are shown in Table S4.1.

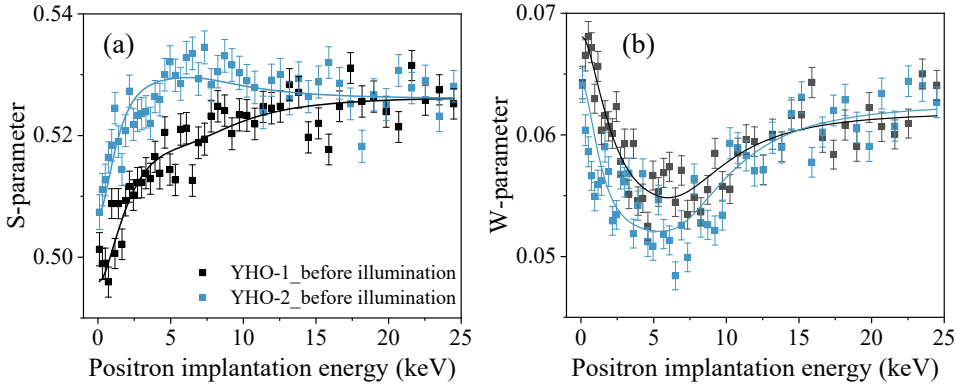


Figure S4.2: DB-PAS (a) S-parameter and (b) W-parameter depth profiles of YHO-1 (black color) and YHO-2 (blue color) thin-film samples before illumination.

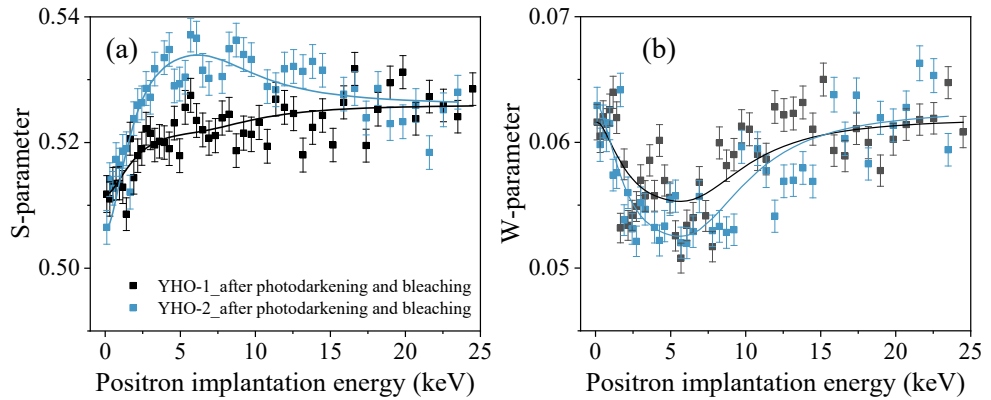


Figure S4.3: DB-PAS (a) S-parameter and (b) W-parameter depth profiles of YHO-1 (black color) and YHO-2 (blue color) thin-film samples after photodarkening and bleaching.

Table S4.1: The best-fit parameters of DB-PAS depth profiles for the oxyhydride layer of YHO-1 and YHO-2 thin-film samples before illumination and after the photodarkening-bleaching cycle.

Sample	State	$d$ (nm)	S	W	$L_d$ (nm)
YHO-1	Before illumination	360	0.519 (1)	0.0538 (3)	30 (1)
	After photodarkening and bleaching	360	0.522 (1)	0.0545 (3)	28 (2)
YHO-2	Before illumination	360	0.530 (1)	0.0518 (2)	16 (1)
	After photodarkening and bleaching	360	0.535 (1)	0.0519 (2)	24 (1)

### Three-component analysis PALS depth profiles

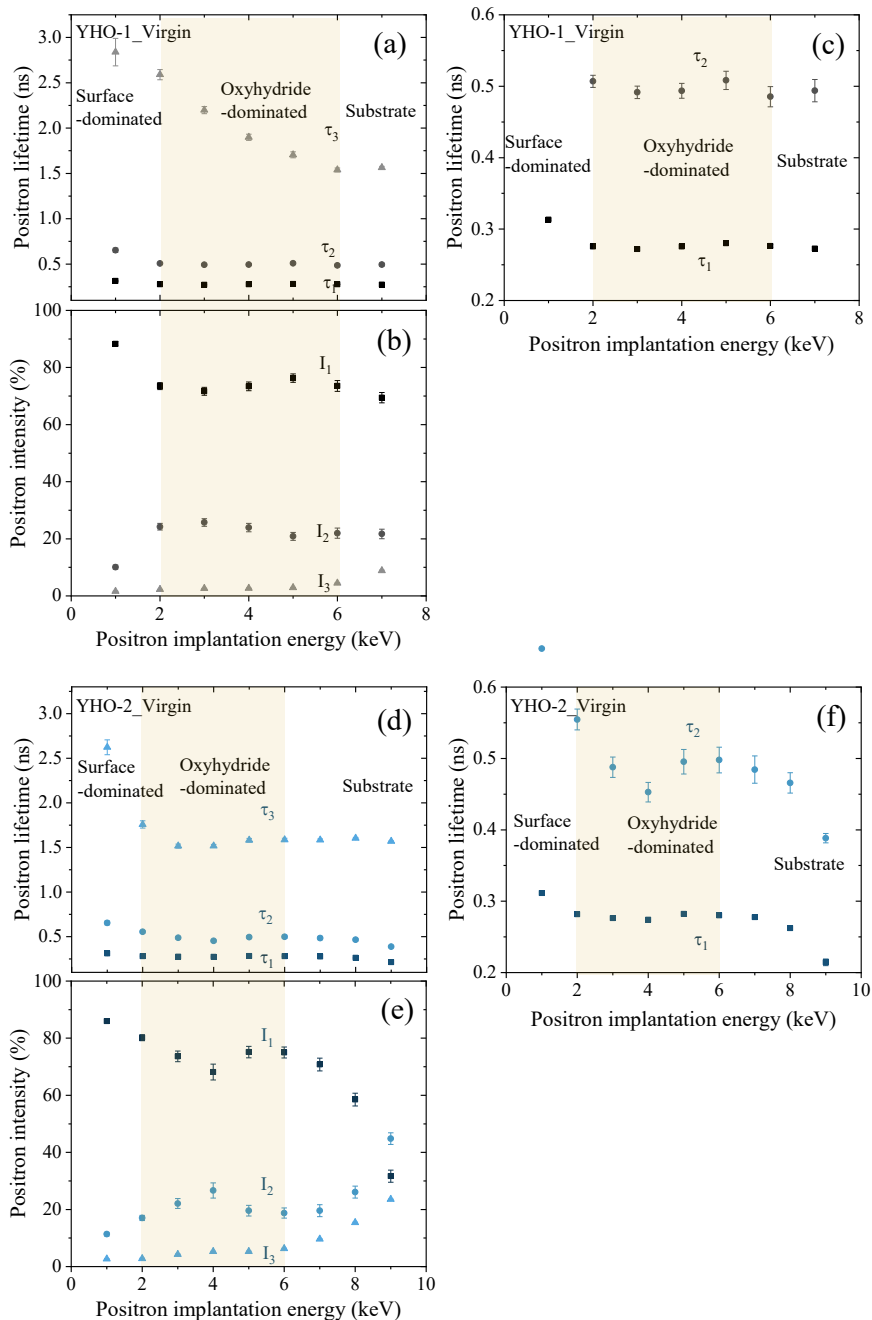


Figure S4.4: Positron lifetimes ( $\tau_i$ ) and the corresponding intensities ( $I_i$ ) as function positron implantation energy for YHO-1 (a-c) and YHO-2 (d-f) thin-film samples in the virgin state.

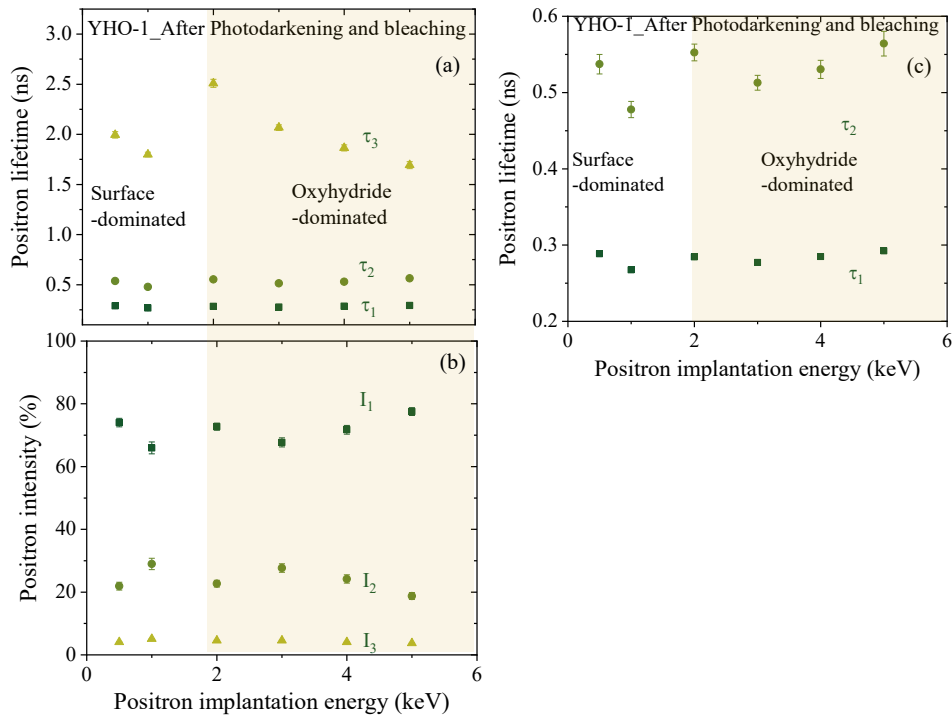


Figure S4.5: Positron lifetimes ( $\tau_i$ ) and the corresponding intensities ( $I_i$ ) as function positron implantation energy for the YHO-1 thin-film sample after the photodarkening-bleaching cycle.

### Positron lifetime calculation methods

We employed the self-consistent two-component density functional theory (TCDFT) calculations in the open-source ABINIT package to calculate the positron bulk lifetime in  $\text{YH}_{1.9}$  [3,4]. Calculations were performed with the  $Fm\bar{3}m$  structure of  $\text{YH}_{1.9}$  using a  $2 \times 2 \times 2$  supercell containing 92 atoms. The atomic configurations were produced using the ATOMPAW code [5]. The ground states of electrons and the positron were calculated by the projector augmented wave (PAW) method. The exchange-correlation interactions were described by the local density approximation (LDA) and the generalized gradient approximation (GGA). For LDA, we employed the Teter-Pade parametrization [6] and the Zero-positron density limit of Arponen and Pajanne, as implemented by Boronski and Nieminen [7]. For the GGA calculations, the Perdew-Burke-Ernzerhof functional [8] was combined with the same exchange-correlation functionals as we used for LDA, supplemented by correction terms provided by Barbiellini et al. [4]. All positron lifetimes were calculated using the enhancement factor given by Boronski and Nieminen in the random phase approximation (RPA) limit [7].

## Photochromic properties for sample YHO-a for three subsequent photodarkening-bleaching cycles

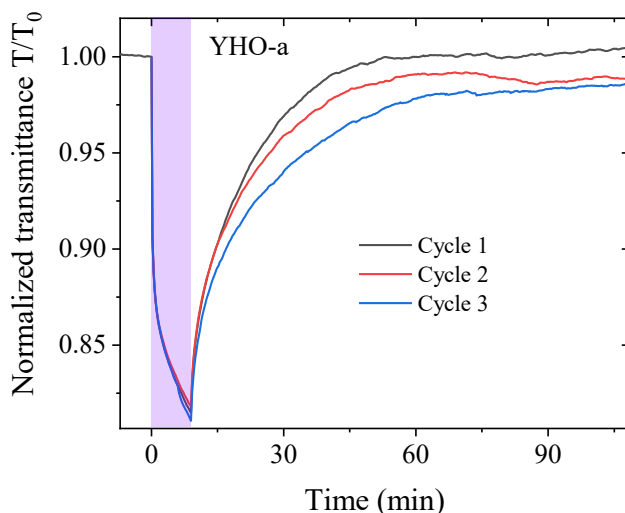


Figure S4.6: Optical transmittance normalized to the initial transmittance ( $T/T_0$ ), averaged in the wavelength range of 450-1000 nm for sample YHO-a during three short photodarkening (~9 min, purple shaded region)-bleaching cycles.

## References

- [1] H. Schut, A Variable Energy Positron Beam Facility with Applications in Materials Science, Ph.D. thesis, Delft University of Technology, Delft, 1990.
- [2] A. van Veen, H. Schut, J. Devries, R. A. Hakvoort, and M. R. Ijpma, Analysis of positron profiling data by means of VEPFIT, AIP Conf. Proc. **218**, 171 (1990).
- [3] M. Torrent, F. Jollet, F. Bottin, G. Zerah, X. Gonze, Implementation of the projector augmented-wave method in the ABINIT code: Application to the study of iron under pressure, Comput. Mater. Sci., **42**, 337 (2008).
- [4] B. Barbiellini, M. J. Puska, T. Torsti, and R. M. Nieminen, Gradient correction for positron states in solids, Phys. Rev. B **51**, 7341 (1995).
- [5] N. A. W. Holzwarth, A. R. Tackett, and G. E. Matthews, A Projector Augmented Wave (PAW) code for electronic structure calculations, Part I: atompaw for generating atom-centered functions, Comput. Phys. Commun. **135**, 329 (2001).
- [6] S. Goedecker, M. Teter, and J. Hutter, Separable dual-space gaussian pseudopotentials, Phys. Rev. B **54**, 1703 (1996).

- [7] E. Boronski and R. M. Nieminen, Electron-positron density-functional theory, *Phys. Rev. B* **34**, 3820 (1986).
- [8] J. P. Perdew, K. Burke, and M. Ernzerhof, Generalized gradient approximation made simple, *Phys. Rev. Lett.* **77**, 3865 (1996).



**5. The formation of metallic domains by  
Anderson-Mott insulator-to-metal transition in  
photochromic yttrium oxyhydride films studied  
by in-situ spectroscopic ellipsometry**

## Abstract

The color-neutral photochromic properties make yttrium oxyhydride films attractive for various applications from smart windows to memory devices. However, the mechanism behind the photochromic effect is not fully clarified. In this study, the optical constants of as-prepared semiconducting  $\text{YH}_x\text{O}_y$  as well as metallic  $\text{YH}_{2.9}$ ,  $\text{YH}_x$  and  $\text{Y}$  thin films are accurately determined by spectroscopic ellipsometry. The observed changes in the optical dielectric function of  $\text{YH}_x\text{O}_y$  during photodarkening are examined employing three different models. First, by applying the Bruggeman effective medium approximation to the ellipsometry data of the photodarkened  $\text{YH}_x\text{O}_y$  film, the best fit obtained corresponds to the formation of a few percent of  $\text{YH}_x$  metallic inclusions within the semiconducting  $\text{YH}_x\text{O}_y$  matrix. Nevertheless, this model is questionable, as it would necessitate the reversible rearrangements and transport of a significant amount of both oxygen and hydrogen. Secondly, as an alternative model, the changes in the dielectric function of the  $\text{YH}_x\text{O}_y$  film in the UV to near-IR range during photodarkening, as derived by employing a Kramers-Kronig consistent basic-spline approach, turn out very similar to those accompanying the optical transition from semiconducting  $\text{YH}_{2.9}$  to metallic  $\text{YH}_{2.5}$  films examined in previous studies on hydrogen switchable mirrors. This suggests that the Anderson-Mott insulator-to-metal transition that occurs in these rare-earth hydride systems also takes place in certain regions of the photodarkened  $\text{YH}_x\text{O}_y$  film, constituting up to ~4% of the film. Finally, a third model, that is based on the formation of small bandgap yttrium monoxide-like domains, can be dismissed as the main origin of the photodarkening of photochromic  $\text{YH}_x\text{O}_y$  films, as the largest photochromic contrast is observed in hydrogen-rich oxyhydride films rather than for compositions close to  $\text{YHO}$ .

## 5.1 Introduction

Yttrium oxyhydride ( $\text{YH}_x\text{O}_y$ ) thin films have received considerable attention since they were discovered to show the color-neutral photochromic effect under ambient conditions in 2011 [1].  $\text{YH}_x\text{O}_y$  films are transparent semiconductors. Upon optical excitation above the bandgap,  $\text{YH}_x\text{O}_y$  films become dark, and the sub-bandgap transmittance reduces in a broad wavelength range from the visible to near infrared (IR). The transparency can be recovered after switching off the light source. The photochromic effect also occurs in other rare-earth oxyhydride films including Gd, Sc, Nd, Dy, Er, and Sm oxyhydride films [2-7]. The photochromic property renders them to be promising candidates for smart windows [8].

However, the mechanism of the photochromic effect and the microstructural origin of photodarkening in oxyhydride films is not fully clarified. The formation of metallic domains was proposed to be responsible for the photodarkening [9-12]. For instance, Montero *et al.* proposed that the photodarkening is correlated with the formation of metallic domains, since the ellipsometry data of the photodarkened  $\text{YH}_x\text{O}_y$  could be well described by the formation of metallic domains at a volume fraction of up to ~6% of the film within a semiconducting  $\text{YH}_x\text{O}_y$  matrix, as was deduced employing an effective medium approximation [9]. In addition, our previous positron annihilation experiments also support mechanisms that involve the formation of metallic domains, based on the observed (partially) reversible shifts of Doppler parameters towards those of metal hydrides [10] (Chapter 2). In ref. [10], two possible types of metallic domains were proposed. The first proposed type corresponds to phase-segregated H-rich domains  $\text{YH}_2\text{O}_x$  ( $x < 0.5$ ), while the second proposed type is related to an Anderson-Mott insulator-to-metal transition in nanoscale domains, resulting from the overlap in electron wave functions of photo-excited electrons trapped at Y(4d) orbitals around light-induced hydrogen vacancies at the octahedral sites. Despite these efforts, the exact nature of the metallic domains causing the photochromic effect in oxyhydride films remained unsettled.

In this study, we employ spectroscopic ellipsometry in order to examine the nature of the metallic regions formed during photodarkening. We first report the optical constants of as-prepared  $\text{YH}_x\text{O}_y$  and  $\text{YH}_{-2}$ ,  $\text{YH}_x$  and Y films. By employing a Bruggeman effective medium approximation (BEMA) model to fit the ellipsometry data obtained in the photodarkened state of  $\text{YH}_x\text{O}_y$  films [13], we examine whether formed Y,  $\text{YH}_x$  or  $\text{YH}_{-2}$  metallic domains in the semiconducting  $\text{YH}_x\text{O}_y$  matrix can explain the optical properties extracted from spectroscopic ellipsometry of the  $\text{YH}_x\text{O}_y$  film during photodarkening. Secondly, we examine whether the formation of metallic domains is related to a hydrogen vacancies-induced insulator-to-metal transition, similar to the  $\text{YH}_{2.9} \rightarrow \text{YH}_{2.5}$  hydrogen switchable mirror system. Here, the optical dielectric function of  $\text{YH}_x\text{O}_y$  during photodarkening is obtained by fitting the ellipsometry data to a Kramers-Kronig-consistent basic-spline (B-Spline) model, and we compared the evolution of the dielectric function to characteristic changes in the dielectric function previously reported for the  $\text{YH}_{2.9} \rightarrow \text{YH}_{2.5}$  system. Finally, the formation of yttrium

monoxide-like (YO) domains in the semiconducting  $\text{YH}_x\text{O}_y$  matrix is examined and discussed.

## 5.2 Experimental

### 5.2.1 Sample preparation and structural characterization

The Yttrium dihydride and oxyhydride films were deposited by reactive direct current (DC) magnetron sputtering of an yttrium metal target in an Ar/H<sub>2</sub> gas mixture with a 7:1 ratio. The total pressure is 0.3 Pa and 0.5 Pa for dihydride and oxyhydride films, respectively. For the latter case, the incorporation of O into the bulk dihydride phase occurs during post-oxidation in air, as this deposition pressure exceeded the critical pressure necessary to induce sufficient porosity of the dihydride film, enabling the subsequent formation of the semiconducting  $\text{YH}_x\text{O}_y$  phase [2]. Another type of yttrium hydride film was deposited at 0.3 Pa but a higher Ar/H<sub>2</sub> ratio of 19:1 was used. This yttrium hydride film is denoted as  $\text{YH}_x$ , because the applied lower H<sub>2</sub> flow results in a lower H content in the hydride film compared to  $\text{YH}_2$ . Both  $\text{YH}_x$  and  $\text{YH}_{-2}$  films do not incorporate oxygen in the bulk of the films upon air exposure, but some oxidation on the surface could occur [14,15]. The yttrium metal film was deposited at 0.3 Pa in a pure Argon atmosphere. All films were deposited on unheated UV-grade fused silica (f-SiO<sub>2</sub>) substrates. Table 5.1 summarizes the Y-based thin films studied in this work and the corresponding deposition conditions and basic properties.

XRD patterns were collected on a PANalytical X'Pert PRO diffractometer at an incident angle of 2° with a Cu "K $\alpha$ " source ( $\lambda = 1.54 \text{ \AA}$ ) at room temperature. The lattice parameters of all as-prepared films were obtained by refining XRD patterns using Fullprof [16].

Table 5.1: Summary of the Y-based thin films studied in this work and the corresponding deposition conditions and basic properties.

Film	Deposition pressure (Pa)	Ar:H <sub>2</sub> (sccm <sup>†</sup> )	flow	Thickness (nm) <sup>‡</sup>	Appearance
Y	0.3	35:0		~300	opaque
$\text{YH}_x$	0.3	38:2		~300	opaque
$\text{YH}_{-2}$	0.3	35:5		~300	opaque
$\text{YH}_x\text{O}_y$	0.5	35:5		~370	transparent

<sup>†</sup>standard cubic centimeters per minute (sccm)

<sup>‡</sup>The thickness listed here were determined by profilometry with ~10% of uncertainty.

### 5.2.2 Transmittance measurements and photochromic effect

Optical transmittance measurements were carried out in the wavelength range of 230-1120 nm employing a custom-built setup equipped with a white source (DH-2000BAL, Ocean Optics) and a silicon CCD array spectrometer (HR4000, Ocean Optics). The light source for triggering the photochromic effect was a narrow wavelength LED (385 nm, I ~ 30 mW/cm<sup>2</sup>).

The same wavelength LED equipped with a Köhler lens system with the same intensity was utilized for the spectroscopic ellipsometry experiments under illumination.

### 5.2.3 Spectroscopic ellipsometry measurements and fitting

Variable-angle spectroscopic ellipsometry is used to determine the optical constants of the films by measuring the changes in polarization of incident light reflected from the sample. The changes in the polarization upon reflectance from the sample are described by two parameters, psi ( $\Psi$ ) and delta ( $\Delta$ ), defined by the equation  $\rho = \frac{r_p}{r_s} = \tan(\Psi) e^{i\Delta}$ , where  $r_p$  and  $r_s$  are the complex reflection coefficient for p-polarized light (polarized parallel to the plane of incidence) and s-polarized light (polarized perpendicular to the plane of incidence).

The  $\Psi$  and  $\Delta$  are measured in the wavelength range of 191-1688 nm using a M-2000DI Ellipsometer (J. A. Woollam Co.) at room temperature. Incidence angles of 60-70° and 50-70° at an interval of 5° are used for the semiconducting oxyhydride and metallic films, respectively, to obtain adequate sensitivity in the spectral range. A Magic™ tape is stuck to the back of the sample (f-SiO<sub>2</sub> sides) in order to reduce backscattering of light for transparent samples. In order to monitor the changes in optical constants of YH<sub>x</sub>O<sub>y</sub> during photodarkening, ellipsometry data is collected at illumination times of 10, 30, 60, 90, 120, and 150 min. The CompleteEASE software is utilized for data collecting and spectral analyses.

The real and imaginary part of the complex refractive index  $n$  and  $k$  are obtained by fitting  $\Psi$  and  $\Delta$  to mathematical models. The real and imaginary part of the dielectric function  $\varepsilon_1$  and  $\varepsilon_2$  are subsequently calculated from  $n$  and  $k$ , based on the equations  $\varepsilon_1 = n^2 - k^2$  and  $\varepsilon_2 = 2nk$ . For the optically thick metallic Y, YH<sub>x</sub> and YH<sub>2</sub> films, a general-oscillator (GEN-OCS) model containing Drude and three Lorentz oscillators is applied to fit the ellipsometry spectra, enabling comparison to data reported in previous studies [9,17-19]. The GEN-OCS guarantees Kramers-Kronig (KK) consistency, meaning that the shape of the real component can be calculated from the imaginary component.

For the YH<sub>x</sub>O<sub>y</sub> thin-film sample before illumination and during photodarkening, a three-layer model containing a surface roughness layer, an oxyhydride layer, and a substrate layer, is used to extract the optical constants of the yttrium oxyhydride layer. In order to reduce the number of fitting parameters for the three-layer model, the parameters for the substrate layer, the roughness layer, and the thickness of the oxyhydride layer are fixed. The A and B parameters of the substrate f-SiO<sub>2</sub> are set to 1.45 and 0.005, determined by a Cauchy model ( $n(\lambda) = A + B/\lambda^2$ ) from an independent measurement on a bare f-SiO<sub>2</sub> substrate. The surface roughness of YH<sub>x</sub>O<sub>y</sub> is determined to be around 6 nm by a BEMA model, where it was assumed that the roughness layer consists of a mixed layer with 50% oxyhydride and 50% air ( $n = 1$ ,  $k = 0$ ). The thickness of the YH<sub>x</sub>O<sub>y</sub> layer is determined to be ~345 nm by fitting the transparent range ( $\lambda > 500$  nm) by a Cauchy model.

For the  $\text{YH}_x\text{O}_y$  layer in the as-prepared transparent  $\text{YH}_x\text{O}_y$  sample, a Cauchy model combined with an Urbach absorption tail is used to fit the ellipsometry data. For the  $\text{YH}_x\text{O}_y$  layer in the photodarkened  $\text{YH}_x\text{O}_y$  sample, the ellipsometry data is simulated using either a BEMA or a Kramers-Kronig-consistent basis-spline (B-spline) approach. The B-spline approach is very suitable for materials that are semi-absorbing in either part of the spectral range or in the whole range, and does not assume any physical properties of the layer besides the presence of a roughness layer and an oxyhydride layer on top of the substrate [20,21]. Physically meaningful results can be ensured by enforcing Kramers-Kronig consistency and a positive  $\varepsilon_2(\lambda) > 0$  [22]. The goodness of each fit is quantified by its mean squared error (MSE), which reflects the difference between modelling data and experimental data. An MSE value below 20 is generally acceptable [20].

## 5.3 Results and discussion

### 5.3.1 The crystal structure and optical constants of as-prepared semiconducting $\text{YH}_x\text{O}_y$ and metallic Y, $\text{YH}_x$ , $\text{YH}_{-2}$ thin films

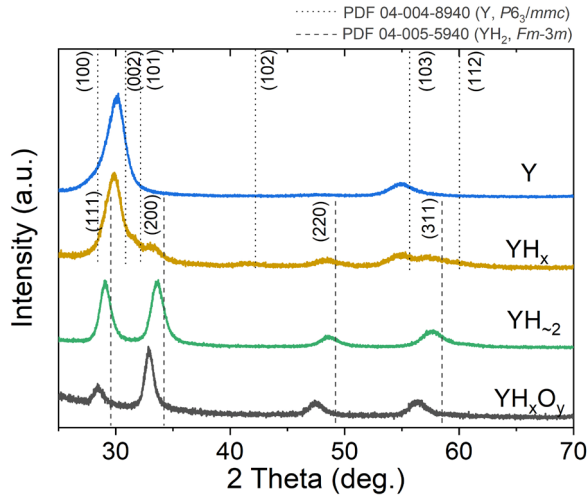


**Figure 5.1:** XRD patterns of as-prepared  $\text{YH}_x\text{O}_y$  and Y,  $\text{YH}_x$ ,  $\text{YH}_{-2}$  thin films, compared with lines from the reference patterns of  $P6_3/mmc$  Y #04-004-8940 (vertical dot lines) and  $Fm-3m$   $\text{YH}_2$  #04-005-5940 (vertical dash lines).

The optical constants  $n(E)$ ,  $k(E)$  and corresponding dielectric function  $\varepsilon_1(E)$ ,  $\varepsilon_2(E)$  of as-prepared transparent semiconducting  $\text{YH}_x\text{O}_y$  and opaque metallic Y,  $\text{YH}_x$ ,  $\text{YH}_{-2}$  thin films are determined, since these optical constants will be used for modelling the ellipsometry data under photodarkening using an EMA model, assuming that either Y,  $\text{YH}_x$  or  $\text{YH}_{-2}$  metallic inclusions are embedded in a semiconducting  $\text{YH}_x\text{O}_y$  matrix. Before the spectroscopic

ellipsometry study, the composition, crystal structure and lattice parameters of the as-prepared transparent  $\text{YH}_x\text{O}_y$  and opaque Y,  $\text{YH}_x$ ,  $\text{YH}_{-2}$  thin films were determined by grazing-incidence X-ray diffraction (XRD). Fig. 5.1 shows the diffraction patterns of all as-prepared films, compared with peak positions of  $Fm-3m$   $\text{YH}_2$  (#04-005-5940) and  $P6_3/mmc$  Y (#04-004-8940). The diffraction peaks of  $\text{YH}_x\text{O}_y$  and  $\text{YH}_{-2}$  films are consistent with the positions of (111), (200) and (220) and (311) planes of the reference  $Fm-3m$   $\text{YH}_2$  (#04-005-5940), indicating the same cubic symmetry, in line with previous studies [5,14]. Compared to the reference  $Fm-3m$   $\text{YH}_2$ , all diffraction peaks of the  $\text{YH}_{-2}$  film shift to the lower angles, signaling a larger lattice parameter. The lattice parameter of the  $\text{YH}_{-2}$  film is refined to be  $5.28 \pm 0.01$  Å. Furthermore, all diffraction peaks of  $\text{YH}_x\text{O}_y$  shift to even lower angles compared to  $\text{YH}_{-2}$ , indicating that incorporation of O into the dihydride lattice enlarges the lattice parameters of the cubic structure. Interestingly, the incorporation of O into the dihydride lattice is also accompanied by a color change from opaque to transparent, indicating a metal-to-insulator transition. The lattice parameter of the  $\text{YH}_x\text{O}_y$  film is determined to be  $5.38 \pm 0.01$  Å.

Finally, the main diffraction peaks at  $30.6^\circ$  and  $54.9^\circ$  of the Y film match the lattice planes (002) and (103) of hexagonal Y with a space group of  $P6_3/mmc$ , and the corresponding lattice parameters are refined to be  $3.64 \pm 0.01$  Å and  $5.83 \pm 0.01$  Å for  $a$  and  $c$ . Compared to the reported lattice parameters of the reference  $Fm-3m$   $\text{YH}_2$  (#04-005-5940) and  $P6_3/mmc$  Y (#04-004-8940), the slightly larger lattice parameters of our Y and  $\text{YH}_{-2}$  films could be due to the strain induced by the lattice mismatch between the film and the f-SiO<sub>2</sub> substrate [23]. We notice that the diffraction pattern of the  $\text{YH}_x$  film contains two sets of diffraction peaks corresponding to Y and  $\text{YH}_{-2}$ , suggesting that the  $\text{YH}_x$  film is a composite of hexagonal Y phase and cubic  $\text{YH}_{-2}$  phase. The diffraction peak of the  $\text{YH}_x$  film peak with the largest intensity aligns well with the one of the (002) plane of the Y film, implying that the hexagonal Y phase is dominant in the  $\text{YH}_x$  film. The mixed-phase characteristic of the  $\text{YH}_x$  film results from a lower  $\text{H}_2$ :Ar ratio in the reactive magnetron sputtering process compared to the ratio used to synthesize the  $\text{YH}_{-2}$  film (see Table 5.1).

The optical constants of the as-prepared transparent  $\text{YH}_x\text{O}_y$  and opaque  $\text{YH}_{-2}$ ,  $\text{YH}_x$ , and Y films were determined by fitting the ellipsometry data to a Cauchy model with an Urbach tail and a GEN-OCS model containing Drude and three Lorentz oscillators. The MSE of the fits for the as-prepared  $\text{YH}_x\text{O}_y$ ,  $\text{YH}_{-2}$ ,  $\text{YH}_x$ , and Y films are 9, 5, 2 and 2, respectively, indicating that these are satisfying fits. The resultant real part (the refractive index  $n$ ) and imaginary part (the extinction coefficient  $k$ ) of the complex refractive index as well as the real part ( $\epsilon_1$ ) and imaginary part ( $\epsilon_2$ ) dielectric function of all as-prepared films are depicted in Fig. 5.2.

For the as-prepared transparent  $\text{YH}_x\text{O}_y$  film,  $k(E)$  and  $\epsilon_2(E)$  are almost zero for energies

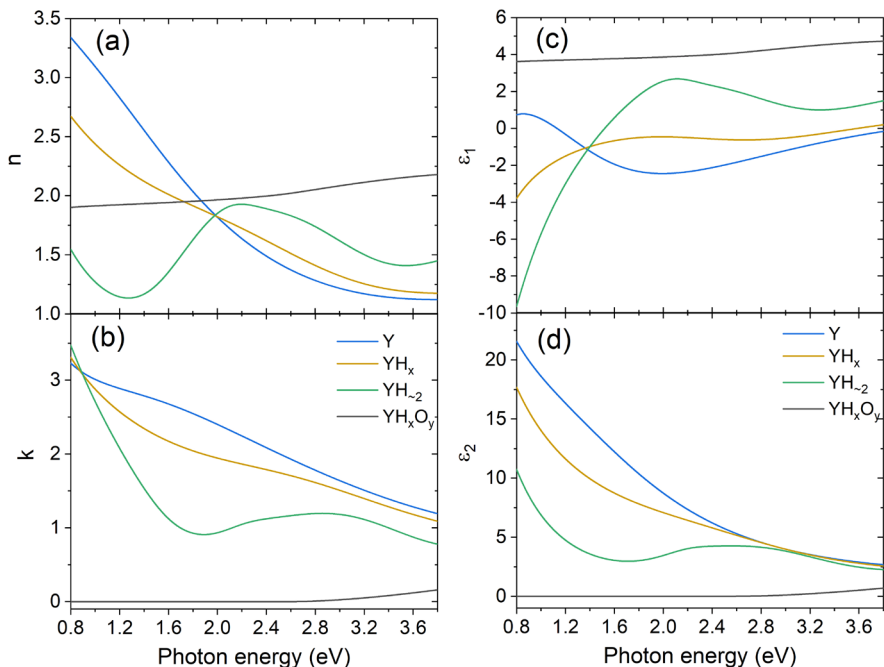


**Figure 5.2:** (a-b) the real part ( $n$ ) and imaginary part ( $k$ ) of the complex refractive index, as well as (c) and (d) the real part ( $\epsilon_1$ ) and imaginary part ( $\epsilon_2$ ) of the dielectric function as a function of photon energy  $E$  for as-prepared YH<sub>x</sub>O<sub>y</sub> and Y, YH<sub>x</sub>, YH<sub>-2</sub> films.

below the bandgap of  $\sim 2.56$  eV (as determined by Tauc analysis in the transmittance measurement), indicating the semiconducting nature of the film. The shape of the dispersion of  $n$  and  $\epsilon_1$  agrees well with that in the previous studies, and the value of  $n$  of 1.95 at a photon energy of 1.96 eV is comparable to previously reported values for YH<sub>x</sub>O<sub>y</sub> films [18,19]. Ref. [18] also showed the presence of an optical gradient and porosity of YH<sub>x</sub>O<sub>y</sub> films, but the corresponding gradient and porosity parameters in our YH<sub>x</sub>O<sub>y</sub> films were negligible in all used fit models. This implies that the YH<sub>x</sub>O<sub>y</sub> film studied here are denser and more homogenous, probably due to the lower deposition pressure employed than that in ref. [18]. Neither a gradient perpendicular to the substrate surface nor porosity were considered for the subsequent fits for the YH<sub>x</sub>O<sub>y</sub> film during photodarkening. The resultant total thickness of 351 nm includes 345 nm of the bulk YH<sub>x</sub>O<sub>y</sub> film and 6 nm of the rough surface layer, and agrees well with the thickness of  $\sim 370$  nm ( $\sim 10\%$  uncertainty) measured by profilometry.

For the opaque Y and YH<sub>-2</sub> metallic films, the shape of the dispersion of the extracted  $n$ ,  $k$  and  $\epsilon_1$ ,  $\epsilon_2$  is similar to the curves reported in [17-19], with slight quantitative differences that may result from the use of different deposition methods and sputtering conditions. The high values of the extinction coefficient  $k$  in the full spectral range for the YH<sub>-2</sub>, YH<sub>x</sub>, and Y films confirm the metallic character of these films. Comparing the optical curves of these three types of metallic films, the curves of YH<sub>x</sub> indicate that this film is a mixture of Y and



$\text{YH}_{-2}$  at a ratio of  $\sim 2:1$ . This is consistent with the XRD data in Fig. 5.1, which show that Y is the dominant phase in the  $\text{YH}_x$  film, while also diffraction peaks are observed that are characteristic for the presence of  $\text{YH}_{-2}$ . For all metallic films, the tails in the imaginary part at low photon energies ( $<1.5$  eV) are due to free carrier absorption, while the oscillations at higher energies correspond to interband transitions [17]. The corresponding fit parameters based on Drude and three Lorentz oscillators are shown in Table S5.1 and Table S5.2.

### 5.3.2 The photochromic effect

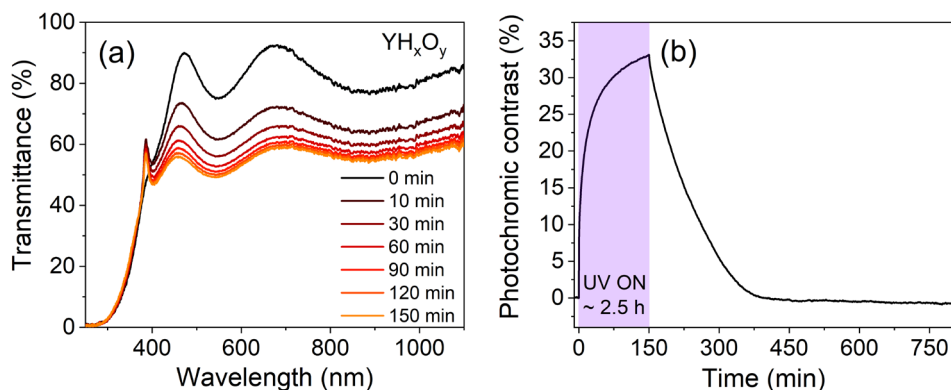


**Figure 5.3:** (a) Transmittance of the  $\text{YH}_x\text{O}_y$  thin-film sample as a function of wavelength at illumination times of 0, 10, 30, 60, 90, 120 and 150 min during UV illumination using a LED with a narrow wavelength of 385 nm, and (b) the corresponding photochromic contrast as a function of time before illumination, during 2.5 h photodarkening and the subsequent bleaching.

The photochromic effect of the  $\text{YH}_x\text{O}_y$  film is assessed by time-dependent optical transmittance measurements. The transmittance as a function of wavelength at illumination times of 0, 10, 30, 60, 90, 120 and 150 min for the  $\text{YH}_x\text{O}_y$  film is as shown in Fig. 5.3 (a). The  $\text{YH}_x\text{O}_y$  film before illumination shows a high transparency over a broad range from the visible to near-IR region, while the transmittance reduces upon illumination. The difference between the initial transmittance averaged in the wavelength range of 450 to 1000 nm  $T_0$  and the averaged transmittance in the same wavelength range at a time  $T$ , with respect to  $T_0$ , is defined as the photochromic contrast  $(T_0 - T)/T_0$ . The photochromic contrast as a function of time before illumination, during photodarkening of 2.5 h and the subsequent bleaching is shown in Fig. 5.3 (b). Upon illumination for 10 min, the photochromic contrast of the  $\text{YH}_x\text{O}_y$  film increases by  $\sim 18\%$ . During longer illumination times, the photo-darkening rate becomes progressively slower, and the photochromic contrast tends to saturate. After illumination for 150 min, the photochromic contrast increases up to  $\sim 33\%$ . When the light source is switched

off, the photochromic contrast starts to decrease, until full transparency is regained after bleaching in dark for ~200-250 min.

### 5.3.3 Spectroscopic ellipsometry study during photodarkening

In order to monitor the changes in the optical dielectric function of  $\text{YH}_x\text{O}_y$  thin films during illumination, a twin sample is employed for the spectroscopic ellipsometry experiments during illumination for 150 min with the same time intervals as in the transmittance measurements. By employing either a BEMA model or a Kramers-Kronig-consistent B-spline approach to fit the ellipsometry data of  $\text{YH}_x\text{O}_y$  in the photodarkened state, we examine three different models for the formation of metallic (or small bandgap semiconducting) light-absorbing domains in a semiconducting  $\text{YH}_x\text{O}_y$  matrix for explaining the photochromic effect.

#### A. Model 1: Yttrium (hydride)-like metallic domains

Montero *et al.* proposed the gradual formation of phase-segregated metallic  $\text{YH}_y\text{O}_z^m$  domains in the semiconducting matrix during photodarkening in order to explain the photochromic effect, in which the ellipsometry data was analyzed with an effective medium approximation (EMA) model [9]. Here, we employ a similar model, employing a Bruggemann EMA to fit the ellipsometry data during illumination, in which we assume that either Y,  $\text{YH}_x$ , or  $\text{YH}_{-2}$  metallic domains are formed in the otherwise homogenous semiconducting  $\text{YH}_x\text{O}_y$  matrix. This model assumes that the sizes of the domains are much smaller than the wavelengths of light and that these inclusions are non-interacting in an optical sense. The Bruggemann EMA is given by the equations below:

$$f_a \frac{\varepsilon_a - \varepsilon_{\text{EMA}}}{\varepsilon_a + \kappa \varepsilon_{\text{EMA}}} + f_b \frac{\varepsilon_b - \varepsilon_{\text{EMA}}}{\varepsilon_b + \kappa \varepsilon_{\text{EMA}}} = 0 \quad (5.1)$$

$$f_a + f_b = 1 \quad (5.2)$$

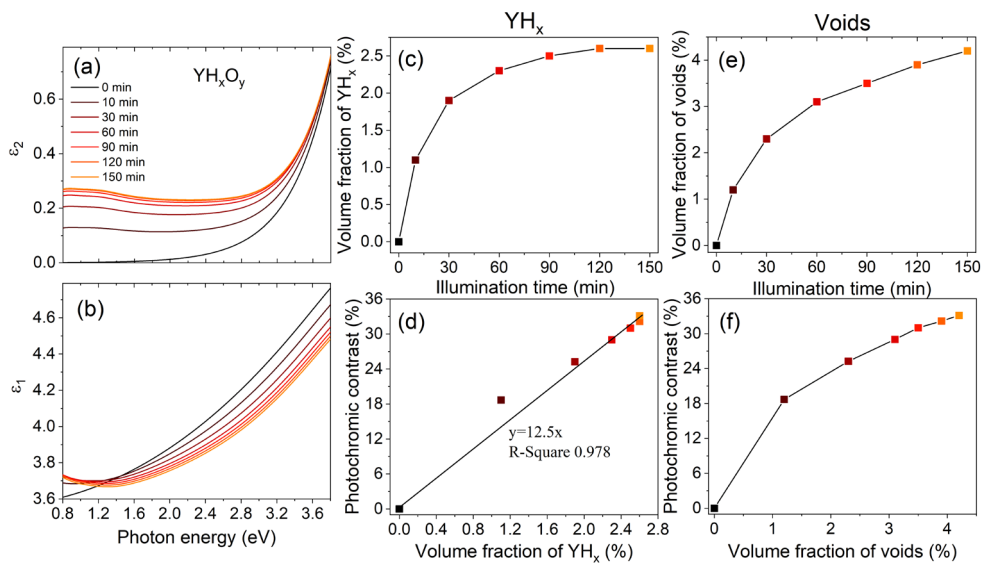
where  $\varepsilon_{\text{EMA}}$  is the dielectric function of the composite EMA layer,  $\varepsilon_a$  is the dielectric function of the  $\text{YH}_x\text{O}_y$  matrix,  $\varepsilon_b$  is the dielectric function of the metallic inclusions, consisting of either  $\text{YH}_{-2}$ ,  $\text{YH}_x$  or Y,  $f_a$  is the fraction of  $\text{YH}_x\text{O}_y$  and  $f_b$  is the fraction of inclusions,  $\kappa = (1 - L)/L$  is the screening parameter, where  $L$  is the depolarization factor.  $L$  is fixed to 1/3, corresponding to the assumption that the inclusions are spherical in shape [24]. The only remaining fit parameter is the fraction of yttrium (hydride) metallic domains ( $\text{YH}_{-2}$ ,  $\text{YH}_x$ , or Y), and the thickness of the photochromic layer is fixed to the one of the as-prepared oxyhydride film. The fraction of metallic domains in all cases is fitted to be of an order of magnitude of a few percent, specifically, 2%, 2.5% and 2.8% after 150 min of illumination for the case of  $\text{YH}_{-2}$ ,  $\text{YH}_x$ , and Y, respectively. As shown in Table S5.3, the  $\text{YH}_x$  case exhibits the lowest MSE, meaning the best agreement between the fits and experimental data in this model. However, the MSE values for the fits in this model exceed the acceptable threshold ( $>20$ ), showing that the photodarkening is not well described by the sole formation of spherically shaped Y,  $\text{YH}_x$  or  $\text{YH}_{-2}$  nanodomains.

Table 5.2: MSE of the fits using a BEMA model where metallic Y,  $\text{YH}_x$ , or  $\text{YH}_{-2}$  inclusions and voids are embedded in a homogenous semiconducting  $\text{YH}_x\text{O}_y$  layer.

	MSE (Y+voids)	MSE ( $\text{YH}_x$ +voids)	MSE ( $\text{YH}_{-2}$ +voids)
10 min	18	14	22
30 min	20	15	27
60 min	22	15	29
90 min	22	15	30
120 min	23	16	30
150 min	23	16	30

We found that including the formation of nanovoids in addition to metallic domains, which introduces an additional fit parameter in the BEMA model, can substantially improve the goodness of the fits for all cases. The fraction of metallic domains in this model is comparable to that in the previous model, while a significant fraction of voids are obtained in the best-fits for the case of  $\text{YH}_{-2}$ ,  $\text{YH}_x$ , and Y inclusions of 2.6%, 4.2%, and 4.6%, respectively, after 150 min of photodarkening. We show representative ellipsometry spectra collected at incident angles of  $60^\circ$ ,  $65^\circ$ , and  $70^\circ$  and corresponding fits using a BEMA model, where either  $\text{YH}_x$  metallic domains and voids (Fig. S5.1), Y metallic domains and voids, or  $\text{YH}_2$  metallic domains and voids (Fig. S5.2) are embedded in a  $\text{YH}_x\text{O}_y$  matrix after illumination of 10 min and 150 min. The corresponding MSE values for all cases are listed in Table 5.2.

As indicated in Table 5.2, the best fits (lowest MSE) are again found for the case of  $\text{YH}_x$  metallic inclusions. The corresponding imaginary and real component of the dielectric function ( $\varepsilon_2$  and  $\varepsilon_1$ ) as a function of photon energy at illumination times of 10, 30, 60, 90, 120, 150 min are shown in Fig. 5.4 (a) and (b). The evolution of the respective real part (n) and imaginary part (k) of the complex refractive index can be found in Fig. S5.5. The imaginary part of the dielectric function  $\varepsilon_2$  increases with illumination time over a broad range covering the visible and near-IR region, while the real part of the dielectric function  $\varepsilon_1$  decreases in a wide range, with a dispersion that is due to the Kramers-Kronig consistency. Fig. 5.4 (c) and (e) show the fitted volume fraction of  $\text{YH}_x$  and voids as a function of illumination time. The fraction of  $\text{YH}_x$  increases with illumination time, and it tends to saturate after illumination of 120 min, while the fraction of voids increases continuously with longer illumination time. Furthermore, the photochromic contrast versus the volume fractions of metallic  $\text{YH}_x$  nanodomains and of voids are plotted in Fig. 5.4 (d) and (f). An almost linear relationship between the photochromic contrast and the volume fraction of  $\text{YH}_x$  is seen, suggesting that the formation of  $\text{YH}_x$  could be responsible for the photodarkening. After illumination of 150 min, the volume fraction of  $\text{YH}_x$  domains reaches  $\sim 2.6\%$  with an increase in the photochromic contrast of  $\sim 33\%$ , *i.e.* very similar to the reported volume fraction of  $\text{YH}_3\text{O}_z^m$  metallic domains of  $\sim 2\%$  with a relative decrease in transmittance of 30% in ref. [9], in which an EMA model was employed assuming that metallic inclusions are inserted to a



**Figure 5.4:** (a) The imaginary part ( $\epsilon_2$ ) and (b) real part ( $\epsilon_1$ ) of the dielectric function as a function of photon energy in the  $\text{YH}_x\text{O}_y$  film before illumination and during illumination of 150 min, extracted from a BEMA model assuming that metallic  $\text{YH}_x$  inclusions and voids are embedded in a semiconducting  $\text{YH}_x\text{O}_y$  matrix, (c-f) the corresponding fitted volume fraction of  $\text{YH}_x$  and voids, as well as the photochromic contrast versus the volume fraction of  $\text{YH}_x$  and voids.

semiconducting  $\text{YH}_x\text{O}_y$  matrix. We further note that the XRD pattern and the extracted dielectric function ( $\epsilon_2$  and  $\epsilon_1$ ) of our  $\text{YH}_x$  thin film are similar to that of the metallic mixed phase  $\text{YH}_y\text{O}_z^m$  studied in Ref. [9], even though the bulk  $\text{YH}_x$  film studied here does not contain oxygen [14,15].

However, the formation of  $\sim 2\%$  nanoscale  $\text{YH}_x$  metallic domains clearly would require the local rearrangement and transport of a large number of both hydrogen and oxygen atoms in a reversible manner. Baba *et al.* suggested that oxygen is mobile, assuming a reversible exchange of oxygen with the ambient environment as samples bleached extremely slow in a nitrogen environment [25]. However, a much slower mobility of oxygen than of hydrogen was demonstrated in a recent  $^1\text{H}$  and  $^{17}\text{O}$  solid-state NMR study [26]. Moreover, molecular dynamics calculations also indicate that oxygen is much less mobile than hydrogen [27], due to the lower polarizability and the heavier weight of oxygen. Therefore, the mobility of hydrogen rather than oxygen mobility is considered to be a key ingredient of the photochromic effect [7]. Accordingly, the formation of  $\text{YH}_x$  in a semiconducting  $\text{YH}_x\text{O}_y$  matrix under illumination for explaining the photodarkening is doubtful, as it requires (reversible) transport of a substantial amount of both oxygen and hydrogen. Moreover, voids need to be included to achieve good correspondence to the spectroscopic ellipsometry data

in this model, with a fraction of voids ( $n=1$ ,  $k=0$ ) that increases up to a few percent (2.6-4.6%) after illumination of 150 min for all cases. Nevertheless, the formation of such a high fraction of voids is implausible, as it requires the local removal of hydrogen, oxygen and yttrium atoms at a relatively high concentration in the film, when yttrium is considered to be static in  $\text{YH}_x\text{O}_y$  [27].

We found that, instead of including voids, adding the depolarization factor as an extra fit parameter in the BEMA model can also significantly improve the quality of the fits, meaning that the shape of metallic domains varies relative to that of a sphere [28]. Ref. [28] shows that the lowest MSE is in the case of Y (10-20) with the depolarization factor varying from 0.1-0.08 and in the case of  $\text{YH}_x$  (15-19) with the depolarization factor in the range of 0.68-0.6, meaning that the Y domains are oblate spheroids, and the  $\text{YH}_x$  domains are prolate spheroids in a semiconducting  $\text{YH}_x\text{O}_y$  matrix [24,29]. The fraction of formed yttrium (hydride)-like metallic domains obtained from the fits are up to 1.8-2.7% after illumination of 150 min, which is comparable to the values obtained from the BEMA model with different fit parameters. However, as discussed above, the formation of Y or  $\text{YH}_x$  in a semiconducting  $\text{YH}_x\text{O}_y$  matrix under illumination is questionable, as this would require substantial rearrangement of both oxygen and hydrogen.

Overall, the BEMA model employing the fraction of  $\text{YH}_x$  or/and Y inclusions and an additional fit parameter, i.e. the fraction of voids or the depolarization factor, can well describe the experimental ellipsometry data of  $\text{YH}_x\text{O}_y$  in the photodarkened state. However, substantial local rearrangements and transport of both hydrogen and oxygen is required, that moreover should occur in a reversible manner, indicating that the formation of these types of metallic domains in a semiconducting  $\text{YH}_x\text{O}_y$  matrix is not a viable model.

## **B. Model 2: Metallic domains related to Anderson-Mott insulator-to-metal transition**

Besides the BEMA model, used to examine the formation of phase-segregated yttrium (hydride) metal regions as described in the previous section, a KK-consistent B-spline approach was applied to fit the ellipsometry data of the  $\text{YH}_x\text{O}_y$  film during photodarkening, in order to assess the possible occurrence of an Anderson-Mott insulator-to-metal transition. The KK-consistent B-spline approach only assumes the presence of a roughness layer and a photochromic layer on top of the f-SiO<sub>2</sub> substrate, and no further assumptions on the physical properties of the film are made. The MSE values of all fits using this approach are in the range of 5-7, indicating a very good quality of fits, validating the above-mentioned approach. Representative ellipsometry spectra for the photodarkened  $\text{YH}_x\text{O}_y$  film at incident angles of 60°, 65°, and 70° and corresponding fits using a KK-consistent B-spline approach after illumination of 10 min and 150 min are shown in Fig. S5.3. The dynamic changes in the imaginary part ( $\epsilon_2$ ) and real part ( $\epsilon_1$ ) of the dielectric function of the  $\text{YH}_x\text{O}_y$  film during illumination of up to 150 min, extracted from this approach are shown in Fig. 5.5 (a) and (b). The corresponding real part ( $n$ ) and imaginary part ( $k$ ) of the complex refractive index can

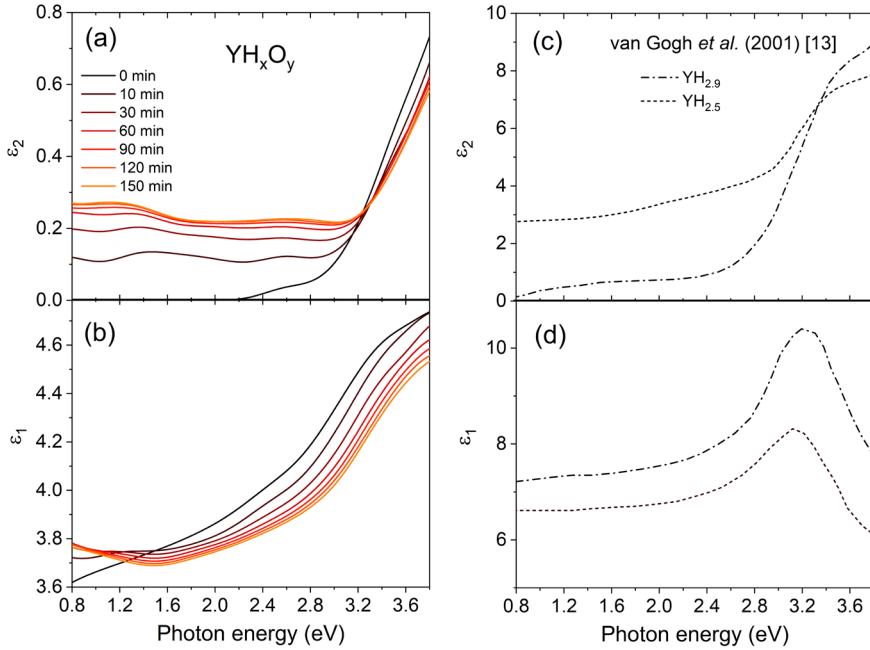


**Figure 5.5:** (a) The imaginary part ( $\epsilon_2$ ) and (b) real part ( $\epsilon_1$ ) of the dielectric function as a function of photon energy in the  $\text{YH}_x\text{O}_y$  film before illumination and during illumination of 150 min extracted from the KK-consistent B-spline approach, compared with (c-d) the changes in  $\epsilon_2$ ,  $\epsilon_1$  from  $\text{YH}_{2.9}$  to  $\text{YH}_{2.5}$  [17]. Fig. 5 (c) and (d) reprinted from Ref. [17].

be found in Fig. S5.6. The imaginary part of the dielectric function  $\epsilon_2$  increases and the real part  $\epsilon_1$  decreases with illumination time in a wide range from the visible to near-IR, similar to the trends and values of the optical constants extracted from the BEMA model in Fig. 5.4 (a) and (b). In addition, we notice from the comparison of Fig. 5.5 (a-b) to Fig. 5.5 (c-d) that the changes in  $\epsilon_2$  and  $\epsilon_1$  in  $\text{YH}_x\text{O}_y$  during illumination resemble those of the optical transition in the switchable-mirror metal hydride thin films with a nominal composition of  $\text{YH}_{2.9}$  (semiconducting) to  $\text{YH}_{2.5}$  (metallic), where an Anderson-Mott insulator-to-metal transition appears around  $\text{YH}_{2.7}$  [17,30,31]. This suggests that a similar Anderson-Mott insulator-to-metal transition takes place in the  $\text{YH}_x\text{O}_y$  film during photodarkening. In this process, upon illumination, electron-hole pairs are generated. Subsequently, some of the  $\text{H}^-$  anions at the octahedral sites capture a photo-excited hole and form  $\text{H}^0$  atoms ( $\text{H}^- + h^+ \rightarrow \text{H}^0$ ), which become mobile and leave their lattice positions, while some of the photo-excited electrons may localize at Y (4d) orbitals around the positively charged hydrogen vacancies  $V_{\text{H}}^{\text{oct}}$  due to charge compensation. When the concentration of such Y (4d) electrons at the  $V_{\text{H}}^{\text{oct}}$  in certain domains in  $\text{YH}_x\text{O}_y$  is sufficiently large, their electron orbitals start to overlap and form an electron band, leading to an Anderson-Mott insulator-to-metal transition in such domains.

Quantitatively,  $\varepsilon_2$  increases homogeneously up to  $\Delta\varepsilon_2 \sim 0.2$  in the sub bandgap range of 0.8-2.6 eV after illumination of 150 min. Compared to the increment from  $\text{YH}_{2.9}$  to  $\text{YH}_{2.5}$  of  $\Delta\varepsilon_2 \sim 2.5-3$ , the increase in  $\varepsilon_2$  after illumination of 150 min in  $\text{YH}_x\text{O}_y$  is about twelve to fifteen times smaller, which suggests that the fraction of film transformation into metallic domains in  $\text{YH}_x\text{O}_y$  is  $\sim 6-8\%$ , when assuming that  $\text{YH}_{2.5}$  is metallic in the whole film and the formation of metallic domains in  $\text{YH}_x\text{O}_y$  is due to a similar Anderson-Mott insulator-to-metal transition. In Ref. [32] it was reported that films with the nominal composition  $\text{YH}_{2.5}$  consist of coexisting phases of cubic  $\beta$ -phase and hexagonal  $\gamma$ -phase. The cubic  $\beta$ -phase is  $\text{YH}_{2+\delta}$ -like and metallic, and the hexagonal  $\gamma$ -phase is  $\text{YH}_{3-\delta}$ -like, but whether its nature is insulating or metallic in the intermediate compositions  $\text{YH}_x$  ( $2.1 < x < 2.7$ ) is indetermined. It is known that yttrium hydrides  $\text{YH}_x$  with compositions  $x > 2.7$  are in a single phase ( $\gamma$ -phase) [32], while the metal-to-insulator transition occurs at  $x = 2.86$  [33]. If the  $\gamma$ -phase in  $\text{YH}_{2.5}$  is insulating, only about half of the insulating  $\gamma$ -phase will have been transformed into the metallic  $\beta$ -phase from the nominal composition of  $\text{YH}_{2.9}$  to  $\text{YH}_{2.5}$ . In this context, the fraction of film transformed into a metallic state in the semiconducting  $\text{YH}_x\text{O}_y$  film can be estimated to be  $\sim 3-4\%$ .

The formation of this type of metallic domains according to an Anderson-Mott insulator-to-metal transition could occur in the H-rich regions in  $\text{YH}_x\text{O}_y$ , as suggested by Dam *et al.* in ref. [7]. In this case, the formation of the metallic domains can be easily achieved chemically as it only requires the local removal of part of hydrogen from octahedral sites. We note that the formation of metallic domains related to an Anderson-Mott insulator-to-metal transition is in line with our previous Doppler broadening positron annihilation studies, that reported partially reversible shifts in the positron Doppler S and W parameters under UV illumination in both  $\text{YH}_x\text{O}_y$  and  $\text{GdH}_x\text{O}_y$  thin films [10]. In order to gain a detailed understanding of the nature and electronic structure of the metallic domains formed by an Anderson-Mott insulator-to-metal transition in  $\text{YH}_x\text{O}_y$  films, further investigations by ab-initio calculations would be needed, similar to the theoretical investigations of the Anderson-Mott transition in the trihydride system [30].

### C. Model 3: Absorbing small-bandgap YO-like domains

Finally, we examine whether the formation of small-bandgap yttrium monoxide (YO) domains could explain the nature of the changes in the optical properties of the photochromic  $\text{YH}_x\text{O}_y$  films during photodarkening. To this end, the absorption coefficient  $\alpha$  was calculated starting from the extinction coefficient  $k$  (extracted from the KK-consistent B-spline approach) based on the equation  $\alpha = \frac{4\pi k}{\lambda}$ . Fig. 5.6 (a) shows the absorption coefficient of the  $\text{YH}_x\text{O}_y$  film as function of photon energy at illumination times at 0, 10, 30, 60, 90, 120 and 150 min, where  $k$  is extracted from the KK-consistent B-spline approach. At an illumination time of 0 min, there is almost no absorption below the bandgap for the  $\text{YH}_x\text{O}_y$  film, as depicted in Fig. 5.6 (a). With increasing illumination time, the absorption coefficient of the

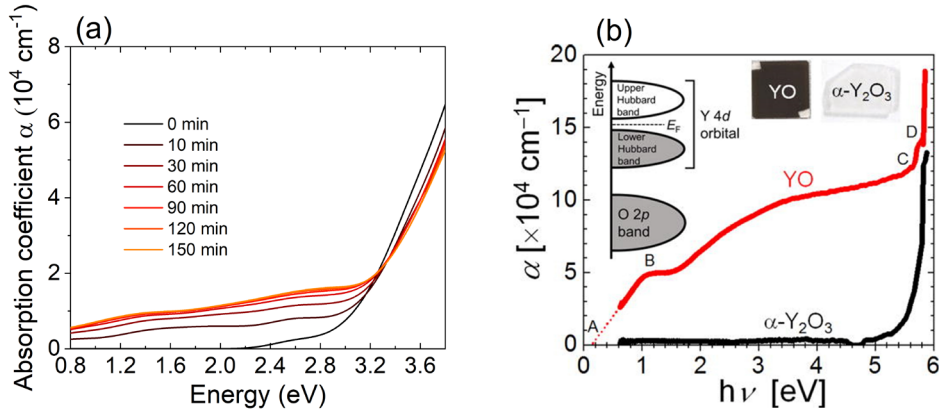


**Figure 5.6:** (a) The evolution of absorption coefficient of the  $\text{YH}_x\text{O}_y$  film as a function of photon energy before illumination and during illumination of 150 min, derived from  $k$  with the Kramers-Kronig-consistent B-spline approach, compared with (b) the absorption coefficient of the epitaxial YO film from [34]. Fig. 5.6 (b) reprinted from Ref. [34].

photodarkened  $\text{YH}_x\text{O}_y$  film increases over a broad range from the visible to near-IR, in line with the reported broad spectral absorption in the illuminated  $\text{GdH}_x\text{O}_y$  film in ref. [2,35]. In addition, we notice that the absorption coefficient decreases towards lower photon energies, which is qualitatively similar to the absorption behaviour of yttrium monoxide (YO) shown in Fig. 5.6 (b). Kaminaga *et al.* [34] reported that YO is a semiconductor with a narrow bandgap ( $\sim 0.1$  eV), and it exhibits a large absorption (coefficient of the order of  $10^4 \text{ cm}^{-1}$ ) and high electrical conductivity (from  $10^{-1}$  to  $10^3 \Omega^{-1}\text{cm}^{-1}$ ) over a wide wavelength range (0.6-5 eV). Therefore, we discuss whether the photodarkening can be caused by opaque metallic-like YO domains formed in the  $\text{YH}_x\text{O}_y$  matrix under illumination. The presence of such light-absorbing YO domains may indeed explain the broad absorption shown in Fig. 5.6 (a), while it could also explain the increased electronic conductivity in ref. [1,35-37] if the concentration of the YO domains is sufficiently large to cross the percolation limit. Furthermore, due to the thermodynamical metastability of YO [34,38], YO domains formed during illumination can be expected to disappear during bleaching in  $\text{YH}_x\text{O}_y$ . We note that the possible formation and disappearance of such rare-earth monoxide domains under illumination are not exclusive to  $\text{YH}_x\text{O}_y$ , but may also apply to gadolinium oxyhydride films, as Gd monoxides are small-bandgap semiconductors as well and exhibit a similarly high optical absorption coefficient, a high conductivity and they are thermodynamically metastable [39]. Within this model of formation of YO domains in  $\text{YH}_x\text{O}_y$  during photodarkening, quantitatively, the absorption coefficient in the range of 0.8-2.6 eV in Fig. 5.6 (a) after 150 min of illumination is on average around eight times smaller than that of the pure YO film reported in ref. [34] (see Fig. 5.6 (b)). This model suggests that  $\sim 12\%$  YO domains are formed after illumination of 150 min in  $\text{YH}_x\text{O}_y$ , i.e. a larger fraction than the



fraction derived from the Anderson-Mott insulator-to-metal transformation (~3-4%) described in section 5.3.3.B.

However, the formation of YO in  $\text{YH}_x\text{O}_y$  with different chemical compositions has distinct requirements for the movement of anions. Here, we only consider overall compositions  $\text{YH}_{3-2y}\text{O}_y$  with  $y$  in the range  $0.5 \leq y \leq 1$ , since only oxyhydride films in this range exhibit photochromism [3,14]. Photochromic oxyhydride films in this composition range of  $0.5 \leq y \leq 1$  tend to have phase segregation during synthesis, as  $\text{YH}_{2.5}\text{O}_{0.25}$  and YHO are energetically favourable compared to intermediate compositions [26]. In the H-rich region with composition of  $\text{YH}_{2.5}\text{O}_{0.25}$ , both the release of hydrogen from tetrahedral and octahedral sites as well as the local rearrangement of oxygen, *i.e.* the absorption of oxygen from other regions are required to attain YO. However, oxygen is much less mobile than hydrogen, as demonstrated by  $^1\text{H}$  and  $^{17}\text{O}$  solid-state NMR and molecular dynamics studies [7,26,40]. In the hydrogen-poor YHO regions, the removal of all hydrogen atoms at the tetrahedral sites is needed to form the YO phase, while hydrogen at the tetrahedral sites is considered to be less mobile than hydrogen at the octahedral sites [27]. In this regard, the formation of  $\text{YH}_x\text{O}$  with  $x < 1$  is chemically more favourable than YO in  $\text{YH}_x\text{O}_y$  as it requires less release of hydrogen. For  $x < 1$ , yttrium in  $\text{YH}_x\text{O}$  will have a mixed valence of  $\text{Y}^{2+}$  and  $\text{Y}^{3+}$ , and the resulting  $\text{YH}_x\text{O}$  phase might become a small bandgap semiconductor with light-absorbing properties in the full energy-range studied, when  $x$  is sufficiently small. The formation of such domains might therefore be a candidate for explaining the observed increase in the absorption coefficient  $\alpha$  in  $\text{YH}_x\text{O}_y$  under photodarkening. However, at which hydrogen composition  $\text{YH}_x\text{O}$  ( $0 < x < 1$ ) will reach the required absorbing characteristics (*i.e.* similar to the small bandgap YO semiconductor) is unknown. The required insights into the electronic structure and absorption properties of  $\text{YH}_x\text{O}$  as a function of hydrogen composition may be investigated by future ab-initio calculations.

Based on the above scenarios, we note that the formation of opaque YO-like domains is more difficult in H-rich oxyhydrides than that in hydrogen-poor oxyhydrides. However, this is contradictory to the experimentally observed higher photochromic contrast (*i.e.* formation of more or better light-absorbing species) in the H-rich  $\text{YH}_2\text{O}_{0.5}$  than in the relatively H-poor YHO [14]. In addition, a diffraction peak of YO around  $36^\circ$  is expected to be observed for the darkened  $\text{YH}_x\text{O}_y$  if ~12% of YO is formed under illumination [34,41], but such a new peak is not present in the XRD pattern of the  $\text{YH}_x\text{O}_y$  film in the photodarkened state after illumination of 2.5 h (Fig. S5.4). Therefore, these observations indicate that the formation of YO-like domains upon illumination in a  $\text{YH}_x\text{O}_y$  matrix can be ruled out as the main mechanism of photodarkening.

## 5.4 Conclusions

The optical constants of the as-prepared transparent semiconducting  $\text{YH}_x\text{O}_y$  and opaque metallic  $\text{YH}_{-2}$ ,  $\text{YH}_x$  and  $\text{Y}$  films are accurately determined by modeling spectroscopic ellipsometry data in the range from UV to near IR (0.8–3.8 eV). The results of the XRD and ellipsometry measurements show that  $\text{YH}_x$  is a mixture of  $\text{Y}$  and  $\text{YH}_{-2}$ . By employing a BEMA model to fit the ellipsometry data of the  $\text{YH}_x\text{O}_y$  film in the photodarkened state, the possibilities of the formation of metallic inclusions of either  $\text{YH}_{-2}$ ,  $\text{YH}_x$  and  $\text{Y}$  in a semiconducting  $\text{YH}_x\text{O}_y$  matrix are examined. The least agreement of the experimental data and the fits within the BEMA model is in the case of  $\text{YH}_2$ , while the best fit is in the  $\text{YH}_x$  case. However, the formation of a few percent of  $\text{YH}_x$  metallic domains in the semiconducting  $\text{YH}_x\text{O}_y$  matrix is unlikely since it requires the rearrangement and reversible local transport of a large number of both hydrogen and oxygen. On the other hand, the changes in the dielectric function of the  $\text{YH}_x\text{O}_y$  film during photodarkening are similar to that of the insulator-to-metal transition from  $\text{YH}_{2.9}$  to  $\text{YH}_{2.5}$ , suggesting that a similar Anderson-Mott insulator-to-metal transition may occur in certain domains in  $\text{YH}_x\text{O}_y$  and provides a proper explanation for the photodarkening of photochromic  $\text{YH}_x\text{O}_y$  films. The increase in  $\epsilon_2$  after illumination for 150 min in  $\text{YH}_x\text{O}_y$  suggests a film fraction transformed in a range of 3–4%. Finally, the absorption coefficient of the photodarkened  $\text{YH}_x\text{O}_y$  is similar to that of  $\text{YO}$ , suggesting that the formation of absorbing  $\text{YO}$ -like domains in the  $\text{YH}_x\text{O}_y$  film might explain the modified optical properties. However, this hypothesis can be dismissed as it contradicts with the higher photochromic contrast observed in H-rich relative to H-poor rare-earth oxyhydride films.

## References

- [1] T. Mongstad, C. Platzer-Bjorkman, J. P. Maehlen, L. P. A. Mooij, Y. Pivak, B. Dam, E. S. Marstein, B. C. Hauback, and S. Z. Karazhanov, A new thin film photochromic material: Oxygen-containing yttrium hydride, *Sol. Energy Mater. Sol. Cells* **95**, 3596 (2011).
- [2] F. Nafezarefi, H. Schreuders, B. Dam, and S. Cornelius, Photochromism of rare-earth metal-oxy-hydrides, *Appl. Phys. Lett.* **111**, 103903 (2017).
- [3] S. Cornelius, G. Colombi, F. Nafezarefi, H. Schreuders, R. Heller, F. Munnik, and B. Dam, Oxyhydride nature of rare-earth-based photochromic thin films, *J. Phys. Chem. Lett.* **10**, 1342 (2019).
- [4] S. M. Adalsteinsson, M. V. Moro, D. Moldarev, S. Droulias, M. Wolff, and D. Primetzhofer, Correlating chemical composition and optical properties of photochromic rare-earth oxyhydrides using ion beam analysis, *Nucl. Instrum. Meth. B* **485**, 36 (2020).
- [5] D. Chaykina, F. Nafezarefi, G. Colombi, S. Cornelius, L. J. Bannenberg, H. Schreuders, and B. Dam, Influence of crystal structure, encapsulation, and annealing on photochromism in Nd oxyhydride thin films, *J. Phys. Chem. Lett.* **126**, 2276 (2022).
- [6] D. Chaykina, G. Colombi, H. Schreuders, and B. Dam, Photochromic samarium oxyhydride thin films, *AIP Adv.* **13**, 055211 (2023).
- [7] B. Dam, F. Nafezarefi, D. Chaykina, G. Colombi, Z. Wu, S. W.H. Eijt, S. Banerjee, G. A. de Wijs, A. Kentgens, Perspective on the photochromic and photoconductive properties of rare-earth oxyhydride thin films, *Sol. Energy Mater. Sol. Cells* **273**, 112921 (2024).
- [8] Y. J. Ke, J. W. Chen, C. J. Lin, S. C. Wang, Y. Zhou, J. Yin, P. S. Lee, and Y. Long, Smart windows: Electro-, thermo-, mechano-, photochromics, and beyond, *Adv. Energy Mater.* **9**, 1902066 (2019).
- [9] J. Montero, F. A. Martinsen, M. Garcia-Tecedor, S. Z. Karazhanov, D. Maestre, B. Hauback, and E. S. Marstein, Photochromic mechanism in oxygen-containing yttrium hydride thin films: An optical perspective, *Phys. Rev. B* **95**, 201301(R) (2017).
- [10] Z. Wu, T. de Krom, G. Colombi, D. Chaykina, G. van Hattem, H. Schut, M. Dickmann, W. Egger, C. Hugenschmidt, E. Brück, B. Dam, and S. W. H. Eijt, Formation of vacancies and metallic-like domains in photochromic rare-earth oxyhydride thin films studied by *in situ* illumination positron annihilation spectroscopy, *Phys. Rev. Mater.* **6**, 065201 (2022).
- [11] D. Chaykina, T. de Krom, G. Colombi, H. Schreuders, A. Suter, T. Prokscha, B. Dam, and S. Eijt, Structural properties and anion dynamics of yttrium dihydride and photochromic oxyhydride thin films examined by *in situ*  $\mu^+$ SR, *Phys. Rev. B* **103**, 224106 (2021).
- [12] J. Montero, P. Svedlindh, and L. Österlund, Photo-induced reversible modification of the Curie-Weiss temperature in paramagnetic gadolinium compounds, *Solid State Commun.* **378**, 115419 (2024).

- [13] D. A. G. Bruggeman, Berechnung verschiedener physikalischer Konstanten von heterogenen Substanzen. II. Dielektrizitätskonstanten und Leitfähigkeiten von Vielkristallen der nichtregulären Systeme, *Ann. Phys.* **417**, 645 (1936).
- [14] G. Colombi, T. De Krom, D. Chaykina, S. Cornelius, S. W. H. Eijt, and B. Dam, Influence of cation (RE = Sc, Y, Gd) and O/H anion ratio on the photochromic properties of  $\text{REO}_x\text{H}_{3-2x}$  thin films, *Acs Photonics* **8**, 709 (2021).
- [15] D. Chaykina, I. Usman, G. Colombi, H. Schreuders, B. Tyburska-Pueschel, Z. Wu, S. W. H. Eijt, L. J. Bannenberg, G. A. de Wijs, and B. Dam, Aliovalent calcium doping of yttrium oxyhydride thin films and implications for photochromism, *J. Phys. Chem. C* **126**, 14742 (2022).
- [16] J. Rodriguez-Carvajal, FULLPROF: a program for Rietveld refinement and pattern matching analysis, satellite meeting on powder diffraction of the XV congress of the IUCr (Toulouse, France, 1990).
- [17] A. T. M. van Gogh, D. G. Nagengast, E. S. Kooij, N. J. Koeman, J. H. Rector, R. Griessen, C. F. J. Flipse, and R. J. J. G. A. M. Smeets, Structural, electrical, and optical properties of  $\text{La}_{1-z}\text{Y}_z\text{H}_x$  switchable mirrors, *Phys. Rev. B* **63**, 195105 (2001).
- [18] M. Zubkins, I. Aulika, E. Strods, V. Vibornijs, L. Bikse, A. Sarakovskis, G. Chikvaidze, J. Gabrusenoks, H. Arslan, J. Purans, Optical properties of oxygen-containing yttrium hydride thin films during and after the deposition, *Vacuum* **203**, 111218 (2022).
- [19] J. Montero and S. Z. Karazhanov, Spectroscopic ellipsometry and microstructure characterization of photochromic oxygen-containing yttrium hydride thin films, *Phys Status Solidi A* **215**, 1701039 (2018).
- [20] CompleteEASE software manual, J. A. Woollam, 2020.
- [21] B. Johs and J. S. Hale, Dielectric function representation by b-splines, *Phys. Status Solidi A* **205**, 715 (2008).
- [22] J. W. Weber, T. A. R. Hansen, M. C. M. van de Sanden, and R. Engeln, B-spline parametrization of the dielectric function applied to spectroscopic ellipsometry on amorphous carbon, *J. Appl. Phys.* **106**, 123503 (2009).
- [23] E. S. Kooij, J. H. Rector, D. G. Nagengast, J. W. J. Kerssemakers, B. Dam, R. Griessen, A. Remhof, and H. Zabel, Growth and hydrogenation of epitaxial yttrium switchable mirrors on  $\text{CaF}_2$ , *Thin Solid Films* **402**, 131 (2002).
- [24] Y. Degani, T. T. Sheng, A. Heller, D. E. Aspnes, A. A. Studna, and J. D. Porter, Transparent metals-preparation and characterization of light-transmitting palladium, rhodium, and rhenium films, *J. Electroanal. Chem.* **228**, 167 (1987).
- [25] E. M. Baba, J. Montero, E. Strugovshchikov, E. O. Zayim, and S. Karazhanov, Light-induced breathing in photochromic yttrium oxyhydrides, *Phys. Rev. Mater.* **4**, 025201 (2020).
- [26] S. Banerjee, D. Chaykina, R. Stigter, G. Colombi, S. W. H. Eijt, B. Dam, G. A. de Wijs, and A. P. M. Kentgens, Exploring multi-anion chemistry in yttrium oxyhydrides: Solid-state NMR studies and DFT calculations, *J. Phys. Chem. C* **127**, 14303 (2023).

- [27] R. Stigter, A computational investigation on the structure of yttrium oxyhydride compounds and their anion mobility, MSc thesis, Delft University of Technology, Delft, the Netherlands, 2020.
- [28] M. Beek, Studying the evolution of photochromic rare-earth metal oxyhydride films with UV exposure & cycling using optical transmission, X-ray diffraction, positron annihilation & ellipsometry MSc thesis, Delft University of Technology, Delft, the Netherlands, 2022.
- [29] D. Dalacu and L. Martinu, Spectroellipsometric characterization of plasma-deposited Au/SiO<sub>2</sub> nanocomposite films, *J. Appl. Phys.* **87**, 228 (2000).
- [30] K. K. Ng, F. C. Zhang, V. I. Anisimov, and T. M. Rice, Electronic structure of lanthanum hydrides with switchable optical properties, *Phys. Rev. Lett.* **78**, 1311 (1997).
- [31] A. F. T. Hoekstra, A. S. Roy, T. F. Rosenbaum, R. Griessen, R. J. Wijngaarden, and N. J. Koeman, Light-induced metal-insulator transition in a switchable mirror, *Phys. Rev. Lett.* **86**, 5349 (2001).
- [32] E. S. Kooij, A. T. M. van Gogh, D. G. Nagengast, N. J. Koeman, and R. Griessen, Hysteresis and the single-phase metal-insulator transition in switchable YH<sub>x</sub> films, *Phys. Rev. B* **62**, 10088 (2000).
- [33] J. N. Huijberts, R. Griessen, J. H. Rector, R. J. Wijngaarden, J. P. Dekker, D. G. de Groot, and N. J. Koeman, Yttrium and lanthanum hydride films with switchable optical properties, *Nature* **380**, 231 (1996).
- [34] K. Kaminaga, R. Sei, K. Hayashi, N. Happo, H. Tajiri, D. Oka, T. Fukumura, and T. Hasegawa, A divalent rare earth oxide semiconductor: Yttrium monoxide, *Appl. Phys. Lett.* **108**, 122102 (2016).
- [35] G. Colombi, B. Boshuizen, D. Chaykina, L. Y. Hsu, H. Schreuders, T. J. Savenije, and B. Dam, Large polaron conduction, photoconductivity, and photochromism in GdH<sub>x</sub>O<sub>3-2x</sub> oxyhydride thin films, *Adv. Opt. Mater.* **11**, 2202660 (2023).
- [36] C. C. You, T. Mongstad, E. S. Marstein, and S. Z. Karazhanov, The dependence of structural, electrical and optical properties on the composition of photochromic yttrium oxyhydride thin films, *Materialia* **6**, 100307 (2019).
- [37] D. Chaykina, Chasing H<sup>-</sup> in Rare-earth Metal Oxyhydrides, PhD thesis, Delft University of Technology, Delft, the Netherlands, 2022.
- [38] J. M. Leger, N. Yacoubi, and J. Loriers, Synthesis of rare-earth monoxides, *J. Solid State Chem.* **36**, 261 (1981).
- [39] T. Yamamoto, K. Kaminaga, D. Saito, D. Oka, and T. Fukumura, Rock salt structure GdO epitaxial thin film with a high ferromagnetic curie temperature, *Appl. Phys. Lett.* **117**, 052402 (2020).
- [40] K. Fukui, S. Limura, T. Tada, S. Fujitsu, M. Sasase, H. Tamatsukuri, T. Honda, K. Ikeda, T. Otomo, H. Hosono, Characteristic fast H ion conduction in oxygen-substituted lanthanum hydride, *Nat. Commun.* **10**, 2578 (2019).

[41] H. Arslan, I. Aulika, A. Sarakovskis, L. Bikse, M. Zubkins, A. Azarov, J. Gabrusenoks, and J. Purans, Reactive pulsed direct current magnetron sputtering deposition of semiconducting yttrium oxide thin film in ultralow oxygen atmosphere: A spectroscopic and structural investigation of growth dynamics, *Vacuum* **211**, 111942 (2023).

## Supplementary information for Chapter 5

Table S5.1: The resulting Drude parameters (the optical resistivity  $\rho_{\text{opt.}}$  and relaxation time  $\tau$ ) for Y, YH<sub>x</sub> and YH<sub>2</sub>, and the calculated mean free path  $l_{\text{mfp}}$ , plasma frequency  $\omega_p$  and electron density  $n_e$  from equations.

sample	$\rho_{\text{opt.}}$ ( $\mu\Omega\cdot\text{cm}$ )	$\tau$ (fs)	$l_{\text{mfp}}$ (nm)	$\omega_p$ ( $10^{16} \text{ s}^{-1}$ )	$n_e$ ( $10^{21} \text{ cm}^{-3}$ )
Y	340	1.6	1.6 ( $\approx 4.5 a$ )	0.45	6
YH <sub>x</sub>	460	1.2	1.2	0.45	6
YH <sub>2</sub>	380	1.0	1 ( $\approx 2 a_{\text{fcc}}$ )	0.54	9

As shown in Table S5.1, the optical resistivity  $\rho_{\text{opt.}}$  of all Y-based metallic films are on the order of hundreds of  $\mu\Omega\cdot\text{cm}$ . The  $\rho_{\text{opt.}}$  of Y and YH<sub>2</sub> films are close to each other, while the higher  $\rho_{\text{opt.}}$  in YH<sub>x</sub> compared to Y and YH<sub>2</sub> could be due to more scattering of electrons from the grain boundaries between two phases that exist in YH<sub>x</sub>. The  $\rho_{\text{opt.}}$  of YH<sub>2</sub> film in this work is at least two times smaller than the values of the sputtered hydride films reported by Zubkins et al. [1], which could be due to the denser structure of our film deposited at a lower pressure. Compared with e-beam evaporated films, our sputtered Y and YH<sub>2</sub> have several times higher  $\rho_{\text{opt.}}$  and shorter relaxation time  $\tau$ , which may be due to more carrier scattering from impurity centers in sputtered films coming from the Y target [2].

In addition, the mean free path  $l_{\text{mfp}}$  can be calculated based on the equation  $l_{\text{mfp}} = v_F \tau$ , where  $v_F$  is the Fermi velocity.  $v_F$  is  $\sim 10^6 \text{ ms}^{-1}$  for Y along LM [2],  $v_F$  is  $10^6 \text{ ms}^{-1}$  for YH<sub>2</sub> along GX [2], so we assume that  $v_F$  is also  $\sim 10^6 \text{ ms}^{-1}$  for YH<sub>x</sub>. Furthermore, the plasma frequency  $\omega_p$  and electron density  $n_e$  can be derived from the equations  $\omega_p = \sqrt{\frac{1}{\rho_{\text{opt.}} \varepsilon_0 \tau}}$  and  $n_e = \frac{\omega_p^2 \varepsilon_0 m^*}{e^2}$ , where,  $\varepsilon_0$  is the vacuum permittivity ( $8.854 \times 10^{-12} \text{ F/m}$ ),  $e$  represents the electron charge ( $1.602 \times 10^{-19} \text{ C}$ ),  $m^*$  is the effective mass that is assumed to be the electron mass in vacuum here. Using the lattice parameters from XRD, the atomic density of Y and YH<sub>2</sub> are estimated to be  $2.9 \times 10^{22}$  and  $2.8 \times 10^{22} \text{ atoms/cm}^3$ , respectively. Hence, the electron density per yttrium atom in Y and YH<sub>2</sub> films can be estimated to be 0.2 and 0.3, respectively. In addition, we employ three Lorentz oscillators to describe interband transitions for Y, YH<sub>x</sub> and YH<sub>2</sub> films. The equation for the Lorentz oscillator function is given by

$$\varepsilon_{\text{Lorentz}}(E) = \frac{A_n B r_n E_n}{E_n^2 - E^2 - i B r_n E}$$

Where  $A_n$  is the unitless amplitude of the oscillator,  $B r_n$  is the broadening of the oscillator in eV, approximately the full width at half-maximum (FWHM),  $E_n$  is the center energy in eV,  $i$  is the imaginary unit,  $n$  is the number of the respective oscillator.

Table S5.2: Lorentz parameters obtained from fits for as-prepared Y, YH<sub>x</sub> and YH<sub>-2</sub> films

	Y	YH <sub>x</sub>	YH <sub>-2</sub>
$\epsilon_{\infty}$	1.5	1.6	1.6
A <sub>1</sub>	9	6.8	1.5
Br <sub>1</sub> (eV)	2.9	5.1	0.7
En <sub>1</sub> (eV)	1.3	1.7	2.3
A <sub>2</sub>	3.2	1	2.6
Br <sub>2</sub> (eV)	4	1.4	1.3
En <sub>2</sub> (eV)	1.6	2.3	2.9
A <sub>3</sub>	1	0.6	2.3
Br <sub>3</sub> (eV)	3.7	2	3.3
En <sub>3</sub> (eV)	5.2	5.3	5.5

Table S5.3: MSE of the fits of the BEMA model where metallic Y, YH<sub>x</sub>, or YH<sub>-2</sub> inclusions are embedded in a homogenous semiconducting YH<sub>x</sub>O<sub>y</sub> layer.

	MSE (Y)	MSE (YH <sub>x</sub> )	MSE (YH <sub>-2</sub> )
10 min	21	18	22
30 min	29	24	28
60 min	34	28	31
90 min	37	30	33
120 min	39	33	34
150 min	40	35	36



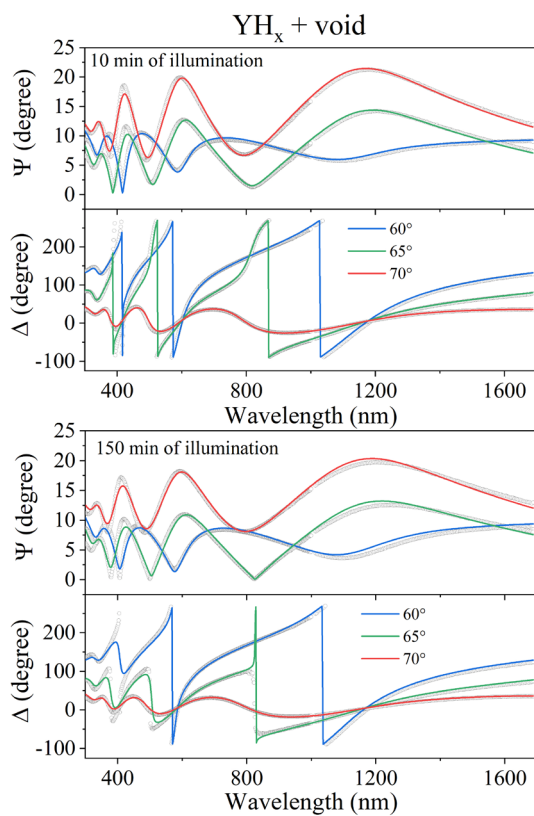


Figure S5.1: Representative ellipsometry spectra for the photodarkened  $\text{YH}_x\text{O}_y$  film collected after illumination of 10 min and 150 min at incident angles of  $60^\circ$ ,  $65^\circ$ , and  $70^\circ$  and corresponding fits using a BEMA model where  $\text{YH}_x$  inclusions and voids are embedded in a  $\text{YH}_x\text{O}_y$  matrix.

Y + void

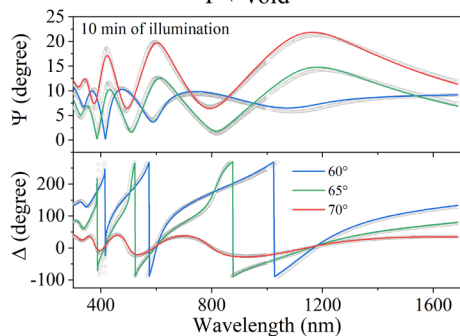
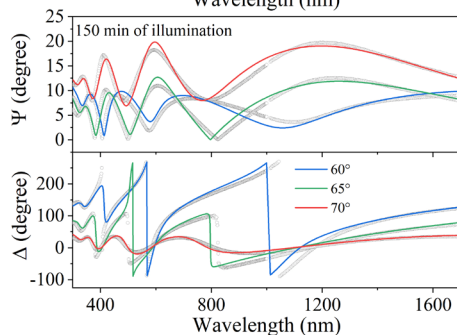
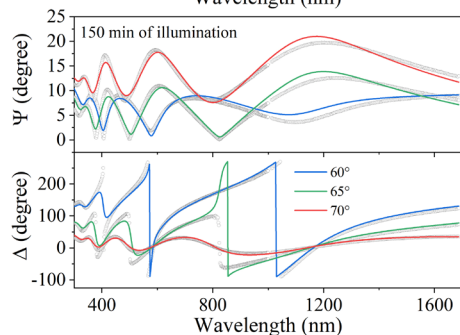
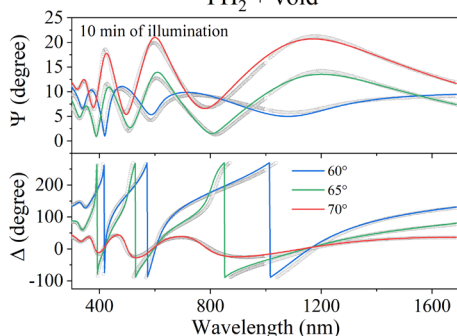
YH<sub>2</sub> + void

Figure S5.2: Representative ellipsometry spectra for the photodarkened YH<sub>x</sub>O<sub>y</sub> film collected after illumination of 10 min and 150 min at incident angles of 60°, 65°, and 70° and corresponding fits using a BEMA model where either Y inclusions and voids or YH<sub>2</sub> inclusions and voids are embedded in a YH<sub>x</sub>O<sub>y</sub> matrix.

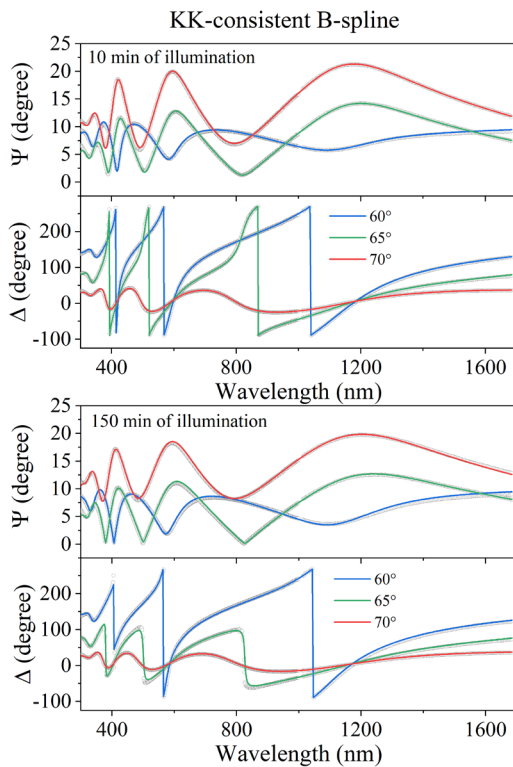


Figure S5.3: Representative ellipsometry spectra for the  $\text{YH}_x\text{O}_y$  sample collected after illumination of 10 min and 150 min at incident angles of  $60^\circ$ ,  $65^\circ$ , and  $70^\circ$  and corresponding fits using a KK-consistent B-spline model.

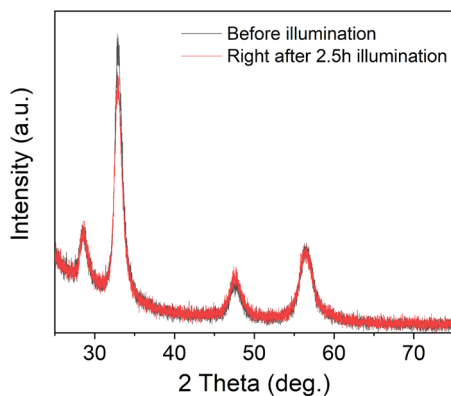


Figure S5.4: XRD patterns of the  $\text{YH}_x\text{O}_y$  sample before and after illumination of 2.5 h.

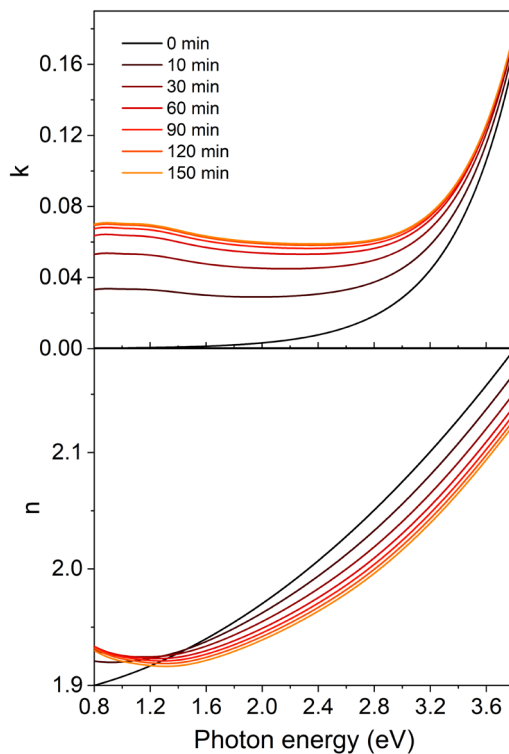


Figure S5.5: The imaginary part ( $n$ ) and real part ( $k$ ) of the complex refractive index as a function of photon energy in the  $\text{YH}_x\text{O}_y$  film before illumination and during illumination of 150 min extracted from the BEMA model.

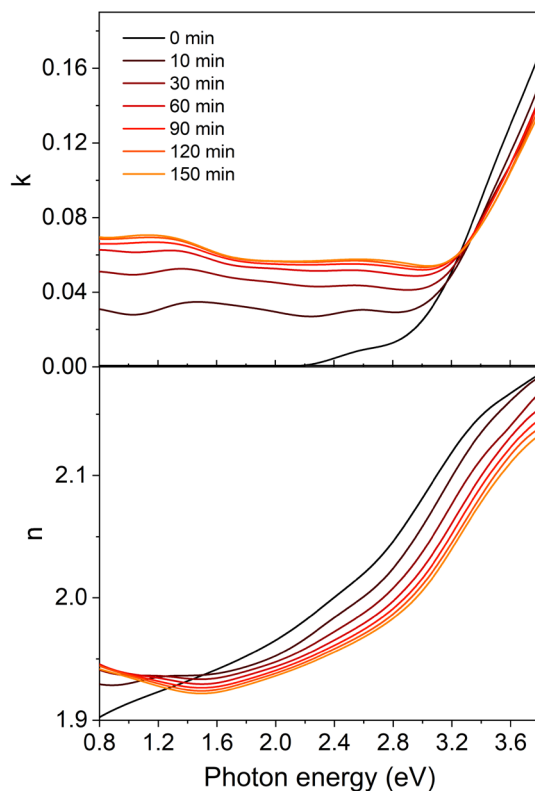


Figure S5.6: The imaginary part ( $n$ ) and real part ( $k$ ) of the complex refractive index as a function of photon energy in the  $\text{YH}_x\text{O}_y$  film before illumination and during illumination of 150 min extracted from the KK-consistent B-spline approach.

## References

- [1] M. Zubkins, I. Aulika, E. Strods, V. Vibornijs, L. Bikse, A. Sarakovskis, G. Chikvaidze, J. Gabrusenoks, H. Arslan, J. Purans, Optical properties of oxygen-containing yttrium hydride thin films during and after the deposition, *Vacuum* **203**, 111218 (2022).
- [2] A. T. M. van Gogh, D. G. Nagengast, E. S. Kooij, N. J. Koeman, J. H. Rector, R. Griessen, C. F. J. Flipse, and R. J. J. G. A. M. Smeets, Structural, electrical, and optical properties of  $\text{La}_{1-z}\text{Y}_z\text{H}_x$  switchable mirrors, *Phys. Rev. B* **63**, 195105 (2001).



## 6. General conclusions and future outlook

### General conclusions

$\text{REH}_x\text{O}_y$  films have attracted considerable attention because of their color-neutral photochromic effect. The photochromism of  $\text{REH}_x\text{O}_y$  films was first reported in yttrium oxyhydride in 2011. At the same time, a systematic slowing down of the bleaching kinetics upon photochromic cycling (the so-called memory effect) was also observed in yttrium oxyhydride films. However, at the time of starting the research described in this thesis, the microscopic mechanism behind the photochromic effect and the memory effect were not well understood. Montero et al. proposed the formation of metallic domains to explain the photochromism in  $\text{YH}_x\text{O}_y$  films, according to his ellipsometry studies. In addition, a previous positron annihilation study suggested the formation of vacancies during photodarkening-bleaching, based on the observed increase in the S-parameter, and speculated that the formed vacancy defects might be linked to the memory effect. This work focuses on investigating the nature and evolution of metallic-like domains and vacancy-related defects during photodarkening and bleaching in both  $\text{YH}_x\text{O}_y$  and  $\text{GdH}_x\text{O}_y$  films, and exploring their relationship with optical properties by a combination of in-situ illumination positron annihilation spectroscopy and spectroscopic ellipsometry studies.

In this work, DB-PAS has been successfully used to investigate the different electronic structure of yttrium-based compounds, ranging from metallic Y,  $\text{YH}_{1.9}$  to semiconducting  $\text{YH}_x\text{O}_y$  to insulating  $\text{Y}_2\text{O}_3$ . PALS results on these as-prepared films show that yttrium monovacancies are the dominant positron trapping sites and vacancy clusters are present in all studied films, while nanopores are additionally present in  $\text{YH}_x\text{O}_y$  and  $\text{Y}_2\text{O}_3$ . Having this information in mind, based on the reversible and irreversible part of the shifts of the S and W parameters obtained from in-situ illumination DB-PAS on both yttrium and gadolinium oxyhydride films, we discuss two types of metallic domains (phase-segregated hydrogen-rich metallic domains with a local composition of  $\text{YH}_2\text{O}_x$  ( $x < 0.5$ ) in a mixed  $\text{Y}^{2+}/\text{Y}^{3+}$  valence state, and Anderson-Mott insulator-to-metal transition in certain domains of the film) as possible cause for the photodarkening and suggest the formation of divacancy-like defects during photodarkening-bleaching, respectively.

The formation of metallic domains under photodarkening is consistent with the reversible part of the shifts in the S and W parameters across six in-situ photochromic cycles, as well as with the fast initial decrease in the first positron lifetime ( $\tau_1$ ) upon illumination and increase during bleaching observed in the in-situ illumination PALS study. Spectroscopic ellipsometry is further applied to examine the nature of metallic domains from an optical perspective. Combining the insights gained from the in-situ illumination PAS and in-situ illumination spectroscopic ellipsometry studies with easier removal of hydrogen from lattice positions compared to oxygen suggests that the formation of metallic domains related to Anderson-Mott insulator-to-metal transition in certain regions is the most probable

mechanism for the photochromism in  $\text{REH}_x\text{O}_y$  films. Nevertheless, the experimental results do not strictly exclude other explanations, such as the formation of yttrium monoxide-like domains in a semiconducting  $\text{REH}_x\text{O}_y$  matrix or phase-segregated  $\text{YH}_x$  metallic domains.

The evolution of light-induced vacancy defects and the bleaching kinetics over six photodarkening-bleaching cycles is further investigated by in-situ illumination DB-PAS and in-situ transmittance on both  $\text{YH}_x\text{O}_y$  and  $\text{GdH}_x\text{O}_y$  films. This establishes a clear link between light-induced vacancy defects and the memory effect. A strong correlation between the S-parameter after bleaching and the bleaching time constant is revealed, suggesting that the microstructural evolution that leads to the slower bleaching involves vacancy creation and agglomeration. This is corroborated by PALS before and after one cycle, showing the irreversible formation of divacancies and the growth of vacancy clusters after bleaching, most probably due to the release of hydrogen liberated during illumination. Furthermore, in-situ illumination PALS monitors detailed time-resolved evolution of various types of vacancy defects during photodarkening and bleaching, showing the gradual formation of divacancy-like defects during photodarkening from clustering of the preexisting yttrium monovacancies with light-induced hydrogen vacancies, as well as the fast release of hydrogen from vacancy clusters during the first few minutes of illumination.

## Future outlook

This work offers key insights into the microscopic mechanisms behind the photochromic effect and the memory effect, providing a basis for designing  $\text{REH}_x\text{O}_y$  films with improved photochromic properties for future applications. However, there are still questions to be answered in future research to fully understand the photochromic effect and the memory effect, as well as to improve the photochromic properties for practical uses.

For instance, an examination of the nature of the Anderson-Mott insulator-to-metal transition in rare-earth oxyhydrides through ab-initio calculations, as done in rare-earth hydride systems, is necessary for a fundamental understanding of the photodarkening. The formation of divacancy-like defects in subsequent cycles can be further validated by in-situ illumination PALS. To prevent the formation of mobile  $\text{H}^0$  and hydrogen vacancies during illumination, dopants with a reduced susceptibility to oxidize during post-oxidation, for example,  $\text{Er}^{2+}$ , may serve as hole trapping centers during illumination, potentially eliminating the memory effect. In addition, the investigation of the influence of the external environments, such as vacuum and other gases, on the photochromic properties of oxyhydride films is crucial for optimizing storage and working environment of  $\text{REH}_x\text{O}_y$  films for various applications. Since uncapped rare-earth oxyhydride films may keep oxidizing and releasing hydrogen in air for long periods of time, it is necessary to assess the long-term stability of the composition, microstructure or photochromic properties of  $\text{REH}_x\text{O}_y$  films with a capping layer or under different storage environments.



## Summary

The tunable color-neutral photochromic properties of rare-earth oxyhydride films render them promising for applications in smart windows, memory devices, and photo-catalysts. The investigation of the microstructural and electronic structure changes during the photodarkening-bleaching cycles and their relationship with the optical properties deepens our understanding of the photochromic effect and the memory effect (slower bleaching rate upon cycling) in rare-earth oxyhydride films. This thesis explores the nature and evolution of metallic-like domains and vacancy defects during photodarkening and bleaching by in-situ illumination positron annihilation spectroscopy and spectroscopic ellipsometry.

First, we employ in-situ illumination Doppler broadening positron annihilation spectroscopy (DB-PAS) to investigate the formation of metallic-like domains and vacancy defects in photochromic yttrium and gadolinium oxyhydride films during a photodarkening-bleaching cycle. Under illumination, partially reversible shifts in the Doppler S and W parameters toward those of the metal hydrides are observed in both yttrium and gadolinium oxyhydride films, indicating the formation of metallic-like domains. Two types of metallic-like domains that could be responsible for the photochromic effect in oxyhydride films are discussed. The first type involves the formation of phase-segregated hydrogen-rich metallic domains with a local composition of  $\text{YH}_2\text{O}_x$  ( $x < 0.5$ ) in a mixed  $\text{Y}^{2+}/\text{Y}^{3+}$  valence state, requiring illumination-induced local rearrangements and transport of both hydrogen and oxygen in the semiconducting oxyhydride matrix. The second type of metallic domains discussed involves the liberation of hydrogen only by illumination, and a hydrogen vacancies-induced Anderson-Mott insulator-to-metal transition, which is inspired by the well-known insulator-to-metal transition observed for the yttrium trihydride to dihydride hydrogen switchable mirror systems. This transition in oxyhydrides may occur when the wave functions of photo-excited electrons that are trapped at Y 4(d) orbitals at neighbouring sites of the illumination-induced hydrogen vacancies  $V_H^+$  at the octahedral sites, overlap and form metallic-like electron bands. In addition, the irreversible part of the shifts of the Doppler parameters, seen after one photodarkening-bleaching cycle, suggest that divacancy-like defects are formed by aggregation of light-induced hydrogen vacancies with yttrium monovacancies  $V_Y$ . These yttrium monovacancies are already present in the as-prepared yttrium oxyhydride films, as detected by the complementary positron annihilation lifetime spectroscopy (PALS) measurements.

Second, the evolution of vacancy defects and metallic domains upon photochromic cycling and their relationship with photochromic performance is further investigated by in-situ DB-PAS under six photodarkening-bleaching cycles in both yttrium and gadolinium oxyhydride films. For the first three cycles, DB-PAS shows a progressive increase in the S-parameter after each full cycle. A strong correlation between the S-parameter after bleaching and the bleaching time constant extracted from the transmittance measurements is observed.

This correlation suggests that the microstructural changes corresponding to the slower bleaching rate upon cycling (the memory effect) involve vacancy creation and aggregation, as the PALS measurements on yttrium oxyhydride films show the formation of divacancy-like defects and growth of vacancy clusters after one cycle. To understand the memory effect microscopically, we propose that if bleaching is a diffusion-related process, the formed vacancy defects, induced by illumination, might affect the diffusion time by reducing the diffusion coefficient. Additionally, hydrogen loss could also be a key factor in the reduced bleaching kinetics. For the second three cycles, the observed reversible shifts in the Doppler parameters between the photodarkened state and the bleached state are consistent with the reversible formation of metallic-like domains, supporting the previously proposed mechanisms of the photochromism.

Third, the time-dependent evolution of metallic-like domains and vacancy defects during photodarkening and bleaching at a time-resolution of minutes in two yttrium oxyhydride films is monitored by in-situ illumination PALS, revealing the dynamic changes in all three extracted positron lifetime components and their close relationship with the time-dependence of the optical transmittance. Upon photodarkening for the first  $\sim 3$  min, a fast decrease in the shortest positron lifetime  $\tau_1$  and a significant reduction in transmittance is seen for both samples, indicating a rapid initial formation of metallic-like domains. Simultaneously, the fast increase in  $\tau_2$  and  $\tau_3$  suggests the release of loosely-bounded hydrogen from vacancy clusters and nanopores. During further photodarkening, a gradual increase in  $\tau_1$  is seen that suggests a rise in the concentration of divacancy-like defects in the semiconducting matrix. After the above bandgap illumination is stopped, two subsequent bleaching phases are observed. In the first bleaching phase of  $\sim 15$  min, a strong linear correlation between the shortest positron lifetime  $\tau_1$  and the photochromic contrast is seen that is quantitatively very similar for both samples, suggesting that the quantity of metallic-like domains decreases, leading to increased positron trapping at yttrium monovacancies and divacancy-like defects. In the second bleaching phase, a subsequent correlation between  $\tau_1$  and the photochromic contrast is observed in the more H-rich sample, possibly due to the additional disappearance of metallic-like domains that grow to larger sizes in that sample. After bleaching, most of the metallic domains and the photoexcited electrons in the semiconducting matrix have disappeared, while the formed small vacancy complexes and grown vacancy clusters remain. Additionally, the PALS depth profiles before and after the photodarkening-bleaching cycle show that the light-induced generation of open-volume defects is homogeneously distributed throughout the oxyhydride layer. This study deepens our understanding of the (nanoscale) structure-optical property relationship in photochromic yttrium oxyhydride films.

Finally, we further examine the nature of the metallic-like domains optically using spectroscopic ellipsometry. Based on the extracted optical parameters of the  $\text{YH}_x\text{O}_y$  film in the photodarkened state, we examine three different models for the formation of metallic (or small bandgap semiconducting) light-absorbing domains in a semiconducting  $\text{YH}_x\text{O}_y$  matrix to explain the photochromic effect. Firstly, by applying the Bruggeman effective medium

approximation to the ellipsometry data of the photodarkened  $\text{YH}_x\text{O}_y$  film, we explore the possibilities of the formation of Y or Y hydride metallic domains in a semiconducting  $\text{YH}_x\text{O}_y$  matrix under illumination. The best fit suggests the formation of a few percent of  $\text{YH}_x$  (a mixture of Y and  $\text{YH}_{-2}$  phases at a ratio of  $\sim 2:1$ ) metallic inclusions within the semiconducting  $\text{YH}_x\text{O}_y$  matrix. Nevertheless, this model is questionable, as it would require the reversible rearrangements and transport of a significant amount of both oxygen and hydrogen. Furthermore, the formation of a high concentration of very large voids or specific (oblate/prolate) shapes of the metallic-like domains are required to explain the optical properties in the photodarkened state. Secondly, as an alternative model, we examine the formation of metallic domains related to the Anderson-Mott insulator-to-metal transition in certain regions of the matrix. The changes in the dielectric function of the  $\text{YH}_x\text{O}_y$  film in the visible to near-IR range during photodarkening, as derived by employing a Kramers-Kronig consistent basis-spline approach, closely resemble the optical transition from semiconducting  $\text{YH}_{2.9}$  to metallic  $\text{YH}_{2.5}$  films observed in studies on hydrogen switchable mirrors. This suggests that the Anderson-Mott insulator-to-metal transition that occurs in these rare-earth hydride systems also takes place in the photodarkened  $\text{YH}_x\text{O}_y$  film with up to  $\sim 4\%$  of metallic domains formed. This model only requires the local removal of a part of the octahedral hydrogen, induced by the above-bandgap optical illumination. Finally, a third model, based on the formation of small bandgap yttrium monoxide-like domains can give a reasonable description of the optical absorption in the photodarkened state, but is dismissed as the main origin of the photodarkening of photochromic  $\text{YH}_x\text{O}_y$  films, as (1) the highest photochromic contrast is observed in hydrogen-rich oxyhydride films rather than compositions close to  $\text{YHO}$ , and (2) significant rearrangements and transport of a significant amount of both oxygen and hydrogen is required also in this model.



## Samenvatting

De instelbare kleur-neutrale fotochrome eigenschappen van zeldzame-aarde oxyhydridelagen maken deze lagen veelbelovend voor toepassingen in slimme ramen, geheugens en fotokatalysatoren. Het onderzoek aan de veranderingen in microstructuur en elektronenstructuur gedurende cycli van door belichting donker en transparant maken en hun relatie met de optische eigenschappen verdiept ons begrip van het fotochroom effect en het geheugeneffect (het langzamer transparant worden ten gevolge van het cycleren) in zeldzame-aarde oxyhydride lagen. Dit proefschrift exploreert de aard en evolutie van metaalachtige domeinen en vacature defecten gedurende het donker maken door belichting en de daaropvolgende relaxatie naar een transparante toestand met behulp van positron annihilatie spectroscopie met in-situ belichting en met spectroscopische ellipsometrie.

Als eerste gebruiken wij Doppler verbreding positron annihilatie spectroscopie (DB-PAS) met in-situ belichting om de vorming van metaalachtige domeinen en vacature defecten in fotochrome yttrium- en gadoliniumoxyhydride dunne lagen gedurende een donker-transparant cyclus te onderzoeken. Onder belichting worden partieel reversibele verschuivingen in de Doppler S en W parameters in de richting van de waarden voor metaalhydriden waargenomen in zowel yttrium- als gadolinium-oxyhydride dunne lagen, wat een indicatie is voor de vorming van metaalachtige domeinen. Twee typen metaalachtige domeinen, die verantwoordelijk zouden kunnen zijn voor het fotochroom effect in oxyhydride dunne lagen, worden besproken. Het eerste type houdt de vorming in van fase-gesegregeerde waterstofrijke metallische domeinen met een lokale samenstelling van  $\text{YH}_2\text{O}_x$  ( $x < 0.5$ ) in een gemengde  $\text{Y}^{2+}/\text{Y}^{3+}$  valentietoestand, wat belichting-geïnduceerde lokale herschikkingen en transport van zowel waterstof als zuurstof in de halfgeleidende oxyhydride matrix vereist. Het tweede type metallische domeinen, dat wordt besproken, houdt de vrijmaking in van alleen waterstof door belichting en een Anderson-Mott isolator-metaal overgang geïnduceerd door waterstofvacatures, wat wordt geïnspireerd door de bekende isolator-metaal overgang van yttrium trihydride naar dihydride, die wordt waargenomen in dit met waterstof schakelbare spiegelsysteem. Deze isolator-metaal overgang in oxyhydriden kan plaats vinden als de golf functies van foto-geëxciteerde elektronen die gevangen zijn in Y 4(d) orbitalen op naburige roosterplaatsen van de door belichting ontstane waterstofvacatures  $V_H^+$  op de octahedrale roosterplaatsen, overlappen en metaalachtige elektronenbanden vormen. Daarnaast suggereert het irreversibele deel van de verschuivingen van de Doppler parameters, die worden gezien na één cyclus van donker en transparant maken door belichting, dat divacatureachtige roosterfouten worden gevormd door aggregatie van door licht geïnduceerde waterstofvacatures met yttrium monovacatures  $V_Y$ , die al aanwezig zijn in de originele yttrium oxyhydride dunne lagen, gedetecteerd door de complementaire metingen met positron annihilatie levensduur spectroscopie (PALS).

Ten tweede wordt de evolutie van vacature roosterfouten en metallische domeinen onder fotochrome cycli en hun relatie met fotochrome prestatie verder onderzocht door in-situ DB-PAS onder zes cycli van donker maken door belichting en relaxatie naar de transparante toestand, in dunne lagen van zowel yttrium als gadolinium oxyhydride. Voor de eerste drie cycli laat DB-PAS een progressieve toename zien in de S-parameter na elke volledige cyclus. Een sterke correlatie tussen de S-parameter na relaxatie naar de transparante toestand en de tijdconstante van relaxatie naar de transparante toestand, verkregen uit de transmissie metingen, wordt waargenomen. Deze correlatie suggereert dat de microstructurele veranderingen, die corresponderen met de tragere relaxatiesnelheid naar de transparante toestand ten gevolge van cycleren (het geheugeneffect), de creatie en aggregatie van vacatures inhouden, aangezien de PALS metingen aan yttrium oxyhydride dunne lagen de vorming van divacatureachtige roosterfouten en de groei van vacatureclusters na één cyclus laten zien. Om het geheugeneffect microscopisch te begrijpen, stellen wij voor, dat, als de relaxatie naar de transparante toestand een diffusie-gerelateerd proces is, de gevormde vacatures, die geïnduceerd worden door belichting, de diffusietijd zouden kunnen beïnvloeden door de diffusiecoëfficiënt te reduceren. Verder zou waterstofverlies ook een sleutelfactor in de gereduceerde kinetiek van relaxatie naar de transparante toestand kunnen zijn. Voor de tweede drie cycli zijn de waargenomen reversibele verschuivingen in de Doppler parameters tussen de donker gemaakte toestand en de transparante gerelaxeerde toestand consistent met de reversibele vorming van metaalachtige domeinen, wat de eerder voorgestelde mechanismen van het fotochroom effect ondersteunt.

Ten derde wordt de tijdafhankelijke evolutie van metaalachtige domeinen en vacatures gedurende het donker maken door belichting en relaxatie naar de transparante toestand in twee yttrium oxyhydride dunne lagen bepaald door PALS onder in-situ belichting met een tijdoplossend vermogen van minuten, waardoor de dynamische veranderingen in alle drie verkregen componenten van het positronlevensduur spectrum en hun nauw verband met de tijdafhankelijkheid van de optische transmissie worden ontrafeld. Onder het donker maken door belichting wordt voor de eerste  $\sim 3$  min. een snelle afname in de kortste positronlevensduur  $\tau_1$  en een significante reductie in transmissie gezien voor beide monsters, wat wijst op een snelle initiële vorming van metaalachtige domeinen. Tegelijkertijd suggereert de snelle toename van  $\tau_2$  en  $\tau_3$  het vrijkomen van zwak gebonden waterstof uit vacatureclusters en nanoporiën. Gedurende het vervolgens verder donker maken door belichting wordt een geleidelijke toename in  $\tau_1$  gezien, die een verhoging van de concentratie van divacatureachtige kristalfouten in de halfgeleidende matrix suggereert. Nadat de UV belichting is gestopt, worden twee daaropvolgende fasen in de relaxatie naar de transparante toestand waargenomen. In de eerste fase van  $\sim 15$  min. wordt een sterke lineaire correlatie tussen de kortste positronlevensduur  $\tau_1$  en het fotochrome contrast gezien, die kwantitatief zeer vergelijkbaar is voor beide monsters, wat suggereert dat de hoeveelheid metaalachtige domeinen afneemt, hetgeen leidt tot verhoogde positronvangst in yttrium monovacatures en divacatureachtige roosterfouten. In de tweede fase wordt een daaropvolgende correlatie

tussen  $\tau_1$  en het fotochrome contrast waargenomen in het waterstofrijker monster, mogelijk te danken aan het additioneel verdwijnen van metaalachtige domeinen, die tot grotere afmetingen zijn gegroeid in dat monster. Na relaxatie naar de transparante toestand zijn de meeste metallische domeinen en de fotogeëxciteerde elektronen in de halfgeleidende matrix verdwenen, terwijl de gevormde kleine vacaturecomplexen en gegroeide vacatureclusters bewaard blijven. Bovendien tonen de PALS diepteprofielen voor en na de cyclus van donker maken door belichting en relaxatie naar de transparante toestand aan, dat de door licht geïnduceerde generatie van open-volume roosterfouten homogeen verdeeld is over de oxyhydride laag. Deze studie verdiept ons begrip van de (nanoschaal) relatie tussen structuur en optische eigenschappen van fotochrome yttrium oxyhydride dunne lagen.

Ten slotte onderzoeken wij de aard van de metaalachtige domeinen nader met behulp van de optische techniek spectroscopische ellipsometrie. Op basis van de verkregen optische parameters van de  $\text{YH}_x\text{O}_y$  dunne laag in de donkere toestand onderzoeken wij de toepasbaarheid van drie verschillende modellen voor de vorming van metallische (of halfgeleidende met kleine bandkloof) licht-absorberende domeinen in een halfgeleidende  $\text{YH}_x\text{O}_y$  matrix om het fotochrom effect te verklaren. Ten eerste onderzoeken wij, door de effectieve medium benadering van Bruggeman toe te passen op de ellipsometriedata van de door belichting donker gemaakte  $\text{YH}_x\text{O}_y$  dunne laag, de mogelijkheid van de vorming van Y of Y hydride metallische domeinen in een halfgeleidende  $\text{YH}_x\text{O}_y$  matrix onder belichting. De beste fit suggereert de vorming van een paar procent  $\text{YH}_x$  (bestaande uit een mengsel van Y en  $\text{YH}_{-2}$  fasen in een verhouding van  $\sim 2:1$ ) metallische insluitingen in de halfgeleidende  $\text{YH}_x\text{O}_y$  matrix. Niettemin is dit model vatbaar voor discussie, omdat het de reversibele herschikking en transport van een significante hoeveelheid van zowel zuurstof als waterstof zou vereisen. Bovendien is de vorming van een hoge concentratie van zeer grote holten of specifieke (oblate/prolate) vormen van de metaalachtige domeinen vereist om de optische eigenschappen in de donker gemaakte toestand te verklaren. Ten tweede onderzoeken wij, als een alternatief model, de vorming van metallische domeinen in verband met een Anderson-Mott isolator-metaal overgang in bepaalde gebieden van de matrix. De veranderingen in de diëlektrische functie van de  $\text{YH}_x\text{O}_y$  dunne laag in het bereik van zichtbaar licht tot nabij-IR gedurende het donker maken door belichting, zoals afgeleid door gebruik te maken van een Kramers-Kronig consistente basis-spline benadering, lijken sterk op de optische overgang van halfgeleidende  $\text{YH}_{2.9}$  naar metallische  $\text{YH}_{2.5}$  dunne lagen waargenomen in studies van met waterstof schakelbare spiegels. Dit suggereert dat de Anderson-Mott isolator-metaal overgang die voorkomt in deze zeldzame-aarde hydride systemen ook plaats vindt in de donker gemaakte  $\text{YH}_x\text{O}_y$  dunne laag, waarin tot  $\sim 4\%$  metallische domeinen zijn gevormd. Dit model vereist alleen het lokaal verwijderen van een deel van de octahedrale waterstof, geïnduceerd door de optische belichting boven de bandkloof. Tenslotte kan een derde model, gebaseerd op de vorming van yttriummonoxide-achtige domeinen met een kleine bandkloof een redelijke beschrijving geven van de optische absorptie in de door belichting donker gemaakte toestand, maar dit wordt afgewezen als de

hoofdoorzaak van het donker worden van fotochrome  $\text{YH}_x\text{O}_y$  dunne lagen, omdat (1) het hoogste fotochrome contrast wordt waargenomen in waterstofrijke oxyhydride dunne lagen en niet bij samenstellingen dicht bij YHO en (2) significante herschikkingen en transport van een significante hoeveelheid van zowel zuurstof als waterstof zijn ook in dit model nodig.



## Acknowledgements

Embarking on a PhD journey in the Netherlands has been one of the most meaningful decisions of my life. As I conclude this chapter and look forward to new beginnings, I wish to express my heartfelt gratitude to everyone who has supported and shared this experience with me.

First, I would like to express my deepest gratitude to my promotor, Dr Stephan Eijt. Working closely with you has been invaluable, and I am grateful for your encouragement, patience, and guidance throughout this journey. You are my guiding light in this journey, constantly illuminating and guiding my way. Thank you for sharing your wealth of knowledge, stories and experience with me. Your positivity in times of challenge have profoundly influenced me. I also have learned so much from your approach to work, research, and mentorship.

Prof. Ekkes Brück, thank you for being my promotor, you can always come up with straight-to-the-point questions. Your generosity and support have greatly benefited both me and Fengqi, both professionally and personally. Prof. Bernard Dam, your critical questions have been instrumental in shaping me as a researcher. You are patient, a good listener, and a sincere advisor. Thank you for your compliments and for giving me room to grow. Dr. Henk Schut, thank you for guiding me from the fundamentals of positron science to problem-solving. Your ability to explain difficult concepts clearly and foster deep thinking has been inspiring, and I appreciate the reassurance that it's okay to make mistakes along the way.

My sincere thanks to my collaborators, without whom this work would not have been possible. I am grateful to Dr. Marcel Dickmann for performing positron lifetime calculations and sharing calculation details, and to Prof. Christoph Hugenschmidt for his valuable feedback on manuscripts and conference abstracts. My thanks also go to the positron team in Dresden. Dr. Maciej Oskar Liedke, thank you for providing enthusiastic support from beamtime application, experiments and data analysis to manuscripts. I am grateful to Dr. Maik Butterling for performing experiments and data analysis, and to Dr. Andreas Wagner for his help with experiments and assistance in an emergent situation. I would also like to thank all members of the Mat4Sus project. Dr. Diana Chaykina, thank you for making good samples, sharing your findings, and commenting on manuscripts. You are a nice person to work with and I have enjoyed the small talks with you. Dr. Giorgio Colombi, thank you for your assistance with PHOCS, LED, samples and transmittance measurements. I appreciate your insights and critical comments. You are intelligent and amusing, and I believe that you will have a bright future. Thanks also go to Dr. Shrestha Banerjee, Prof. Arno Kentgens and Dr. Gilles deWijs for the insightful discussions during project meetings. I also thank Yilong Zhou for the help with ellipsometry. I thank Andrea Bracesco and Prof. Adriana Creatore for providing perovskite samples, although these results are not included in this thesis.

Many thanks to the technician team in Delft. Martijn de Boer, I appreciate your assistance in positron experiments in both Dresden and Delft. Herman Schreuders, thank you for your

technical support in the ChemE labs and for preparing new samples. Both of you are warm hearted and thank you for your care and support. Thanks to Walter Legerstee for granting us access to and assisting with the AFM located in the RID basement, and to Marcel Bus for capturing AFM images. Thanks to Kees Goubitz, Robert Dankelman, and Michel Steenvoorden for the help with XRD.

My appreciation also goes to all MSc and BSc students I have had the pleasure to supervise. Tess, you are a kindhearted, delightful and lovely girl, thank you for exploring the adventure of perovskite with me. Lidwin, you are bright and disciplined. I am impressed by your insights and ideas for the research as a bachelor student. Melanie, you are independent and easy to work with. Marieke, no worries, everyone has their own pace. Julius, your intelligence, adaptability, and energy give me confidence in your future success.

Further, I would like to thank my wonderful colleagues and friends. Nicole and Ilse, we would not have such a well-organized and joyful group without your endless help and dedication. Anton, you are kind and sincere, thank you for the help with SQUID. Jouke, thank you for helping with software issues and for translating the summary into Dutch. Thanks to Bert for welcoming me to your home for the New Year party, and organizing Spring outings. Piet, thank you for driving me to my doctor at an emergent situation. Your comforting words were like a ray of sunshine at a time when I needed. Diego, we have shared happy and difficult moments, thank you for being a companion on this journey. Thanks to Bowei for the help in life. I also want to thank other FAME group members, Niels, Iulian, Hamutu, Xinmin, Ivan, Qi, Defang, Anika, Hangai, Zamran, Øyvind and Suye for the nice discussion and friendly conversations. Thanks to my officemates Yifan and Yueer for your company. Yueer, you are warm and delightful, thanks for your care over the years. Jingjing, our time spent playing games, exercising, and hanging out has been a good way to relax. Min, Speaking Cantonese with you brings me a sense of home and I have enjoyed fun stories and the time together. My thanks also extend to other colleagues and friends, including Zhaolong, Zhu, Chenglong, Qidi, Shengnan, Chaofan, Runze, Juncheng, Jackey, Bing, Justin, David, Huanhuan, Chao, Hanan, Katja, Bifo, Max, Marc, Casper, Xuehang, Lars, Swapna, Pedro, Steven, Lambert, Wim, Femke, Hao, Wenxuan, Tian, Xavier, Tingting, Xinxin, Qingru, Jin, etc., for sharing the enjoyable moments with me. Meeting positron experts at SLOPOS-16, including Marie, Torsten, Jacob, David, Zhiwei, Eryang, Tiancheng, Yamin, etc. has been a pleasure. I am grateful to the former badminton team for the fun times we shared at X.

Finally, I greatly thank my family, especially my mom and dad for their unwavering love and great support in every way. Thank my younger brother for taking such good care of our family during these years, allowing me to focus on my research and life here without worry. Fengqi, you have been an incredible partner in both life and work. Thank you for your care, understanding and support. You are my rock, with you by my side, I face the long road ahead without fear.

Ziying  
Delft, November 2024

## Curriculum Vitae



Ziying Wu was born on the 14<sup>th</sup> of November, 1992 in Dongguan, China. With a postgraduate recommendation, she started her graduate studies under the supervision of Prof. Lei Zhang at South China University of Technology. During her master's program, she stepped into the field of chemochromic materials. Specifically, she designed, synthesized and characterized novel Rhodamine B-based organic molecules for detecting Fe (III) in solvent solutions and living cells. Those molecules exhibit a color change and emit characteristic fluorescence in solvent upon selectively binding to Fe (III). In 2019, she received her Master's degree in medicinal biology. In February 2020, she shifted

her research direction to photochromic materials and embarked on her PhD journey at Delft University of Technology under the supervision of Dr. Stephan Eijt and Prof. dr. Ekkes Bruck, in close collaboration with Prof. dr. Bernard Dam. Her research explores the relationship between microstructure and optical properties in inorganic photochromic rare-earth oxyhydride thin films. The findings of her research are presented in this thesis.



# List of publications

## Publications related to the PhD study

1. **Z. Wu**, M. Beek, G. Colombi, Y. Zhou, D. Chaykina, H. Schreuders, E. Brück, B. Dam, S. W.H. Eijt, The formation of metallic domains by Anderson-Mott insulator-to-metal transition in photochromic yttrium oxyhydride films studied by in-situ spectroscopic ellipsometry, in preparation.
2. **Z. Wu**, D. Chaykina, H. Schreuder, H. Schut, M. de Boer, M. Oskar Liedke, M. Butterling, A. Wagner, M. Dickmann, E. Brück, B. Dam, S. W.H. Eijt, The evolution of vacancies and metallic domains in photochromic yttrium oxyhydride films studied by in-situ illumination positron annihilation lifetime spectroscopy, in peer review.
3. **Z. Wu**, L. de Wit, M. Beek, G. Colombi, D. Chaykina, H. Schreuder, H. Schut, M. Oskar Liedke, M. Butterling, A. Wagner, M. Dickmann, E. Brück, B. Dam, and S. W.H. Eijt, The memory effect in photochromic rare-earth oxyhydride thin films studied by in-situ positron annihilation spectroscopy upon photodarkening-bleaching cycling, *Physical Review Materials* 8, 045201 (2024).
4. B. Dam, F. Nafezarefi, D. Chaykina, G. Colombi, **Z. Wu**, S. W.H. Eijt, S. Banerjee, G. A. de Wijs, A. Kentgens, Perspective on the Photochromic and Photoconductive properties of Rare-Earth Oxyhydride thin films, *Solar Energy Materials and Solar Cells*, 273, 112921 (2024).
5. F. Zhang, **Z. Wu**, J. Wang, W. Chen, Z. Wu, X. Chi, C. Zhao, S. Eijt, H. Schut, X. Bai, Y. Ren, N. van Dijk, E. Brück, Impact of fast-solidification on all-*d*-metal NiCoMnTi based giant magnetocaloric Heusler compounds, *Acta Materialia*, 265, 11595 (2024).
6. **Z. Wu**, T. de Krom, G. Colombi, D. Chaykina, G. van Hattem, H. Schut, M. Dickmann, W. Egger, C. Hugenschmidt, E. Brück, B. Dam, and S. W. H. Eijt, Formation of vacancies and metallic-like domains in photochromic rare-earth oxyhydride thin films studied by in-situ illumination positron annihilation spectroscopy, *Physical Review Materials* 6, 065201 (2022).
7. D. Chaykina, I. Usman, G. Colombi, H. Schreuders, B. Tyburska-Pueschel, **Z. Wu**, S. W. H. Eijt, L. J. Bannenberg, G. A. de Wijs, and B. Dam, Aliovalent calcium doping of yttrium oxyhydride thin films and implications for photochromism, *Journal of Physical Chemistry C*, 126, 14742 (2022).
8. F. Zhang, I. Batashev, Q. Shen, **Z. Wu**, R. I. Smith, G. A. de Wijs, N. van Dijk, E. Brück, Impact of F and S doping on (Mn,Fe)<sub>2</sub>(P,Si) giant magnetocaloric materials, *Acta Materialia*, 234, 118057 (2022).

## Publications related to the Master study

9. **Z. Wu**, Z. Xu, H. Tan, X. Li, J. Yan, C. Dong, L. Zhang, Two novel rhodamine-based fluorescent probes for the rapid and sensitive detection of  $\text{Fe}^{3+}$ : Experimental and DFT calculations, Spectroscopic and computational investigations, *Spectrochimica Acta Part A: Molecular and Biomolecular Spectroscopy*, 213, 167 (2019).
10. **Z. Wu**, Z. Xu, J. Yan, Y. Li, Q. Kou, L. Zhang, Development of rhodamine based fluorescent probes for sensitive detection of  $\text{Fe}^{3+}$  in water: Spectroscopic and computational investigations, *New Journal of Chemistry*, 43, 1725 (2019).
11. Z. Xu, **Z. Wu**, H. Tan, J. Yan, L. Zhang, Piperazine tuned NBD based colorimetric and fluorescent turn off probes for hydrogen sulphide, *Analytical Methods*, 10, 3375 (2018).

## Conference presentations

1. **Z. Wu et al.**, Spectroscopic ellipsometry investigations of the photochromic effect in yttrium oxyhydride films, NWO Physics, the Netherlands, Jan. 2024 (Oral presentation)
2. **Z. Wu et al.**, Study of the memory effect in photochromic rare-earth oxyhydride thin films during multiple UV illumination cycles, 16th International Workshop on Slow Positron Beam Techniques & Applications (SLOPOS-16), Orléans, France, Jul. 2023 (Oral presentation)
3. **Z. Wu et al.**, “Study of the memory effect in photochromic yttrium oxyhydride during multiple UV illumination cycles”, NWO Physics, the Netherlands, Apr. 2023 (Poster)
4. **Z. Wu et al.**, “Positrons reveal nano-domain formation in photochromic oxyhydrides”, Chemistry As Innovating Science (NWO CHAINS), the Netherlands, Sep. 2022 (Oral presentation)
5. **Z. Wu et al.**, “Study of photochromic  $\text{YH}_x\text{O}_y$  and  $\text{GdH}_x\text{O}_y$  thin films during UV illumination (cycles) by in-situ positron annihilation spectroscopy”, 19th International Conference on Positron Annihilation (ICPA-19), Aug. 2022 (Oral presentation)
6. **Z. Wu et al.**, “Photochromism of rare-earth oxyhydride thin films - New insights from positron annihilation spectroscopy”, European Materials Research Society (E-MRS) Spring Meeting, May 2022 (Oral presentation)
7. **Z. Wu et al.**, “Photochromism of oxyhydride films studied by positron annihilation spectroscopy”, International Conference on Mixed-Anion Compounds (ICMAC), Dec. 2021 (Oral presentation)
8. **Z. Wu et al.**, “Investigation of open volume in photochromic  $\text{YH}_x\text{O}_y$  thin films by positron annihilation lifetime spectroscopy”, 12.5th International Workshop on Positron and Positronium Chemistry (PPC 12.5), Aug. 2021 (Oral presentation)
9. **Z. Wu et al.**, “Visualization of vacancy defects in Y,  $\text{YH}_2$ ,  $\text{YH}_x\text{O}_y$  and  $\text{Y}_2\text{O}_3$  thin films by positron annihilation techniques”, Chemistry As Innovating Science (NWO CHAINS), the Netherlands, Dec. 2020 (Poster)

